Isomerization and fragmentation of polyatomic molecules induced by ultraviolet and extreme UV light

by

Shashank Pathak

M.Sc., University of Mumbai - Center for Excellence in Basic Sciences, India, 2014

AN ABSTRACT OF A DISSERTATION

submitted in partial fulfillment of the
requirements for the degree

DOCTOR OF PHILOSOPHY

Department of Physics
College of Arts and Sciences

KANSAS STATE UNIVERSITY
Manhattan, Kansas

2021

Abstract

Imaging molecular structures evolving at their natural timescales, during a chemical reaction, with an atomic-scale resolution has been a long-standing goal for physicists and chemists. With the recent developments in experimental techniques, as well as the light sources, such as synchrotron radiation sources, free-electron lasers (FELs), ultrafast lasers, and high-harmonic sources, it is now possible to study the molecular dynamics and structural changes with femtosecond (in some cases attosecond) time-resolution, for near-infrared to x-ray wavelengths. These advancements are particularly useful in studying a wide range of photoinduced chemical reactions and photoinduced fragmentation. In this thesis, some of the advanced techniques are used to study photoinduced isomerization and fragmentation. This thesis also partly focuses on developing the tools and techniques which can be used to study these molecular structural changes.

Several molecular systems are studied throughout the thesis. Some of them are studied with the goal of understanding the chemistry post photoexcitation and photo-fragmentation, while others were aiming for method development for future experiments. Specifically, some of the experiments are performed on a prototypical heterocyclic ring molecule, thiophenone. One such experiment studies photochemistry after ultraviolet light absorption, using time-resolved photoelectron spectroscopy at a free-electron laser. The experimental results are combined with ab-initio molecular dynamics and electronic structure calculation for the ground state and excited state molecules, which revealed insights about the electronic and nuclear dynamics. Ring-opening is the most dominant process upon photoexcitation, driven by a ballistic extension of C-S bond, and is completed within ∼350 fs. The ground state trajectories also confirm the formation of three ring-opened products, providing detailed

insights into this reaction. Ring-opening reactions of similar types are considered as candidates for designing fast molecular switches. In another study, the fragmentation pathways of thiophenone are studied using ion-electron coincidence experiments. With these experiments, it is observed that some of the fragmentation pathways may be decoupled purely based upon the photoelectron energy, which is also a measure of the internal energy of an ion. Another method, which is often used to study dissociation, fragmentation, and isomerization pathways, is coincident ion momentum imaging. The sensitivity of this method in distinguishing similar-looking structures is demonstrated by distinguishing conformational isomers of 1,2-dibromoethane, which only differ by a rotation around a single bond and coexist in a particular ratio at any given temperature. Sequential and concerted breakup pathways were disentangled using a newly developed Native frames method to obtain information about the initial molecular geometry. These experiments may trigger future time-resolved studies to monitor subtle molecular structural changes using coincidence ion momentum imaging.

The work presented in this thesis uses a wide variety of techniques to understand light-induced isomerization and fragmentation dynamics, from simple molecules to moderately complex systems. This work contributes to the understanding developed for the prototypical systems, which may help formulate general principles underlying some light-induced reactions and processes.

Isomerization and fragmentation of polyatomic molecules induced by ultraviolet and extreme UV light

by

Shashank Pathak

M.Sc., University of Mumbai - Center for Excellence in Basic Sciences, India, 2014

A DISSERTATION

submitted in partial fulfillment of the
requirements for the degree

DOCTOR OF PHILOSOPHY

Department of Physics
College of Arts and Sciences

KANSAS STATE UNIVERSITY
Manhattan, Kansas

2021

Approved by:

Major Professor
Daniel Rolles

Copyright

Abstract

Imaging molecular structures evolving at their natural timescales, during a chemical reaction, with an atomic-scale resolution has been a long-standing goal for physicists and chemists. With the recent developments in experimental techniques, as well as the light sources, such as synchrotron radiation sources, free-electron lasers (FELs), ultrafast lasers, and high-harmonic sources, it is now possible to study the molecular dynamics and structural changes with femtosecond (in some cases attosecond) time-resolution, for near-infrared to x-ray wavelengths. These advancements are particularly useful in studying a wide range of photoinduced chemical reactions and photoinduced fragmentation. In this thesis, some of the advanced techniques are used to study photoinduced isomerization and fragmentation. This thesis also partly focuses on developing the tools and techniques which can be used to study these molecular structural changes.

Several molecular systems are studied throughout the thesis. Some of them are studied with the goal of understanding the chemistry post photoexcitation and photo-fragmentation, while others were aiming for method development for future experiments. Specifically, some of the experiments are performed on a prototypical heterocyclic ring molecule, thiophenone. One such experiment studies photochemistry after ultraviolet light absorption, using time-resolved photoelectron spectroscopy at a free-electron laser. The experimental results are combined with ab-initio molecular dynamics and electronic structure calculation for the ground state and excited state molecules, which revealed insights about the electronic and nuclear dynamics. Ring-opening is the most dominant process upon photoexcitation, driven by a ballistic extension of C-S bond, and is completed within ∼350 fs. The ground state trajectories also confirm the formation of three ring-opened products, providing detailed

insights into this reaction. Ring-opening reactions of similar types are considered as candidates for designing fast molecular switches. In another study, the fragmentation pathways of thiophenone are studied using ion-electron coincidence experiments. With these experiments, it is observed that some of the fragmentation pathways may be decoupled purely based upon the photoelectron energy, which is also a measure of the internal energy of an ion. Another method, which is often used to study dissociation, fragmentation, and isomerization pathways, is coincident ion momentum imaging. The sensitivity of this method in distinguishing similar-looking structures is demonstrated by distinguishing conformational isomers of 1,2-dibromoethane, which only differ by a rotation around a single bond and coexist in a particular ratio at any given temperature. Sequential and concerted breakup pathways were disentangled using a newly developed Native frames method to obtain information about the initial molecular geometry. These experiments may trigger future time-resolved studies to monitor subtle molecular structural changes using coincidence ion momentum imaging.

The work presented in this thesis uses a wide variety of techniques to understand light-induced isomerization and fragmentation dynamics, from simple molecules to moderately complex systems. This work contributes to the understanding developed for the prototypical systems, which may help formulate general principles underlying some light-induced reactions and processes.

Table of Contents

List of Figures

List of Tables

Acknowledgments

This thesis would not have been possible without the support and help of extraordinary colleagues, to whom I am forever indebted. My deepest gratitude goes to everyone who helped and encouraged me throughout this journey.

First and foremost, I would like to thank my advisor, Daniel Rolles. Daniel, you have not only taught me how to think critically and scientifically but also how to be patient, optimistic, and think clearly under stressful situations. Your scientific knowledge combined with your enthusiasm and energy has motivated me throughout my Ph.D. and will stay with me forever. I am also extremely grateful to you for allowing me to travel to perform experiments at various national and international laboratories. These experiences helped me immensely in broadening my scientific understanding.

I am also incredibly grateful to Artem Rudenko for his critical insights on various in-house projects. Artem's comments, suggestions, and questions helped in maintaining the quality and rigor of my work. I would like to thank my committee members: Daniel Rolles, Vinod Kumarrappan, Loren Greenman, Viktor Chikan, Shuting Lei, and Jeremy Roberts. I also appreciate kind help from Shuting Lei for stepping in at the last minute as an outside committee member.

I have been fortunate to have worked with extraordinary graduate students and postdocs at James R. Macdonald lab (JRML) throughout these years. I would like to thank Seyyed Javad Robatjazi for helping me throughout my Ph.D. Javad, you have been an excellent mentor and even better friend. I learned a great deal from you and enjoyed the countless hours we spent in the lab while building and working on KAMP. I also appreciate working with Surjendu Bhattacharyya, Anbu Venkatachalam, Kurtis Borne, Farzaneh Ziaee, Enliang Wang, Keyu Chen, Travis Severt, Kanaka Raju Pandiri, Tomthin N. Wangjam and Huynh

Lam throughout these years at JRML in some form or another. None of these experiments and research would be possible without the support from Kevin Carnes and Charles Fehrenbach. JRML technical staff, specifically Chris Aikens and Justin Millette, helped maintain smooth operations and offered technical help even on short notice.

The experiments performed at FERMI free-electron laser in Italy would not be possible without Carlo Callegari, Michele Di Fraia, Oksana Plekan, and the extraordinary FERMI team. I also want to express my gratitude to Michael Ashfold, Basile Curchod, and Lea M. Ibele for helping me gain theoretical insights and for scintillating discussions throughout this work.

Several experimental campaigns at the Advanced Light Source (ALS) in Berkeley were performed in collaboration with Nora Berrah's group. Thank you, Nora, for always being supportive and helpful. I would also like to express my gratitude towards the graduate students and postdocs whom I worked with during the ALS experiments. I would like to thank Razib Obaid for helping me understand the experimental setup and introducing me to the coincidence analysis. Thank you, Razib, for being a fantastic mentor and great friend. I would also like to thank Utuq Ablikim, Nora Kling, Jan Tross, Xiang Li, Anbu Venkatachalam, Kurtis Borne, Johannes Buerger, and Debadarshini Mishra for their support and help during the beamtimes.

I am also extremely grateful to Martin Centurion and his group, especially Joao Pedro Nunes for helping me learn about MeV UED experiment and data analysis. I am thankful to Thomas Wolf and extremely talented MeV UED team for helping and providing valuable insights during the MeV UED experiment at SLAC.

Finally, I would like to thank my parents for believing me and constantly pushing me to reach my fullest potential.

Dedication

To my parents and my family for their endless love, support and encouragement.

Chapter 1

Introduction and motivation

Our scientific understanding related to observing matter in its simpler forms, such as single molecules, polymers and bio-molecules, has benefited greatly from the ability to determine structure at the atomic scale. One of the key ideas from structural biology, that *structure* determines *function*, has been a driving force in developing an understanding a variety of natural phenomena at the molecular level. The atomic scale arrangement of molecules or bio-molecules in their (quasi static) ground state has been successfully determined and understood by traditional methods such as x-ray and electron diffraction, which have been refined over several decades. One key aspect which is much less understood and which has been a topic of active research in recent years is the dynamics happening at the atomic scale, such as the correlated electronic and nuclear motion in a molecule leading to bond formation, bond breaking, chemical reaction or phase change in a condensed matter system.

The timescales of electronic, vibrational and rotational motion within the molecules are typically on the order of attoseconds (10^{-18} s), femtoseconds (10^{-15} s) and picoseconds (10^{-12} s), respectively. It is natural to study molecules or systems at these timescales, since they would govern some of the key steps in chemical reactions, such as transformation of one geometry into another or redistribution of energy leading to structural changes in a molecule. With the advent of free-electron lasers (FEL) and the advancement of table-top

light sources, it is now possible to generate light pulses in ultraviolet and x-ray wavelength range with time duration closer to the natural timescales of the molecules [1, 2]. This has also opened a new realm of studies to probe light-induced reactions, which are fundamental to many processes happening in nature. Pump-probe spectroscopy is a simple and commonly used technique where two optical pulses are used to investigate chemical dynamics. A pump pulse usually initiates the dynamics, which are then studied by a probe pulse. By changing the delay between pump and probe pulses the progression of the reaction is studied, with a time resolution that is generally dependent on the temporal width of the pump and probe pulses.

The field of *femtochemistry* was first introduced [3] by Ahmed H. Zewail in 1988, who later in 1999 received the Nobel Prize in Chemistry. In his prize winning work [4], it was shown that it is possible to "see" the chemistry in action, such as making and breaking of chemical bonds, using a femtosecond laser. This also led to the idea of creating *molecular movies*, which are series of snapshots of molecules taken at angstrom level precision in position and femtosecond precision in time. This is a "dream" project for the scientific community, and this dissertation will explore several prototypical molecules which may help develop understanding for studying bigger systems. Creating molecular movies often requires a combination of different techniques and light sources.

Over the past few decades, several techniques have been applied to study light-driven molecular dynamics using pump-probe spectroscopy. To broadly categorize, these techniques involve either the detection of photons, electrons (from electron probe or from the photoionization of molecules) or molecular fragments (ions or neutral). The transient absorption spectroscopy technique involves initializing reaction by a pump pulse and detecting photons and characterizing the absorption spectrum of the probe pulse as a function of pump-probe delay to map the chemical reaction [5, 6]. The x-ray diffraction technique also involves detection of diffracted x-ray photons which have the structural information imprinted on them due to the interaction with the molecular target. This technique for imaging molecu-

lar structure [7] has immensely benefited from the astonishing progress in the development of x-ray FELs. In comparison with synchrotron sources, which were the traditional x-ray sources prior to the FELs, an x-ray FEL provides three orders of magnitude shorter pulses in time (few tens of femtoseconds) and about a billion times brighter x-rays.

In this dissertation, the focus is on the techniques which involve detection of charged ionic fragments and/or electrons. One of the several techniques, which takes advantage of the rich information carried out by the outgoing electron is time-resolved photoelectron spectroscopy (TRPES) [8–11]. In this dissertation, the TRPES technique is applied on a prototypical heterocyclic ring molecule, 2(5H)-thiophenone (C_4H_4OS), to trace the ultrafast ring-opening of gas-phase thiophenone molecules after ultraviolet (UV) photoexcitation. One key aspect of this study is the combination of the TRPES technique with ab initio electronic structure and molecular dynamics calculations of the excited- and ground-state molecules, which provides insights into both the electronic and nuclear dynamics. This study is performed using the extreme ultraviolet (XUV) photon beam from a seeded FEL (20 eV) as a probe pulse. The advantage of using a FEL is that the photon energy and flux is sufficient to ionize the molecule from the ground state and to obtain a good signal-to-noise ratio. This type of experiment can also be performed using lab based high-harmonic sources if one can select narrow photon energies. Efforts are currently underway in this direction.

Coincidence momentum imaging [12, 13] is another technique which possesses high potential but requires further studies to explore the possibilities of its application in decoupling structural dynamics in the excited state with femtosecond or sub-femtosecond temporal resolution. Coincidence momentum imaging can offer an alternative to other structure-sensitive techniques and pave the way for time-dependent structure determination of dilute targets. Some of the challenges and problems that still need to be overcome in that respect, such as distinguishing conformational isomers by disentangling sequential and concerted breakup, are addressed in the photoion coincident momentum imaging study on conformational isomers of 1,2-dibromoethane ($C_2H_4Br_2$). In addition to photoion coincidences,

this dissertation also discusses some of the unique aspects related to photoion-photoelectron coincidences.

1.1 Document organization

This dissertation work provided an invaluable opportunity to be involved in a wide range of research projects and experimental work both at the James R. Macdonald Laboratory (JRML) and at national and international free-electron laser and synchrotron facilities. This thesis presents a subset of those studies and focuses on those where I made a particularly a significant contribution. In chapter 2, an effort is made to discuss all the techniques used, with a special focus on the experimental setup (double-sided spectrometer) which was built as a part of this work, and that of my colleague Seyyed Javad Robatjazi [14]. This chapter also provide details about various light sources and instruments used in the experiments described in this thesis. In chapter 3, the results from the TRPES experiments performed on thiophenone at the FERMI FEL in Trieste, Italy, are described. These experiments help provide insights into both the electronic and nuclear dynamics of the ring-opening reaction post photoabsorption of UV light. A published manuscript is included with additional results included in later sections. The results from delay-dependent photoion signals are discussed, which reveal the signatures of certain fragmentation pathways. Chapter 4 describes the coincidence ion momentum imaging method and its application in distinguishing conformational isomers of 1,2-dibromoethane. This chapter discusses the possibility of expanding ion coincidence momentum imaging to certain molecules to track subtle molecular structural changes. A new method of analyzing molecular fragmentation, which was developed by some of my colleagues at JRML and which is dubbed the "native frames method", and its application in separating sequential events for 1,2-dibromoethane is also discussed. The published manuscript is shown, followed by the relevant discussion and additional details. Chapter 5 includes a discussion on several photoelectron-photoion coincidence studies per-

formed on furan and thiophenone with an XUV source and a synchrotron radiation source. Finally, chapter 6 contains a summary and outlook related to studies presented in this thesis.

Chapter 2

Experimental methods

To study molecular structures and observe dynamics on a femtosecond time-scale, several experimental techniques coupled with various light sources were employed in this dissertation. The goal of this chapter is to briefly introduce each method which was used and highlight the experimental parameters for the results shown in later chapters. Some of the common charged particle detection techniques, spectrometer design, and position- and time-sensitive detectors are also summarized in this chapter. Finally, we describe the coincident ion-electron imaging setup, which was built and commissioned during a significant portion of my dissertation work.

2.1 Overview of techniques

The experimental techniques used in this dissertation for studying structural dynamics, such as isomerization, involve either detecting electrons (from post-ionization of the molecule or from an electron beam) or fragmenting the molecule to detect ion and electron in coincidence. Our problem warrants investigation of reaction using different methods as each method possesses some unique capability. For example, in the coincident ion momentum imaging and time-resolved photoelectron spectroscopy experiments, the molecule needs to be ionized

or broken up into several fragments in order to obtain information about the structure. This makes the interpretation of dynamics complicated because of the involvement of cationic and dicationic or even tricationic states. On the other hand, diffraction imaging methods are not hindered by this problem as they can efficiently map the structure of a molecule before destroying it. However, diffraction imaging methods also face a few challenges. One, for example, is that they often require high target densities, making it harder to apply them for low vapor pressure samples. For electron diffraction, reaching smaller pulse duration is a fundamental challenge. Hence, it is of great interest to study the reaction using different techniques in order to map all the observables and understand the photochemistry. In the following sections, the light sources, detection instruments, spectrometers and experimental techniques that were also used in this dissertation work are explained.

2.2 Light sources

The work outlined in this dissertation uses soft x-ray free-electron lasers (FELs), synchrotrons, and ultrafast laser sources. These sources possess certain unique properties that can be used to study structural and molecular dynamics.

2.2.1 Synchrotron radiation sources

Synchrotron radiation sources are powerful sources of x-rays and XUV light. Synchrotron light sources are widely used for research in material science, physics and chemistry, along with techniques such as x-ray diffraction, x-ray absorption, x-ray crystallography, and x-ray tomography, to name a few. Synchrotron-based experiments using x-ray crystallography helped in determining the structure of ribosome [15]. This work won the Nobel Prize in Chemistry in the year 2009 [16]. In comparison to a free-electron laser (FEL) (see section 2.2.2), synchrotron radiation sources are much less bright and have a much longer temporal pulse profiles, but they have the advantage of being able to easily tune the photon

energy while maintaining high energy resolution. The coincident ion momentum imaging experiments for distinguishing conformational isomers (described in chapter 4) were performed at a synchrotron radiation source, the Advanced Light Source (ALS), at Lawrence Berkeley National Laboratory (LBNL).

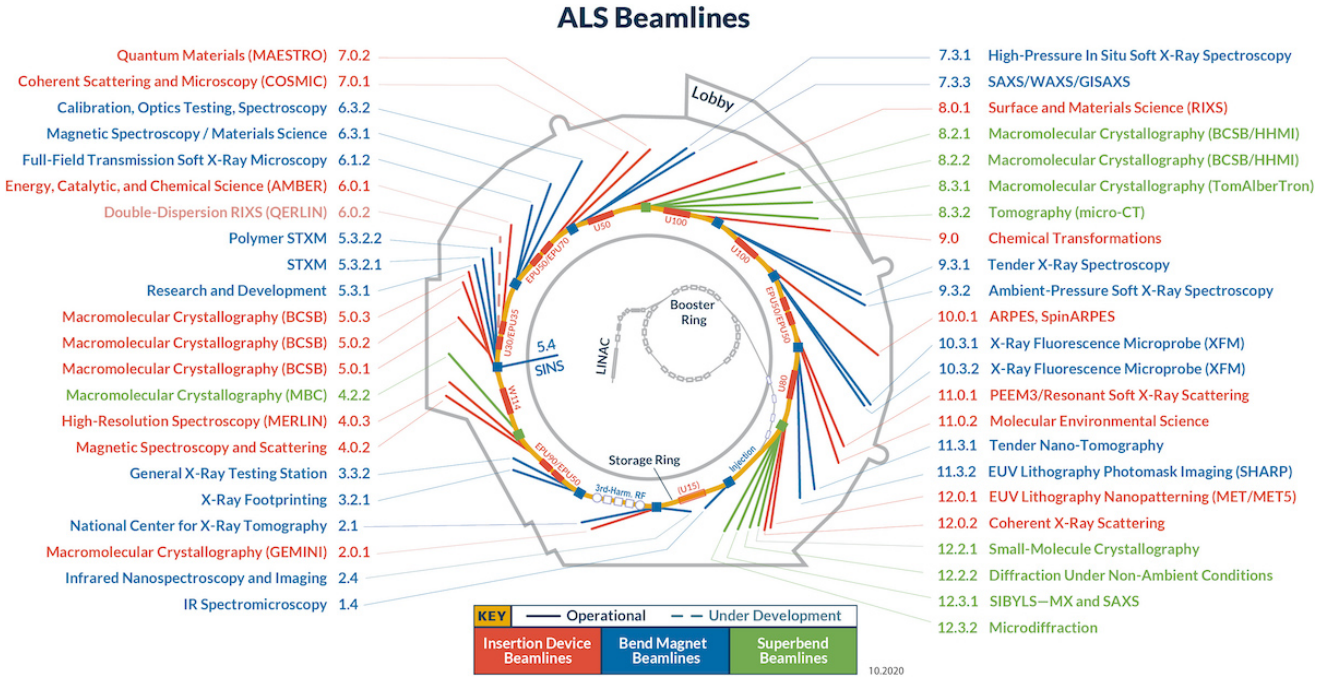

Figure 2.1: *Beamlines at the Advanced Light Source, Berkeley [17]*

The ALS is the world's first third-generation synchrotron which began operation in 1993. The electrons are accelerated up to 1.9 GeV energy and fed into the storage ring. The storage ring has a diameter of 62 meter and uses bending magnets to steer the electrons. Between the bending magnets are straight sections where the electron beam passes through undulators. Undulators are series of magnets with alternating polarity. When the electron beam passes through an undulator, it emits electromagnetic radiation with wavelengths ranging from infrared to x-rays. This electromagnetic radiation is then distributed to different beamlines and further operations like monocromatization and focusing are performed whenever required. Figure 2.1 shows the schematic of ALS with several beamlines around the ring.

ALS has two modes of operation to allow for the experiments requiring either smaller or larger bunch spacings. (a) Multibunch mode: the spacing between consecutive electron bunches is 2 ns. The number of electron bunches in the storage ring is between 276-320. (b) Two-bunch mode: the spacing between electron bunches is 328 ns. As the name suggests, two electron bunches are fed in the storage ring in this mode of operation. The experiments were performed in both modes of operation, but mainly experiments performed using multibunch mode are discussed in this dissertation. For the coincident momentum imaging experiments at ALS in multibunch mode, the time interval (2 ns) between the soft x-ray pulses is too short to unambiguously assign photoelectrons, Auger electrons, and fragment ions to a specific soft x-ray pulse. Moreover, 2 ns is also too short to record all the ions which have time-of-flight (TOF) typically in microseconds. To overcome this, in multibunch mode, we use the electron TOF signal as the trigger to our data acquisition (see Sec. 2.3.5). This allows us to detect all the ions and 2D electron information without being restricted by the master-clock signal from the synchrotron.

The multibunch-mode experiments were performed at beamline 10.0.1. This beamline provides photon energies ranging from 17 eV to 340 eV [18] with an extremely good energy resolution of $\Delta E/E \approx 10^{-4}$ [19]. The experimental setup is a roll-up endstation, which is described in later sections.

2.2.2 Soft x-ray seeded free-electron laser

Free-electron lasers (FELs) are fourth-generation synchrotron light sources capable of producing extremely bright light with laser-like properties in the extreme ultraviolet (XUV) and x-ray regions of the electromagnetic spectrum. The basic principle behind light amplification in a traditional FEL is the resonant coupling between ultra-relativistic electrons and their emitted x-ray radiation. The electrons are first accelerated to relativistic speeds using linear accelerators and then guided by a periodic magnetic field generated by a long undulator. Due to the interaction of the electrons with the electromagnetic field, the highly

energetic electron beam is modulated in energy. As the electron beam travels further through the undulator, the energy modulation is transformed into spatial modulation, causing the bunching of electrons. This leads to in-phase emission of radiation via these micro-bunches of electrons in the electron beam. FELs can be divided into two categories based on the

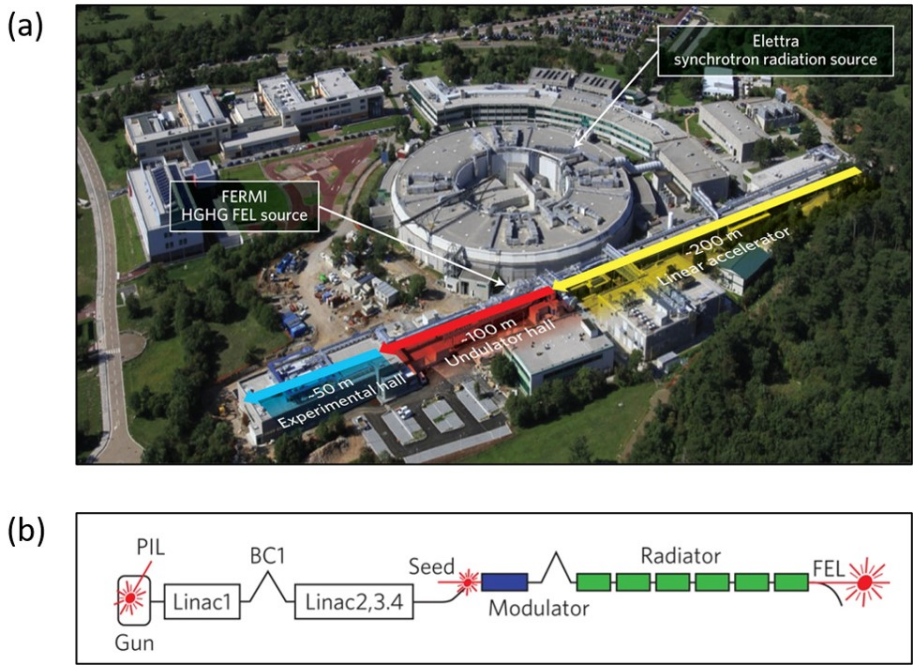

Figure 2.2: *The FERMI FEL in Trieste, Italy. (a) Aerial view of the facility (b) Schematic of the FEL generation (Adapted from [20]).*

origin of the electromagnetic radiation which causes microbunching-

- Self Amplified Spontaneous Emission (SASE) FELs (incoherent spontaneous electron emission) [21],
- Seeded FELs (by using a coherent external source such as a seed laser [20] or self-seeding [22]).

Since SASE FELs are generated by spontaneous emission, they have lower shot-to-shot temporal and spectral stability compared to seeded FELs. For performing a spectroscopic experiment, a smaller bandwidth is highly advantageous in order to obtain precise information about the final states. The FERMI FEL in Trieste, Italy is a soft x-ray seeded

FEL [20, 23] designed to produce coherent radiation in the range of 4 nm (310 eV) to 100 nm (12.4 eV). Figure 2.2(a) shows an aerial view of the FEL and the nearby Elettra synchrotron. A long linear accelerator and undulator section, which can be seen in the image, generates high-flux XUV and x-ray radiation. Figure 2.2(b) shows the schematic where a photoinjector laser (PIL) is employed to generate electrons that are accelerated within the radiofrequency (RF) gun. BC1 is a bunch compression unit. After passing through the linear particle accelerators (LINACs), the electron beam is sent to undulators. After this the electron beam is overlapped with the seed laser within the modulator. This process helps emit XUV/x-ray radiation at any desired harmonic of the seed laser.

2.2.3 Ultrafast lasers

Some of the results presented in this dissertation use the following laser light sources:

- **P**rairie **U**ltrafast **L**ight **S**ource for **A**ttosecond **R**esearch (PULSAR): This is a Ti:Sapphire laser producing linearly polarized light with a central wavelength of 780 nm, pulse energies up to 2 mJ, and a typical pulse duration of 25 fs, at a 10 kHz repetition rate. This laser is coupled with an XUV source for performing XUV pump and near-infrared (NIR) probe experiments. PULSAR is a commercial laser designed by KM Labs, and is described in detail by Ren *et al.* [24].

- **F**emtosecond **LA**ser for **M**ulticolor **E**xperiments (FLAME): FLAME is also a Ti:Sapphire laser producing 805 nm central wavelength (bandwidth = 60 nm), pulse energies up to 5 mJ, and a typical pulse duration of 24 fs, at a 3 kHz repetition rate. The laser is designed by Coherent, Inc. and is coupled with an optical parametric amplifier (OPA) which can deliver output wavelengths from 190 nm to 2600 nm. This system is used to perform ultraviolet/deep-ultraviolet pump and NIR probe experiments.

2.3 Double-sided velocity map imaging setup for ion and electron coincidence

To detect charged particles generated from ionization by light sources described in previous sections, we use the velocity map imaging (VMI) technique. VMI, developed by Eppink and Parker [25], is a powerful technique that resulted in the improvement of velocity resolution, which was earlier limited by a finite interaction volume between the molecular beam and the ionizing laser. The technique overcomes this by using an electrostatic lens. At a defined voltage the electrostatic lens maps the velocities of the charged particles to a unique radius, regardless of the position where the charged particle was created. VMI is particularly useful for photoionization experiments that use XUV/x-ray photons for photoionization because these photons can ionize the molecules along the entire beam path, and not just in a high-intensity focal region, which is the case for femtosecond NIR lasers. A double-sided VMI setup is a slightly modified version that can detect both ions and electrons in coincidence, if equipped with time- and position-sensitive detectors. This dissertation work is based on two different double-sided VMI setups, as described below.

2.3.1 Kansas Atomic and Molecular Physics apparatus

Kansas **A**tomic and **M**olecular **P**hysics (KAMP) apparatus is a multipurpose instrument, compatible with a double-sided VMI spectrometer as well as a reaction microscope spectrometer, cold molecular beam source and an effusive jet for target delivery, and time- and position-sensitive detectors for detecting charged particles. Its core design is similar to its sister instruments, CAMP [26, 27] and LAMP [28], which are user endstations at FEL facilities. KAMP apparatus is built as a part of this dissertation, and the design is modified based on requirements such as coupling KAMP with an XUV (EUV) source.

KAMP consists of several sections that are used for different purposes. The schematic

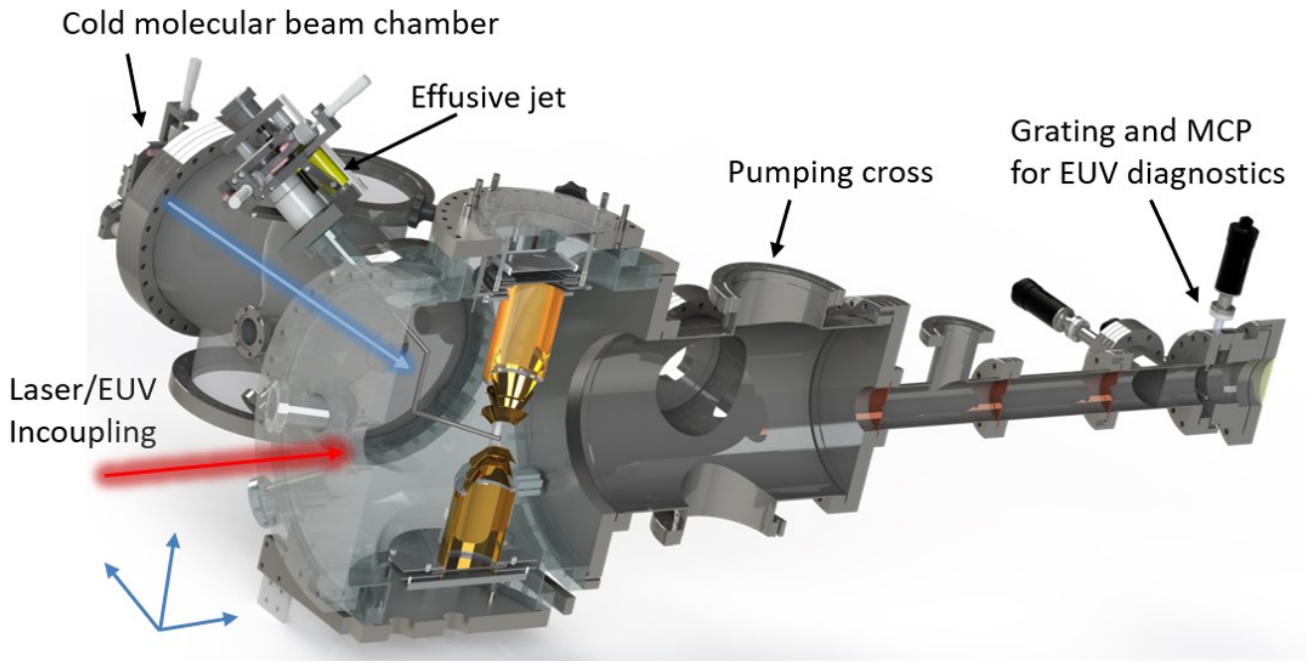

Figure 2.3: *Schematic of the KAMP setup, which includes a double-sided VMI, an effusive jet and a cold molecular beam source for target delivery, and an XUV spectrometer for diagnostics.*

of KAMP is shown in Figure 2.3.

- **Cold molecular beam**: The molecular target is introduced into the chamber using a bubbler (for liquid samples), from which liquid evaporates and expands through a 30 μm nozzle. The molecular beam is skimmed by a skimmer of 500 μm in diameter. The first stage (where the nozzle and skimmer are) is equipped with a turbomolecular pump with 1000 l/s pumping speed for efficient pumping. The second stage is separated from the main chamber via an aperture of size 0.7 mm. The second stage is pumped via a 700 l/s turbomolecular pump. The base pressure of the first and second stage of the molecular beam preparation chamber is 10^{-10} Torr. During operation, the first stage can reach 10^{-3} - 10^{-4} Torr and the second stage usually reaches 10^{-6} - 10^{-7} Torr.

- **Cold molecular beam "catcher"**: It consists of two differentially pumped stages through which the molecular beam passes to efficiently pump out all of the molecular

target, minimizing backflow to the main chamber. The base pressure of the first and second stage of the catcher is 10^{-10} Torr. During operation, the first stage can reach 5×10^{-10} Torr and the second stage usually reaches 10^{-9} Torr.

- **Interaction chamber with spectrometer**: The interaction chamber is the main chamber where the laser interacts with the molecular target and ionizes it into ions and electrons. The ions and electrons are guided toward the detectors using the electric field applied via the voltages on the spectrometer. Figure 2.3 also shows the effusive jet, which consists of only a capillary of diameter 200 μm to achieve higher molecular target densities, if required. Since the capillary is inserted inside the spectrometer, voltage can be applied to it in order to correct for the electric field distortion caused by the capillary. The base pressure of the interaction chamber is 9×10^{-11} Torr. During operation with cold molecular jet, the pressure does not increase in the interaction chamber as the molecular beam is dumped into the catcher. When operating with the effusive jet, the interaction chamber pressure increases to 10^{-6} - 10^{-7} Torr. The interaction chamber is bigger in volume and its efficient pumping for reaching ultrahigh vacuum requires multiple turbomolecular pumps. Since most of the ports are occupied with detectors and molecular beam chambers, another chamber is attached to support turbomolecular pumps. The pumping chamber has 3 turbomolecular pumps mounted to it, two of which are 700 l/s and the other a 1000 l/s pump.

2.3.2 Double-sided VMI endstation at the Advanced Light Source, Berkeley

This instrument [29] (henceforth referred as ALS-DVMI) was designed for efficient performance at beamline 10.0.1 at the ALS (described in Sec. 2.2.1), but in principle, it can be used at different beamlines and light sources. ALS-DVMI has three differentially pumped chambers, (a) spectrometer chamber, (b) molecular beam chamber, and (c) differential pumping

section to decouple the chamber from the beamline. The spectrometer chamber has a base pressure of high 10^{-9} Torr. The molecular beam chamber contains a target delivery system which consists of a stainless steel tube terminated by a flat 30 μm aperture. The stainless steel tubing can be heated (designed during this dissertation) using resistive heating and can also be cooled by flowing liquid nitrogen. The molecular beam chamber is pumped by two 1000 l/s pumps and is separated from the spectrometer chamber by a skimmer of 500 μm diameter.

2.3.3 Design and operation of a double-sided VMI spectrometer

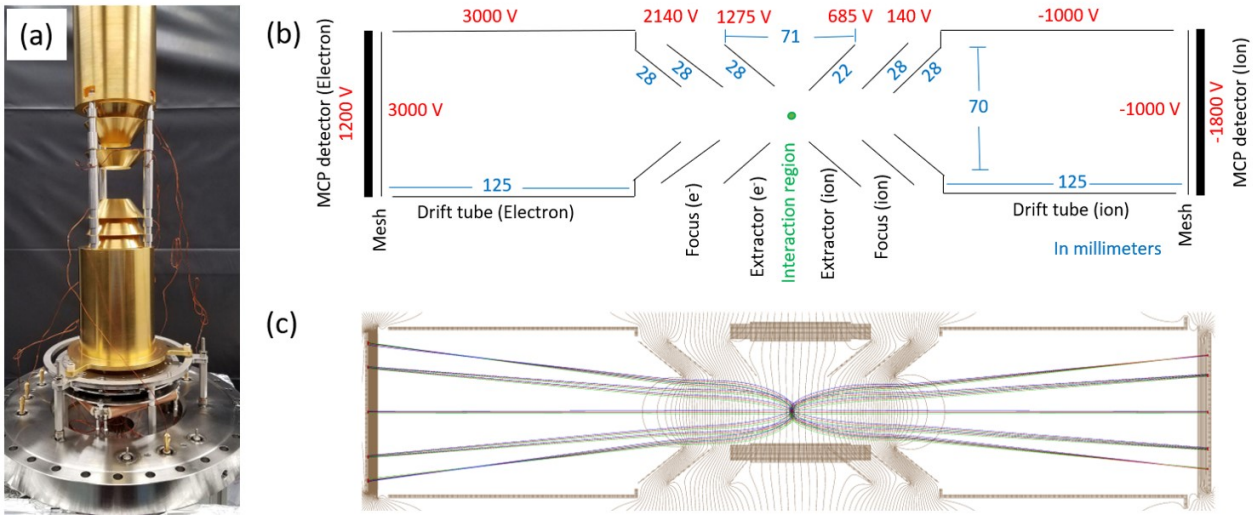

Figure 2.4: *Spectrometer design of KAMP (a) Photograph of the spectrometer taken during assembling (b) Schematic diagram showing various physical dimensions in millimeters (numbers in blue) and typical voltages applied (in red) (c) Simulation performed using SIMION showing equipotential lines and trajectories for ions with 25 eV kinetic energy and electrons with 35 eV kinetic energy. The simulation results performed for three source positions- (0,0,0), (0,1,0), and (0,-1,0) shows that the final position at the detector does not depend on the initial source position.*

The spectrometer design for a typical double-sided VMI requires a minimum of two electrodes and one drift tube for each side (ions and electrons), namely the extractor, the focus and the drift tube. The extractor electrode for the ion side also acts as a repeller

for the electron side and vice-versa. This makes the performance of the ion side and the electron side interconnected with each other as they share a common extraction field. The "focus" electrode acts as an electrostatic lens, which helps tremendously in focusing the spread-out interaction region [30] and also in compensating field distortions [31]. Since the ion and electron sides are coupled, the drift tube length determines the energy ranges which can be detected.

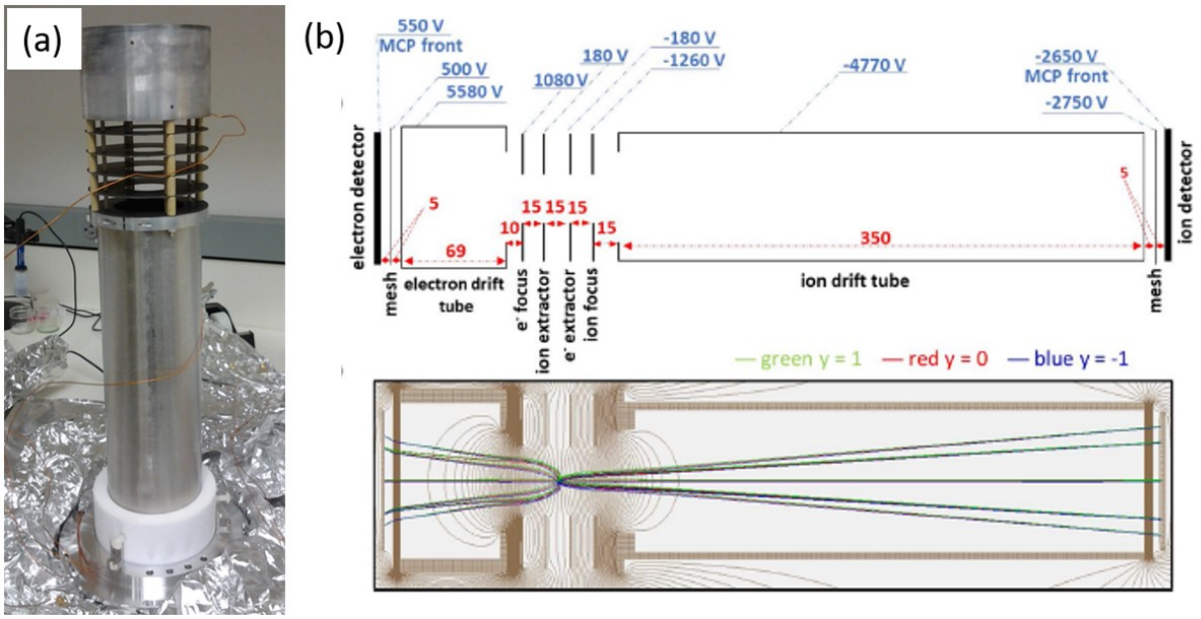

Figure 2.5: *Spectrometer design of ALS-DVMI (a) Photograph of spectrometer (b) Schematic showing various physical dimensions, typical voltages and SIMION simulation results (Adapted from [29])*

Figure 2.4 shows the spectrometer design for KAMP. Note that the spectrometer in KAMP has conical electrodes. This unique electrode design is borrowed from the previously built CAMP [26, 27] and LAMP instruments [28]. Such a design provides a better field of view to image the interaction region, which is useful for fluorescence and x-ray scattering experiments. The spectrometer in KAMP is gold-plated, which is advantageous in reducing secondary electrons from the photons with energy below the work function of gold (5.1 eV). A typical set of voltages are shown in Fig. 2.4(b) along with some of the relevant dimensions of the spectrometer. Figure 2.4(b) also shows that a mesh is placed after the drift tube but

before the microchannel plate (MCP) detector. This mesh is placed at the same voltage as the drift tube in order to close the field of the spectrometer and avoid field penetration. The mesh is commercially bought and is made of Cu with a maximum transmission of 90%, an opening width of 344 μm / .01355 inch and the wire width of 19 μm / .00073 inch. Figure 2.4(c) shows the simulated trajectories of ions (right) and electrons (left) generated at 3 different starting positions, namely (0,0,0), (0,1,0) and (0,-1,0) using SIMION [32]. For each starting position, ions and electrons have a fixed kinetic energy of 25 eV and 35 eV, respectively, but have five different directions of emission with respect to the spectrometer axis. As seen from the trajectories in Fig. 2.4(c), the voltages satisfy the VMI condition where the ions and electrons with the same velocity, irrespective of the source position, are detected at the same spot on the detector. Equipotential lines based on these voltages are also calculated using SIMION and are shown by brown curves in Fig. 2.4(c).

Figure 2.5 shows the spectrometer design for ALS-DVMI. The design of this spectrometer enables the detection of electrons with energies up to 300 eV. The spectrometer is used to perform experiments with XUV and soft x-ray radiation at beamline 10.0.1 at the ALS as described in Section 2.2.1. The photon energies accessible at this beamline are in the range of 17 eV to 350 eV. This energy range covers the first inner-shell ionization threshold of many halogens, such as chlorine, bromine and iodine. This means that after photoionization of molecules containing halogens, Auger electrons and photoelectrons with high energy up to 290 eV could be emitted and need to be detected. This inspired the design of the spectrometer for ALS-DVMI, which was equipped with a very short drift tube on the electron side in order to allow detection of ions with energies up to 25 eV and electrons up to 300 eV. Figure 2.5(b) shows typical voltages and dimensions of the ALS-DVMI's spectrometer. The figure also shows that particles with identical velocities are mapped to the same position on the detector irrespective of source positions by simulating trajectories at different source positions with kinetic energies for ions of 15 eV and for electrons of 120 eV [29].

2.3.4 Ion and electron detection

The electric field produced by the spectrometer guides and accelerates the charged particles toward the time- and position-sensitive detectors. The working of these detectors is described below.

- **Microchannel plate (MCP) detector**: MCPs are made from a highly resistive material and consist of honeycomb structure glass capillaries (5 - 15 μm in diameter), each of which acts as an independent secondary electron multiplier [33]. When the charged particle accelerated inside the spectrometer reaches the MCP detector and hits the wall of the capillary, it emits secondary electrons. These electrons accelerate toward the back of the MCP detector due to the positive bias across the MCP detector. While moving toward the back, they hit the wall of the capillary again and again, ejecting secondary electrons each time and generating a cascade of electrons, which can then be measured. The very first step, i.e. the charged particle hitting the wall of one of these capillaries is crucial for efficient signal detection. To ensure this, the MCP channels are tilted at an angle, usually 8, 10, or 12 degrees w.r.t. the axis perpendicular to the plane of the MCP. This increases the detection efficiency. To further increase the detection efficiency, MCPs are often stacked in a chevron (two MCP plates stacked with channels aligned to form a 'V' shape) or Z-Stack (three MCP plates stacked with channels aligned to form a 'Z' shape) configuration. For the KAMP instrument, the chevron configuration is used for ion and electron detection.

- **Microchannel plate (MCP) detector coupled with a delay-line anode**: To record positional information of the charged particles hitting the MCP detector, a delay-line anode [34] is installed at the back of the MCP detector.

A delay-line anode consists of either two (quad delay-line anode) or three (hex delay-line anode) pairs of wires, which are wound around an insulator holder. Each set of wires consists of two wires which are called *signal* and *reference* wires and are used to remove

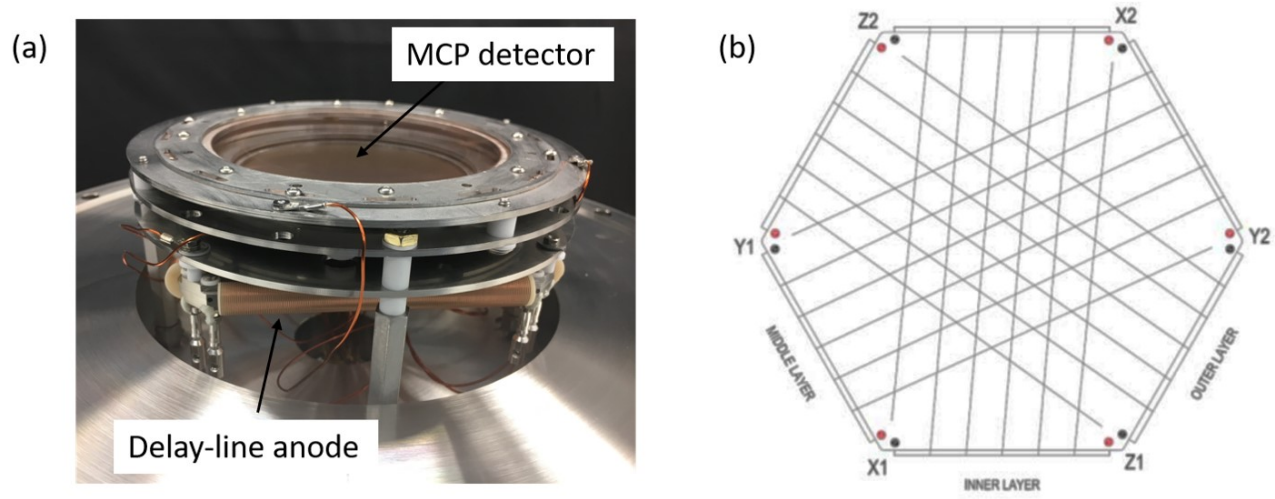

Figure 2.6: *Microchannel plate detector with delay-line anode (a) Photograph of MCP and quad delay-line anode stack used for ion detection in KAMP (b) Schematic of hex delay-line anode (Adapted from [34])*

background noise. The signal wires are the ones which detect the electron cloud from the back of the MCP. This is done by applying a slightly higher voltage (about 50 V higher) on the signal wires compared to the reference wires. The electron cloud picked-up by the delay-line anode (DLD) wires travels along the wires. The time it takes to reach both ends of the wire, say t_1 and t_2, is used to calculate the position of the charged particle.

To determine the position of charged particles (X, Y), we use the signal velocity (v_{signal}) and the distance (d) that is travelled along the length of wire for 1 mm propagation in the perpendicular direction (along the winding):

$$X = \frac{v^x_{signal}}{2d^x}(t^x_1 - t^x_2) + O_x \tag{2.1}$$

$$Y = \frac{v^y_{signal}}{2d^y}(t^y_1 - t^y_2) + O_y \tag{2.2}$$

where O_x and O_y are the arbitrary offsets.

The above expression is for a quad DLD which has two sets of wires. Another version called hex DLD, has three sets of wires, and offers higher detection efficiency as it is possible

to obtain the position information by only using the signals from two wire pairs. The third wire pair better enables the detection of a "lost" signal due to dead-time (multiple hits at the same time) or noise in one of the wire pairs. For the data shown in chapter 4, the ion positions are determined using the signals from all 3 wires of the hex DLD. The position information from a hex DLD can be calculated from the timing information in a similar manner as the quad DLD by using any two wire pairs and transforming the signal into cartesian coordinates. The equations for positional information from the hex DLD are summarized in RoentDek MCP manual [34]. Figure 2.6(a) shows the MCP and quad DLD stack, which is used for ion detection in the KAMP instrument. Figure 2.6(b) shows the schematic of the hex DLD, showing the winding directions of the three wire pairs.

2.3.5 Data acquisition and analysis

For a double-sided VMI, both the ion and electron sides are equipped with MCP and DLD detectors. For an MCP and hex (quad) DLD stack, there are in total seven (five) signals to be processed and recorded. One for the MCP and six (four) for the hex (quad) DLD anode. For example, in the KAMP setup, the ion detector is a MCP quad DLD stack, while the electron detector is a MCP hex DLD stack. So, in total there are 12 signals which need to be processed, namely, t^{ion}_{mcp}, t^{ion}_{u1}, t^{ion}_{u2}, t^{ion}_{v1} and t^{ion}_{v2} for ions and t^{e}_{mcp}, t^{e}_{u1}, t^{e}_{u2}, t^{e}_{v1}, t^{e}_{v2}, t^{e}_{w1} and t^{e}_{w2} for electrons, where u, v and w are the signals from the DLD. The magnitudes of these signals is usually very small (few mV), so they are amplified using a commercial fast amplifier (Ortec FTA820A). Once these signals are amplified, an important task is to precisely determine the arrival time of different signals. This is crucial because incorrect determination can ruin the best time resolution achievable in the experiment. Several methods could be considered, but *constant fraction discrimination* (CFD) is the best way to determine the arrival time since it is independent of signal height and works efficiently even if multiple signals are arriving close together. We use a constant fraction discriminator (Ortec 935 QUAD CFD) to process the signals further. Once the center in time is determined for the signals using CFDs, the arrival

time is measured w.r.t. a trigger signal, which is usually from a photodiode (measuring the arrival of each pulse from the laser system). For the experiments performed at the ALS synchrotron (multibunch mode) using ALS-DVMI, the trigger signal is the detection of the electron (electron MCP signal). With the typical spectrometer voltage setting used at ALS-DVMI, the electrons arrive at the detector after about 5 ns of flight time. The ion TOF is measure w.r.t. the first detected electron. This helps us perform experiments and tag the coincident events even if the repetition rate of pulses from the synchrotron is 500 MHz (2 ns spacing between pulses). In the two-bunch mode of operation, the bunch spacing (328 ns) is sufficient to assign the electrons to specific light pulses and hence we can also extract the electron TOF by using the ALS bunch marker.

The signals are recorded by using a time-to-digital converter (TDC, CAEN V1290N) for KAMP and by using two TDC8HP systems from RoentDek [35] for ALS-DVMI. Once all the signals are digitized, the data is saved for further determination of ion or electron hit position from the DLD signals as explained in Sec. 2.3.4. The final data consists of the time and positions of all charged particles detected for a particular trigger (or event).

For both KAMP and ALS-DVMI, we can obtain the full 3D momenta of ions and electrons from the measured TOF and position signals. The momentum and energy of electrons ejected corresponding to certain ionic fragments can also be determined. This technique is known as photoelectron-photoion coincidence (PEPICO) spectroscopy. Also, for determining the breakup pathways of molecules after photoionization, photoion-photoion coincidence (PIPICO) maps or photoion-photoion-photoion coincidence (PIPIPICO, also known as TRIPICO) maps are often used. Figure 2.7 shows the results from an experiment performed using ALS-DVMI to study the fragmentation of thiane ($C_5H_{10}S$) after photoionization at 220 eV photon energy. Figure 2.7(a) shows a PIPICO map from photoionization of thiane, measured experimentally using ALS-DVMI. To reconstruct the 3D momentum of ionic fragments, first, a coincident channel is selected. Figure 2.7(b) shows a coincidence channel ($C_2H_3^+ + C_3H_7S^+$) selected after gating on the TOF of ionic fragments. Figure 2.7

(c),(d) also shows the corresponding fragment position map.

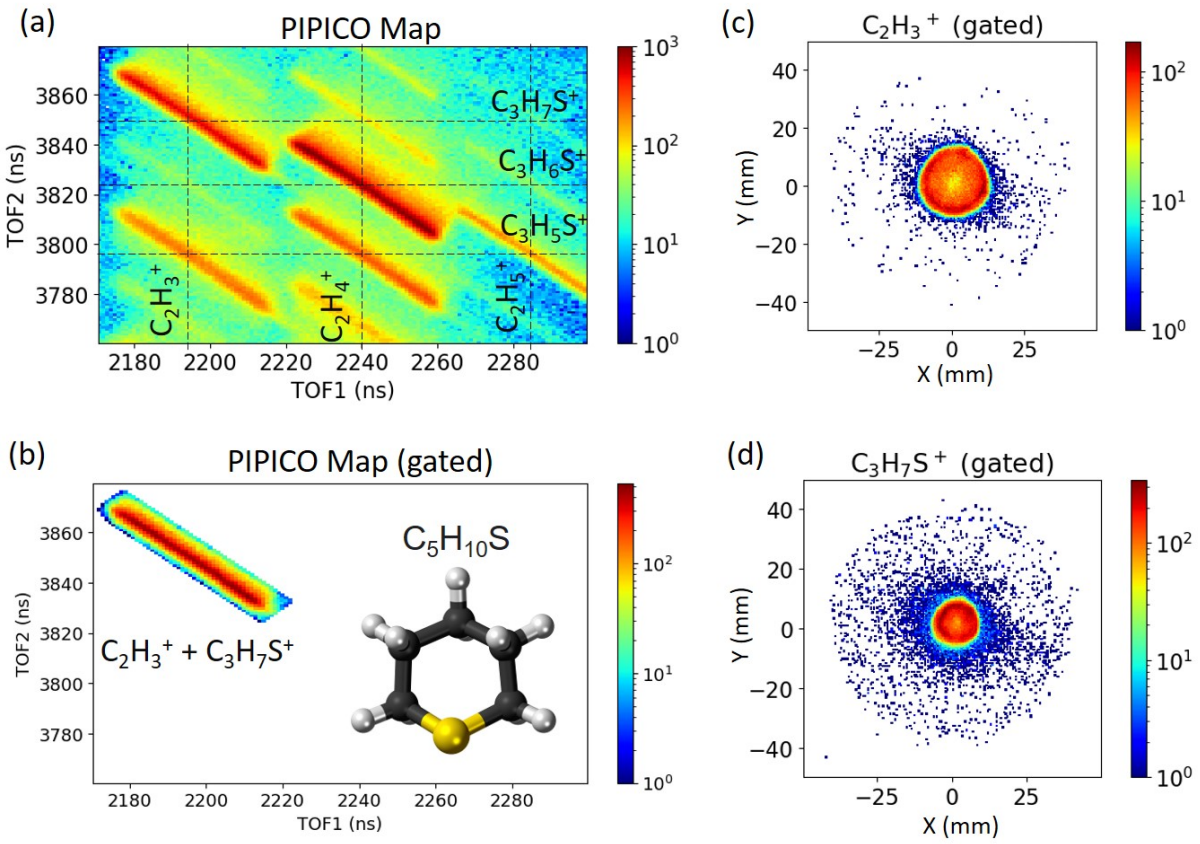

Figure 2.7: *Photoionization of thiane ($C_5H_{10}S$), a heterocyclic molecule, at 220 eV photon energy recorded using ALS-DVMI (a) Part of the PIPICO map showing different breakup channels (b) Gated channel, $C_2H_3^+ + C_3H_7S^+$, based on time-of-flight (c),(d) Gated ion images for fragments $C_2H_3^+$ and $C_3H_7S^+$.*

After photoionization, due to the electric field in the spectrometer, the ionic fragments fly toward the detector. Depending on the spectrometer configuration and the electric field applied, the initial momenta acquired by ionic fragments can be calculated based on the TOF and positions (x,y) of fragments. The spectrometer field in KAMP and ALS-DVMI is inhomogenous, as shown in Fig. 2.4 and 2.5. Due to this inhomogeneity, simple formulae do not exist to calculate the initially acquired momenta from the TOF and detector position (x,y). For this case, we use SIMION [32] to generate empirical equations by performing

fragment-dependent simulations for a subset of energies and fitting the data points. A multidimensional fitting approach can be followed but requires carefully simulating the data using SIMION to obtain a proper fitting function. Following this approach, one can find the fitting functions (f, g and h) for calculating the momenta based on the TOF and positions.

$$P_x = \mathbf{f}(TOF, x, y) \tag{2.3}$$

$$P_y = \mathbf{g}(TOF, x, y) \tag{2.4}$$

$$P_z = \mathbf{h}(TOF, x, y) \tag{2.5}$$

Another method which can be applied if the motions of charged particles in the x, y and z directions can be assumed to be decoupled from each other. In this case, the simulations can be performed using SIMION independently in each initial-velocity direction, and one can find the calibration equations.

$$v_x \propto x \tag{2.6}$$

$$v_y \propto y \tag{2.7}$$

$$v_z \propto TOF \tag{2.8}$$

Once the calibration equations are found the momenta can be calculated from the velocities and can then be used to calculate kinetic energies of the fragments. Since the initial momentum of the molecule is zero, the sum of momenta of fragments in each direction (x, y and z) should be close to zero. This can be seen from Fig. 2.8. The kinetic energies of the ionic fragments in the coincidence channel $C_2H_3^+ + C_3H_7S^+$ are shown in Fig. 2.9. The kinetic energy release (KER) is also shown in green.

To determine the 3D momenta of electrons, it is a common technique to reconstruct the Newton sphere (the 3D spatial distribution of particles moving with acquired initial momen-

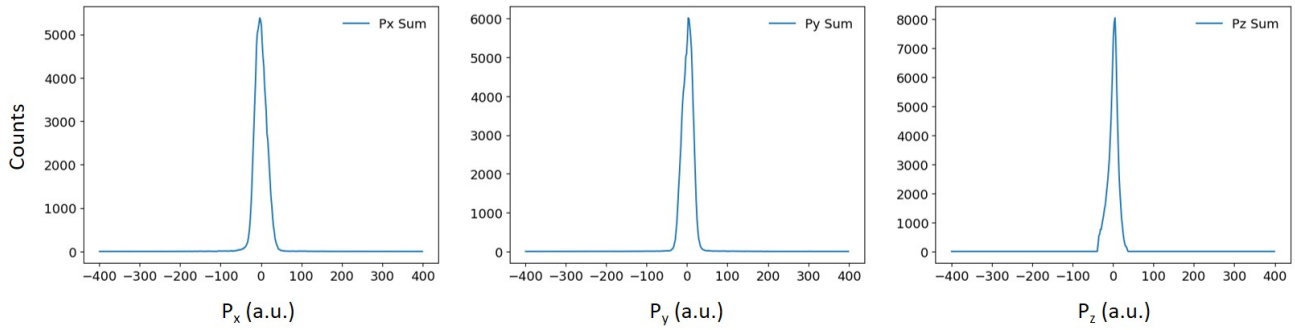

Figure 2.8: *Momentum sum in x (left), y (center) and z (right) direction for the coincidence channel $C_2H_3^+$ + $C_3H_7S^+$, obtained in the photoionization of thiane ($C_5H_{10}S$) at 220 eV photon energy.*

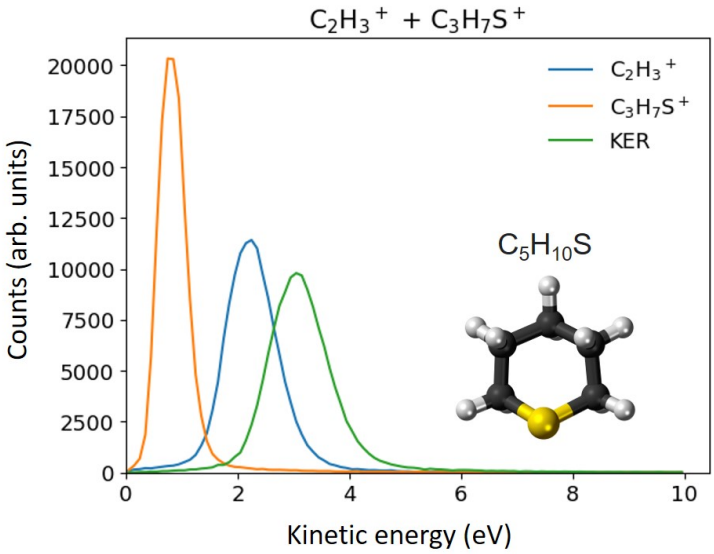

Figure 2.9: *Kinetic energy of ionic fragments and kinetic energy release (KER) in the coincidence channel, $C_2H_3^+$ + $C_3H_7S^+$, obtained by photoionization of thiane ($C_5H_{10}S$) at 220 eV photon energy.*

tum), using the 2D image recorded in the experiment. This procedure is known as an inverse Abel transform, which has been a crucial component in photoion and photoelectron imaging experiments. Several methods exist to perform Abel inversion and image analysis [36–39]. For performing Abel inversion on the data in this dissertation, we have used the pBasex method, which reconstructs the Newton sphere from the detector image by fitting a set of polar basis functions with a known inverse Abel integral [37]. Figure 2.10 shows the results

from the photoionization of furan (C_4H_4O) using four different harmonics (13th, 15th, 17th and 19th) of NIR (1.57 eV) from an XUV source. Figure 2.10(a) shows the raw and inverted images (using the pBasex algorithm) and Fig. 2.10(b) shows the calibrated photoelectron energy spectrum from the inverted image.

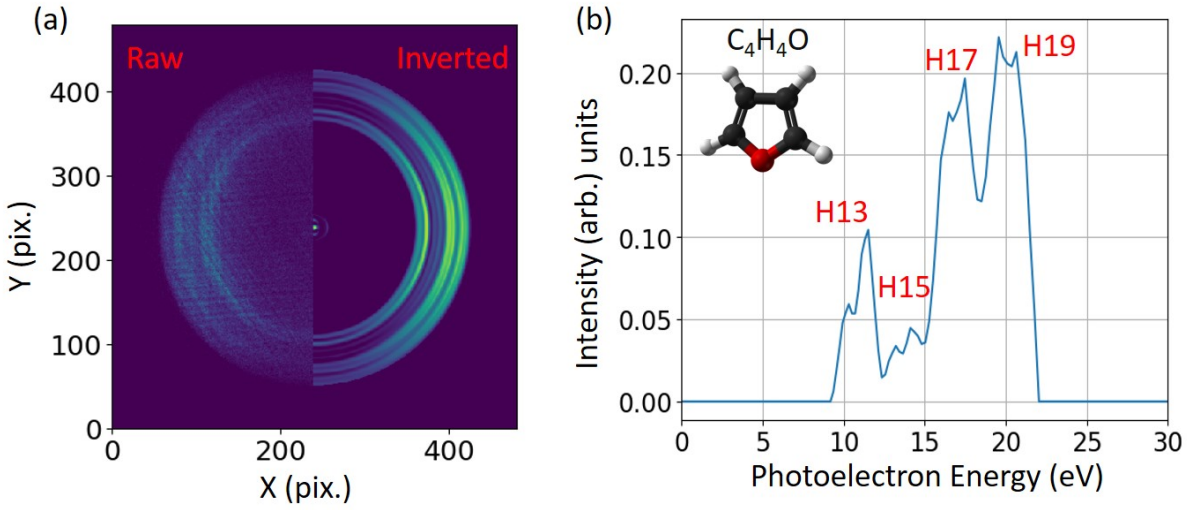

Figure 2.10: *Photoionization of furan (C_4H_4O) using an XUV source at photon energies between 20 to 30 eV (Harmonics of NIR at 1.57 eV: 13^{th}, 15^{th}, 17^{th} and 19^{th}) detected in the KAMP apparatus. (a) Raw and inverted photoelectron images corresponding to $C_4H_4O^+$ ions (b) Photoelectron energy spectrum shows four peaks corresponding to ionization due to each individual harmonic.*

2.4 Magnetic-bottle spectrometer endstation at FERMI FEL for photoelectron spectroscopy

Time-resolved photoelectron spectroscopy (TRPES) is a commonly used technique to track electronic relaxation upon photoexcitation as it involves a direct observation and measurement of the evolution of electronic and vibrational structure. In a typical TRPES experiment, a pump pulse excites the target molecule, which is then ionized by a probe pulse arriving at a variable delay. The energy (sometimes angular distribution as well) of pho-

toelectrons ejected by the probe pulse is measured as a function of delay. TRPES has a unique advantage over other pump-probe techniques, for example, transient absorption and fluorescence spectroscopy, namely that ionization is always possible and not restricted by the selection rules. In other words, there are no optically dark states for photoionization.

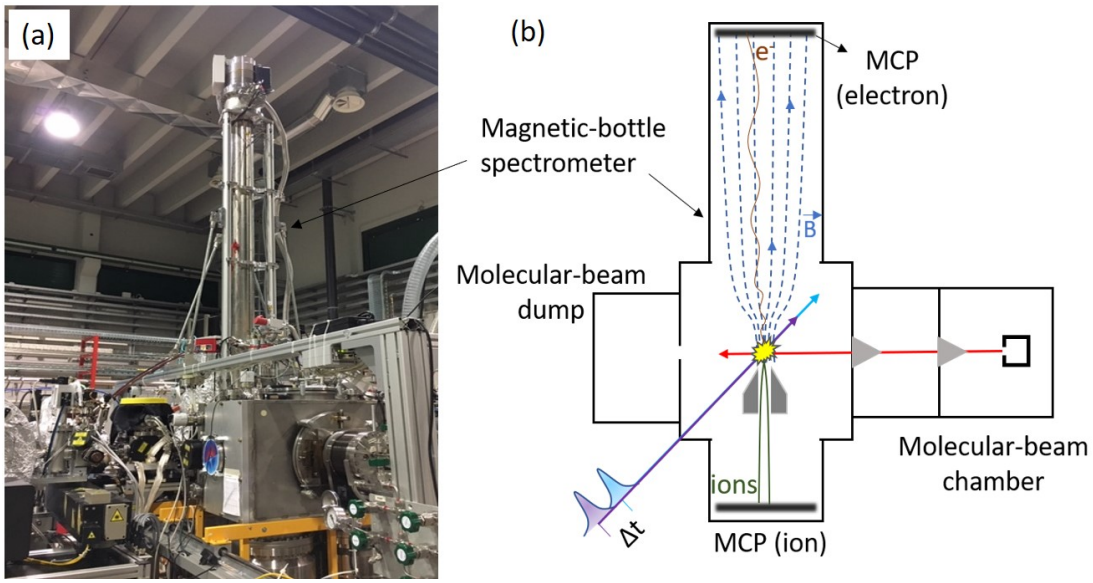

Figure 2.11: *(a) Photograph of the magnetic-bottle spectrometer installed at the Low Density Matter (LDM) beamline of the FERMI FEL, Trieste, Italy (b) Schematic diagram showing the interaction region and photoelectron trajectories in the magnetic field.*

Some of the commonly used equipment for measuring photoelectron spectra include velocity map imaging (VMI) and time-of-flight (TOF) spectrometers. The VMI technique is discussed in Sec. 2.3. This section will focus on TOF spectrometers, specifically the magnetic-bottle spectrometer (MBS).

MBS is a commonly used TOF spectrometer where the photoelectrons created in the interaction region are guided toward the electron detector (usually a MCP detector) using a magnetic field. These kinds of spectrometers are extremely powerful and are usually constructed to achieve higher energy resolution. Here we specifically describe the MBS used for some of the results in this dissertation. Figure 2.11 shows the schematic of the highly efficient, high-resolution magnetic-bottle spectrometer installed at the LDM beamline [41]

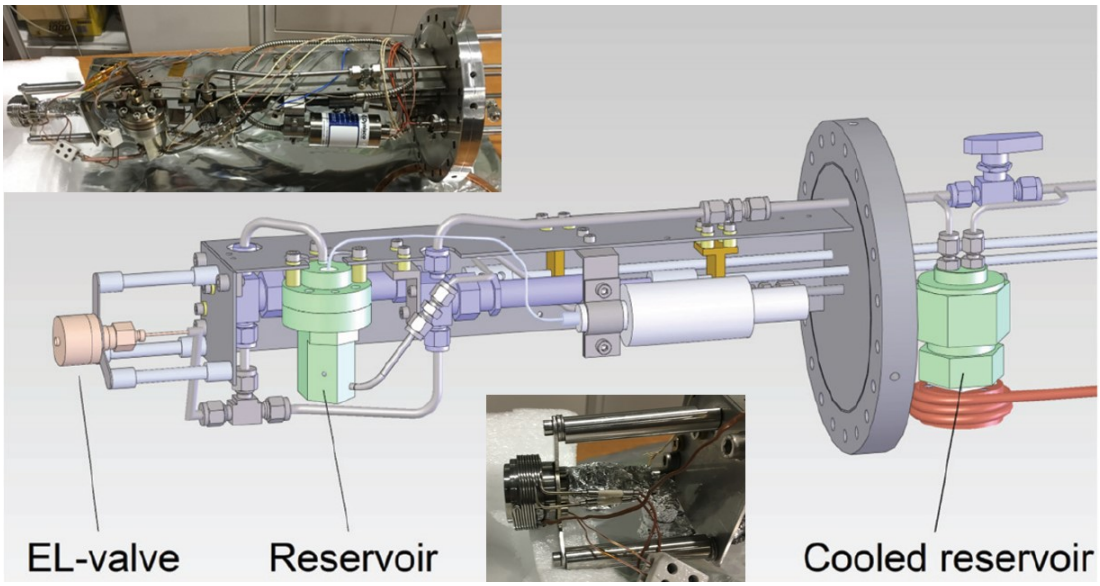

Figure 2.12: *Schematic of the molecular beam source attached to the magnetic-bottle spectrometer at the Low Density Matter (LDM) beamline of the FERMI FEL, Trieste, Italy [Adapted from [40]]. The inset on top shows the actual image taken after the experiment. The inset at the bottom shows a closer look at the heating arrangement of the nozzle.*

of the FERMI FEL [20], Trieste, Italy. The spectrometer is equipped with a permanent magnet, a solenoid and a retardation lens system of the Eland type [42–44]. The spectrometer has a collection efficiency close to 4π for photoelectrons and can also detect ions, which provides the capability to perform covariance analysis [44]. The energy resolution ($\Delta E/E$), where E is the final kinetic energy of the photoelectrons) for photoelectrons is 0.03. For the experiments shown in chapter 3, the voltages used while recording photoelectrons are: 8 V retardation voltage, 2000 V at the anode and 1800 V on the MCP back. For ion detection, the voltages used are -200 V on the magnet, -560 V on the ion mid plate and -1000 V on the ion tube. The anode and the MCP back voltages are 300 V and 1600 V, respectively.

The molecular beam source consists of an Even-Lavie (EL) valve and has the capability of heating the nozzle and the internal reservoir. This is crucial for molecular targets with low vapor pressure. The opening time of the EL valve is generally about 25-30 μs but closely depends on the length of the current pulse applied to the magnetic coil. Figure 2.12 shows the schematic of the molecular beam source. The inset also shows the heating arrangement

of the nozzle. For the experiments shown in chapter 3, the EL valve opening time is 26.5 μs and the temperature is 80 °C. Helium gas is also used as a carrier gas with a backing pressure of 2 bar.

Chapter 3

Ultraviolet-induced photochemistry in a heterocyclic molecule, thiophenone

This chapter presents the findings of several experiments studying the photochemistry of a prototypical heterocyclic ring-molecule, 2(5H)-thiophenone (C_4H_4OS). Specifically, the formation of ring-opened photoproducts (starting from the ring-closed molecule) and the subsequent isomerization after ultraviolet (UV) photon absorption are studied by time-resolved photoelectron spectroscopy and mega-electron-volt ultrafast electron diffraction (MeV-UED).

3.1 Background and motivation

With the advances in ultrafast light sources and the resulting improvements in the temporal and spatial resolution that can be achieved in pump-probe experiments, it is now possible to closely observe the delicate interplay of the nuclear and electronic motions that can be triggered when optical radiation interacts with a molecule. An interesting class of reactions are electrocyclic reactions, where it is possible to study the ring-opening and closing timescales of organic ring-molecules. Many naturally occurring processes involve photochemical elec-

trocyclic reactions, and these reactions possess numerous uses in synthetic organic chemistry. The timescales at which this structural rearrangements happen are typically of the order of a few hundred femtoseconds. In most cases, this is due to rapid nuclear motion along steeply sloped potential energy surfaces. These characteristics make electrocyclic reactions an exciting candidate to build light-controlled molecular switches [45–47]. Since the chemical and physical properties are different for the molecules defining either state of the switch, these properties can be measured and enable us to conclude if the switching action has occurred. Due to the change in the properties after photoisomerization, such reactions can also be used in light-controlled molecular data processing and storage applications [45]. Electrocyclic ring-opening and ring-closing reactions are also considered an important candidate for nano-mechanical devices [48, 49] and molecular logic gates [50].

One of the most commonly studied ring-opening reactions, which is also an important step in the formation of vitamin D_3 from sunlight [51], is the ring-opening of a compounds containing single units of cyclohexadiene (CHD). This reaction has been studied closely in recent years, with a variety of techniques such as x-ray and electron diffraction [52–56] and photoelectron and mass spectrometry methods [57–60]. The observations related to symmetries between CHD and its ring-opened product, cyclohexatriene (CHT), as well as studies on other polyenes, led to the formulation of Woodward-Hoffman rules conceptualizing the conservation of orbital symmetries based on molecular orbital analysis [61]. These rules are applicable to many other polyenes and can predict certain aspects of the stereochemistry [62, 63]. Although some of the earlier studies were focused on CHD, recently, several other model systems have been studied with the goal of understanding general principles underlying all electrocyclic reactions including several heterocyclic compounds, i.e. ring-molecule molecules with different atomic species making up the ring.

Heterocyclic compounds, especially sulfur- and nitrogen-containing ring molecules, are a part of some of the biochemicals essential for life. Naturally occurring vitamins, pigments, and antibiotics contain heterocyclic compounds and are used in drugs, dyes, pesticides,

etc. Studying these molecules and understanding rules governing photoinduced reactions for these heterocyclic molecules would thus be beneficial in understanding the chemistry of larger systems. One such prototypical heterocyclic ring molecule is 2(5H)-thiophenone (hereafter referred to as thiophenone). Thiophenone is a five-membered ring structure, with sulfur as a part of the ring and an oxygen atom attached to one of the adjacent carbon atoms (see Fig. 3.1). An earlier study by Murdock *et al.* [64] examined the ring opening of thiophenone in the liquid phase where thiophenone was dissolved in CH_3CN. This experiment successfully confirmed the ring-opening in thiophenone based on the observation of ketene as a photoproduct and provided the first insights related to the ring-opening timescale (< 1 ps). The formation time and distribution of photoproducts are usually affected by the solvent, [65], and it would be useful to compare these timescales for a gas-phase experiment, where the relaxation mechanisms are quite different.

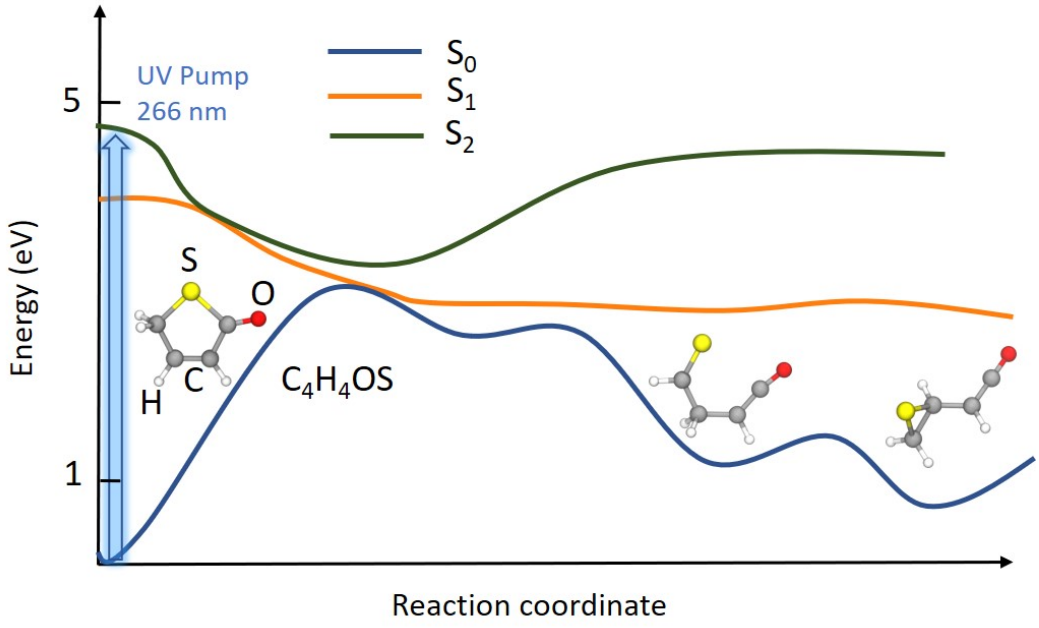

Figure 3.1: *Schematic potential energy curves showing ground and excited electronic 2(5H)-thiophenone (C_4H_4OS).*

Figure 3.1 shows the qualitative potential energy curves for the ground (S_0), first (S_1), and second (S_2) electronic excited states of thiophenone. As shown by the blue arrow,

absorption of one UV photon at ∼266 nm (∼4.66 eV) excites the thiophenone molecule from the S_0 to S_2 state. After the initial excitation to the S_2 state, the population can efficiently relax to the ground state via the S_2/S_1 and S_1/S_0 seams of intersection along the C-S bond distance coordinate [66]. After relaxation to the ground state, the molecules can either form ring-opened photoproducts or ring-closed vibrationally hot thiophenone molecules.

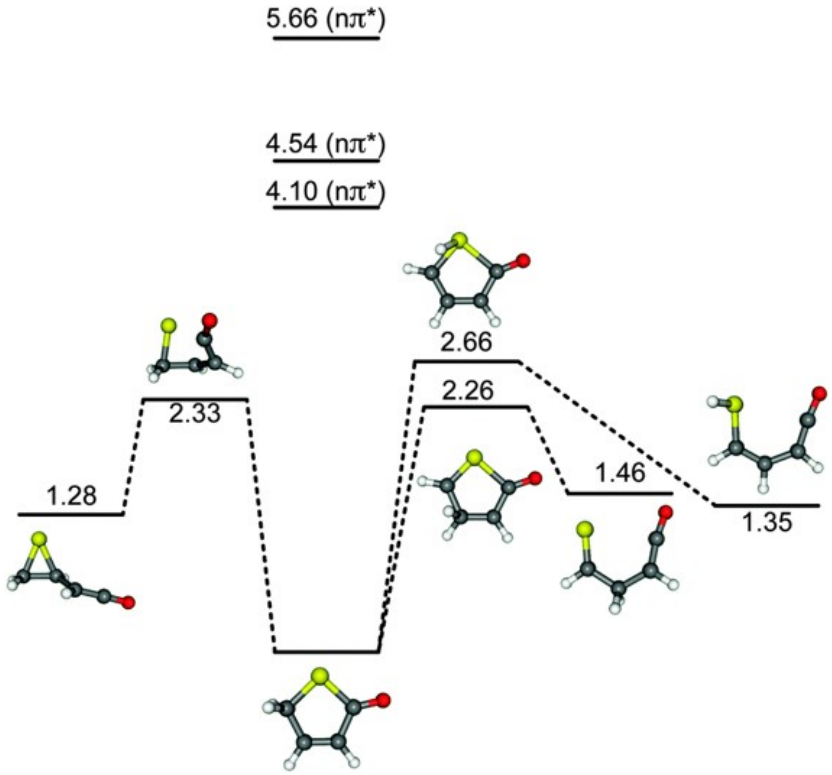

Figure 3.2: *Theoretically calculated ground state equilibrium structure of thiophenone and the products. Also shown are the energies (in eV) relative to the ground state [Adapted from [64]].*

Figure 3.2 shows some of the predicted photoproduct geometries and their relative energies calculated by Murdock *et al.* [64]. To calculate the S_0 equilibrium structure of thiophenone and three possible ring-opened products, the MP2/6-311+G(d,p) level of theory was used. Our goal is to resolve the excited state pathways which lead to the formation of photoproducts, to distinguish the photo products, and also to unravel the timescales involved

in their formation.

3.2 Time-resolved photoelectron spectroscopy of thiophenone

This section describes the results of a time-resolved photoelectron spectroscopy (TRPES) experiment performed on thiophenone at the seeded XUV free-electron laser (FEL) FERMI in Trieste, Italy. Specifically, a femtosecond UV pump laser (266 nm, 4.66 eV) was used to excite the thiophenone molecules, followed by a femtosecond XUV pulse (64.44 nm, 19.24 eV) from the FERMI FEL (described in section 2.2.2). The resulting photoelectron yield was monitored as a function of UV and XUV delay, ranging from a few tens of femtoseconds to a few hundred picoseconds. The photon energy of the probe pulse was chosen high enough to ionize molecules from the ground state , thus enabling us to monitor the evolution of the initially excited state molecules all the way to the ground state and, in particular, also ionized the ground state photoproducts. This allowed the measurement of the timescales related to the formation of the photoproducts.

Compared to self-amplified spontaneous emission (SASE) based FELs, the FERMI FEL offers narrower bandwidth (0.02 eV at ∼19 eV photon energy), is intrinsically stable, and produces negligible temporal jitter (Section 2.2.2). The narrow bandwidth allows achieving higher energy resolution, and the negligible temporal pulse-to-pulse jitter (see Section 2.2.2) helps to achieve better temporal resolution in the experiment. Lab-based high-harmonic sources can also be used as an XUV probe if their output is monochromatized and a sufficiently high photon flux can be achieved (see section 5.3.2).

Figure 3.3 shows the UV absorption cross-section of thiophenone measured using a Agilent Cary 60 UV-vis spectrophotometer. The black arrow shows the UV pump excitation wavelength used in the FERMI experiment, which had a central wavelength of 264.75 nm and a bandwidth of 1.2 nm. The UV pulses were generated by using a third-harmonic

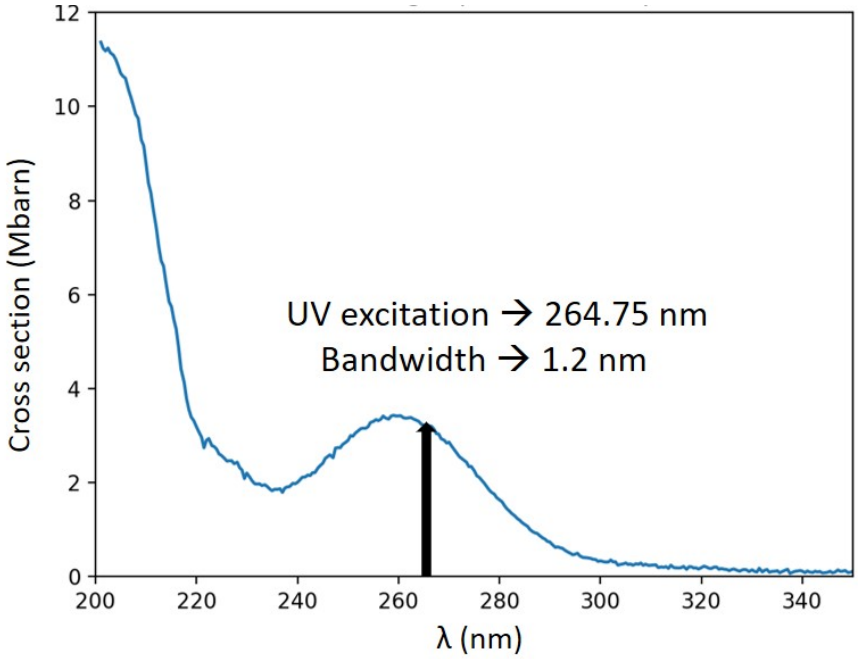

Figure 3.3: *UV absorption cross-section (measured) of thiophenone [67]. The excitation wavelength used in the experiment is indicated by the black arrow.*

generation of 800 nm from a Ti: Sapphire laser source.

Figure 3.4 shows a typical photoelectron TOF spectrum of thiophenone recorded during the experiment. The XUV photons from the FEL have sufficient energy to ionize the ground-state thiophenone molecules. The peaks in the eTOF spectrum from the FEL represent ionization of thiophenone molecules from the ground-state (S_0) to the cationic states (D_0, D_1, and D_2). It can be seen that the UV pulse alone does not ionize the molecules. The absence of ionization is because the ionization potential of thiophenone is 9.63 eV [68], and a single UV photon (4.66 eV) has insufficient energy to ionize it. It requires careful adjustment of the UV intensity to avoid multiphoton absorption, as discussed later in this section.

For calibrating the energy of photoelectrons, helium photoelectron spectra were recorded for several FEL (XUV) energies. The FERMI FEL produces coherent emission for several harmonics of the seed laser. For each harmonic, the FEL can be optimized by tuning the amount of energy modulation produced in the modulator (controlling the seed power) and

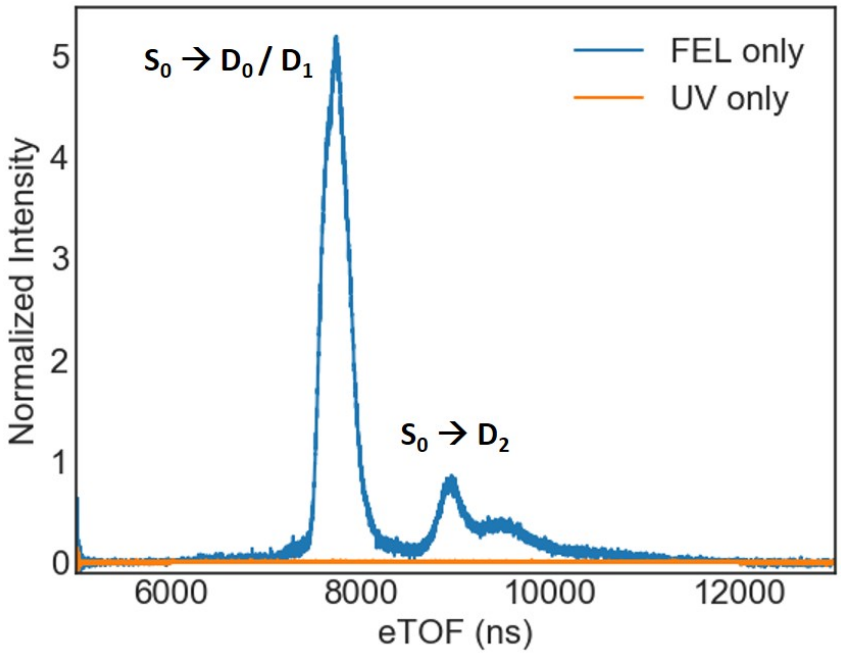

Figure 3.4: *Photoelectron time-of-flight (eTOF) spectrum of thiophenone post irradiation with FEL (XUV) and UV pulses. Note that no ionization is happening by the UV pulse alone.*

the strength of the dispersive section [20] (also, see section 2.2.2). The first ionization energy of helium is 24.58 eV. The photoelectron energy can be calculated by subtracting the ionization energy from the XUV energy. The resulting calibration curve is shown in Fig. 3.5. The curve is fitted with the equation:

$$E = \frac{L^2}{(t - t_0)^2} + C \tag{3.1}$$

where E is the photoelectron energy, t is electron TOF, t_0 is the time offset, L is the (effective) length of the spectrometer (which can also be derived from the fit), and C is the energy offset.

Using the fit values from the fit described before, the photoelectron spectrum shown in Fig. 3.4 are converted from TOF to photoelectron energy. The photoelectron energies are then converted to binding energies by subtracting the photoelectron energy from the FEL

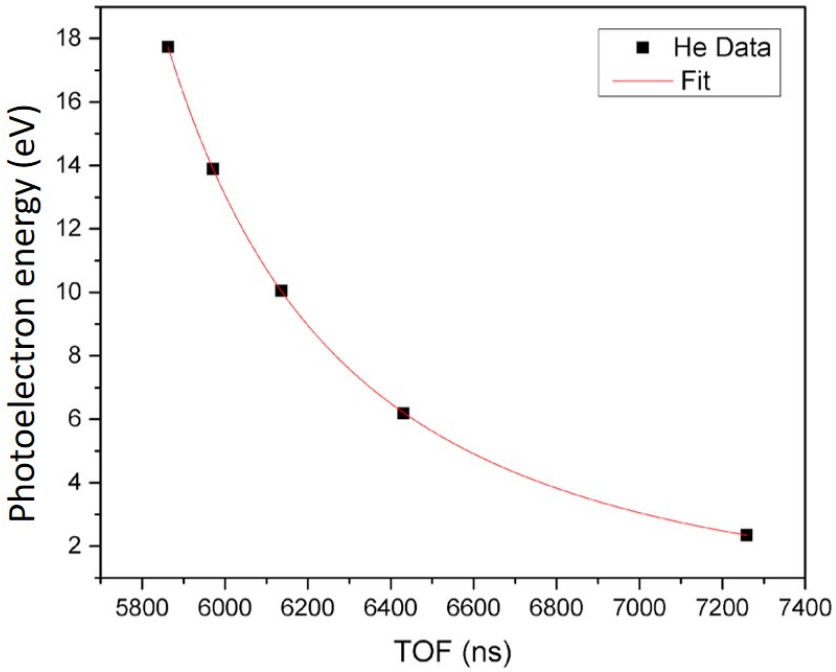

Figure 3.5: *Calibration curve for conversion of electron TOF to photoelectron energy. Each point represents a different FEL photon energy for which helium photoelectron TOF is recorded.*

energy.

$$BE = 19.24\,eV - PE \tag{3.2}$$

where BE is the binding energy, PE is the photoelectron energy, and 19.24 eV is the FEL energy, which was used in the experiment.

Figure 3.6(a) shows the photoelectron spectra measured at the FERMI FEL converted to binding energy (shown in blue). Also shown is the part of the photoelectron spectra of thiophenone recorded by Chin *et al.* [68] using a helium lamp (HeI). The measurement from Chin *et al.* [68] had a resolution of 25 meV. The features in both spectra agree well. The differences in peak positions between the two spectra is less than 0.1 eV, which is within the experimental resolution ($\Delta E/E = 0.03$) for the FEL results. It should be noted that the FEL spectrum is cut off at ∼11 eV. This is because a retardation voltage of 8 V was applied to increase the resolution of the electrons within the region of interest, and

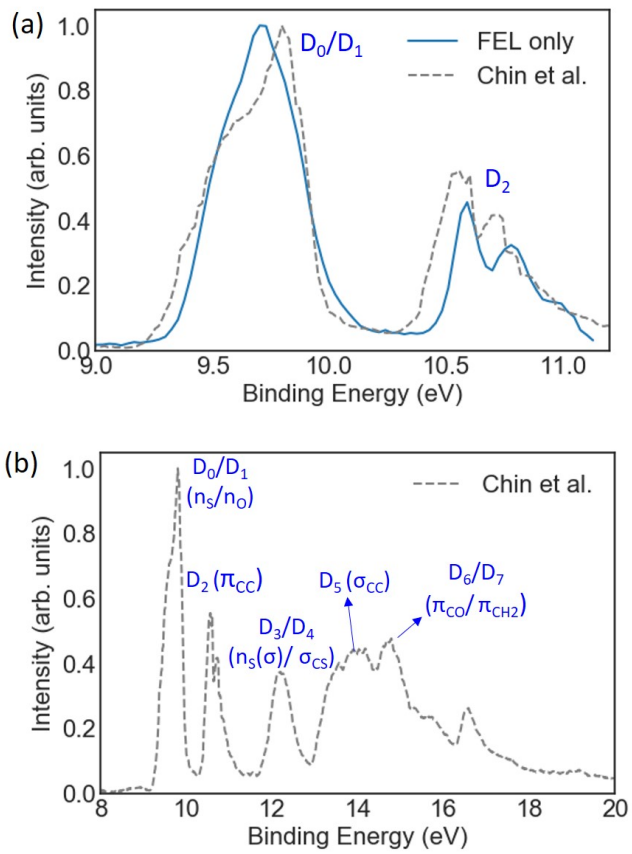

Figure 3.6: *Photoelectron spectrum of thiophenone (a) Spectrum recorded at FERMI FEL and by Chin et al. [68] (both spectra converted to binding energy), (b) Full spectrum by Chin et al. indicating the ionic states and orbitals.*

hence the photoelectrons with kinetic energy less than 8 eV (or BE $>$ 11.24 eV) are not detected. Figure 3.6(b) shows the complete spectrum recorded by Chin *et al.*, with different ionic states and orbitals labeled. The ground and first excited cationic states, D_0 and D_1, correspond to the removal of an electron from n_S and n_O, respectively. The cationic state D_2 corresponds to the removal of an electron from the π_{CC} orbital [68]. The energy resolution (for the FEL experiment) is insufficient to resolve the photoelectron signal from D_0 and D_1. It is also not possible in the FEL experiment to resolve the vibrational progression of D_1. However, the vibrational progression of the D_2 state is observed, which is attributed to skeletal stretching of the thiophenone molecules [70].

In order to determine if the pulse energies of the UV and FEL are within the single-

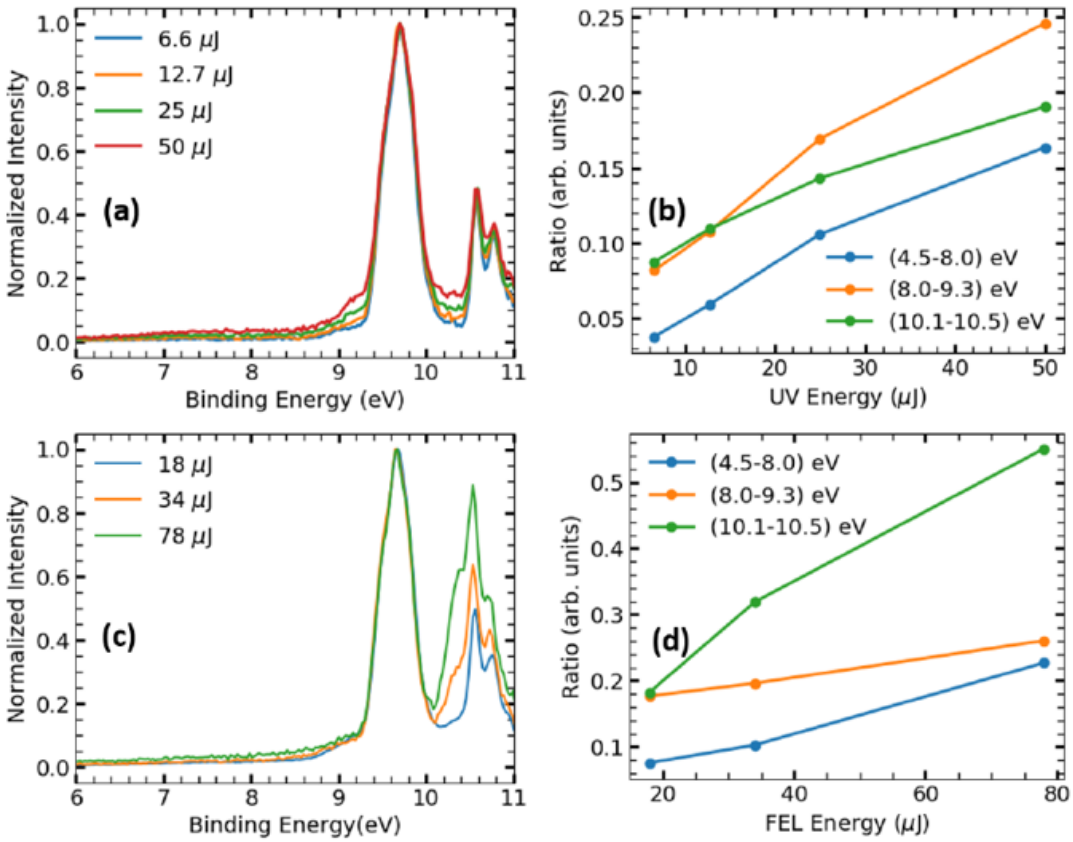

Figure 3.7: *FEL and UV pulse energy dependence of the pump-probe signal in the photoelectron spectrum. (a),(b) Dependence on UV pulse energy. (c),(d) Dependence on FEL pulse energy. The ratio of photoelectron signal for different binding energy ranges to the photoelectron signal from unpumped molecules is shown in (b) and (d), Adapted from [69].*

photon absorption regime, the photoelectron spectrum is recorded for different FEL and UV pulse energies at a fixed delay between the FEL and UV pulses. Figure 3.7(a),(b) shows the dependence of photoelectron spectrum on UV pulse energy. Figure 3.7(c),(d) shows the dependence on FEL pulse energy. All the photoelectron spectra are normalized w.r.t. the maximum of the photoelectron peak at 9.6 eV. Panel (b) and (d) show the ratio of changing photoelectron signal (specified by binding energy ranges) w.r.t. unpumped molecules (peak at 9.6 eV). Panels (b) and (d) gives an estimate of how the pump-probe signal changes with pulse energy. For the three energy ranges shown in Fig. 3.7(b), the ratio changes close to linearly with UV energy up to 25 μJ and then starts to deviate. In Fig. 3.7(d), the

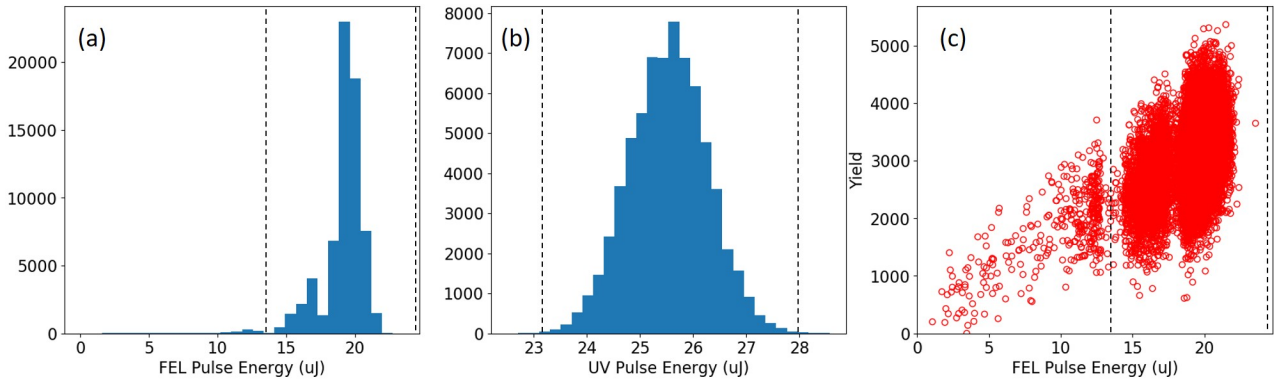

Figure 3.8: *One-dimensional histogram showing spread in (a) FEL pulse energy, (b) UV pulse energy (c) Two-dimensional histogram showing photoelectron yield vs. FEL pulse energy. Black dashed vertical lines represent the boundaries outside which the shots were rejected in the analysis.*

linearity of the ratio change is not conclusive. Hence, the lowest FEL energy was chosen for the experiment for which a good signal-to-noise ratio could be achieved. The FEL and UV pulse energies chosen for the experiments were 25 μJ and 19 μJ, respectively. It is to be noted that the FEL pulse energies are measured upstream of the beamline transport optics, and transmission values were measured [41] previously. Figure 3.8(a),(b) shows histograms representing a typical spread in pulse energies of FEL and UV pulses during the experiment. The shots where the pulse energies deviated more than four times the standard deviation were rejected during the analysis. The variation of the total photoelectron yield with FEL pulse energy is also shown in Fig. 3.8(c).

3.3 Excited- and ground-state dynamics of thiophenone post 266 nm absorption

This section presents our published work in *Nature Chemistry* [71], which demonstrated the formation and interconversion of different photoproducts upon UV excitation of thiophenone. This study combines experimental work with state-of-the-art ab-initio molecular

dynamics calculations to study the relaxation pathways post UV absorption in thiophenone. The theoretical work for this study is done by Prof. Basile Curchod and Lea M. Ibele at Durham University, U.K. My specific role in this project was to perform the experiment along with other collaborators and the team at the LDM endstation at FERMI FEL, who worked on setting up the experiment. I also worked on analyzing the data post-experiment, interpreting the results, and writing the manuscript, in close collaboration with my advisor Prof. Daniel Rolles and with Prof. Michael N.R. Ashfold, Bristol University, U.K.

In this study, thiophenone molecules are excited by absorption of a UV photon, followed by ionization using XUV photons from the FERMI FEL. The experimental delay-dependent photoelectron intensity, shown in Fig. 2 of the Nature Chemistry article, shows a clear time-dependent signal when the UV precedes the FEL pulses. The photoelectron intensity increases at lower binding energies when the UV and FEL pulses are near overlap temporally. As the delay between the UV and FEL pulses is increased (UV preceding FEL), the photoelectron intensity shifts toward higher binding energies and settles down at binding energies slightly lower than the binding energy of the unpumped thiophenone molecule. The precise energy measurement at each time step, coupled with theoretical calculations, as described below, allows us to interpret the relaxation pathways and formation of several photoproducts.

The experimental results are combined with theoretical calculations to gain insights into both the excited-state and the ground-state dynamics. The excited-state dynamics of thiophenone post excitation to the S_2 state is studied using the mixed classical/quantum trajectory surface hopping (TSH) method. The trajectories are initiated in the bright S_2 state, and 46 initial conditions of TSH dynamics are sampled from the Wigner distribution for the ground state molecule. The TSH calculations are performed using time steps of 0.5 fs and SA(4)-CASSCF(10/8) for the electronic structure [69], using Molpro 2012. They show ultrafast de-excitation of the population from S_2 to S_1 to S_0, driven by ballistic ring-opening along the C-S bond. The trajectories start reaching the ground state within $\sim$ 50 fs, and all

the population reaches the ground state within $\sim$ 350 fs. These timescales correlate with the increase in photoelectron intensity at higher binding energies seen in the experiment, suggesting that the photoelectron intensity change traces the movement of population (or wave-packets) from the excited state to the ground state.

To study the ground state dynamics, the TSH calculations are combined with ab-initio molecular dynamics (AIMD) calculations. In an AIMD calculation, dynamical trajectories are generated by using the forces calculated directly from the electronic structure, which is obtained during each step of the calculation. The AIMD simulations were initiated from the nuclear coordinates using the momenta obtained by the TSH trajectories once they had reached the S_0 state [69]. These calculations revealed the formation of three ring-opened photoproducts (with a minor contribution from other photoproducts). All the photoproducts lie in a narrow band of the ionization potential distribution. The narrow band computed by the AIMD calculation and the binding energy range, for which the photoelectron intensity increase is observed during the experiment, matched very well. Hence, the rise in photoelectron intensity at higher binding energy were attributed mainly to the formation of the three ring-opened photoproducts.

nature chemistry

ARTICLES

https://doi.org/10.1038/s41557-020-0507-3

Check for updates

Tracking the ultraviolet-induced photochemistry of thiophenone during and after ultrafast ring opening

Shashank Pathak[1,16], Lea M. Ibele[2,16], Rebecca Boll[3], Carlo Callegari[4], Alexander Demidovich[4], Benjamin Erk[5], Raimund Feifel[6], Ruaridh Forbes[7], Michele Di Fraia[4], Luca Giannessi[4,8], Christopher S. Hansen[9], David M. P. Holland[10], Rebecca A. Ingle[11], Robert Mason[12], Oksana Plekan[4], Kevin C. Prince[4,13], Arnaud Rouzée[14], Richard J. Squibb[6], Jan Tross[1], Michael N. R. Ashfold[15] ✉, Basile F. E. Curchod[2] ✉ and Daniel Rolles[1] ✉

Photoinduced isomerization reactions lie at the heart of many chemical processes in nature. The mechanisms of such reactions are determined by a delicate interplay of coupled electronic and nuclear dynamics occurring on the femtosecond scale, followed by the slower redistribution of energy into different vibrational degrees of freedom. Here we apply time-resolved photoelectron spectroscopy with a seeded extreme ultraviolet free-electron laser to trace the ultrafast ring opening of gas-phase thiophenone molecules following ultraviolet photoexcitation. When combined with ab initio electronic structure and molecular dynamics calculations of the excited- and ground-state molecules, the results provide insights into both the electronic and nuclear dynamics of this fundamental class of reactions. The initial ring opening and non-adiabatic coupling to the electronic ground state are shown to be driven by ballistic S–C bond extension and to be complete within 350 fs. Theory and experiment also enable visualization of the rich ground-state dynamics that involve the formation of, and interconversion between, ring-opened isomers and the cyclic structure, as well as fragmentation over much longer timescales.

Recent advances in time-resolved experimental techniques and in computational methods for treating (coupled) electronic and nuclear dynamics are revolutionizing the field of ultrafast photochemistry, enabling direct probing of evolving molecular structures with unprecedented structural and temporal resolution[1–8]. Such studies provide the ultimate test of our knowledge and understanding of light-initiated chemistry. Photoinduced ring-opening/closing reactions play a crucial role in many key processes in nature, such as the synthesis of natural products (for example, the synthesis of previtamin D_3 by sunlight) and are currently attracting interest as molecular and biomolecular switches for photocontrolled switching of enzyme activity, optical data storage, the modulation of energy and electron transfer processes[9,10] and potential medical applications[11]. Ring-opening reactions featured prominently in the development of the Woodward–Hoffmann rules, which help rationalize the mechanisms and outcomes of pericyclic reactions. It is now recognized that photoinduced isomerization (including ring-opening) reactions are governed by strong non-adiabatic coupling between multiple electronic states of the molecule via conical intersections, which represent a breakdown of the Born–Oppenheimer approximation[5,12].

The photoinduced ring opening of the polyene 1,3-cyclohexadiene[13] is widely employed as a model system for benchmarking and validating ultrafast methods such as ultrafast X-ray[1,7,8] and electron[6] diffraction, femtosecond transient X-ray absorption[4] and fragmentation[14], and time-resolved photoelectron spectroscopy (TRPES)[15,16]. However, few other photoinduced ring-opening reactions have been probed so thoroughly and, of these, even fewer have provided a comprehensive picture of the reaction dynamics on both the excited and ground (S_0) state potential energy surfaces (PESs).

Here we report a combined theoretical and experimental study of the UV photoinduced ring opening of a prototypical heterocyclic molecule, 2(5H)-thiophenone (C_4H_4OS, henceforth thiophenone; see Fig. 1). Heterocyclic compounds are fundamental building blocks in the synthesis of many organic compounds. Studying these 'single units' may help in validating the (necessarily more complex and less resolvable) photochemistry of ever-larger molecules. The study is conducted in the gas phase (that is, under collision-free conditions) and thus reveals information on the purely intramolecular relaxation pathways, without the solvation effects present in previous matrix-isolation[17] and liquid-phase[18] studies of this system. Theory and experiment combine to afford detailed insights into both the mechanism and timescale of the initial ring-opening process and the subsequent evolution of the vibrationally excited ground-state photoproducts.

[1]J.R. Macdonald Laboratory, Department of Physics, Kansas State University, Manhattan, KS, USA. [2]Department of Chemistry, Durham University, Durham, UK. [3]European XFEL, Schenefeld, Germany. [4]Elettra-Sincrotrone Trieste S.C.p.A., Trieste, Italy. [5]Deutsches Elektronen-Synchrotron, Hamburg, Germany. [6]Department of Physics, University of Gothenburg, Gothenburg, Sweden. [7]Stanford PULSE Institute, SLAC National Accelerator Laboratory, Menlo Park, CA, USA. [8]Istituto Nazionale di Fisica Nucleare, Laboratori Nazionali di Frascati, Frascati, Italy. [9]School of Chemistry, University of New South Wales, Sydney, New South Wales, Australia. [10]Daresbury Laboratory, Warrington, UK. [11]Department of Chemistry, University College London, London, UK. [12]Department of Chemistry, University of Oxford, Oxford, UK. [13]Centre for Translational Atomaterials, Swinburne University of Technology, Melbourne, Victoria, Australia. [14]Max-Born-Institut, Berlin, Germany. [15]School of Chemistry, University of Bristol, Bristol, UK. [16]These authors contributed equally: Shashank Pathak, Lea M. Ibele. ✉e-mail: mike.ashfold@bristol.ac.uk; basile.f.curchod@durham.ac.uk; rolles@phys.ksu.edu

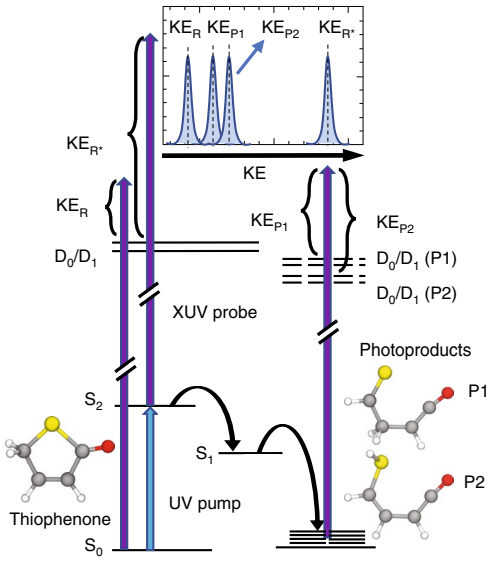

Fig. 1 | Schematic of the UV excitation, ring opening and photoionization of thiophenone. The molecule is photoexcited from its ring-closed ground state (S_0) to an electronically excited state (S_2). It evolves through an optically dark excited state (S_1) back to the (vibrationally excited) S_0 state of several possible reaction products (P1, P2 and so on). The XUV probe photon energy is sufficient to ionize thiophenone and all reaction products from both ground and excited states into several ionic final states (D_0, D_1 and so on). The time-evolving electron kinetic energy (KE) spectrum (top) thus consists of contributions from the ground and excited states of thiophenone (denoted as R and R*, respectively) and from the different products. In the depictions of the molecular geometry, carbon atoms are shown in grey, hydrogen in white, oxygen in red and sulfur in yellow.

The experimental study employs the extreme UV (XUV) radiation provided by the free-electron laser (FEL) FERMI[19]. TRPES[20,21] is sensitive to both electronic and structural dynamics, which is essential for any full understanding of the coupled electronic and nuclear dynamics that govern most photoinduced reactions. TRPES also allows access to so-called 'dark' states that may not be amenable to study by transient absorption methods. XUV probe pulses (from an FEL or a high harmonic generation source) are sufficiently energetic to ionize molecules in the electronic ground state (S_0), thereby overcoming a long-recognized shortcoming of previous TRPES studies that employed lower energy (UV) photons and were thus unable to reveal the ultimate structural dynamics following transfer from an electronically excited state to the ground state[16,22–26]. FERMI is a seeded FEL[19,27], in which an external laser is used to initiate the XUV generation, offering the advantages of (1) a narrower photon energy bandwidth (that is, higher energy resolution) and higher stability compared to FELs based on self-amplified spontaneous emission (SASE), and (2) higher pulse energies and photon fluxes as compared to monochromatized XUV sources based on high harmonic generation.

In the present experiment, gas-phase thiophenone molecules are excited to the optically bright S_2 electronic state by a UV pulse ($\lambda \approx 265$ nm). The excited molecules evolve through one or more conical intersections at progressively greater C–S bond separations en route back to the S_0-state PES, where they can adopt the original closed-ring or one of several possible open-ring geometries[18,28], some of which are sketched in Fig. 1. The evolving wavepacket and the formation of open- and closed-ring photoproducts are probed by ionizing the molecule with a time-delayed 19.24 eV ($\lambda = 64.44$ nm) XUV pulse. Time-dependent photoelectron time-of-flight spectra are recorded as a function of the time delay (Δt) between the UV and FEL pulses using a magnetic bottle spectrometer (see Methods and Supplementary Fig. 1). The FEL photon energy is deliberately chosen to be well above the first ionization potential (IP) of the ground-state molecule (~9.7 eV)[29] but below the IP of the helium carrier gas, ensuring that the electronic character of the target molecule can be traced throughout the complete structural evolution with only minimum background signal from the carrier gas. The experimental results are complemented by high-level ab initio electronic structure and molecular dynamics calculations of both excited- and ground-state molecules. These calculations afford insight into the ultrafast electronic de-excitation that accompanies ring opening and the subsequent interconversion between different isomeric forms of the highly vibrationally excited ground-state photoproducts.

Results and discussion

Experimental results. The experiment measures electron time-of-flight spectra of thiophenone as a function of Δt. The spectra are converted to electron kinetic energy spectra and then, by energy conservation, into spectra of the valence binding energies (see Methods). Figure 2a shows such spectra in the form of a two-dimensional plot of electron yield as functions of binding energy (BE) and Δt. The dominant feature, at BE ≈ 9.7 eV, is due to photoionization of the 'cold' (that is, non-excited) closed-ring S_0-state thiophenone molecule[29]. This peak is depleted by ~20% for positive Δt, as shown in Fig. 2b (red circles), confirming excitation of ground-state molecules by the UV pulse. A fit to the delay-dependent yield of photoelectrons originating from S_0-state parent molecules yields an upper limit for the temporal instrument response function of $\sigma = 72 \pm 8$ fs. Figure 2a reveals photoelectrons with BEs as low as ~5 eV at the shortest positive Δt. The prompt appearance and subsequent decay of this contribution is also emphasized in Fig. 2b, which shows a Gaussian-shaped transient signal with $\sigma = 76 \pm 6$ fs (blue triangles). With increasing delay, the signal at BE ≈ 5 eV fades, and the peak intensity shifts towards higher BE. As Fig. 2c shows, the peak in the intensity versus Δt transient obtained by taking contiguous 0.6 eV-wide slices for BE ≥ 5.3 eV shifts to progressively later Δt with increasing BE, and the transients gain an increasingly obvious tail.

The thiophenone cation has close-lying ground (D_0) and first excited (D_1) states at a vertical IP (IP_{vert}) of ~9.7 eV and higher excited states at IP_{vert} values of 10.58 eV (D_2), 12.25 eV (D_3) and 14.1 eV (D_4)[29]. Given the present pump photon energy of 4.67 eV, the signal appearing at a binding energy of ~5 eV at $\Delta t \approx 0$ is readily attributed to vertical ionization of photoexcited molecules in the S_2 state to the (unresolved) D_0 and D_1 states. Ionization to the D_1 state is strongly disfavoured due to selection rules, as discussed in Section 2.3 of the Supplementary Information. The evolution of the signal at BE ≈ 5 eV, the peak shift towards higher BE at later Δt and the more intense tail in the Δt traces for higher BE slices all reflect the complex evolution of the photoprepared wavepacket, which the accompanying theory shows involves ultrafast depopulation of the S_2 state to yield 'hot', that is, highly vibrationally excited, S_0 (henceforth $S_0^{\#}$) molecules (revealed by the teal green stripe in Fig. 2a at BE ≈ 9 eV). Note that any photoelectrons arising from ionization of $S_0^{\#}$ molecules to excited D_n ($n > 1$) cation states are likely to appear at BE > 10 eV (see extended spectrum in Supplementary Fig. 2) and thus do not affect the discussion that follows.

Calculations of decay pathways and excited-state dynamics. To interpret the dynamics revealed in the TRPES spectra, the lowest-lying PESs of thiophenone were computed and different critical points were located using SA(4)-CASSCF(10/8) calculations, and their energies further refined using XMS(4)-CASPT2(10/8) (see Computational details for more information). The Franck–Condon (FC) geometry corresponds to the equilibrium structure of

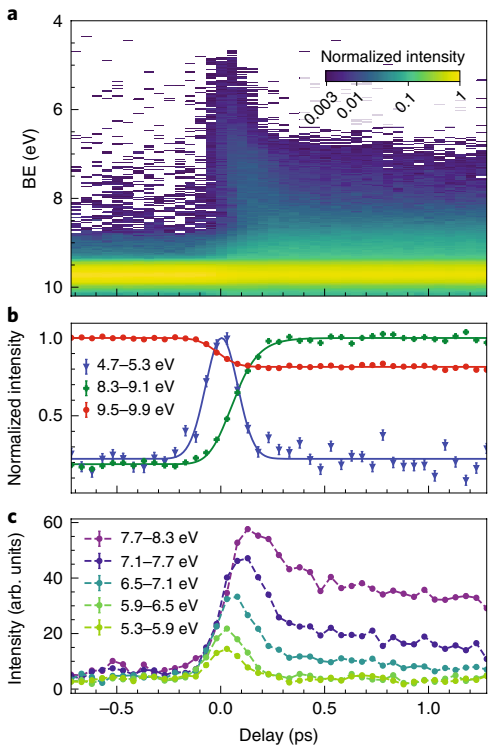

Fig. 2 | Time-dependent photoelectron spectra of UV-excited thiophenone. a, Measured photoelectron yield as a function of BE and time delay (Δt) between pump and probe pulses (see Supplementary Fig. 2 for a plot over a wider range of signal intensities, binding energies and delays). Negative Δt corresponds to the FEL pulse preceding the UV pulse and positive Δt to the UV pulse preceding the FEL pulse, while the colour represents the normalized photoelectron intensity. Regions with an intensity below 0.003 are shown in white. **b**, Delay-dependent photoelectron yields for three BE ranges selected to illustrate the photoinduced depopulation of the S_0 state (red circles), population of the S_2 state (blue triangles) and the build-up of vibrationally excited $S_0^\#$ photoproducts (green crosses). **c**, Delay-dependent photoelectron yields five contiguous 0.6 eV-wide BE slices that inform on the evolution from photoexcited S_2 to internally excited $S_0^\#$ molecules. Statistical error bars are included but are generally smaller than the symbol size. The parameters of the least-square fits shown as solid lines in **b** are summarized in Supplementary Table 1, while the dashed lines in **c** just join the dots for better visibility. The data in **b** have been normalized such that the maximum value of the fit is at 1 for each curve, whereas the data in **c** are displayed on a common intensity scale.

the S_0 state of thiophenone, wherein the highest occupied molecular orbital (HOMO) is an out-of-plane π orbital largely localized on the sulfur atom, henceforth labelled n(S). At our chosen pump photon energy, thiophenone is predominantly excited to its S_2 state. At the XMS(4)-CASPT2(10/8) level of theory, the $S_0 \rightarrow S_2$ transition has $n(S)/\pi^\star$ character, a calculated transition energy of 4.67 eV and an appreciable oscillator strength (0.036), reflecting the constructive overlap of the donating n(S) and accepting $\pi^\star$ orbitals. The $S_0 \rightarrow S_1$ transition (with a calculated energy of 4.20 eV), by contrast, is dark (the donating O-atom centered, lone pair n(O) orbital lies in the plane of the ring and is thus orthogonal to the accepting orbital; see Section 2.1 in the Supplementary Information). Different minimum energy conical intersections (MECIs) were located between the S_2, S_1 and S_0 states of thiophenone, as shown in Fig. 3a. All of these MECIs indicate a ring opening in the excited electronic state (that is, formation of a biradical), followed by geometrical relaxation—for example, twisting of the CH_2–S moiety out of the molecular plane and bending of the C–C=O moiety (see also Section 2.2 in the Supplementary Information).

To determine the possible connections between these critical structures and the relaxation pathways of thiophenone following UV photoexcitation, linear interpolations in internal coordinates (LIICs) were performed using XMS(4)-CASPT2(10/8) (see Computational details). Starting from the FC geometry, the LIICs smoothly connect the different critical points and confirm that photoexcited thiophenone (S_2) molecules can relax efficiently towards the S_0 state via the S_2/S_1 and S_1/S_0 seams of intersection in the C–S bond extension coordinate[28]. The energies of the low-lying D_0 and D_1 states of the thiophenone cation were also computed at selected geometries along the LIIC pathways (Fig. 3a, dashed lines). In the FC region, these states are characterized by removal of an electron from, respectively, the n(S) and n(O) lone pair orbitals. As Fig. 3a shows, the topographies of the various PESs of neutral thiophenone vary strongly along the LIIC pathways, but the energies of the D_0 and D_1 states of the cation show a smooth and very gradual increase. The energy differences (ΔE) between the D_1/D_0 and the S_2/S_1 potentials along the LIIC pathways (inset in Fig. 3a) increase dramatically from the FC point out to the S_1/S_0 MECI. The calculations allow assignment of the experimentally observed rapid increase in BE with increasing Δt to the ultrafast depopulation of the S_2 state and electronic deactivation to the S_0 state, resulting in highly vibrationally excited ground-state molecules. We note that the calculated ΔE values are consistently slightly lower than the experimental BE values. Such underestimation of (experimental) IP values by (X)MS-CASPT2 methods is well-known[30] and, in the present case, can also be related to the choice of basis set (see Section 2.2 of the Supplementary Information).

The fates of the photoexcited thiophenone molecules were further explored by running trajectory surface hopping (TSH) calculations from the photoprepared S_2 state at the SA(4)-CASSCF(10/8) level of theory. These results are detailed in Section 2 of the Supplementary Information, and only the main features of the dynamics are highlighted here. As expected from inspection of the LIIC pathways, the initial S_2 population rapidly decays to the S_1 state and population appears almost immediately on the S_0 PES, as shown in Fig. 3b. All population is transferred to the S_0 state within 350 fs of UV excitation. Figure 3c displays a swarm of 46 TSH trajectories that mimic the relaxation dynamics of the thiophenone wavepacket and demonstrate that the ultrafast deactivation from S_2 to S_1 to S_0 is driven by a ballistic ring-opening process. The trajectories start to spread after ~50 fs; most remain ring-opened upon becoming $S_0^\#$ molecules, but some readopt a (vibrationally hot) cyclic configuration.

The conclusions from the TSH calculations match well with the experimental time-resolved photoelectron yields for the BE ranges selected to span the predicted IP_{vert} values along the LIIC (Fig. 2b,c). The yield in the BE range corresponding to vertical ionization from the S_2 state (blue trace in Fig. 2b) shows a narrow transient signal, the width of which is largely determined by the instrument response function. With increasing Δt, this transient signal shifts to higher BE, broadens somewhat and gains a longer time tail (Fig. 2c). Recalling the inset in Fig. 3a, these observed changes are all consistent with the wavepacket evolving on the S_2 PES (sampled most cleanly by intensities at BE ≤ 5.5 eV) and subsequent non-adiabatic coupling with the S_1 state (which are sampled most efficiently in the 6 ≤ BE ≤ 7 eV range) and thence with the S_0 PES (which start to be sampled at BE ≥ 7 eV). Ionization of $S_0^\#$ molecules accounts for the tails in the transients for the higher energy BE slices in Fig. 2c; the build-up of $S_0^\#$ population (green crosses in Fig. 2b) plateaus at $\Delta t \geq 300$ fs. These comparisons serve to reinforce the interpretation, developed from considering the LIIC pathways (Fig. 3a), that the experimentally observed increase in BE is a signature of the ultrafast decay of thiophenone (S_2) molecules to high $S_0^\#$ levels.

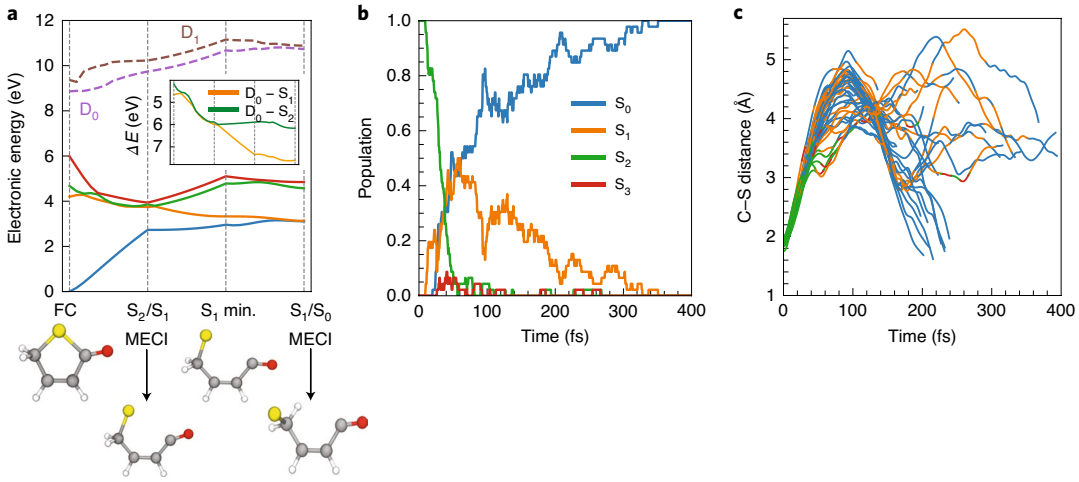

Fig. 3 | Ab initio calculations of PESs and excited-state dynamics. a, PESs for the lowest neutral singlet (solid lines; S_0 in blue, S_1 in orange, S_2 in green and S_3 in red) and cationic doublet (dashed lines) electronic states of thiophenone along LIIC pathways between different critical geometries. Electronic energies were obtained using XMS(4)-CASPT2(10/8) for the neutral and XMS(4)/CASPT2(9/8) for the cationic form of thiophenone. The critical geometries, minima and MECIs, located using the SA(4)-CASSCF(10/8) level of theory, are indicated with light-grey vertical lines, and the geometries of these critical points on the PESs of neutral thiophenone are shown below. LIIC pathways were then computed between each critical point, and the inset shows the electronic energy gap ΔE between the D_0 state of the cation and the second (S_2) or first (S_1) singlet states of neutral thiophenone for each point along the LIIC pathway. **b**, Time-dependence of the S_3, S_2, S_1 and S_0 state populations provided by the TSH dynamics (46 trajectories). **c**, Time-evolution of the C–S bond distance for each of these 46 trajectories, illustrating the prompt initial bond extension in all cases and (via the colour coding) the trajectory-dependent evolution from S_2 through S_1 to the S_0 state. The TSH trajectories were propagated until they experienced electronic structure instabilities in the ground state (see text).

Ground-state dynamics and reaction products. One key feature of the present experimental study is that the response of UV-excited thiophenone molecules can be followed not just en route to, but also after reaching, the S_0 PES. Figure 4a shows photoelectron spectra recorded at several pump–probe delays in the range $10 \leq \Delta t \leq 600$ ps. Most of the photoelectron intensity of interest at these large Δt values lies in the range $8.0 \leq \mathrm{BE} \leq 9.6$ eV, and the spectrum appears to consist of different contributions whose weights are Δt dependent; the intensity of the feature at lower BE (peaking at BE ≈ 8.8 eV) appears to increase relative to that of the feature peaking at BE ≈ 9.3 eV as Δt increases. To simulate the ground-state dynamics, the foregoing non-adiabatic molecular dynamics calculations using TSH in the lowest four electronic states were combined with ab initio molecular dynamics (AIMD, see Computational details) on the S_0 PES. From an electronic structure perspective, this required switching from an SA-CASSCF description (used for the excited-state dynamics) to an unrestricted density functional theory (UDFT) picture using the PBE0 exchange/correlation functional. The SA-CASSCF active space employed for the TSH dynamics became unstable when the trajectories were prolonged on the S_0 PES, but AIMD with UDFT was found to offer a stable alternative and allowed long-time simulation of the $S_0^{\#}$ species (see, for example, a previous study by Mignolet et al. [31]). Tests demonstrating the validity of this approach for the present system are reported in Supplementary Section 2.5.

To initiate the $S_0^{\#}$ molecular dynamics after passage through the S_1/S_0 seam of intersection, the AIMD trajectories were launched from the nuclear coordinates and with the momenta extracted from the TSH trajectories after the S_0 state had been reached. Thus, the present AIMD simulations are not per se in a ground-state thermal equilibrium, since the internal energy of the molecule at the start of the S_0-state dynamics calculation depends on the history of the TSH trajectory in the excited state; that is, the approach allows description of non-statistical effects in the hot S_0-state dynamics. In total, 22 AIMD trajectories were propagated until $t = 2$ ps and, to explore the longer-time dynamics, 10 of these were propagated further to $t = 100$ ps (see Computational details and Section 2.10 in the Supplementary Information). Since each is a continuation of an excited-state trajectory, the starting configuration in each case involves a ring-opened or highly stretched molecule.

The AIMD simulations reveal formation of several different photoproducts within the earliest timescales of these dynamics. Ring closure (resulting in re-formation of hot thiophenone molecules) is observed, as is the formation of the acyclic isomers 2-thioxoethylketene (P1), 2-(2-sulfanylethyl)ketene (P2) and 2-(2-thiiranyl)ketene (P3) (see Fig. 4b for structures). Interconversion between these isomers was observed in most trajectories within 2 ps (see Supplementary Fig. 12). The histogram labelled 'other' in Fig. 4b includes all molecular geometries that could not be attributed to P1, P2, P3 or closed-ring thiophenone products. These rare other geometries often correspond to transient configurations in the act of interconverting between the dominant photoproducts and are mostly observed within 500 fs of accessing the S_0-state PES. It is important to emphasize that these AIMD calculations (and the gas-phase experiments) involve isolated molecules. The potential energy acquired by thiophenone upon photoexcitation is converted, in part, to nuclear kinetic energy during the non-radiative decay to the S_0 state, but these are closed systems: no energy dissipation is possible and the resulting $S_0^{\#}$ species are highly energetic.

Experimentally, the BEs of the $S_0^{\#}$ species formed via non-radiative de-excitation are concentrated in a narrow (~1 eV, full width at half maximum (FWHM)) band centred at ~9 eV, as shown in Figs. 4a,c. Yet the AIMD simulations indicate that this ensemble of $S_0^{\#}$ species must contain a range of structures with high internal energies. Thus, the 22 AIMD outputs were analysed further. Specifically, the molecular geometry was extracted every 10 fs from each AIMD trajectory, yielding a pool of >4,000 geometries. These were grouped by photoproduct (see Section 2.6 in the Supplementary Information) and, for each geometry, the IP_{vert} value between the S_0 and D_0 states was calculated using MP2-F12/cc-pVDZ-F12 to provide an estimate of the BE. As Fig. 4b shows, the histograms of the IP_{vert} values for

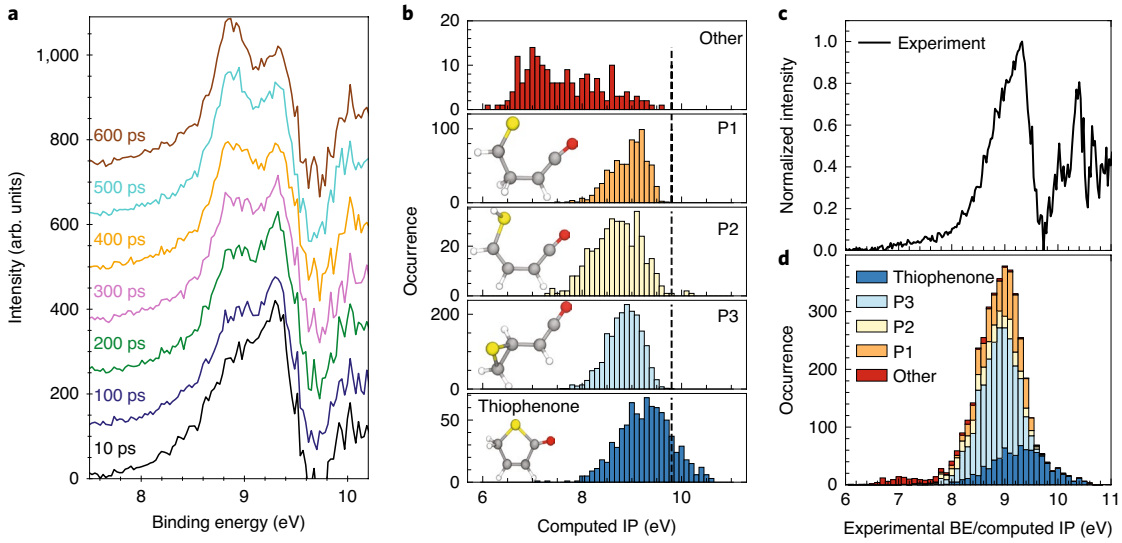

Fig. 4 | Dynamics on the S_0 PES following photoexcitation and non-radiative decay. a, Photoelectron spectra for different pump–probe delays after subtraction of the signal from 'unpumped' thiophenone (S_0) molecules (see Supplementary Fig. 3 for details). The spectra are offset vertically for better visibility. **b**, Histograms showing the number of occurrences of the various $S_0 \rightarrow D_0$ IP_{vert} values computed at the MP2/cc-pVDZ-F12 level of theory every 10 fs (for a total of 2 ps) along each AIMD trajectory on the S_0 PES, grouped by similarity to the molecular geometries identified as P1, P2, P3 and closed-ring thiophenone, along with a further small group labelled 'other' associated with internally hot molecules that were in the act of converting between stable isomeric forms at the time the trajectory was sampled (see text). The calculated IP_{vert} for thiophenone at its optimized ground-state geometry is indicated by a dashed vertical black line. **c**, Experimental (subtracted) photoelectron spectrum summed over the delay range $0.5 \leq \Delta t \leq 2$ ps; the contribution at BE > 9.8 eV is due to ionization of $S_0^{\#}$ molecules to excited cationic states, which are not included in the present calculations (see also Supplementary Figs. 2, 3 and 15). **d**, Sum of the five distributions of IP_{vert} values shown in **b**.

each photoproduct span a narrow range, and the ground-state photoproducts P1, P2 and P3 display similar IP_{vert} distributions. This reflects the fact that, in each case, ionization involves removal of an electron from an orbital with a high degree of *n*(S) character. The distribution associated with re-formed closed-ring thiophenone species is centred at slightly higher IP_{vert} values. For completeness, we note that the predicted distribution of $S_0 \rightarrow D_0$ IP_{vert} values for thiophenone molecules without the extra kinetic energy induced by photoexcitation and subsequent relaxation (derived from AIMD simulations of thiophenone initiated with an internal energy equal to the zero-point energy only) is centred at yet higher IP_{vert}, is much narrower and, as Supplementary Fig. 15 shows, is in very good accord with the lowest energy peak in the measured He I photoelectron spectrum[29].

Returning to the hot $S_0^{\#}$ molecules, the 22 AIMD outputs predict a narrow overall distribution of IP_{vert} values (Fig. 4d) that, as Fig. 4c shows, matches well with the TRPES data summed over the delay range $0.5 \leq \Delta t \leq 2$ ps. The 10 AIMD outputs propagated to $t = 100$ ps (see Supplementary Fig. 17) provide additional insights into the longer-time dynamics of these $S_0^{\#}$ molecules. Analysis of the (admittedly small number of) long-time trajectories reveals (1) irreversible conversion of closed-ring to open-ring isomers and (2), in several cases, unimolecular decay of the $S_0^{\#}$ species to CO + thioacrolein ($CH_2CHC(H)S$) products. The first IP_{vert} of thioacrolein is 8.9 eV (see a study by Bock et al.[32]), a value reproduced computationally in the present work (see Section 2.10 in the Supplementary Information). Thus, recalling Fig. 4b, we note that all closed-ring to open-ring transformations (including the fragmentation process) will cause a net transfer of $S_0^{\#}$ population to species with lower IP_{vert} (that is, lower BE) values—consistent with the experimental observations (Fig. 4a).

Conclusions

A previous transient infrared absorption spectroscopy study of the UV photoexcitation of thiophenone in solution (that is, in an environment where any product vibrational excitation is rapidly dissipated through interaction with the solvent)[18] demonstrated the formation of acyclic photoproduct(s) with ketene structures and the recovery of (vibrationally cold) ground-state thiophenone molecules. These earlier studies lacked the temporal resolution to probe the ring-opening mechanism directly, and the only $S_0^{\#}$ dynamics amenable to investigation were vibrational relaxation dynamics via interaction with the solvent molecules. Such limitations are not an issue in this study, wherein time-resolved XUV photoelectron spectroscopy studies of the isolated (gas-phase) molecules at a seeded FEL, in combination with high-level ab initio theory, have enabled detailed visualization of the electronic and, particularly, the structural dynamics of this complex photoinduced ring-opening reaction. We have revealed the initial motion following photoexcitation, the non-adiabatic coupling to the S_0 PES as an open-ring biradical, and the subsequent isomerizations and eventual decay of the highly vibrationally excited S_0-state species. The match between theory and experiment spans both the excited-state decay rates and the more challenging athermal rearrangements to photoproducts that occur after non-adiabatic coupling to the S_0 state.

The use of sufficiently high-energy probe photons is key to tracking the full decay dynamics, that is, the ultrafast evolution of the photoexcited wavepacket to the S_0 state and the nuclear dynamics of the resulting highly vibrationally excited S_0 molecules. The increase in BE observed immediately post-photoexcitation is a signature of the ultrafast decay of the nuclear wavepacket from the S_2 state, via the S_1 state, towards the electronic ground state, enabled by elongation and eventual scission of the S–CO bond. The evolving molecules couple to the S_0 PES with a range of geometries and nuclear momenta, which govern the subsequent athermal rearrangements of the $S_0^{\#}$ species. These vibrationally excited S_0 molecules are highly fluxional and can adopt at least three identified open-ring structures or re-form the parent thiophenone, and they have sufficient internal energy to dissociate (by loss of a CO moiety). The deduced ground-state dynamics serve to bolster a recent

prediction that isomerization of energized molecules prior to dissociation might well be the rule rather than the exception in many polyatomic unimolecular processes[33]. The IP_{vert} distribution computed from the AIMD trajectories on the S_0 PES reproduces the narrow spread of BEs observed experimentally and can be traced to the localized nature of the sulfur lone pair orbital that is the dominant contributor to the HOMO in each species. Distinguishing the various open-ring products by valence-shell photoelectron spectroscopy is challenging given their very similar first IPs. Ultrafast X-ray or electron diffraction studies might be able to address such structural challenges if sufficient scattering signal can be obtained despite the low sample vapour pressure.

Online content

Any Nature Research reporting summaries, source data, extended data, supplementary information, acknowledgements, peer review information; details of author contributions and competing interests; and statements of data and code availability are available at https://doi.org/10.1038/s41557-020-0507-3.

Received: 10 November 2019; Accepted: 11 June 2020;
Published online: 20 July 2020

References

1. Minitti, M. P. et al. Imaging molecular motion: Femtosecond X-Ray scattering of the ring opening in 1,3-cyclohexadiene. *Phys. Rev. Lett.* **114**, 255501 (2015).
2. Pullen, M. G. et al. Imaging an aligned polyatomic molecule with laser-induced electron diffraction. *Nat. Commun.* **6**, 7262 (2015).
3. Wolter, B. et al. Ultrafast electron diffraction imaging of bond breaking in di-ionized acetylene. *Science* **354**, 308–312 (2016).
4. Attar, A. R. et al. Femtosecond X-ray spectroscopy of an electrocyclic ring-opening reaction. *Science* **356**, 54–59 (2017).
5. Schuurman, M. S. & Stolow, A. Dynamics at conical intersections. *Annu. Rev. Phys. Chem.* **69**, 427–450 (2018).
6. Wolf, T. J. A. et al. The photochemical ring-opening of 1,3-cyclohexadiene imaged by ultrafast electron diffraction. *Nat. Chem.* **11**, 504–509 (2019).
7. Ruddock, J. M. et al. A deep UV trigger for ground-state ring-opening dynamics of 1,3-cyclohexadiene. *Sci. Adv.* **5**, eaax6625 (2019).
8. Stankus, B. et al. Ultrafast X-ray scattering reveals vibrational coherence following Rydberg excitation. *Nat. Chem.* **11**, 716–721 (2019).
9. Browne, W. R. & Feringa, B. L. Light switching of molecules on surfaces. *Annu. Rev. Phys. Chem.* **60**, 407–428 (2009).
10. Kumpulainen, T., Lang, B., Rosspeintner, A. & Vauthey, E. Ultrafast elementary photochemical processes of organic molecules in liquid solution. *Chem. Rev.* **117**, 10826–10939 (2017).
11. Qi, J. et al. Light-driven transformable optical agent with adaptive functions for boosting cancer surgery outcomes. *Nat. Commun.* **9**, 1848 (2018).
12. Deb, S. & Weber, P. M. The ultrafast pathway of photon-induced electrocyclic ring-opening reactions: The case of 1,3-cyclohexadiene. *Annu. Rev. Phys. Chem.* **62**, 19–39 (2011).
13. Arruda, B. C. & Sension, R. J. Ultrafast polyene dynamics: the ring opening of 1,3-cyclohexadiene derivatives. *Phys. Chem. Chem. Phys.* **16**, 4439–4455 (2014).
14. Petrović, V. S. et al. Transient X-ray fragmentation: Probing a prototypical photoinduced ring opening. *Phys. Rev. Lett.* **108**, 253006 (2012).
15. Rudakov, F. & Weber, P. M. Ground state recovery and molecular structure upon ultrafast transition through conical intersections in cyclic dienes. *Chem. Phys. Lett.* **470**, 187–190 (2009).
16. Adachi, S., Sato, M. & Suzuki, T. Direct observation of ground-state product formation in a 1,3-cyclohexadiene ring-opening reaction. *J. Phys. Chem. Lett.* **6**, 343–346 (2015).
17. Breda, S., Reva, I. & Fausto, R. UV-induced unimolecular photochemistry of 2(5H)-furanone and 2(5H)-thiophenone isolated in low temperature inert matrices. *Vib. Spectrosc.* **50**, 57–67 (2009).
18. Murdock, D. et al. Transient UV pump–IR probe investigation of heterocyclic ring-opening dynamics in the solution phase: the role played by nσ* states in the photoinduced reactions of thiophenone and furanone. *Phys. Chem. Chem. Phys.* **16**, 21271–21279 (2014).
19. Allaria, E. et al. Highly coherent and stable pulses from the FERMI seeded free-electron laser in the extreme ultraviolet. *Nat. Photonics* **6**, 699–704 (2012).
20. Stolow, A., Bragg, A. E. & Neumark, D. M. Femtosecond time-resolved photoelectron spectroscopy. *Chem. Rev.* **104**, 1719–1757 (2004).
21. Suzuki, T. Time-resolved photoelectron spectroscopy of non-adiabatic electronic dynamics in gas and liquid phases. *Int. Rev. Phys. Chem* **31**, 265–318 (2012).
22. Iikubo, R., Sekikawa, T., Harabuchi, Y. & Taketsugu, T. Structural dynamics of photochemical reactions probed by time-resolved photoelectron spectroscopy using high harmonic pulses. *Faraday Discuss.* **194**, 147–160 (2016).
23. Nishitani, J., West, C. W., Higashimura, C. & Suzuki, T. Time-resolved photoelectron spectroscopy of polyatomic molecules using 42-nm vacuum ultraviolet laser based on high harmonics generation. *Chem. Phys. Lett.* **684**, 397–401 (2017).
24. Smith, A. D. et al. Mapping the complete reaction path of a complex photochemical reaction. *Phys. Rev. Lett.* **120**, 183003 (2018).
25. von Conta, A. et al. Conical-intersection dynamics and ground-state chemistry probed by extreme-ultraviolet time-resolved photoelectron spectroscopy. *Nat. Commun.* **9**, 3162 (2018).
26. Squibb, R. J. et al. Acetylacetone photodynamics at a seeded free-electron laser. *Nat. Commun.* **9**, 63 (2018).
27. Gorobtsov, O. Y. et al. Seeded X-ray free-electron laser generating radiation with laser statistical properties. *Nat. Commun.* **9**, 4498 (2018).
28. Xie, B.-B. & Fang, W.-H. Combined quantum trajectory mean-field and molecular mechanical (QTMF/MM) nonadiabatic dynamics simulations on the photoinduced ring-opening reaction of 2(5H)-thiophenone. *ChemPhotoChem* **3**, 897–906 (2019).
29. Chin, W. S. et al. He I and He II photoelectron spectra of thiophenones. *J. Electron Spectrosc. Relat. Phenomena* **88-91**, 97–101 (1998).
30. Tao, H. et al. Ultrafast internal conversion in ethylene. I. The excited state lifetime. *J. Chem. Phys.* **134**, 244306 (2011).
31. Mignolet, B., Curchod, B. F. E. & Martínez, T. J. Rich athermal ground-state chemistry triggered by dynamics through a conical intersection. *Angew. Chem. Int. Ed. Engl.* **55**, 14993–14996 (2016).
32. Bock, H., Mohmand, S., Hirabayashi, T. & Semkow, A. Gas-phase reactions. 29. Thioacrolein. *J. Am. Chem. Soc.* **104**, 312–313 (1982).
33. Yang, C.-S., Bhattacharyya, S., Liu, L., Fang, W.-H. & Liu, K. Real-time tracking of the entangled pathways in the multichannel photodissociation of acetaldehyde. *Chem. Sci.* https://doi.org/10.1039/d0sc00063a (2020).

Methods

Experimental. The experiment was performed at the low-density matter (LDM) beamline[34,35] at the FERMI free-electron laser facility[19]. The FEL was operated at a photon energy of 19.24 eV, corresponding to the fourth harmonic of the seed laser, with an estimated pulse duration of 80 fs (FWHM)[36]. The UV pump pulses, with a centre wavelength of 264.75 nm and a 1.2 nm bandwidth, were generated as the third harmonic of a Ti:Sapphire laser. Details relating to gas sample delivery, other laser pulse parameters (energies, durations and spot sizes) and tests to ensure that the reported effects scale linearly with pump and probe pulse parameters are reported in Section 1 of the Supplementary Information. A magnetic bottle type spectrometer[26,37] (see Supplementary Fig. 1) was used to detect photoelectrons with high collection efficiency. A retardation voltage of 8 V was used to increase the resolution in the photoelectron range of interest (the approximate kinetic energy resolution is $\delta E/E \approx 0.03$, with E being the final kinetic energy after retardation), cutting off the photoelectron spectrum at a binding energy of approximately 11 eV, as shown in Supplementary Fig. 2.

Data acquisition and analysis. Time-of-flight traces were recorded shot-by-shot while scanning the delay between the pump and probe pulses. The data shown in Fig. 1a consist of ~1,650 shots per 50 fs delay bin. The single-shot spectra were summed for each delay bin and then normalized with respect to the summed FEL intensity (measured shot-to-shot[38]). The electron time-of-flight was converted into photoelectron kinetic energy by calibrating the spectrometer using photoelectrons from the single-photon single ionization of helium at multiple harmonics (that is, different photon energies) of the FEL. The photoelectron energies were then converted to binding energies by subtracting the photoelectron energy from the FEL photon energy.

Computational details. *Critical points and linear interpolation in internal coordinates.* Critical points of the thiophenone PESs—S_0 minimum, S_1 minima, and S_2/S_1 and S_1/S_0 MECIs—were located using SA(4)-CASSCF(10/8)[39,40] and a 6-31G* basis set[41,42] as implemented in Molpro 2012[43]. Pathways connecting these different critical points of the PESs were produced by LIICs[44]. Some of the advantages and limitations of LIICs are summarized in Section 2.2 in the Supplementary Information. Electronic energies for thiophenone were computed along the LIIC pathways at the SA(4)-CASSCF(10/8) and XMS(4)-CASPT2(10/8)[45,46] levels of theory using, in all cases, a 6-31G* basis set (see Supplementary Figs. 7 and 8). The electronic energies for the thiophenone cation were also computed along the LIICs using SA(4)-CASSCF(9/8) and XMS(4)-CASPT2(9/8). All XMS-CASPT2 calculations were performed with the BAGEL software[47], employing the corresponding SA-CASSCF wavefunction from Molpro 2012 as a starting point. A level shift[48] of 0.3 E_h was used in all XMS-CASPT2 calculations to prevent the appearance of intruder states. For details on the calculations of IPs, including benchmarking studies justifying this choice of basis set, see Section 2 in the Supplementary Information.

TSH dynamics. The excited-state dynamics of thiophenone following photoexcitation were simulated using the mixed quantum/classical dynamics TSH method, employing the fewest-switches algorithm[49]. All details regarding these dynamics are provided in Section 2 of the Supplementary Information.

Ab initio molecular dynamics to $t = 2$ ps and $t = 100$ ps. AIMD calculations of the photoproducts formed during the TSH dynamics were conducted on the S_0-state PES using unrestricted DFT with the PBE0 exchange/correlation functional[50] and a 6-31G* basis set, employing the GPU-accelerated software TeraChem[51]. The initial conditions (nuclear coordinates and velocities) for each AIMD trajectory (22 in total, drawn randomly from the pool of TSH trajectories) were extracted from the TSH dynamics when the trajectory reached the S_0 state. At this initial point in configuration space, the SA-CASSCF wavefunction already exhibits a dominant closed-shell character (confirmed at the XMS-CASPT2 level of theory; see Section 2.5 in the Supplementary Information for additional details). A small (0.1 fs) time step was used to ensure proper total energy conservation for all trajectories, and the length of each (constant total energy) trajectory was set such that the total TSH + AIMD dynamics extend to 2 ps. This strategy necessarily restricts the dynamics to the S_0 PES; the legitimacy of this procedure was validated by test trajectories on S_0, which show the energy separation between the ground and excited electronic states increasing rapidly upon leaving the region of the S_1/S_0 seam of intersection. To explore the long-time dynamics of the different photoproducts, 10 of the 22 trajectories were propagated further, to $t = 100$ ps, using the same methodology except for a slightly longer time step of 0.25 fs.

Analysis of the 2 ps AIMD and vertical ionization energy distribution. The 22 AIMD trajectories propagated until $t = 2$ ps were used to analyse the distribution of IP_{vert} values for the $S_0^{\#}$ photoproducts. For each AIMD trajectory, molecular geometries were sampled every 10 fs, leading to a pool of >4,000 S_0 molecular configurations. Each configuration was assigned to one of the possible photoproducts identified by Murdock et al.[18] based on characteristic atomic connectivities determined by measuring bond lengths or angles (see Supplementary Fig. 13). If such assignment was not possible, the configuration was given the label 'others'. These were often due to a transient configuration between two photoproducts. The IP_{vert} of each configuration was then computed at the MP2-F12/cc-pVDZ-F12 level of theory (this level of theory was benchmarked against CCSD(T)-F12/cc-pVDZ-F12; see Section 2.8 in the Supplementary Information). The resulting distribution of $S_0 \rightarrow D_0$ IP_{vert} values provides an approximation of the low-energy part of the experimental BE spectra. The same methodology, applied to ground-state dynamics of cold thiophenone, successfully reproduces the first peak in the experimental He I photoelectron spectrum (see Supplementary Fig. 15). All calculations were performed with Molpro 2012.

Data availability

Data generated or analysed during this study are included in this Article (and its Supplementary Information). Source data are provided with this paper.

Code availability

The analysis codes used to generate the data presented in this study are available from the corresponding authors upon reasonable request. Source data are provided with this paper.

References

34. Svetina, C. et al. The low density matter (LDM) beamline at FERMI: optical layout and first commissioning. *J. Synchrotron Radiat.* **22**, 538–543 (2015).
35. Lyamayev, V. et al. A modular end-station for atomic, molecular, and cluster science at the low density matter beamline of FERMI@Elettra. *J. Phys. B* **46**, 164007 (2013).
36. Finetti, P. et al. Pulse duration of seeded free-electron lasers. *Phys. Rev. X* **7**, 021043 (2017).
37. Eland, J. H. D. et al. Complete two-electron spectra in double photoionization: the rare gases Ar, Kr, and Xe. *Phys. Rev. Lett.* **90**, 053003 (2003).
38. Zangrando, M. et al. Recent results of PADReS, the photon analysis delivery and reduction system, from the FERMI FEL commissioning and user operations. *J. Synchrotron Radiat.* **22**, 565–570 (2015).
39. Werner, H.-J. in *Advances in Chemical Physics: Ab Initio Methods in Quantum Chemistry Part 2* Vol. 69 (ed. Lawley, K. P.) Ch. 1 (Wiley, 1987).
40. Roos, B. O. in *Advances in Chemical Physics: Ab Initio Methods in Quantum Chemistry Part 2* Vol. 69 (ed. Lawley, K. P.) Ch. 7 (Wiley, 1987).
41. Hehre, W. J., Ditchfield, R. & Pople, J. A. Self-consistent molecular orbital methods. XII. Further extensions of Gaussian-type basis sets for use in molecular-orbital studies of organic-molecules. *J. Chem. Phys.* **56**, 2257–2261 (1972).
42. Hariharan, P. C. & Pople, J. A. Influence of polarization functions on molecular-orbital hydrogenation energies. *Theor. Chem. Acc.* **28**, 213–222 (1973).
43. Werner, H.-J. et al. MOLPRO, v.2012.1 (Molpro, 2012); https://www.molpro.net
44. Hudock, H. R. et al. Ab initio molecular dynamics and time-resolved photoelectron spectroscopy of electronically excited uracil and thymine. *J. Phys. Chem. A* **111**, 8500–8508 (2007).
45. Shiozaki, T., Győrffyet, W., Celani, C. & Werner, H.-J. Communication: Extended multi-state complete active space second-order perturbation theory: Energy and nuclear gradients. *J. Chem. Phys.* **135**, 081106 (2011).
46. Granovsky, A. Extended multi-configuration quasi-degenerate perturbation theory: The new approach to multi-state multi-reference perturbation theory. *J. Chem. Phys.* **134**, 214113 (2011).
47. BAGEL Brilliantly Advanced General Electronic-Structure Library v.1.2.2 (Shiozaki Group, 2018); http://www.nubakery.org
48. Ghigo, G., Roos, B. O. & Malmqvist, P. A. A modified definition of the zeroth-order Hamiltonian in multiconfigurational perturbation theory (CASPT2). *Chem. Phys. Lett.* **396**, 142–149 (2004).
49. Tully, J. C. Molecular dynamics with electronic transitions. *J. Chem. Phys.* **93**, 1061–1071 (1990).
50. Adamo, C. & Barone, V. Toward reliable density functional methods without adjustable parameters: The PBE0 model. *J. Chem. Phys.* **110**, 6158–6169 (1999).
51. Ufimtsev, I. S. & Martínez, T. J. Quantum chemistry on graphical processing units. 3. analytical energy gradients, geometry optimization, and first principles molecular dynamics. *J. Chem. Theory Comput.* **5**, 2619–2628 (2009).

Acknowledgements

S.P., J.T. and D.R. were supported by the National Science Foundation (NSF) grant PHYS-1753324. S.P. was also partially supported by the Chemical Sciences, Geosciences, and Biosciences Division, Office of Basic Energy Sciences, Office of Science, US Department of Energy (DOE) under grant no. DE-FG02-86ER13491. Travel to FERMI for S.P., D.M.P.H., R.M., J.T. and D.R. was supported by LaserLab Europe. This work made use of the facilities of the Hamilton HPC Service of Durham University. M.N.R.A., C.S.H. and R.A.I. acknowledge the Engineering and Physical Sciences Research Council (EPSRC) for funding (EP/L005913/1), while L.M.I. acknowledges the EPSRC for a doctoral

studentship (EP/R513039/1). C.S.H. also acknowledges funding from the Australian Research Council (ARC, DE200100549). M.N.R.A. thanks W.-H. Fang (Beijing Normal University) for permission to share data[28] prior to its publication. B.F.E.C. acknowledges funding from the European Union Horizon 2020 research and innovation programme under grant agreement no. 803718 (SINDAM). D.M.P.H. was supported by the Science and Technology Facilities Council, UK. R.F. and R.J.S. acknowledge financial support from the Swedish Research Council, the Knut and Alice Wallenberg Foundation, Sweden, and the Faculty of Natural Science of the University of Gothenburg. We thank the technical and scientific teams at FERMI for their hospitality and their support during the beamtime. We also acknowledge helpful discussions with A. Rudenko during the preparation of the beamtime proposal and during the data interpretation and with S. Bhattacharyya during the data analysis and interpretation.

Author contributions

R.B., R.A.I., C.S.H., M.N.R.A. and D.R. conceived the experiment, the plans for which benefitted from further input from R. Forbes, D.M.P.H. and A.R. The experiment was conducted by S.P., R.A.I., R.B., C.C., A.D., B.E., R. Feifel, M.D.F., L.G., C.S.H., D.M.P.H., R.M., O.P., K.C.P., A.R., R.J.S., J.T., M.N.R.A. and D.R. at the FERMI free-electron laser facility. R. Feifel and R.J.S. provided and operated the magnetic bottle spectrometer. C.C., M.D.F. and O.P. prepared and operated the beamline and the low-density matter (LDM) instrument. A.D. and L.G. prepared and operated the optical laser and the free-electron laser, respectively. L.M.I. and B.F.E.C. performed the ab initio simulations, with contributions from R.A.I. Experimental data were analysed by S.P. and J.T. with contributions from C.C., R. Forbes, C.S.H., R.A.I., R.M. and A.R. Finally, S.P., L.M.I., R.B., R. Forbes, M.N.R.A., B.F.E.C. and D.R. interpreted the results and wrote the manuscript with input from all the authors.

Competing interests

The authors declare no competing interests.

Additional information

Supplementary information is available for this paper at https://doi.org/10.1038/s41557-020-0507-3.

Correspondence and requests for materials should be addressed to M.N.R.A., B.F.E.C. or D.R.

Reprints and permissions information is available at www.nature.com/reprints.

3.4 Ionization into D_2 cationic states via XUV

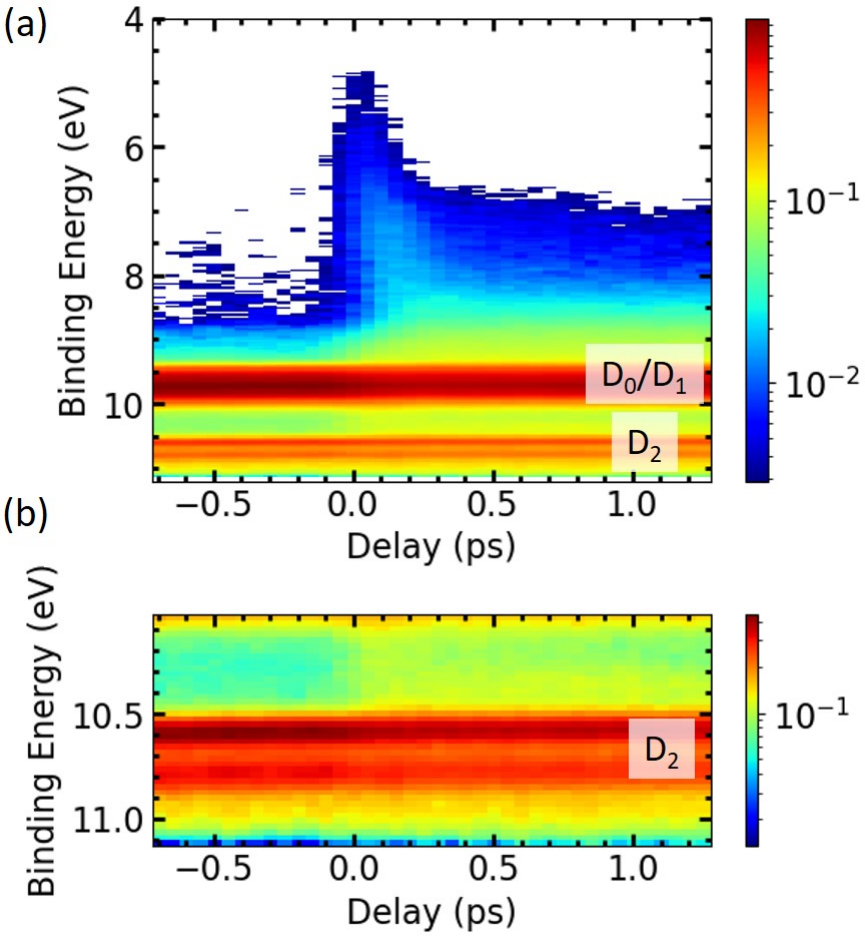

Figure 3.9: *Delay-dependent photoelectron intensity spectrum of thiophenone. (a) Full spectrum. (b) Zoomed-in higher binding energy region from panel (a) showing the signal from ionization of ground-state thiophenone molecules into the D_2 cationic state and the increase in photoelectron intensity in the binding energy range, 10.2 eV<BE<10.5 eV, for positive delays (UV preceding FEL).*

In the previous section, the main focus was on the ionization to the D_0/D_1 cationic states. Figure 3.9(a) shows the delay-dependent photoelectron spectrum of thiophenone, similar to the one described in section 3.3, but also including the photoelectron spectrum at binding energies higher than 10.2 eV. Negative delay values correspond to the FEL preceding the UV, and positive delay values correspond to the UV preceding the FEL. The photoelectron

intensity signal from ground-state thiophenone molecules ionized to different cationic states is labeled by D_0/D_1 and D_2 (also shown in Fig. 3.6).

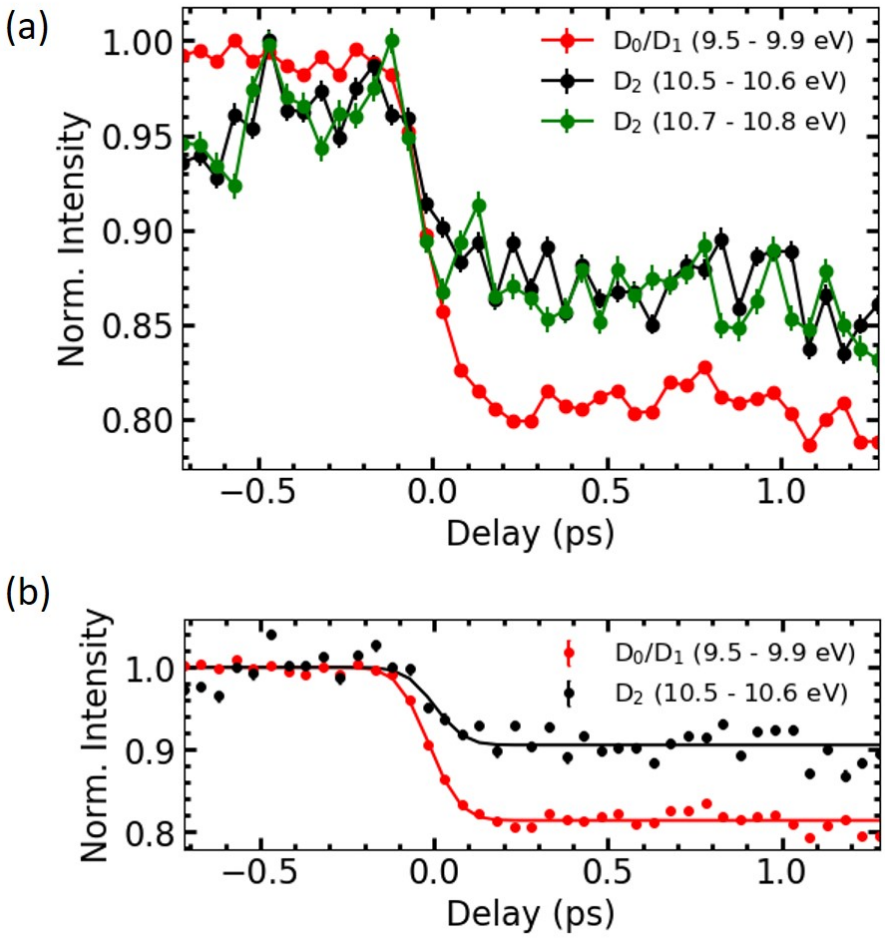

Figure 3.10: *Delay-dependent intensity change for different BE ranges. (a) Comparison of depletion in the intensity of photoelectron signal from unpumped molecules, ionized to other cationic states. (b) The depletion intensity fitted with a cumulative distribution function for two binding energy ranges (see table 3.1 for fit parameters).*

The theoretical calculations detailed in section 3.3 do not attempt modeling $S_0 \rightarrow D_2$ ionization. In this section, we discuss the experimental results corresponding to the transitions to these cationic states. Figure 3.9(b) shows a zoomed-in photoelectron intensity spectrum where the depletion in the delay-dependent photoelectron intensity is observed for the ground-state thiophenone molecules ionized to D_2 cationic state. An increase in the

Cationic State	Energy Range (eV)	x_0 (fs)	σ (fs)
D_0/D_1	9.5 - 9.9	-15 ± 5	72 ± 8
D_2 ($\nu = 0$)	10.5 - 10.6	2 ± 24	68 ± 33
D_2 ($\nu = 1$)	10.7 - 10.8	-29 ± 21	50 ± 16

Table 3.1: *The center values and standard deviation for the fitted cumulative distribution function to the depletion of delay-dependent photoelectron intensity of the ground-state thiophenone molecules.*

phototoelectron intensity can be seen in the binding energy range 10.2 eV<BE<10.5 eV. Figure 3.10(a) shows the comparison of depletion in photoelectron intensity for unpumped thiophenone molecules ionized into D_0/D_1, D_2 ($\nu = 0$) and higher vibrational level of D_2 ($\nu = 1$). Figure 3.10(b) shows the fit results after fitting the depletion with a cumulative distribution function (CDF), which is represented by

$$y(x) = \frac{h}{2}\left[1 + erf(\frac{x - x_0}{\sqrt{2\sigma^2}})\right] + y_0 \tag{3.3}$$

where σ is the standard deviation and x_0 is the center value of the distribution.

The results from the fit are summarized in table 3.1. As can be seen from the fitting results, there are no significant differences, both in the center values and the width of the distribution. The larger errors in the signal from the D_2 state are due to the low signal-to-noise ratio. We can also compare the timescales of photoelectron intensity change for the binding energy range of 10.2 eV<BE<10.5 eV and the photoproducts discussed in section 3.3. Figure 3.11 shows the delay-dependent photoelectron intensity increase, fitted with a convolution of a Gaussian and an exponential function. The Gaussian function represents the temporal resolution of the experiment, and the time constant (τ) gives an estimate of the rise-time of the photoelectron intensity. The fit function used for the fitting shown in Fig. 3.11 is discussed in the supporting information [69] of the article discussed in section 3.3. From the fitting results shown in table 3.2, we see the center values (x_0) differ slightly. The smaller x_0 value for D_2 could be due to overlapping features in the selected binding energy range. The time constants (τ), on the other hand, matches within the error limits for

Cationic State	Energy Range (eV)	x_0 (fs)	σ (fs)	τ (fs)
D_0/D_1	8.3 - 9.1	-2 ± 7	75 (fixed)	72 ± 9
D_2 ($\nu = 0$)	10.3 - 10.4	-99 ± 30	75 (fixed)	61 ± 33

Table 3.2: *The center values and time constant for the fitted delay-dependent intensity change for photoproducts ionized into D_0/D_1 and D_2 cationic states. The fit function used is a convolution of a Gaussian and an exponential.*

the photoelectron signals for D_0/D_1 and D_2 cationic states. The photoelectron intensity increase in the binding energy range 8.3 eV<BE<9.1 eV was assigned to the formation of photoproducts (ionized to D_0/D_1) based on theoretical calculations (see section 3.3). As the time constants in table 3.2 match well, we conclude that the photoelectron intensity increase in the binding energy range 10.3 eV<BE<10.4 eV can most likely be assigned to the photoproduct formation and subsequent ionization to D_2 cationic state.

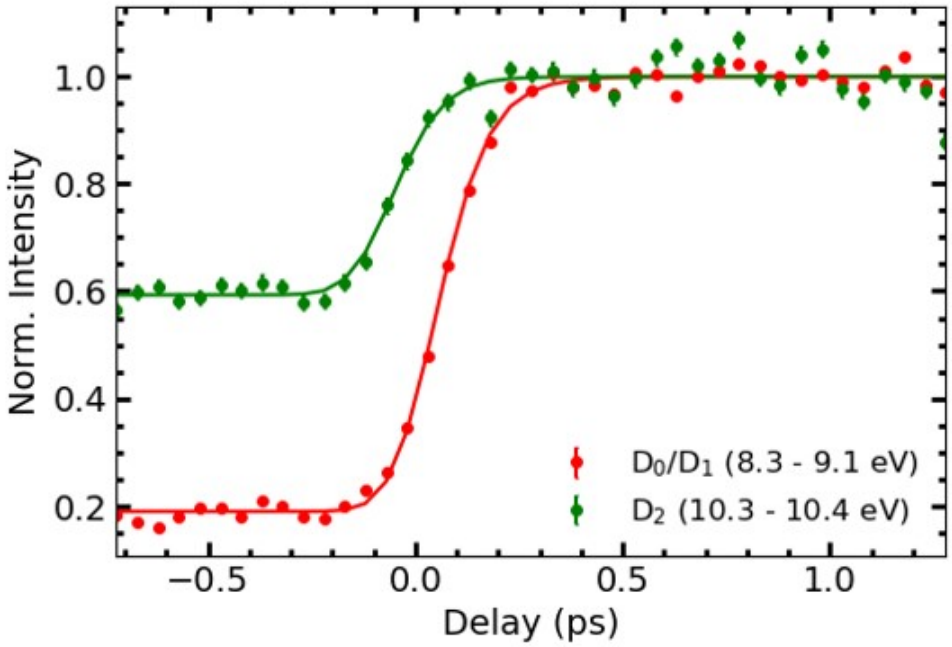

Figure 3.11: *Fitted delay-dependent intensity change for photoproducts ionized into D_0/D_1 and D_2 cationic states.*

To interpret the ionization of photoproducts, theoretical insights related to cross-sections and transition probabilities are essential. A theoretical study in collaboration with Prof.

Fernando Martin's group at Universidad Autónoma de Madrid in Spain is underway, and some of the preliminary results from this work are discussed below. These calculations are performed by Jorge D. Guerrero.

To understand the ionization of molecules after the absorption of an XUV photon, the cross-sections of different molecular orbitals are calculated. The transition probabilities for different orbitals are also calculated using the cross-sections of the molecular orbitals. These calculations were performed using static-exchange DFT formalism [72] that works within the fixed-nuclei approximation. The key idea of this method is to use Kohn-Sham orbitals to describe the ground state. These are calculated using Amsterdam density functional package [73]. In the next step, the bound and continuum states are calculated considering B-Spline basis functions [74]. Finally, the couplings between bound and continuum states are calculated. For determining the transition probabilities, the calculations consider an XUV pulse centered at 64.4 nm (19.25 eV), with a temporal pulse duration of ∼80 fs. For calculating photoelectron spectra, a Gaussian convolution is performed assuming a 2 eV FWHM pulse. Figure 3.12 shows the calculated cross-section for different valence orbitals in thiophenone. The inner orbitals correspond to a lower number (for example, 11a corresponds to the innermost valence orbital and 26a corresponds to the outermost orbital). It can be seen from this figure that multiple orbitals are accessible by an XUV pulse with 19.25 eV photon energy.

Figure 3.13 shows the convoluted transition probabilities for the ground-state thiophenone molecules and for different ring-opened photoproducts. It can be observed that a few of the photoproducts have higher photoelectron energy (lower binding energies) compared to thiophenone molecules, considering ionization from the outermost orbitals. This agrees well with the results shown in Sec. 3.3, where the photoelectron intensities at a slightly lower binding energy w.r.t. the ground-state thiophenone molecule binding energy, were attributed to the photoproducts. This work is currently ongoing and may provide insights related to the dominant fragmentation pathways for the photoproducts.

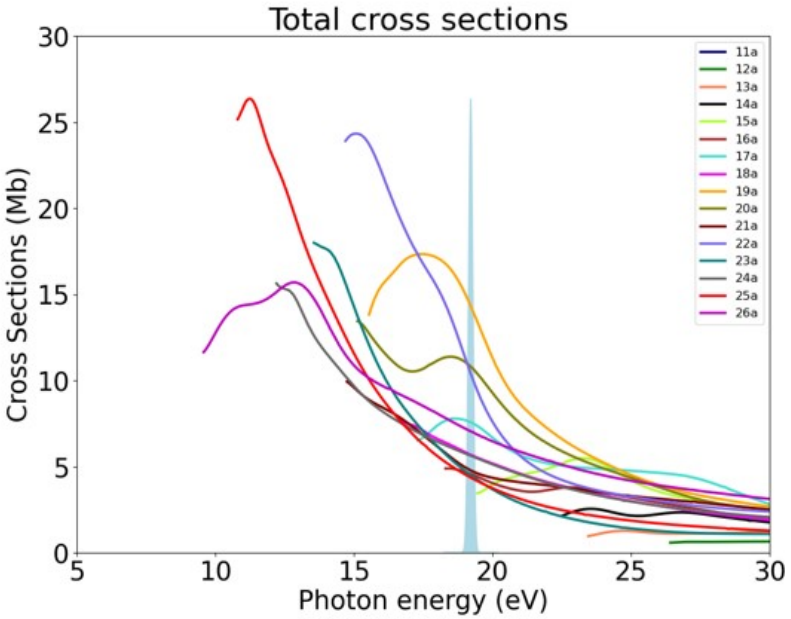

Figure 3.12: *Calculated photoionization cross-sections of different valence orbitals in thiophenone. An XUV pulse centered around 19.25 eV is also shown, which is similar to the one used in the experiment.*

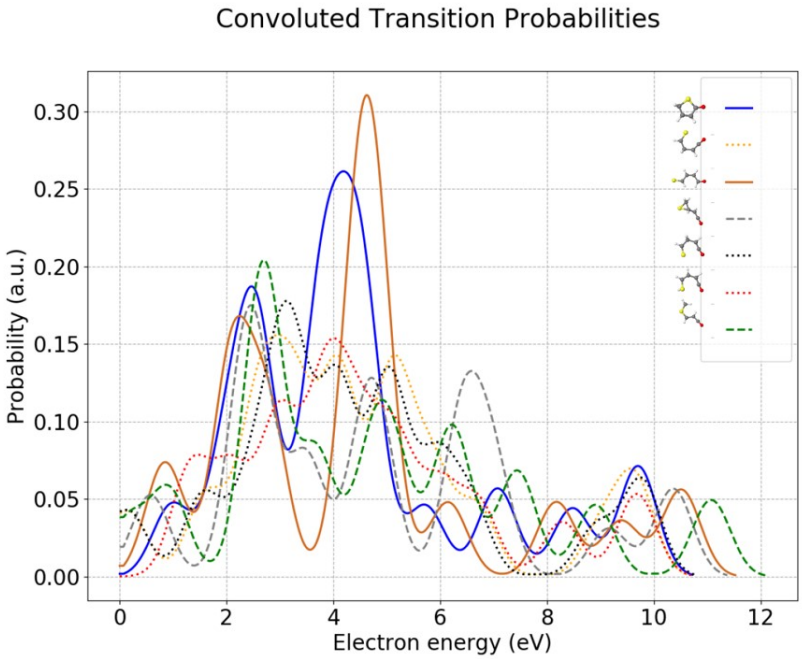

Figure 3.13: *Convoluted transition probabilities for the ground-state thiophenone molecules and the photoproducts after ionization with an XUV pulse of 19.25 eV photon energy.*

3.5 Time-dependent mass spectroscopy post UV absorption in thiophenone

In this section, the delay-dependent photoion yield post photoionization of thiophenone is discussed for several major ionic channels. Figure 3.14 shows the delay-integrated ion time-of-flight (TOF) spectrum. After ionization with XUV, the molecule breaks up into various fragments, which are labeled in the calibrated TOF spectrum.

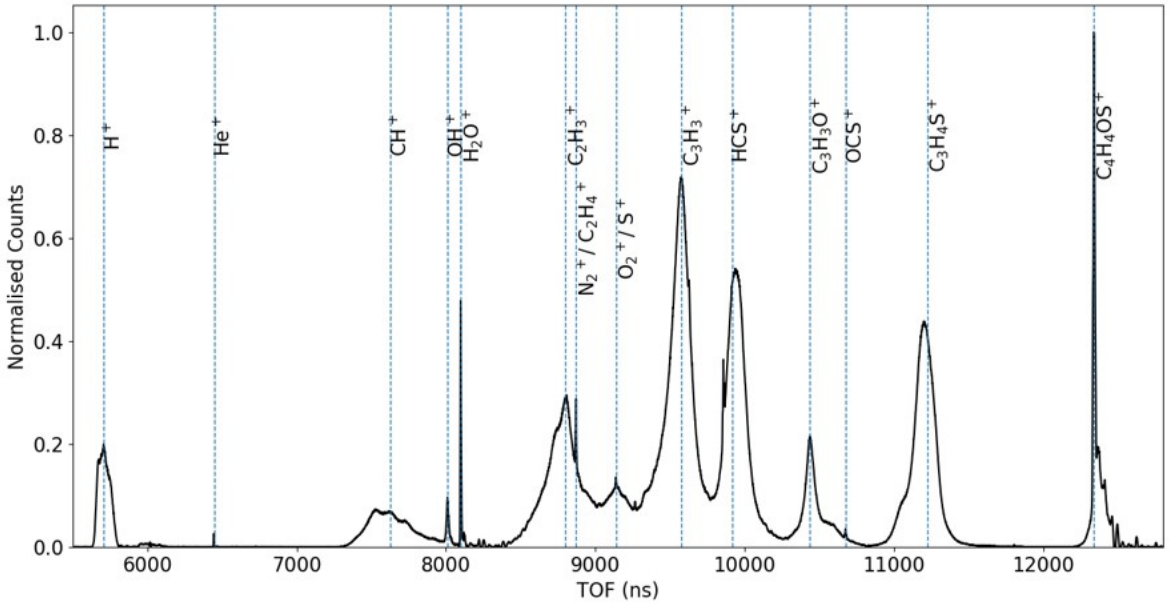

Figure 3.14: *Delay integrated ion time-of-flight (TOF) spectrum of thiophenone.*

The evolution of the intensity of each ionic fragment can be plotted as a function of pump-probe delay. Figure 3.15 shows the delay-dependent yield of the parent ion ($C_4H_4OS^+$). Similar to the observations made in the photoelectrons, a depletion can be seen when UV precedes FEL (XUV). The standard deviation is slightly longer ($\sigma = 107 \pm 11$ fs) compared to photoelectrons (∼70 fs) suggesting that the photoelectron signal is a more direct probe of the excitation process. The parent ion yield is most likely similar for molecular geometries close to the Franck-Condon (FC) region, independent of the electronic state of the molecule, and the decrease in its yield reflects a departure from the FC geometry rather than the

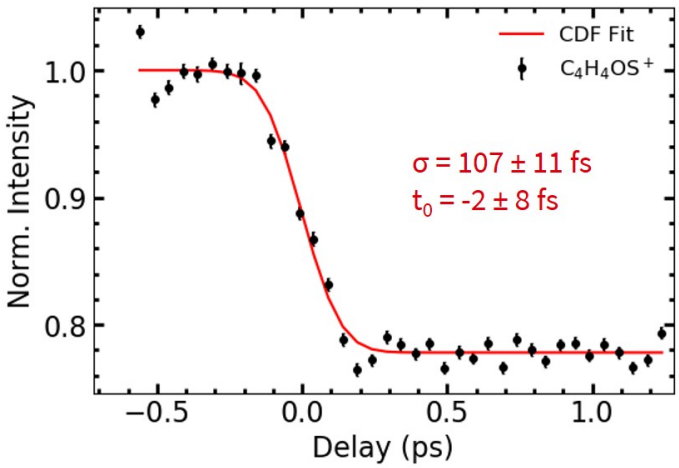

Figure 3.15: *Delay-dependent change in photoion intensity for singly ionized thiophenone molecules ($C_4H_4OS^+$). The depletion in intensity is fitted with a cumulative distribution function.*

electronic excitation. The depletion of the intensity for photoions and photoelectrons (from ionization to D_0) is about 20 % in each case.

The delay-dependent intensities can be plotted for different fragments shown in the TOF spectrum (Fig. 3.14). Figure 3.16 shows the delay-dependent intensities for some of the major fragments, which exhibit a change in intensity as a function of UV-FEL delay. Note that the fragments for which the intensities did not change w.r.t. delay are not included in Fig. 3.16. Most of the fragments (except H^+ and CH_x^+) show an increased intensity when UV precedes FEL, suggesting that they are more likely to be formed after ionization of vibrationally hot and/or ring-open molecules. It may be possible to gain some insights by comparing the geometry of the thiophenone molecule to the photoproducts P1, P2 and P3 (see Section 3.3). The fragments CO^+, S^+, $C_3H_xS^+$ and $C_3H_xO^+$ can be formed by just breaking a single bond in the photoproducts while the formation of these fragments from thiophenone requires breaking of at least two bonds. The increase in the intensity of these fragments might indicate the photoproduct formation post UV excitation. In contrast, no such differences can be seen for the formation of H^+ and $C_2H_3^+$ from photoproducts and thiophenone molecules. We also do not see a prominent increase in the intensity of these

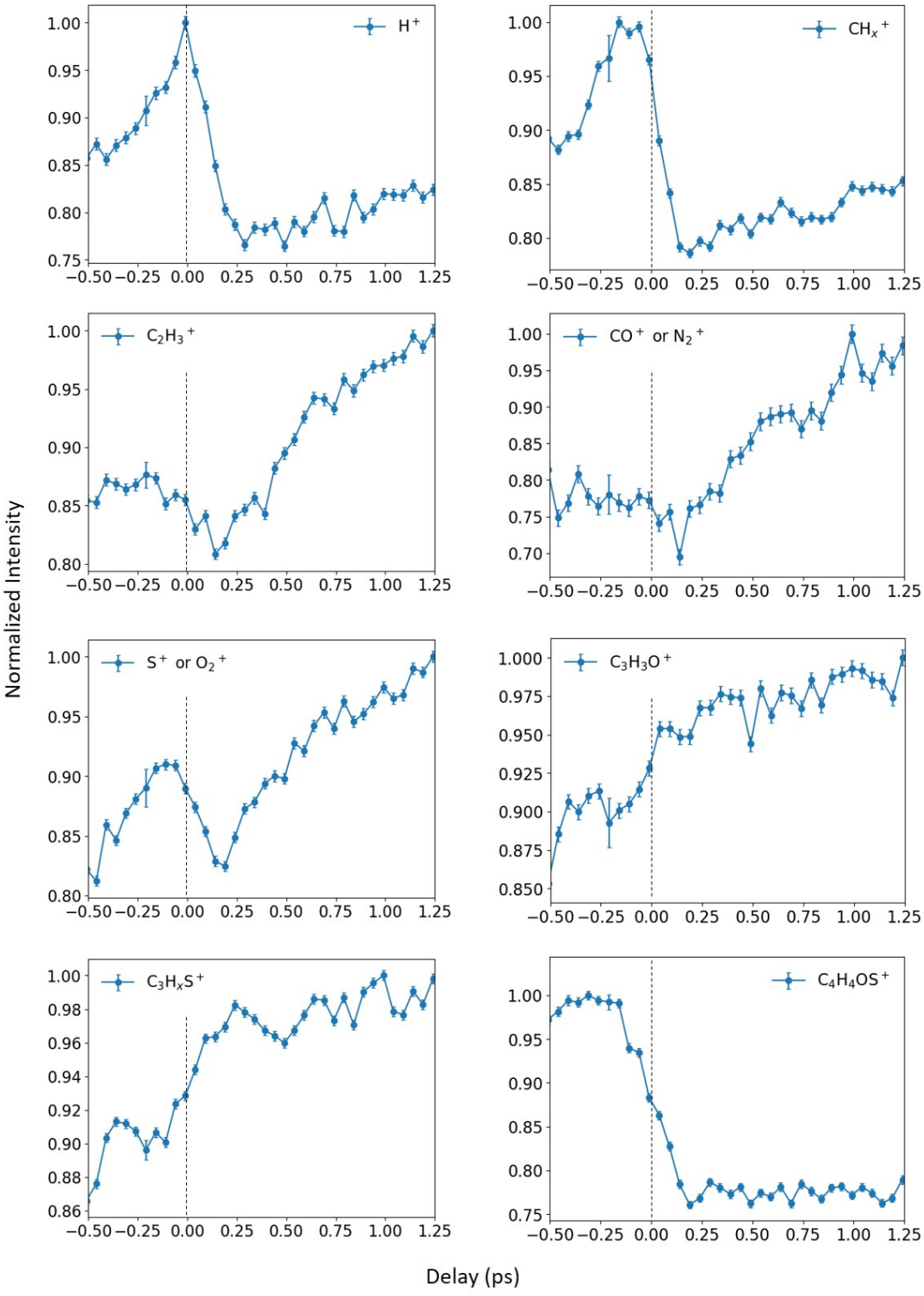

Figure 3.16: *Delay-dependent yield of different ionic fragments post ionization with FEL pulses. Except for H^+, CH_x^+, and $C_4H_4OS^+$, all other fragments show an increase in yield when the UV precedes the FEL. The black dashed lines show the zero delay between UV and FEL.*

fragments in the experiment when UV precedes FEL. To interpret the ionic intensities in greater detail, theoretical modeling of the ionization from the FEL (XUV) and the subsequent fragmentation is essential. This is the final goal of the collaborative theoretical work (described in section 3.4), which would help understand the time-dependent mass spectra obtained in the experiment.

3.5.1 Dynamics at longer time-scales (up to 600 ps)

In section 3.3, we saw that after photoexcitation of thiophenone in the gas-phase, the isomerization and relaxation continued to happen over a few hundred picoseconds. Such longer timescales, particularly in gas-phase experiments, are a result of the unavailability of a medium (or "bath"), where the highly vibrationally excited molecules returning to the ground-state can transfer vibrational energy. In liquid-phase studies, the solvent can absorb this extra energy and assists in cooling down the vibrationally hot ground-state molecules. As a result, the gas-phase and condensed-phase experiments often show different product distributions [65]. In this section, we will discuss the isomerization and dissociation dynamics that happen at these longer timescales, based on photoion intensity changes.

Figure 3.17 shows the delay-dependent intensity change of the same ions as shown in Fig. 3.16, but now on a much longer delay scale up to 600 ps. All the selected fragments show an increase in intensity for positive delays (UV precedes FEL). The maximum increase in intensity is seen for the CO^+ fragment ($\sim$25%). This is also supported by the theoretical modeling, which was performed by the group of Prof. Basile Curchod, Durham University, U.K. Many of the results are summarized in section 3.3 but Fig. 3.18 shows the ab-initio molecular dynamics (AIMD) trajectory calculation performed by propagating trajectories up to 100 ps in the ground state [69]. One of the main observations from these calculations is that in some of the trajectories, the 'hot' thiophenone molecule and the photoproduct P1 dissociate into thioacrolein and CO. This observation also matches the photoelectron signal change at longer timescales as discussed in section 3.3 and the supporting information [69].

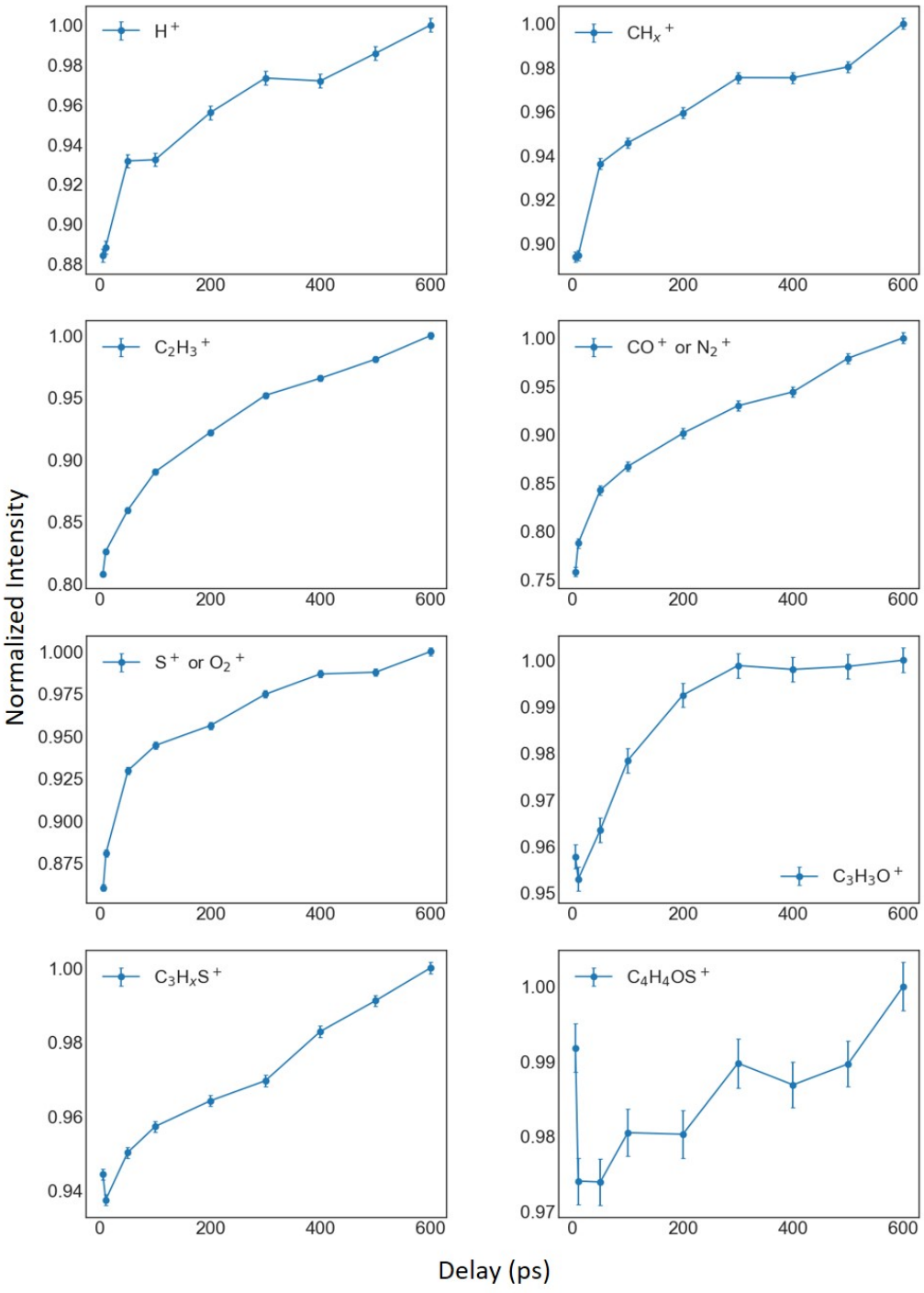

Figure 3.17: *Delay-dependent change in photoion intensity for different fragments post ionization with XUV pulses for longer delays up to 600 ps. The most significant change in intensity is seen for the CO^+ fragment.*

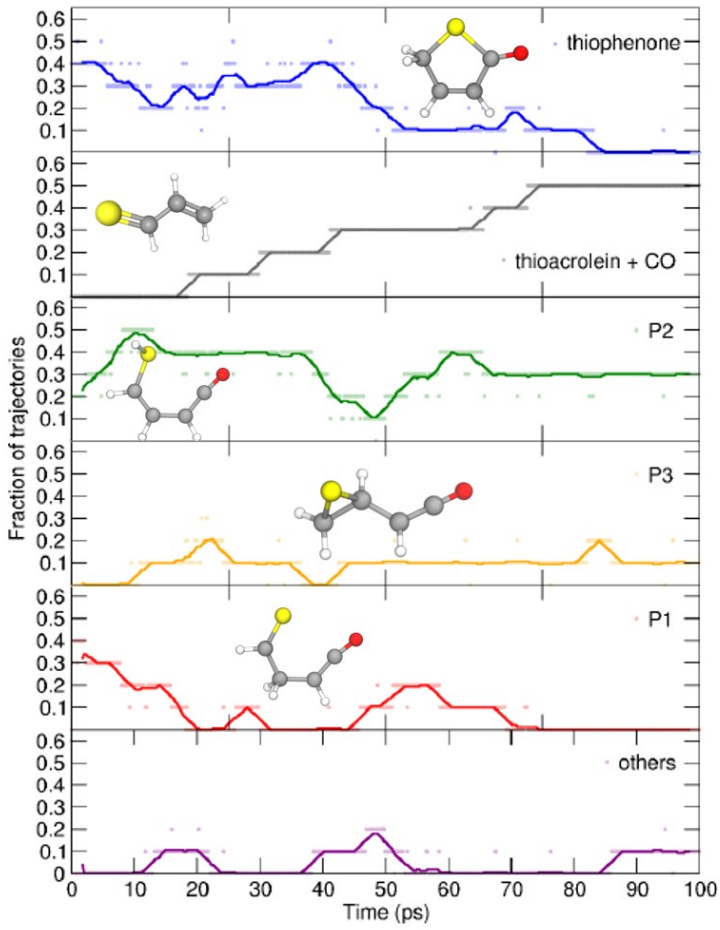

Figure 3.18: *Change in photoproduct distribution based on ab-initio molecular dynamics (AIMD) trajectory simulations performed up to 100 ps. Dots correspond to the actual proportion obtained every 0.25 ps while solid lines represent the moving average (Adapted from [69]).*

This can also explain why CO^+ shows the highest increase in yield among all fragments, as the neutral CO molecules which are formed after dissociation are ionized by XUV and contribute to an increase in intensity.

3.6 Mega-electronvolt ultrafast electron diffraction of thiophenone

Diffraction methods using x-rays or electrons possess a unique capability to determine molecular structure with high (sub-angstrom) spatial resolution. In x-ray diffraction, the high-energy x-ray photons are diffracted by the electrons in the molecule due to *Thompson scattering*, and thus the electronic density determines the diffraction intensity. Since most of the electrons are localized close to the atoms (especially heavier atoms) in a molecule, the electron densities (and hence x-ray diffraction intensities) also reflect the positions of the nuclei. Unlike x-ray photons, electrons are scattered by the electron distribution as well as the atomic nuclei due to *Coulomb scattering* [75]. The electron scattering cross-section is about six orders of magnitude higher than the x-ray scattering cross-section in molecules [76]. However, electron scattering suffers from the low number of electrons that can be packed in an electron pulse due to the broadening of the pulse caused by Coulomb repulsion.

Compared to x-ray photons, electrons are less damaging to the target specimen. Hence, electrons are often used in microscopy applications [77, 78]. Due to strong interaction with matter, electrons have a short penetration depth, which is useful for surface characterization, thin samples, and gases [75].

The gas-phase electron diffraction technique was first introduced in 1930 by Mark and Wierl [79, 80]. This was followed by further developments by Brockway and Pauling [81, 82]. In the late 1990s, the first experiments were performed to determine the structures of molecules with femtosecond temporal resolution using ultrafast electron diffraction [83]. Several studies [84–88] on gas-phase ultrafast electron diffraction have described electron scattering with different levels of detail. Below we describe the equations used to analyze the scattering patterns and to extract the internuclear distances from the experimental results of the ultrafast electron diffraction experiments.

The electron scattering intensity is typically represented in terms of momentum transfer (s) between the incident electron and the elastically scattered electron. Momentum transfer is written as

$$s = \frac{4\pi}{\lambda} \sin\left(\frac{\theta}{2}\right) \tag{3.4}$$

where λ is the *de Broglie* wavelength of the electrons and θ is the scattering angle. The total scattering intensity in an electron diffraction experiment is a sum of atomic (I_A) and molecular scattering (I_M):

$$I(s) = I_A(s) + I_M(s) \tag{3.5}$$

The atomic-scattering term can be written as [75]

$$I_A(s) = C \sum_{i=1}^{N} \left(|f_i(s)|^2 + 4\frac{S_i(s)}{a_0^2 s^4} \right) \tag{3.6}$$

where f_i and S_i are the elastic and inelastic scattering amplitudes for atom i, respectively, N is the number of atoms in the molecule, a_0 is the Bohr radius and C is a proportionality constant. The molecular-scattering intensity is a superposition of intensities from all the atom pairs in a molecule and is useful for structure determination. It can be written as [75]

$$I_M(s) = C \sum_{i=1}^{N} \sum_{j \neq i}^{N} |f_i(s)||f_j(s)| exp\left(-\frac{l_{ij}^2 s^2}{2}\right) cos(\eta_i - \eta_j) \frac{sin(sr_{ij})}{sr_{ij}} \tag{3.7}$$

where f_i and η_i are the elastic-scattering amplitude and corresponding phase for the i^{th} atom, r_{ij} is the distance between the i^{th} and j^{th} atom, l_{ij} is the vibrational amplitude and C is the proportionality constant. The elastic scattering amplitude (f) scales as Z/s^2, where Z is the atomic number. The values of f and η can be obtained from the literature [89]. From the equation above, it can be seen that the $I_M(s)$ decays as $1/s^5$. To highlight the oscillatory behaviour of $I_M(s)$, a modified molecular-scattering intensity (sM(s)) is used,

which is defined as,

$$sM(s) = s\frac{I_M(s)}{I_A(s)} \tag{3.8}$$

To understand the molecular structure in an intuitive manner, the modified molecular-scattering intensities (sMs) are transformed into the pair distribution function (PDF). This is achieved by taking the Fourier (sine) transform of sM(s),

$$PDF(r) = \int_0^{s_{max}} sM(s)\, sin(sr)\, e^{-ks^2}\, ds \tag{3.9}$$

where k is a damping constant to reduce the oscillations caused by the cutoff of signal at $s{=}s_{max}$.

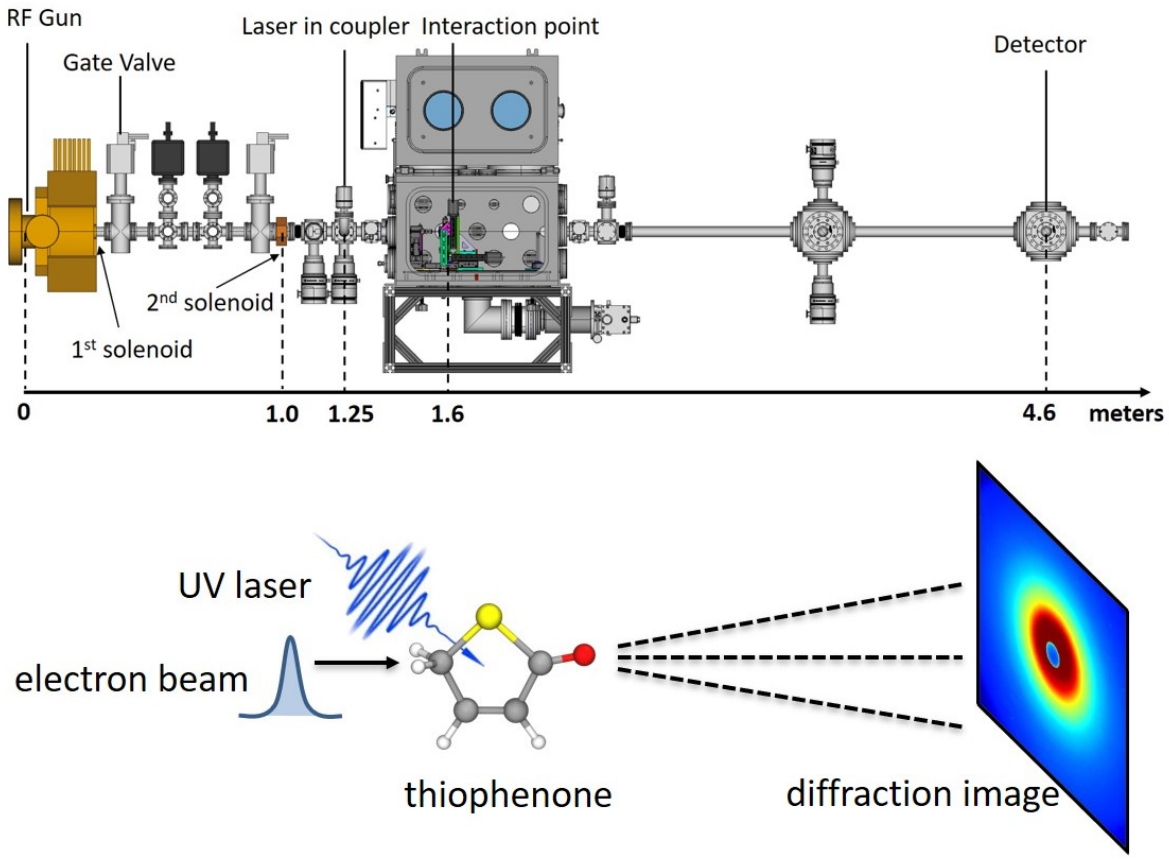

Figure 3.19: *Schematic of the electron diffraction of thiophenone (adapted from [90]).*

The mega-electronvolt ultrafast electron diffraction (MeV UED) study of thiophenone was performed as the last part of this dissertation work. The experimental part was performed at the MeV UED facility at SLAC National Accelerator Laboratory. The experimental setup and instruments are described in earlier studies [91, 92] and are depicted in Fig. 3.19. Below, we briefly discuss the experimental parameters used for the experiment performed on thiophenone. UV pulses with a pulse duration of ∼75 fs were used to excite the thiophenone molecules. The UV pulse duration in the interaction region was not characterized during the experimental campaign and the given value reflects the experience from previous experimental campaigns using the same optical setup. The electron beam had a typical pulse duration of 150-200 fs for low bunch-charge and 500-1000 fs for high bunch-charge. The UV laser pulses and the electron beam interacted with the thiophenone molecules inside a flow cell with an opening of ∼200 μm. Since thiophenone has a low vapor pressure (<1 Torr) at 25 °C, the assembly for sample delivery was heated to 60 °C. Once the sample flow was stabilized, static (no UV excitation) electron diffraction images were recorded using a P43 phosphor screen and Andor iXon Ultra 888 EMCCD camera. Figure 3.19 shows the schematic of the electron diffraction experiment on thiophenone. The analysis procedure and the static diffraction results are described in appendix B. Below, we focus on the experimental results obtained from time-resolved MeV UED and compare them with the results discussed in section 3.3.

The excitation fraction of molecules by the laser pulse is generally less than 10 %. Hence the time-dependent signal is dominated by the parent molecules. To extract the diffraction contribution from the photoproducts, the *diffraction-difference* method [93] is used. Here we subtract the diffraction intensities at later times (UV preceding electron beam) from the diffraction intensities at earlier times (electron beam preceding UV). Using equation 3.8, the difference modified molecular intensity can then be written as

$$\Delta sM(s) = s\frac{I(s, t > t_0) - I(s, t < t_0)}{I_A(s)} \tag{3.10}$$

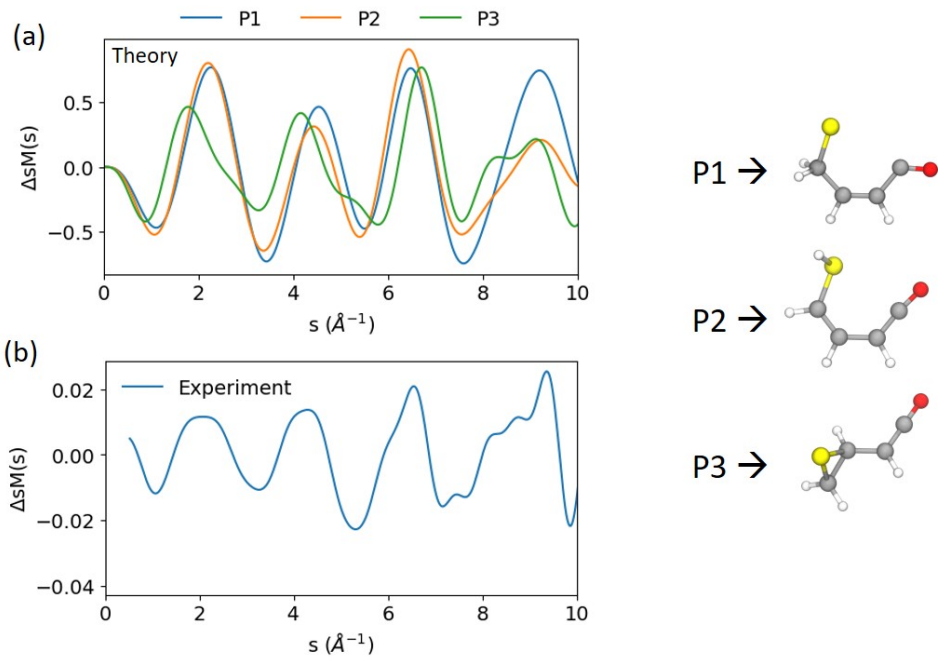

Figure 3.20: *Comparison of the modified molecular scattering intensities, $\Delta sM(s,t)$ = $sM(s,t>t_0)$ - $sM(s,t<t_0)$, where t_0 is the time where UV pulse and electron beam are overlapped. (a) Expected $\Delta sM(s)$ for the (ground-state) photoproduct geometries shown on right. (b) Experimentally obtained $\Delta sM(s)$ for 1 ps < t < 1.5 ps.*

where t_0 is the time where UV pulse and electron beam are overlapped.

Figure 3.20(a) shows the ΔsM(s) calculated for the ground state equilibrium geometries of the three photoproducts formed after UV absorption in thiophenone that were predicted by our earlier study (see section 3.3). The experimental spectrum (Fig. 3.20(b)) shows similar peak positions and variations, which strongly suggest the formation of the three dominant photoproducts P1, P2, and P3 as shown in Fig. 3.20. For a more quantitative comparison, it is important to keep in mind that these three photoproducts are formed in high vibrational states after photoexcitation of thiophenone. To incorporate this, we compare the experimental results with the results from the *ab-initio* molecular dynamics (AIMD) trajectory calculations (discussed in section 3.3). Figure 3.21(a) shows the experimentally observed delay-dependent change in ΔsM(s). The same quantity produced from the molecular geometries extracted from the AIMD trajectories is shown in Fig. 3.21(b).

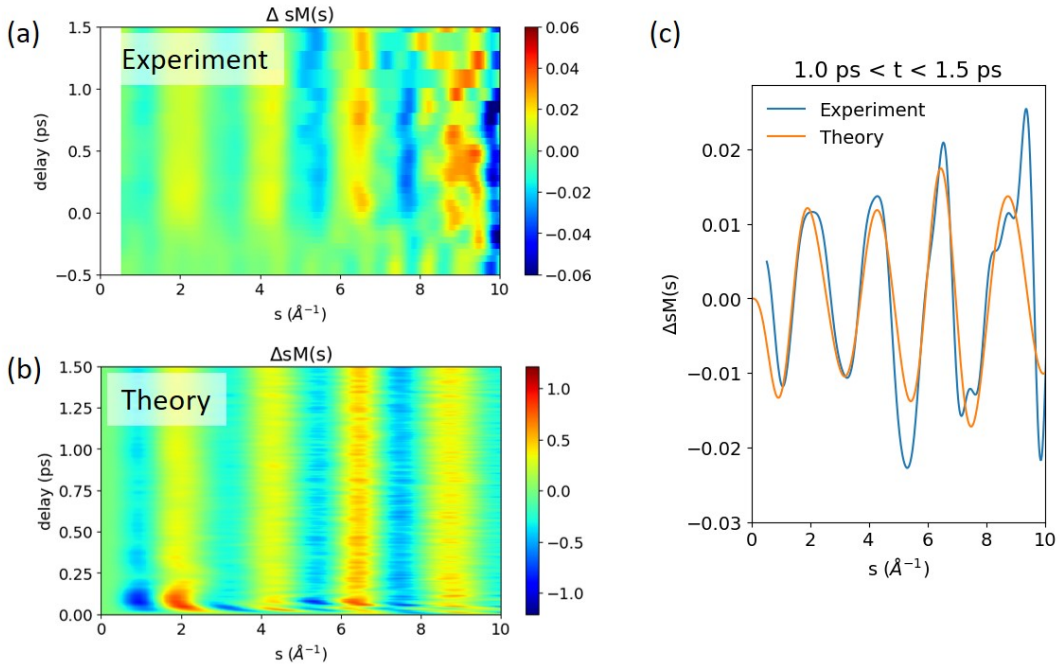

Figure 3.21: *Comparison of delay-dependent ΔsM(s). (a) Experiment (convolved in time with a Gaussian instrument response function of 150 fs FWHM), (b) Theory, (c) Delay-integrated plot for the time range of 1 ps to 1.5 ps.*

The features show close agreement between the theory and the experiment. Figure 3.21(c) shows the delay-integrated ΔsM(s) for the time range of 1 ps to 1.5 ps for the experiment and theory. The deviations in amplitude could be due to a slightly different distribution of photoproducts obtained in the experiments. The photoproduct branching ratio can be obtained by fitting the experimental spectra with the geometries observed in the AIMD calculations, which is planned for analysis in the future.

In order to gain direct insights about the internuclear distances, the experimental data can be transformed from the momentum transfer space (sM(s)) to the real space (PDF(r)), as discussed before. Figure 3.22(a) shows the simulated PDFs for the ground-state thiophenone molecules. The dominant contribution from the O-S distance is seen, followed by C-C, C-S, and C-O bond distances. When a UV pulse excites the thiophenone molecules, the delay-dependent ΔPDF (PDF(t>0) - PDF (t<0)) shows a depletion in the peak corresponding to the O-S distance and an increase in signal at longer distances. This is shown in Fig. 3.22(b),

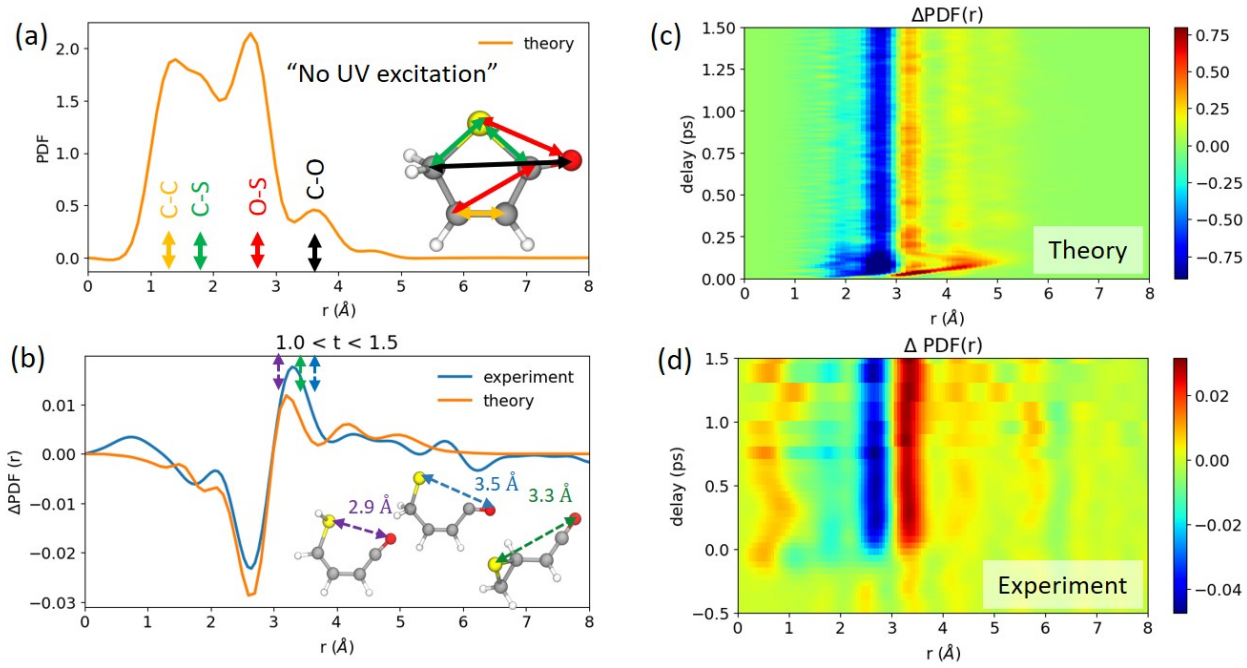

Figure 3.22: *Experimental and simulated PDFs for visualizing changes in internuclear distances. (a) Simulated PDF for the ground-state thiophenone molecule showing peaks at different internuclear distances. (b) Delay-integrated ΔPDF(r) for 1 ps < t < 1.5 ps. (c) Simulated delay-dependent ΔPDF(r) for the molecular geometries obtained by AIMD calculations. (d) Experimentally obtained delay-dependent ΔPDF(r).*

where the peak at longer distances (centered at ∼3.2 $\mathring{A}$) corresponds to the O-S distances in the ring-opened photoproducts P1, P2, and P3. The delay-dependent ΔPDF(r) simulated for the geometries obtained by AIMD calculations is shown in Fig. 3.22(c). The simulated results agree well with the experimental results shown in Fig. 3.22(d), except for the time-delays near zero due to the limited time resolution of the experiment. These results strongly confirm the ring-opening and formation of photoproducts with geometries similar to those predicted by our time-resolved photoelectron spectroscopy study. Further analysis may reveal the branching ratio of these photoproducts, which are formed after UV absorption by thiophenone.

Chapter 4

Imaging molecular geometries using coincidence ion momentum imaging

The motivation of this dissertation work lies in understanding light-induced reactions and subsequent isomerization and molecular dynamics happening at femtosecond time scales. To do this, one important step is to be able to distinguish molecular structures with subtle structural differences. One such example is of conformational isomers, which only differ by a rotation around a single (sigma) bond. This chapter demonstrates that the coincidence momentum imaging can be extremely sensitive to the molecular geometry and can be, in certain cases, used as an exquisite tool to monitor such subtle structural changes.

4.1 Background and motivation

Isomers are molecules with identical molecular formulas, but different arrangements of atoms. Despite containing the same number of atoms, isomers often possess very different physical and chemical properties. Isomers are known to play an important role in many chemical and biological processes in nature [94–98]. One of the well known examples, which is often quoted, is the isomerization in retinal chromophore (specifically, 11-cis to 11-trans)

of rhodopsin, a light sensitive receptor protein [99, 100], shown schematically in Fig. 4.1. This isomerization reaction happens within 200 fs and is a primary step involved in human vision [101].

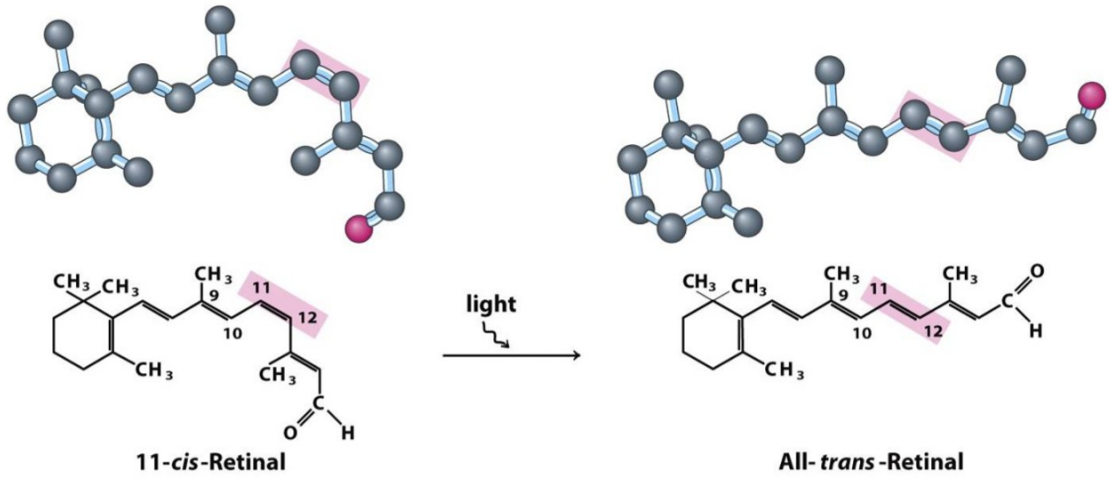

Figure 4.1: *Isomerization in retinal chromophore of rhodopsin upon light absorption (Adapted from [100]).*

Ring-opening isomerizations as discussed in chapter 3 are another form of isomerization which is also ubiquitous in nature, as is hydrogen migration [102], where a hydrogen moves from one site to another in a molecule. In recent years, hydrogen migration in simple hydrocarbons such as acetylene [13, 103–112] as well as in simple alcohols such as methanol and ethanol [113–116] has been studied in depth by using several different techniques, including coincident ion momentum imaging technique [13, 113].

In this chapter, we mainly discuss a category of stereoisomers called *conformers*, which differ in geometrical structure just by a rotation around a single bond. Figure 4.2 shows the equilibrium geometries of the conformational isomers of 1,2-dibromoethane ($C_2H_4Br_2$), as an example. Conformational isomerism is a common phenomenon in several proteins and enzymes and plays a crucial role in their biological activity and molecular recognition [117]. Several neurological diseases can result from altered protein conformations [118]. For example, in Alzheimer's disease patients, Abeta-amyloid/amyloid beta protein undergoes a conformational transformation from a soluble helix-rich state to a state rich in Abeta or

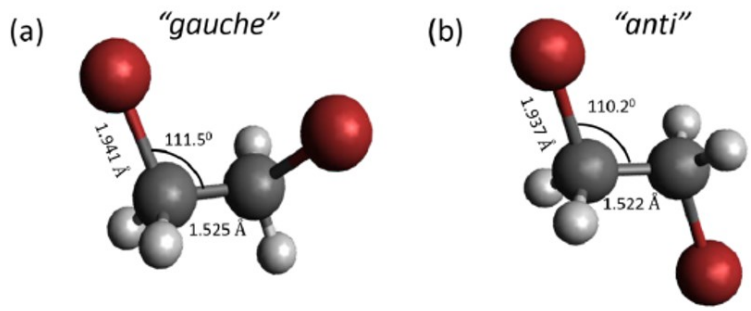

Figure 4.2: *Equilibrium geometries of (a) Gauche and (b) Anti conformers of 1,2-dibromoethane ($C_2H_4Br_2$).*

amyloid beta sheets and prone to self-aggregation. Consequently, conformational isomerism is an inherent phenomenon in many drugs used in the present-day pharmaceutical industry, and it closely defines the activity of drug molecules. The difference in physical and chemical properties of these conformational isomers owing to just the rotation around a single bond has been a subject of study for a long time. A major challenge in this regard is to study conformer specific properties since these types of isomers can, in many cases, interconvert into one another even at room temperature (∼0.59 kcal/mol) as the rotational energy barrier between different conformers is generally very small (within a few kcal/mol or a few tens of meV).

In recent years, several studies have been performed to understand conformer-specific photodissociation [119, 120] and photoinduced conformations [121, 122]. However, studies of conformer specific reaction pathways in the gas-phase are rather limited. Mega-electron-volt ultrafast electron diffraction (MeV-UED) technique offers direct insight into structural information, but is limited by the temporal resolution due to the coulomb repulsion between electrons. In general, gas-phase studies of conformational isomers would strongly benefit from techniques that are able to separate or distinguish isomers in dilute molecular beams. One novel method that could be very useful in this regard involves spatially separating

conformers in a molecular beam by deflecting them in an inhomogeneous electric field [123], thus exploiting the difference in dipole moments of these isomers. However, this method has difficulties in separating non-polar molecules.

Ion momentum imaging offers an alternative to spectroscopic and diffractive imaging techniques for determining the structure of molecules and enables shot-by-shot structure determination for single molecules when used in a multi-ion coincidence mode [124–126]. It has been demonstrated using a number of different light sources including femtosecond lasers, synchrotron radiation sources, and free-electron lasers in recent years [127–129], potentially paving the way for femtosecond time-resolved experiments on conformational isomers. However, the first step is to demonstrate that ion momentum imaging can indeed distinguish the conformational isomers, which coexist and can interconvert between each other. In order to build our understanding and to demonstrate the technique, we start with relatively simple molecules, namely, conformational isomers of 1,2-dibromoethane ($C_2H_4Br_2$), also commonly known as ethylene dibromide (EDB). EDB is present in high abundance in the stratosphere and possess the ability to destroy the ozone layer in the atmosphere [130]. This makes EDB a pressing target to study in future UV induced time-resolved studies. The ability to distinguish conformational isomers of EDB can potentially be useful for studying conformer specific UV photoexcitation dynamics of EDB.

EDB has two conformational isomer, namely, *gauche* and *anti* (see Fig. 4.2). These conformers can interconvert between each other by the rotation around C-C bond. Figure 4.3 shows the Newman projection for each of the conformations and the transition state and the relative energies between them [131]. The transition state where the two Br atoms are close together has the highest energy.

Coincident ion-momentum imaging experiments on EDB were performed at beamline 10.0.1.3 of the Advanced Light Source (ALS) at the Lawrence Berkeley National Laboratory during the standard ALS multi-bunch top-off mode of operation. The details of the experimental setup and light source are described in detail in chapter 2 and hence discussed

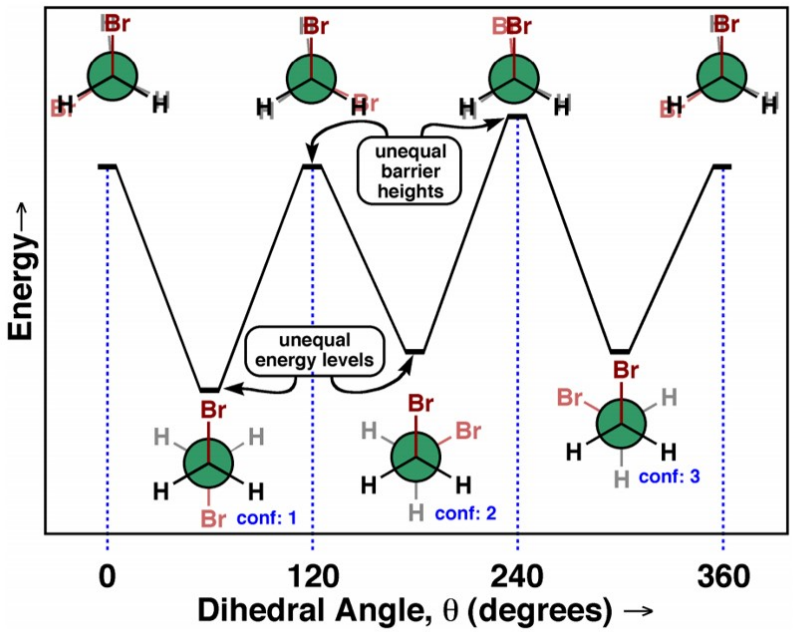

Figure 4.3: *Schematic of the conformations, the transition states and the relative energies between them (Adapted from [131]).*

very briefly here. The momentum imaging experiments were performed using a double-sided VMI setup (ALS-DVMI, see section 2.3.2). 1,2-dibromoethane or EDB (purity > 99%) was purchased commercially from Sigma Aldrich. EDB is liquid at room temperature and has a vapor pressure of 11.7 Torr (at 25 °C). It was filled in a bubbler (∼10-15 ml), degassed using several freeze-pump-thaw cycles, and inserted into the experimental chamber, which is under ultra-high vacuum, using a supersonic expansion through a nozzle of 30 μm in diameter. The vapor pressure of EDB was high enough to introduce it in the chamber without using a carrier gas. The molecular beam is skimmed by using a 500 μm skimmer before it interacts with the soft x-ray photons at the interaction region inside the VMI spectrometer.

4.2 Inner-shell photoionization of dibromoethane

When 1,2-dibromoethane (EDB) molecules are irradiated with photons of 140 eV energy, the principal result is the ejection of an electron from the 3d shell of one of the bromine

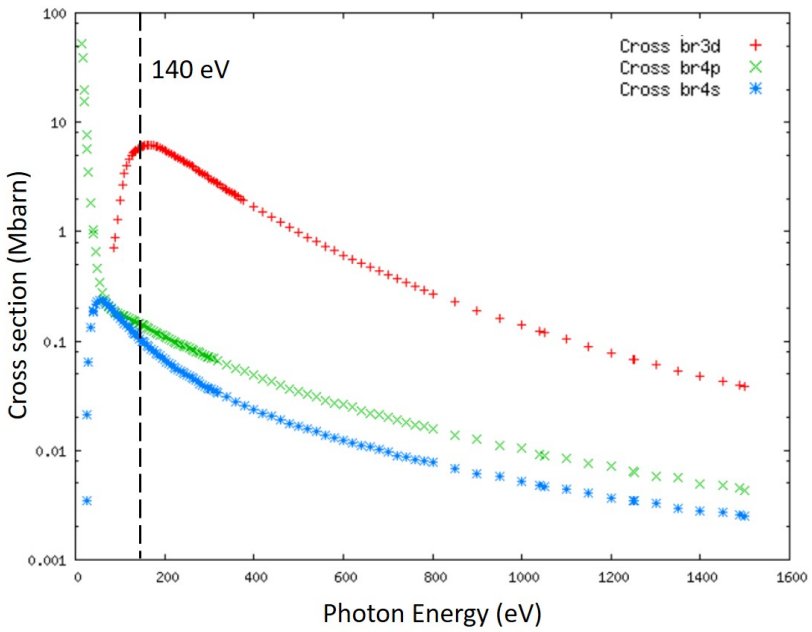

Figure 4.4: *X-ray photoionization cross-section as a function of photon energy for different shells in bromine. Vertical dashed line shows the photon energy (140 eV) used in the experiment. The cross sections of Br(3d), Br(4p) and Br(4s) in atomic Br are 5.76 Mbarn, 0.15 Mbarn and 0.11 Mbarn respectively (Acquired from database [132]).*

atoms. This is known as site-specific absorption and happens because the cross-section of Br(3d) is much higher then that of the other valence shells. To specify, the cross sections of Br(3d), Br(4p) and Br(4s) are 5.76 Mbarn, 0.15 Mbarn and 0.11 Mbarn respectively [132]. The variation of photoionization cross section with photon energy is shown in Fig. 4.4. It is to be noted that the electrons from other deeper shells, i.e. 3p, 3s for Br, as well as from carbon, C(1s), cannot be ionized at 140 eV since the binding energy of those are much higher than the photon energy [133]. The binding energies of $Br(3d_{3/2})$ and $Br(3d_{5/2})$ are 70 eV and 69 eV respectively.

The dominant process upon photoionization at 140 eV photon energy is the removal of an electron from Br(3d) shell with an estimated energy of ∼70 eV (Photon energy (140 eV) - Br(3d) binding energy (70 eV)). This is followed by Auger relaxation process where one or two secondary electrons are emitted post filling-up of the inner-shell (Br(3d)) by an electron

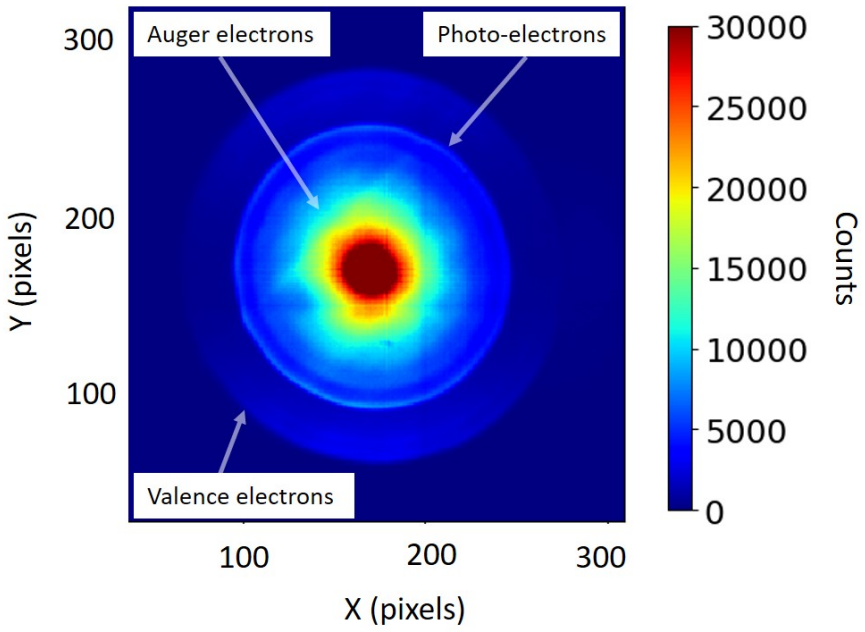

Figure 4.5: *Photoelectrons image after photoionization of EDB at 140 eV photon energy using ALS-DVMI.*

from outer shell. The electron emitted is known as Auger electron and it acquires the energy via Coulomb interaction with the electron that fills the inner shell hole. It is to be noted that the energy of Auger electron is not dependent on photon energy but only depends on the energy difference between energy of initial electronic transition into the vacancy and the ionization energy for the shell from which the Auger electron was ejected. Sometimes two photoelectrons are emitted post filling up of inner shell and the process is called *shake off* process [134–138]. Figure 4.5 shows the photoelectrons from EDB recorded using ALS-DVMI (see section 2.3.2), post photoionization at 140 eV. The signal from Auger electrons, photo electrons and valance electrons are marked. After the removal of multiple electrons from the molecule, the highly charged EDB molecule breaks up into multiple fragment ions. As we show in the following, after reconstructing the initial momentum for ionic fragments in certain fragmentation channel, it is possible to gain insights about the initial geometry of the molecule prior to fragmentation.

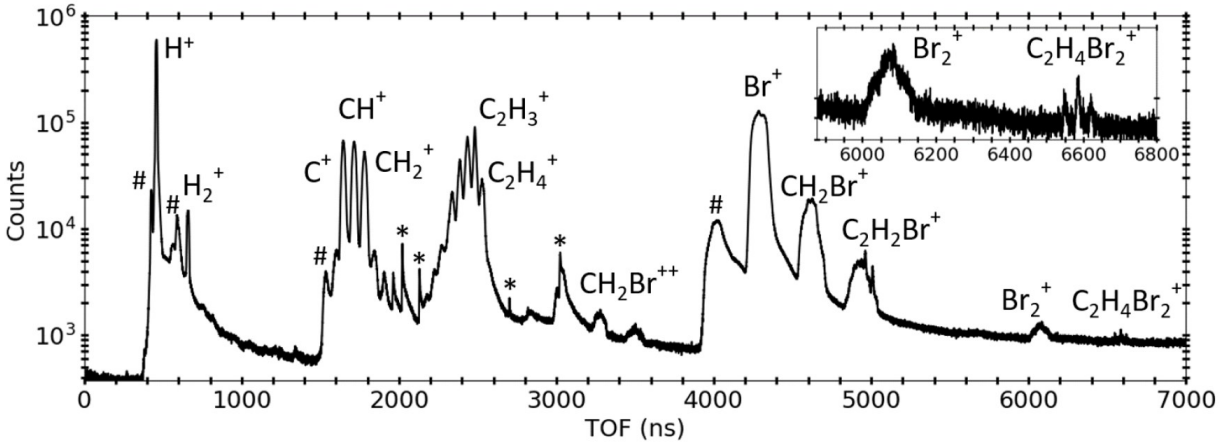

Figure 4.6: *Ion time-of-flight spectrum of 1,2-dibromoethane recorded after photoionization at 140 eV photon energy.*

After photoionization and removal of multiple electrons, EDB molecules fragment and the ion time of flight (TOF) can be recorded for all the ionic fragments. Figure 4.6 shows the ion TOF spectra of EDB post photoionization at 140 eV. The inset shows a zoomed-in view of the spectral region including singly charged molecular bromine and the singly ionized parent, EDB^+. Peaks from background residual gas are marked with '*'. The peaks marked with '#' are from secondary electrons created by ion impact on the mesh that terminates the drift tube. These electrons are accelerated toward the MCP, where they are detected at slightly shorter flight times than the corresponding ions. The spectrum displays many peaks, indicating rich fragmentation into various ionic species along several pathways. The parent ion (EDB^+) has 3 peaks (inset in Figure 4.6) due to the two stable isotopes of Br, ^{79}Br and ^{81}Br, with natural abundances of 50.7% and 49.3%, respectively. The yield of EDB^+ is relatively low compared to those of fragments ion such as CH^+, $C_2H_3^+$ and Br^+ since the singly charged parent ion is almost exclusively produced by valence ionization, which has a low cross section at this photon energy, as discussed before. We do not observe peaks in the TOF spectrum corresponding to the parent dication (EDB^{2+}) or trication (EDB^{3+}), suggesting that those are unstable and dissociate into several fragments on a timescale faster

than the typical flight times of a few microseconds.

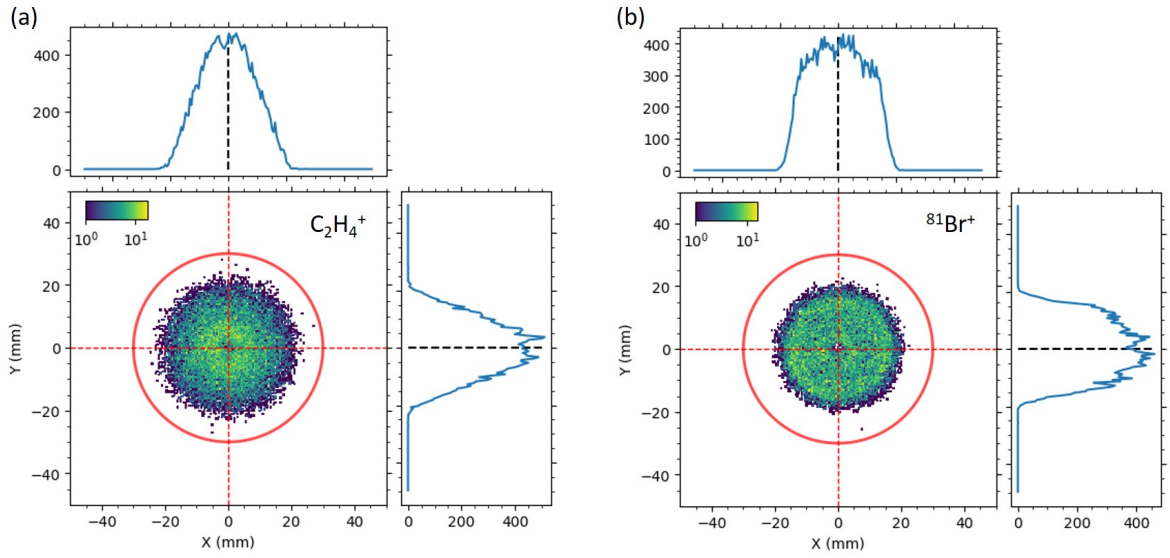

Figure 4.7: *Photoion images of $C_2H_4^+$ and $^{81}Br^+$ for the coincidence channel $C_2H_4^+$ + $^{81}Br^+$ + $^{81}Br^+$. Also shown are the x and y projections.*

As described in section 2.3.5, we can record the data corresponding to ions and electrons in coincidence mode, and the events corresponding to breakup into certain fragmentation channel can be selected by plotting PIPICO or TRIPICO maps. For the goal of determining geometry, the coincidence channel $C_2H_4^+$ + $^{81}Br^+$ + $^{81}Br^+$ is chosen. This is because the geometries of *gauche* and *anti* conformers are such that the momentum gained in post ionization by the ionic fragments $^{81}Br^+$ and $C_2H_4^+$ is expected to be very different for the two geometries. The coincidence channel $C_2H_4^+$ + Br^+ + Br^+ (with any combination of isotopes) represents $\sim 60\%$ of the total triple ion coincidence yield, and the $C_2H_4^+$ + $^{81}Br^+$ + $^{81}Br^+$ coincidence channel contains a quarter of those events. Figure 4.7 shows the position map for $C_2H_4^+$ and $^{81}Br^+$ for the coincidence channel, $C_2H_4^+$ + $^{81}Br^+$ + $^{81}Br^+$, along with the projections on both the axis. Isotropic distribution in position can be seen for both the fragments. For this coincidence channel, the positions and TOF for the selected subset of data is used to calculate the initial momentum and kinetic energies (section 2.3.5). Insights

about certain aspects of initial geometry and molecular fragmentation can be obtained by plotting the momentum of the three ionic fragments as a Newton diagram. This is discussed in the next section.

4.3 Visualization of initial geometry via Newton diagram

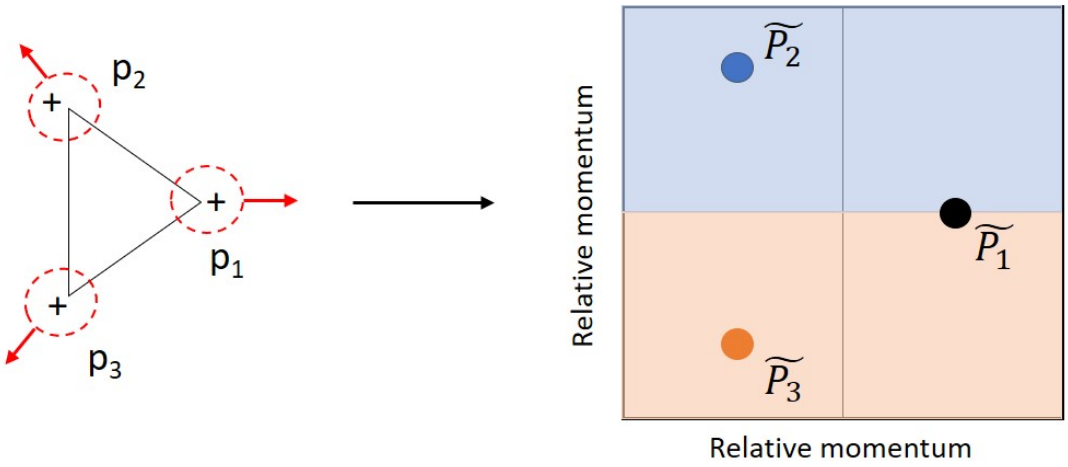

Figure 4.8: *An intuitive visualization of Newton plot for a molecule where all three bonds break simultaneously and the momentum is acquired purely by Coulomb repulsion.*

A Newton plot or Newton diagram allows an intuitive way of visualizing momentum correlations [139]. The Newton plot is a two-dimensional map in which the relative momenta of two of the fragments are plotted with respect to the momentum of the third fragment. The momentum of the fragment relative to which the other two fragments are plotted is set to unity and is plotted at x=1, while the momenta of the other two fragments are normalized to the magnitude of this reference fragment's momentum. Figure 4.8 shows a Newton plot for a hypothetical molecule breaking up into three atoms with initial momentum $\vec{p}_1$, $\vec{p}_2$ and $\vec{p}_3$. If all the bonds break simultaneously and the momentum acquired by charged

particles is purely by Coulomb repulsion, the Newton plot should look like the plot on right side. It should be noted that the condition that all bonds break simultaneously is crucial, and the effect it has on the Newton plot when the condition is not fulfilled is discussed in section 4.5. The momenta $\widetilde{P}_2$ and $\widetilde{P}_3$ are the relative momenta with respect to the first particle and the magnitude of the relative momentum can be calculated as, $|\widetilde{P}_2| = |p_2|/|p_1|$ and $|\widetilde{P}_3| = |p_3|/|p_1|$, while setting $|\widetilde{P}_1| = 1$. The direction can be obtained by calculating the relative angle, $\cos\theta_{12}=\frac{\vec{p_2}.\vec{p_1}}{|p_2||p_1|}$ and $\cos\theta_{13}=\frac{\vec{p_3}.\vec{p_1}}{|p_3||p_1|}$, while fixing the direction of $\widetilde{P}_1$ along the x axis.

Another common method of for determining energy sharing between the ionic fragments and sometimes geometrical interpretation, is the Dalitz plot [140]. These are discussed for EDB in later sections.

4.4 Differentiating and quantifying gas-phase conformational isomers of dibromoethane

In this section, we present our publication in *The Journal of Physical Chemistry Letters* [141] about the identification and quantification of the conformer ratio in 1,2-dibromoethane ($C_2H_4Br_2$). In this work, we were able to demonstrate that coincident momentum imaging is a sensitive tool to differentiate between *anti* and *gauche* conformers of 1,2-dibromoethane (EDB, $C_2H_4Br_2$) by analyzing the three-body fragmentation channel, $C_2H_4^+ + {}^{81}Br^+ + {}^{81}Br^+$. The signatures observed in Newton plots are confirmed using Coulomb explosion simulations (CES) for near-equilibrium geometries. The details regarding these simulations are discussed in detail in Appendix A.

For the fragmentation channel $C_2H_4^+ + {}^{81}Br^+ + {}^{81}Br^+$, the ionic fragments are formed via *sequential* (bonds break in a stepwise manner) and *concerted* (bonds break simultaneously) fragmentation. Before quantifying the yield, sequential fragmentation needs to be subtracted, which is done with native frames [142, 143], as discussed in section 4.5.

Moreover, to establish the sensitivity of our method, the experiment is performed for different initial temperatures of the EDB molecules. The sample delivery system was heated to change the ratio of *gauche* and *anti* conformer in the experiment. The experimental findings are compared with the theoretical estimates of conformer ratio at different temperatures and show a good agreement. If this method can be extended, it would be suitable to perform time-resolved experiments, using lab-based HHG sources, to monitor the timescale of these interconversion between conformational isomers. Furthurmore, it may also provide some insights related to the intermediate structures which may form while transitioning from one conformer to another.

THE JOURNAL OF PHYSICAL CHEMISTRY Letters

pubs.acs.org/JPCL Letter

Differentiating and Quantifying Gas-Phase Conformational Isomers Using Coulomb Explosion Imaging

Shashank Pathak,* Razib Obaid, Surjendu Bhattacharyya, Johannes Bürger, Xiang Li, Jan Tross, Travis Severt, Brandin Davis, René C. Bilodeau, Carlos A. Trallero-Herrero, Artem Rudenko, Nora Berrah, and Daniel Rolles*

Cite This: J. Phys. Chem. Lett. 2020, 11, 10205−10211 Read Online

ACCESS | Metrics & More | Article Recommendations | Supporting Information

ABSTRACT: Conformational isomerism plays a crucial role in defining the physical and chemical properties and biological activity of molecules ranging from simple organic compounds to complex biopolymers. However, it is often a significant challenge to differentiate and separate these isomers experimentally as they can easily interconvert due to their low rotational energy barrier. Here, we use the momentum correlation of fragment ions produced after inner-shell photoionization to distinguish conformational isomers of 1,2-dibromoethane ($C_2H_4Br_2$). We demonstrate that the three-body breakup channel, $C_2H_4^+ + Br^+ + Br^+$, contains signatures of both sequential and concerted breakup, which are decoupled to distinguish the geometries of two conformational isomers and to quantify their relative abundance. The sensitivity of our method to quantify these yields is established by measuring the relative abundance change with sample temperature, which agrees well with calculations. Our study paves the way for using Coulomb explosion imaging to track subtle molecular structural changes.

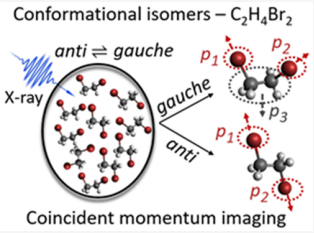

Conformational isomers, or conformers, are defined as molecules with the same chemical formula but different geometrical structures, caused by rotation around a single bond.[1] Conformational isomerism is a common phenomenon in a wide range of molecules from simple polyatomics to large biomolecules and plays a crucial role, e.g., in their biological activity and molecular recognition.[2] Several neurological diseases are known to be caused by altered protein conformations.[3] Consequently, conformational isomerism is omnipresent in the present-day pharmaceutical industry and, to a large extent, defines the activity of drug molecules.[4] Conformations also dictate physical and chemical properties, including photoabsorption. However, studying conformer-specific properties, even for small molecules, represents a major experimental challenge since they can interconvert. This internal rotation of one conformer into another is extremely prevalent even at room temperature because of the low rotational energy barrier between different conformers, which is usually a few kcal/mol.

Due to its ubiquity and fundamental nature, conformational isomerism continues to be investigated in a variety of systems using different experimental methods. In recent years, several investigations have studied conformer-specific photodissociation[5,6] and photoinduced conformations[7] for unimolecular reactions. Some of these studies not only have shown strong conformation specific reaction yields but also have uncovered disagreement with predictions from statistical rate theory,[8] which warrants further investigations on different systems. Gas-phase studies of conformational isomers would strongly benefit from techniques that are able to separate or distinguish isomers in dilute molecular beams. One such method spatially separates the conformers in a molecular beam by deflecting them in an inhomogeneous electric field,[9] thus exploiting the difference in inherent dipole moments of the isomers. However, this method has difficulties in separating nonpolar molecules. Recently, the mega electronvolt ultrafast electron diffraction (MeV-UED) technique was used to distinguish transient conformational structures of photoexcited 1,2-diiodotetrafluoroethane molecules.[10]

Another simple yet powerful technique for structure determination in single molecules is Coulomb explosion imaging[11] (CEI) in a coincident ion momentum imaging mode.[12,13] Photon-induced CEI has been demonstrated using different light sources including femtosecond lasers,[14−19] synchrotron radiation sources,[20,21] and free-electron lasers[22] in recent years. Here, we show that CEI using coincident ion momentum imaging is a suitable method to differentiate and quantify conformational isomers and to study conformer specific photoabsorption properties. Our experiment is performed on 1,2-dibromoethane ($C_2H_4Br_2$), also known as ethylene dibromide (EDB). EDB is a simple organobromide that is often scrutinized due to its environmental impact,[23] which makes it a pressing target for light-induced studies. EDB

Received: September 27, 2020
Accepted: November 10, 2020
Published: November 18, 2020

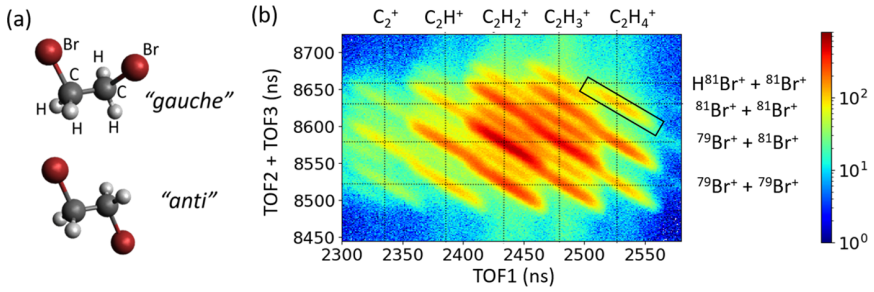

Figure 1. (a) *Gauche* and *anti* conformations of 1,2-dibromoethane (EDB, $C_2H_4Br_2$). (b) Triple-ion-coincident time-of-flight spectrum for EDB zoomed in near the channel of interest (marked by the black rectangle).

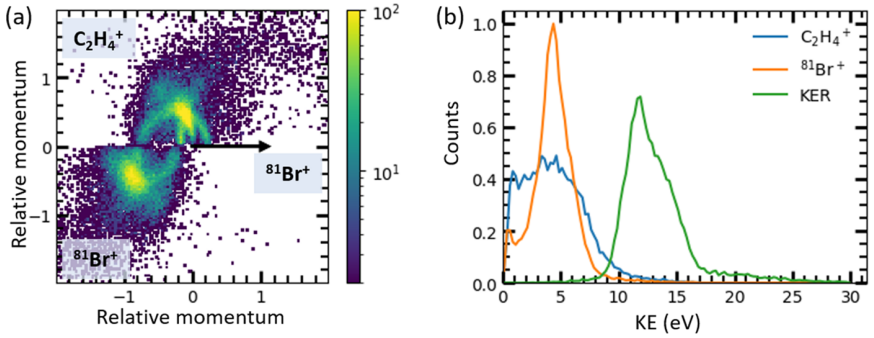

Figure 2. Newton plot (a) and kinetic energy distributions (b) of $C_2H_4^+$ (blue) and $^{81}Br^+$ (orange) fragments and sum of the three ion kinetic energies or KER (green) for the $C_2H_4^+ + {}^{81}Br^+ + {}^{81}Br^+$ coincidence channel. The Newton plot shows the normalized relative momenta of $C_2H_4^+$ and $^{81}Br^+$ plotted with respect to the other $^{81}Br^+$ (represented by the black arrow), whose momentum is fixed to unity in the positive *X*-direction.

is known to exist in both the *anti* and *gauche* conformations, which are separated in this study using coincident ion momentum imaging in combination with state-of-the-art analysis techniques that allow structure determination on a molecule-by-molecule level. Specifically, we consider the three-body fragmentation of EDB after bromine 3*d* inner-shell ionization at 140 eV photon energy (see Methods) and use the momenta of three ionic fragments detected in coincidence to determine the geometry of EDB prior to fragmentation. The kinetic energies and the angular correlation between the ionic fragments give a clear signature of two different geometries, which are assigned to *gauche* and *anti* conformers of EDB based on classical Coulomb explosion simulations (CES). To test the sensitivity of our method, we analyze the change in the ratio of the measured yield of these conformers with the change in temperature of the sample. The results of the experiment performed at three different temperatures agree well with the theoretically expected change in the ratio of *gauche* to *anti* conformers in the molecular beam.

The molecular structures of the *gauche* and *anti* conformers of EDB are shown in Figure 1(a). The interconversion happens by the rotation around the C−C bond. Figure 1(b) shows a region of the triple-ion-coincidence spectrum near the channel of interest for this study, $C_2H_4^+ + Br^+ + Br^+$. The time-of-flight of the first detected light fragment ion (TOF1) is shown on the *x*-axis, the sum of the times of flight of the second and third heavier fragment ions (TOF2+TOF3) is shown on the *y*-axis, while the color represents the yield of the corresponding triple coincidence events. For breakup channels where no further fragments with significant momentum are produced, the triple-ion-coincidence plot shows sharp diagonal lines due to momentum conservation during the breakup process.

Each diagonal line corresponds to a specific three-body fragmentation channel, whose relative yields are given in the Supporting Information. For the present investigation, we focus on the $C_2H_4^+ + {}^{81}Br^+ + {}^{81}Br^+$ coincidence channel as it is well separated from other channels and gives a clear indication of the geometry before fragmentation, as explained in the following. The momenta and kinetic energies of the three coincident ions are calculated from the time-of-flight and detector hit position of each ion (see Supporting Information, Section 1), and the results are shown in Figure 2(a) as a Newton plot, which allows an intuitive visualization of the momentum correlations.[24] Here, the momentum of one of the $^{81}Br^+$ ions is fixed to unity, and the normalized relative momenta (magnitude and direction) of $C_2H_4^+$ and the other $^{81}Br^+$ are plotted in the upper ($y > 0$) and lower ($y < 0$) half of the plot, respectively. For the selected breakup channel, the Newton plot shows two semicircular structures and several local maxima (yellow spots) that partially overlap with the semicircles. These features need to be understood and deconvoluted to separate the contribution from *gauche* and *anti* conformers. Semicircular structures in a Newton plot are typically a consequence of a *sequential* breakup,[25] while the local maxima are due to *concerted* (*synchronous*) breakup of EDB subsequent to photoionization. Eqs 1 and 2 show examples of concerted and sequential breakup pathways that contribute to the selected coincidence channel:

$$C_2H_4Br_2^{3+} \rightarrow C_2H_4^+ + Br^+ + Br^+ \quad \text{(concerted/synchronous)} \qquad (1)$$

$$C_2H_4Br_2^{3+} \rightarrow C_2H_4Br^{2+} + Br^+ \rightarrow C_2H_4^+ + Br^+ + Br^+ \quad \text{(sequential)} \qquad (2)$$

The breakage of two molecular bonds in a trication is defined as *sequential* if an intermediate dication (here: $C_2H_4Br^{2+}$) is

https://dx.doi.org/10.1021/acs.jpclett.0c02959
J. Phys. Chem. Lett. 2020, 11, 10205−10211

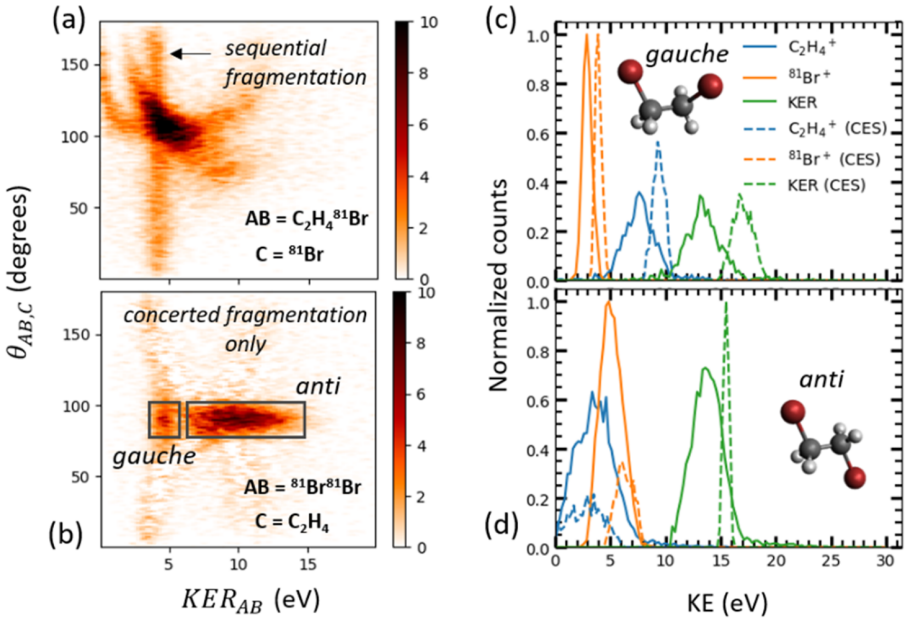

Figure 3. (a) All events in the $C_2H_4^+ + {}^{81}Br^+ + {}^{81}Br^+$ coincidence channel, plotted as a function of second-step KER ($KER_{C_2H_4{}^{81}Br}$) and angle ($\theta_{C_2H_4{}^{81}Br,{}^{81}Br}$) between the relative momenta describing each step of a sequential fragmentation with $(C_2H_4{}^{81}Br)^{2+}$ as the intermediate dication (see text). (b) Similar to panel (a) but after subtraction of sequential breakup events using the native frames method and plotted for a hypothetical intermediate dication $({}^{81}Br{}^{81}Br)^{2+}$. The black rectangles show the ROIs chosen to separate *anti* and *gauche* conformers. (c), (d) Experimental kinetic energy distributions (solid lines) for the fragments and total KER for *gauche* and *anti* conformers selected from panel (b) along with results from Coulomb explosion simulations (CES, dashed lines) for both cases.

formed with a lifetime longer than its rotational period.[26] The semicircular ring in the Newton plot is thus a manifestation of the rotation of the intermediate dication.

Figure 2(b) shows the kinetic energy distribution of individual fragment ions and the kinetic energy release (KER). The rather broad distribution in kinetic energies of the fragments also suggests the presence of several contributing channels, such as both concerted and sequential fragmentation, as well as the presence of *gauche* and *anti* conformers. Only the concerted breakup pathways can be used to extract the molecular geometry using CEI,[27] hence the sequential pathways need to first be disentangled by further analysis.

For separating the concerted breakup events from the sequential breakup events, we use the recently developed *native frames* method.[28] To briefly summarize, the native frames method takes advantage of the rotation of the intermediate metastable molecular fragment produced during a sequential breakup to distinguish sequential from concerted fragmentation. The main idea of the native frames method is to analyze each fragmentation step in its respective center-of-mass reference frame, i.e., its *native* frame, which we accomplish using the conjugate momenta derived from Jacobi coordinates associated with each fragmentation step (see Supporting Information, Figure S3), and then, we identify sequential fragmentation as a uniform angular distribution between the conjugate momenta for each step, assuming that the intermediate fragment (dication) is rotating in the fragmentation plane. By taking advantage of the uniform angular distribution, we reconstruct parts of the distribution of sequential breakup events masked by competing concerted fragmentation, allowing us to separate the sequential and concerted breakup distributions in any plot created from the measured momenta. More details regarding the application of the native frames analysis on EDB can be found in the Supporting Information.

As the first step in the native frames method, Figure 3(a) shows all three-body fragmentation events in the $C_2H_4^+ + {}^{81}Br^+ + {}^{81}Br^+$ breakup channel, plotted as a function of the second-step kinetic energy release, $KER_{C_2H_4{}^{81}Br}$, and the angle between the relative momenta describing each step of sequential fragmentation with $(C_2H_4{}^{81}Br)^{2+}$ as an intermediate dication, $\theta_{C_2H_4{}^{81}Br,{}^{81}Br}$. The second-step KER is obtained using the relative momentum of the second step.[28] In this representation, the events in the vertical structure at $KER_{C_2H_4{}^{81}Br} \approx 4$ eV (shown by the black arrow), which are uniformly distributed over all angles, stem from sequential fragmentation. For further analysis, they can be subtracted, as detailed in the Supporting Information, such that all following plots contain only coincidence events from a concerted breakup.

In order to identify and separate the contributions corresponding to a concerted breakup of *gauche* and *anti* conformers, which are partially overlapping in the Newton plot (see Supporting Information, Figure S5), Figure 3(b) shows a plot similar to Figure 3(a) but after subtraction of the sequential events and by calculating the relative momenta for a hypothetical sequential breakup with a $({}^{81}Br\ {}^{81}Br)^{2+}$ intermediate dication (see the Supporting Information). We can clearly identify two different contributions and select each contribution by gating on the regions of interest (ROI) shown by the black rectangles. To verify this selection, the fragment kinetic energies for the events selected in each of the two ROIs in Figure 3(b) are plotted in Figure 3(c) and 3(d), which show two distinctly different patterns. From Figure 3(c), it is apparent that for the *gauche* conformer, the $C_2H_4^+$ fragment is

https://dx.doi.org/10.1021/acs.jpclett.0c02959
J. Phys. Chem. Lett. 2020, 11, 10205−10211

produced with higher kinetic energy as compared to the $^{81}Br^+$ fragments since it is repelled by both $^{81}Br^+$ fragments, which are emitted in the same hemisphere. For the *anti* conformer (Figure 3(d)), the kinetic energy of the $C_2H_4^+$ fragment is smaller than that of the $^{81}Br^+$ fragments since the $C_2H_4^+$ fragment is trapped in between the two $^{81}Br^+$ fragments as they impart their momenta onto the $C_2H_4^+$ fragment in almost exactly opposite directions, a condition often referred to as 'obstructed instantaneous explosion'.[29]

The dashed lines in Figure 3(c) and 3(d) show the results of a Coulomb explosion simulation performed for concerted breakup of both conformers. The simulation starts from the equilibrium geometry of the neutral conformers and assumes point charges at the positions of two bromine atoms and at the center-of-mass (c.o.m.) of the third fragment (C_2H_4). For each point charge, a small random variation of the position within a sphere corresponding to a 5% change in one of the C−Br bond lengths is chosen in order to account for small geometry changes of the molecule prior to fragmentation, e.g., as a result of vibrations in the neutral or ionic states, either due to the initial temperature of the sample or due to vibrational excitation during the ionization process. The trajectories (and hence velocities and momenta) for 1000 such "near-equilibrium" geometries for both conformations are calculated by numerically solving the classical equations of motions assuming pure Coulombic repulsive interaction between the point charges (see Supporting Information, section 3). The simulation results reproduce the overall observations in the experimental data but overestimate the energies for each fragment. Such overestimation of the kinetic energies is common for simple CES and can indicate an increase of the bond lengths prior to fragmentation, tricationic potential energy surfaces that are not purely Coulombic, or a finite internal energy stored in the fragments.[30]

Figure 4(a) and 4(c) show the Newton plots for the *gauche* and *anti* conformers in the experiment, separated as described above, while Figure 4(b) and 4(d) show the simulated Newton plots obtained from the CES. The good agreement between simulation and experimental results further confirms that the separated events indeed correspond to the concerted breakup events from different conformers. Therefore, the ratio of *gauche* to *anti* conformers can simply be determined from the respective yields in the ROIs in Figure 3(b), and we can, in the following, investigate the change in the conformer ratio as a function of sample temperature.

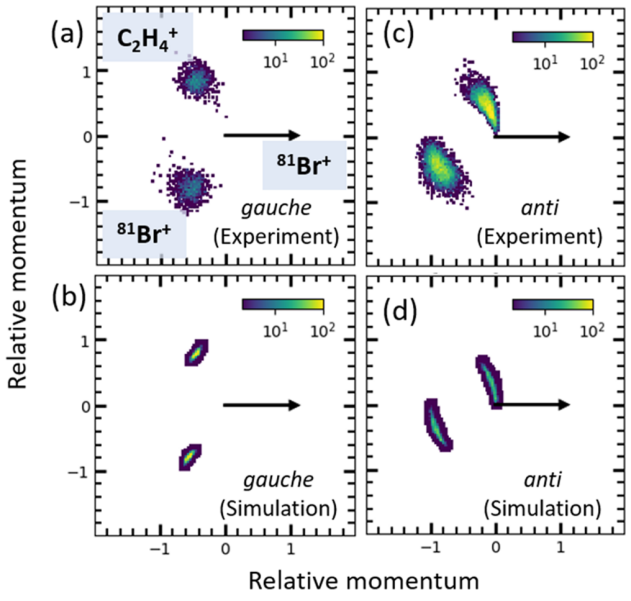

Figure 4. (a), (b) Newton plots from experimental data and CES for the *gauche* conformer. (c), (d) Newton plots from experimental data and CES for the *anti* conformer.

Conformational isomers often coexist in a dynamic equilibrium, with the conformer ratio being determined by temperature of the system and the difference in free energies of the conformers. This can be expressed as[31]

$$\Delta G = -RT \ln(K) \tag{3}$$

where ΔG is the difference in the free energy of the two conformers, R is the universal gas constant, T is the temperature of the sample, and K is the equilibrium constant, which, in the present case, corresponds to the ratio of *gauche* and *anti* conformers. In order to verify the ability of our CEI technique to quantify the conformer ratio and to test its sensitivity, we recorded fragmentation data for EDB at three different sample temperatures while keeping all other experimental parameters constant. The three different temperatures, measured at the molecular beam nozzle, were T_1 = 20 °C (i.e., without heating), T_2 = 60 °C, and T_3 = 95 °C. The theoretical estimate of the *gauche* to *anti* ratio for EDB can be calculated using eq 3. For the equilibrium, *anti* ⇌ *gauche*, the degrees of freedom are the same between the reactant and product. We thus assume $\Delta S = 0$, which implies $\Delta G = \Delta H$, where ΔH is the change in enthalpy and ΔS is the change in entropy. To determine the energy barrier and enthalpy difference between the *gauche* and *anti* conformers, quantum chemical calculations were performed using the Gaussian software package[32] (see Methods). These values were then used to calculate the expected ratio of *gauche* to *anti* conformer for different temperatures using eq 3. Here, our assumption is that the vibrational degrees of freedom do not cool significantly during the molecular beam expansion in the nozzle of the target preparation chamber, which has been reported for small molecules.[33] To the best of our knowledge, this has not been studied for complex molecules such as dibromoethane. This allows us to consider the sample temperature to be equal to the nozzle temperature.

Figure 5(a) shows the coincident ion yield of the experiment attributed to *gauche* and *anti* conformers for the three temperatures. The yield of the *gauche* conformer clearly increases at higher temperatures, while the yield of the *anti* conformer decreases. This is expected since more molecules can cross the rotational energy barrier between *anti* and *gauche* conformers at higher temperatures. Figure 5(b) shows the resulting *gauche* to *anti* ratio obtained from the experiment compared to the theoretical values (shown in blue) obtained using eq 3. The error bars on the experimental data show the statistical error. The blue band around the theoretical curve shows the variation in the theoretical value corresponding to an uncertainty of the absolute temperature of ±10 °C in order to visualize the uncertainty in the ratio, e.g., due to possible differences between the thermocouple readings and the actual temperature of the sample. The experimental and theoretical values are in good agreement except at room temperature, where the experiment yields a larger amount of the *gauche* conformer than predicted by theory. We attribute this to the very small contribution (in absolute numbers) of *gauche*

https://dx.doi.org/10.1021/acs.jpclett.0c02959
J. Phys. Chem. Lett. 2020, 11, 10205−10211

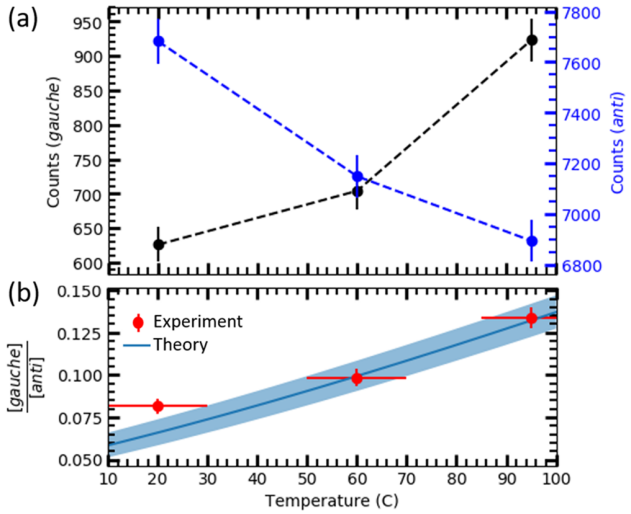

Figure 5. (a) Experimental yield of *gauche* (black) and *anti* (blue) conformers as a function of sample temperature. The yield of the *gauche* conformer increases and the yield of the *anti* conformer decreases, suggesting an increased conversion from *anti* to *gauche* at higher temperature, as expected based on the difference in the free energy of the two conformers. (b) Theoretical and experimental change in ratio as a function of sample temperature. The blue band represents the uncertainty of the theoretical ratio when assuming an uncertainty of ±10 °C in the sample temperature.

conformers at room temperature, which makes the value for the ion yield from *gauche* conformers more susceptible to small contributions from "background" counts that may not be fully discriminated (see Figure 3(b)). Furthermore, we note that the overall good agreement between experiment and theory suggests that the triple ionization and dissociation probability into the channel of interest is the same for each conformer, which is reasonable for inner-shell ionization but may be different, e.g., for strong-field ionization.

In conclusion, we have demonstrated that we can distinguish and quantify the yields of the conformational isomers of EDB, which coexist in a dynamic equilibrium and are separated by an extremely small energy difference (~0.1 eV). Specifically, our methodology can distinguish between *anti* and *gauche* conformers of EDB by selecting triple ion coincidences combined with a detailed analysis of the different fragmentation pathways using Newton plots and fragment kinetic energies combined with the novel native frames analysis technique. Our measurements performed at different sample temperatures indicate that our technique is sensitive to subtle change in the conformer ratio and in good agreement with theoretical calculations. This level of sensitivity of the CEI technique is crucial for future molecular dynamics studies, such as time-resolved experiments studying the interconversion of conformers, where the quantitative determination of small changes in conformer population is essential.

METHODS

The experiment was performed at beamline 10.0.1.3 of the Advanced Light Source (ALS) at the Lawrence Berkeley National Laboratory. Fragment ions and electrons were measured in coincidence using a double-sided velocity map imaging (VMI) spectrometer. The VMI spectrometer and data collection has been described elsewhere in detail.[34] EDB was introduced into the ultrahigh vacuum experimental chamber, using a supersonic expansion through a nozzle of 30 μm in diameter. The molecular beam is skimmed by using a 500 μm skimmer before it interacts with the soft X-ray photons at the interaction region inside the VMI spectrometer. The experiment was performed at a photon energy of 140 eV (bandwidth: 15 meV), which is above the 3*d* photoionization threshold (~77.5 eV) of Br and near the (broad) peak of the 3*d* giant resonance found in Br-containing molecules.[35] As the resonantly enhanced Br 3*d* photoionization cross section dominates the total cross section at this photon energy, photoionization occurs predominantly by removal of a 3*d* inner-shell electron, followed by an Auger process that emits one or two further electrons. As the multiply charged EDB molecule dissociates into fragment ion, the time-of-flight and position of all the ionic fragments are recorded, which are then used to calculate the three-dimensional momenta and kinetic energies for each ion recorded in coincidence.[34]

Quantum chemical calculations were performed for calculating the enthalpy difference between the conformers. Both conformer structures were initially optimized at the ωB97X-D level of theory[36] using the 6-31G basis set to estimate the electronic energies. The energies were verified against different choices of basis sets. The highest methodology used was MP2, and the largest basis set used was aug-cc-pVDZ, which gave an enthalpy difference between the *gauche* and *anti* conformers of ΔH = 0.086 eV (1.985 kcal/mol), after zero-point energy correction. Our calculations also match with previous work[37] where the computations were performed at the MP2/6-311++G(d, p) level of theory and yielded a value of 0.091 eV (2.099 kcal/mol). These values are approximately 15% higher than the experimentally determined value of 1.68 kcal/mol found by infrared absorption measurements performed in a gas cell.[38] We note that the *gauche* conformer exists as *gauche*$^+$ and *gauche*$^-$, which are mirror images of one another and have the same enthalpy. For the theoretical calculation, they are considered as two separate dynamic equilibria with the *anti* conformer. Since the CEI technique cannot distinguish between *gauche*$^+$ and *gauche*$^-$, we therefore multiply the theoretically calculated *gauche* to *anti* ratio by a factor of 2 to account for the two types of the *gauche* conformer.

ASSOCIATED CONTENT

Supporting Information

The Supporting Information is available free of charge at https://pubs.acs.org/doi/10.1021/acs.jpclett.0c02959.

Experimental details and momentum reconstruction, subtraction of sequential events using native frames method, and CES for concerted breakup channel $C_2H_4^+ + Br^+ + Br^+$ (PDF)

AUTHOR INFORMATION

Corresponding Authors

Daniel Rolles − *J.R. Macdonald Laboratory, Department of Physics, Kansas State University, Manhattan, Kansas 66506, United States;* orcid.org/0000-0002-3965-3477; Email: rolles@phys.ksu.edu

Shashank Pathak − *J.R. Macdonald Laboratory, Department of Physics, Kansas State University, Manhattan, Kansas 66506, United States;* orcid.org/0000-0002-7916-0191; Email: shashankp@phys.ksu.edu

https://dx.doi.org/10.1021/acs.jpclett.0c02959
J. Phys. Chem. Lett. 2020, 11, 10205−10211

Authors

Razib Obaid − *Department of Physics, University of Connecticut, Storrs, Connecticut 06269, United States*

Surjendu Bhattacharyya − *J.R. Macdonald Laboratory, Department of Physics, Kansas State University, Manhattan, Kansas 66506, United States;* orcid.org/0000-0001-7107-8006

Johannes Bürger − *Department of Physics, Ludwig Maximilian University of Munich, Munich 80539, Germany*

Xiang Li − *J.R. Macdonald Laboratory, Department of Physics, Kansas State University, Manhattan, Kansas 66506, United States*

Jan Tross − *J.R. Macdonald Laboratory, Department of Physics, Kansas State University, Manhattan, Kansas 66506, United States*

Travis Severt − *J.R. Macdonald Laboratory, Department of Physics, Kansas State University, Manhattan, Kansas 66506, United States*

Brandin Davis − *Department of Physics, University of Connecticut, Storrs, Connecticut 06269, United States*

René C. Bilodeau − *Department of Physics, University of Connecticut, Storrs, Connecticut 06269, United States; Advanced Light Source, Lawrence Berkeley National Laboratory, Berkeley, California 94720, United States*

Carlos A. Trallero-Herrero − *Department of Physics, University of Connecticut, Storrs, Connecticut 06269, United States*

Artem Rudenko − *J.R. Macdonald Laboratory, Department of Physics, Kansas State University, Manhattan, Kansas 66506, United States*

Nora Berrah − *Department of Physics, University of Connecticut, Storrs, Connecticut 06269, United States*

Complete contact information is available at: https://pubs.acs.org/10.1021/acs.jpclett.0c02959

Notes

The authors declare no competing financial interest.

■ ACKNOWLEDGMENTS

This work is supported by the U.S. Geosciences and Biosciences Division, Office of Basic Energy Sciences, Office of Science, U.S. Department of Energy, grant no. DE-FG02-86ER13491 (Kansas group) and DE-SC0012376 (UConn group). S.B. was supported by grant no. DE-SC0020276 from the same funding agency, and J.T. was supported by the National Science Foundation (NSF) grant PHYS-1753324. J.B. acknowledges support through the DAAD RISE program. This research used resources of the Advanced Light Source, which is a DOE Office of Science User Facility under contract no. DE-AC02-05CH11231. We thank the staff of the Advanced Light Source for their hospitality and their help during the beamtime.

■ REFERENCES

(1) IUPAC. *Compendium of Chemical Terminology*, 2nd ed. (the "Gold Book"); 1994.

(2) Boehr, D. D.; Nussinov, R.; Wright, P. E. The role of dynamic conformational ensembles in biomolecular recognition. *Nat. Chem. Biol.* **2009**, *5*, 789−796.

(3) Sweeney, P.; Park, H.; Baumann, M.; Dunlop, J.; Frydman, J.; Kopito, R.; McCampbell, A.; Leblanc, G.; Venkateswaran, A.; Nurmi, A.; et al. Protein misfolding in neurodegenerative diseases: implications and strategies. *Transl. Neurodegener.* **2017**, *6*, 6.

(4) Harrold, M. W. The Influence of Conformational Isomerism on Drug Action and Design. *Am. J. Pharm. Educ.* **1996**, *60*, 192−197.

(5) Kim, M. H.; Shen, L.; Tao, H.; Martinez, T. J.; Suits, A. G. Conformationally Controlled Chemistry: Excited-State Dynamics Dictate Ground-State Reaction. *Science* **2007**, *315*, 1561.

(6) Park, S. T.; Kim, S. K.; Kim, M. S. Observation of conformation-specific pathways in the photodissociation of 1-iodopropane ions. *Nature* **2002**, *415*, 306−308.

(7) Dian, B. C.; Clarkson, J. R.; Zwier, T. S. Direct Measurement of Energy Thresholds to Conformational Isomerization in Tryptamine. *Science* **2004**, *303*, 1169−1173.

(8) Dian, B. C.; Brown, G. G.; Douglass, K. O.; Pate, B. H. Measuring Picosecond Isomerization Kinetics via Broadband Microwave Spectroscopy. *Science* **2008**, *320*, 924−928.

(9) Chang, Y.-P.; Długołęcki, K.; Küpper, J.; Rösch, D.; Wild, D.; Willitsch, S. Specific Chemical Reactivities of Spatially Separated 3-Aminophenol Conformers with Cold Ca^+ Ions. *Science* **2013**, *342*, 98−101.

(10) Wilkin, K. J.; Parrish, R. M.; Yang, J.; Wolf, T. J. A.; Nunes, J. P. F.; Guehr, M.; Li, R.; Shen, X.; Zheng, Q.; Wang, X.; et al. Diffractive imaging of dissociation and ground-state dynamics in a complex molecule. *Phys. Rev. A: At., Mol., Opt. Phys.* **2019**, *100*, No. 023402.

(11) Vager, Z.; Naaman, R.; Kanter, E. P. Coulomb Explosion Imaging of Small Molecules. *Science* **1989**, *244*, 426−431.

(12) Pitzer, M.; Kunitski, M.; Johnson, A. S.; Jahnke, T.; Sann, H.; Sturm, F.; Schmidt, L. P. H.; Schmidt-Böcking, H.; Dörner, R.; Stohner, J.; et al. Direct Determination of Absolute Molecular Stereochemistry in Gas Phase by Coulomb Explosion Imaging. *Science* **2013**, *341*, 1096−1100.

(13) Pitzer, M.; Kastirke, G.; Kunitski, M.; Jahnke, T.; Bauer, T.; Goihl, C.; Trinter, F.; Schober, C.; Henrichs, K.; Becht, J.; et al. Absolute Configuration from Different Multifragmentation Pathways in Light-Induced Coulomb Explosion Imaging. *ChemPhysChem* **2016**, *17*, 2465−2472.

(14) Hishikawa, A.; Matsuda, A.; Fushitani, M.; Takahashi, E. J. Visualizing Recurrently Migrating Hydrogen in Acetylene Dication by Intense Ultrashort Laser Pulses. *Phys. Rev. Lett.* **2007**, *99*, 258302.

(15) Christensen, L.; Nielsen, J. H.; Brandt, C. B.; Madsen, C. B.; Madsen, L. B.; Slater, C. S.; Lauer, A.; Brouard, M.; Johansson, M. P.; Shepperson, B.; et al. Dynamic Stark Control of Torsional Motion by a Pair of Laser Pulses. *Phys. Rev. Lett.* **2014**, *113*, No. 073005.

(16) Ibrahim, H.; Wales, B.; Beaulieu, S.; Schmidt, B. E.; Thiré, N.; Fowe, E. P.; Bisson, É.; Hebeisen, C. T.; Wanie, V.; Giguére, M.; et al. Tabletop imaging of structural evolutions in chemical reactions demonstrated for the acetylene cation. *Nat. Commun.* **2014**, *5*, 4422.

(17) Burt, M.; Amini, K.; Lee, J. W. L.; Christiansen, L.; Johansen, R. R.; Kobayashi, Y.; Pickering, J. D.; Vallance, C.; Brouard, M.; Stapelfeldt, H. Communication: Gas-phase structural isomer identification by Coulomb explosion of aligned molecules. *J. Chem. Phys.* **2018**, *148*, No. 091102.

(18) Kling, N. G.; Díaz-Tendero, S.; Obaid, R.; Disla, M. R.; Xiong, H.; Sundberg, M.; Khosravi, S. D.; Davino, M.; Drach, P.; Carroll, A. M.; et al. Time-resolved molecular dynamics of single and double hydrogen migration in ethanol. *Nat. Commun.* **2019**, *10*, 2813.

(19) McDonnell, M.; LaForge, A. C.; Reino-González, J.; Disla, M.; Kling, N. G.; Mishra, D.; Obaid, R.; Sundberg, M.; Svoboda, V.; Díaz-Tendero, S.; et al. Ultrafast Laser-Induced Isomerization Dynamics in Acetonitrile. *J. Phys. Chem. Lett.* **2020**, *11*, 6724−6729.

(20) Ablikim, U.; Bomme, C.; Xiong, H.; Savelyev, E.; Obaid, R.; Kaderiya, B.; Augustin, S.; Schnorr, K.; Dumitriu, I.; Osipov, T.; et al. Identification of absolute geometries of cis and trans molecular isomers by Coulomb Explosion Imaging. *Sci. Rep.* **2016**, *6*, 38202.

(21) Ablikim, U.; Bomme, C.; Savelyev, E.; Xiong, H.; Kushawaha, R.; Boll, R.; Amini, K.; Osipov, T.; Kilcoyne, D.; Rudenko, A.; et al. Isomer-dependent fragmentation dynamics of inner-shell photoionized difluoroiodobenzene. *Phys. Chem. Chem. Phys.* **2017**, *19*, 13419−13431.

(22) Liekhus-Schmaltz, C. E.; Tenney, I.; Osipov, T.; Sanchez-Gonzalez, A.; Berrah, N.; Boll, R.; Bomme, C.; Bostedt, C.; Bozek, J.

D.; Carron, S.; et al. Ultrafast isomerization initiated by X-ray core ionization. *Nat. Commun.* **2015**, *6*, 8199.
(23) Christiansen, C. J.; Francisco, J. S. Atmospheric Oxidation Mechanism of 1,2-Dibromoethane. *J. Phys. Chem. A* **2009**, *113*, 7189−7204.
(24) Hsieh, S.; Eland, J. H. D. Reaction dynamics of three-body dissociations in triatomic molecules from single-photon double ionization studied by a time- and position-sensitive coincidence method. *J. Phys. B: At., Mol. Opt. Phys.* **1997**, *30*, 4515−4534.
(25) Neumann, N.; Hant, D.; Schmidt, L. P. H.; Titze, J.; Jahnke, T.; Czasch, A.; Schöffler, M. S.; Kreidi, K.; Jagutzki, O.; Schmidt-Böcking, H.; et al. Fragmentation Dynamics of CO_2^{3+} Investigated by Multiple Electron Capture in Collisions with Slow Highly Charged Ions. *Phys. Rev. Lett.* **2010**, *104*, 103201.
(26) Maul, C.; Gericke, K.-H. Photo induced three body decay. *Int. Rev. Phys. Chem.* **1997**, *16*, 1−79.
(27) Hu, X.; Peng, Y.; Zhu, X.; Yan, S.; Liu, L.; Feng, W.; Guo, D.; Gao, Y.; Zhang, S.; Zhao, D.; et al. Breakdown of the Coulomb-explosion imaging technique induced by the ultrafast rotation of fragments. *Phys. Rev. A: At., Mol., Opt. Phys.* **2020**, *101*, No. 012707.
(28) Rajput, J.; Severt, T.; Berry, B.; Jochim, B.; Feizollah, P.; Kaderiya, B.; Zohrabi, M.; Ablikim, U.; Ziaee, F.; Raju, P. K.; et al. Native Frames: Disentangling Sequential from Concerted Three-Body Fragmentation. *Phys. Rev. Lett.* **2018**, *120*, 103001.
(29) Eland, J. H. D. The dynamics of three-body dissociations of dications studied by the triple coincidence technique PEPIPICO. *Mol. Phys.* **1987**, *61*, 725−745.
(30) Légaré, F.; Lee, K. F.; Litvinyuk, I. V.; Dooley, P. W.; Wesolowski, S. S.; Bunker, P. R.; Dombi, P.; Krausz, F.; Bandrauk, A. D.; Villeneuve, D. M.; et al. Laser Coulomb-explosion imaging of small molecules. *Phys. Rev. A: At., Mol., Opt. Phys.* **2005**, *71*, No. 013415.
(31) Atkins, P. W.; De Paula, J. *Atkins' Physical Chemistry*; Macmillan Higher Education: 2006.
(32) Frisch, M. J. et al. *Gaussian 09 Rev.*, C.01; Wallingford, CT, 2016.
(33) Maté, B.; Tejeda, G.; Montero, S. Raman spectroscopy of supersonic jets of CO_2: Density, condensation, and translational, rotational, and vibrational temperatures. *J. Chem. Phys.* **1998**, *108*, 2676−2685.
(34) Ablikim, U.; Bomme, C.; Osipov, T.; Xiong, H.; Obaid, R.; Bilodeau, R. C.; Kling, N. G.; Dumitriu, I.; Augustin, S.; Pathak, S.; et al. A coincidence velocity map imaging spectrometer for ions and high-energy electrons to study inner-shell photoionization of gas-phase molecules. *Rev. Sci. Instrum.* **2019**, *90*, No. 055103.
(35) Boo, B. H.; Saito, N.; Suzuki, I. H.; Koyano, I. Dissociation processes of core-excited CBr4 involving the Br(3d, 3p, 3s) and C(1s) inner-shells in the range 50−460 eV. *J. Electron Spectrosc. Relat. Phenom.* **2002**, *123*, 73−84.
(36) Chai, J.-D.; Head-Gordon, M. Long-range corrected hybrid density functionals with damped atom−atom dispersion corrections. *Phys. Chem. Chem. Phys.* **2008**, *10*, 6615−6620.
(37) Sreeruttun, R. K.; Ramasami, P. Conformational behaviour of 1,2-dichloroethane and 1,2-dibromoethane: 1H-NMR, IR, refractive index and theoretical studies. *Phys. Chem. Liq.* **2006**, *44*, 315−328.
(38) Tanabe, K. Calculation of infrared band intensities and determination of energy differences of rotational isomers of 1,2-dichloro-, 1,2-dibromo- and 1-chloro-2-bromoethane. *Spectrochim. Acta Part A: Mol. Spectrosc.* **1972**, *28*, 407−424.

https://dx.doi.org/10.1021/acs.jpclett.0c02959
J. Phys. Chem. Lett. 2020, 11, 10205−10211

4.5 Native frames analysis for separating *sequential* and *concerted* breakup events post photoionization of dibromoethane

To gain insights about the geometry of molecules from 3-body fragmentation, we rely on concerted breakup events. However, as discussed in the previous section, the coincidence channel $C_2H_4^+ + {}^{81}Br^+ + {}^{81}Br^+$ has a fair contribution from sequential fragmentation. This section describes the details of the method adopted to separate the contribution of *sequential* and *concerted* breakup pathways. Parts of this section are adapted from the supporting information [144] of the publication shown in the last section.

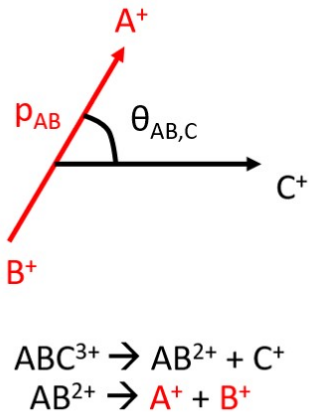

Figure 4.9: *A schematic representation of the relative angle and momenta for a generic 3-body sequential breakup. The black arrow and red arrow represent the first and second step, respectively (Adapted from [144]).*

One of the main ideas of the native frames method [142, 143] is to analyze each fragmentation step in its respective center-of-mass (c.o.m.) frame, i.e. its native frame. This is accomplished by using the conjugate momenta derived from Jacobi coordinates associated with each fragmentation step. To be specific, for a sequential breakup of type $ABC^{3+} \rightarrow AB^{2+} + C^+$ as a first step, and $AB^{2+} \rightarrow A^+ + B^+$ as second step, the first step is analyzed

in the c.o.m. frame of ABC^{3+}, and the second step is analyzed in the c.o.m. frame of AB^{2+}. If the intermediate fragment AB^{2+} rotates with a lifetime longer than its rotation period and in the final fragmentation plane, a uniform distribution of the angle $\theta_{AB,C}$ is expected, where $\theta_{AB,C}$ is the relative direction of the unimolecular dissociation of AB^{2+} with respect to the emission direction of C^+ (as shown in Fig 4.9). In Fig. 4.9, the red arrow represent the second step breakup and the black arrow represents first step breakup. From the analysis in the native frames, we can also calculate the kinetic energy release (KER) of the second step, denoted by KER_{AB}. KER_{AB} frequently helps in identifying metastable states of the intermediate fragment [142]. The second step KER (KER_{AB}) is defined as,

$$KER_{AB} = \frac{p_{AB}^2}{2\mu_{AB}} \tag{4.1}$$

where p_{AB} is the relative momentum and μ_{AB} is the reduced mass of A^+ and B^+ fragments. In the next step, all 3-body fragmentation events in the channel $A^+ + B^+ + C^+$ are plotted as a function of KER_{AB} and $\theta_{AB,C}$. In this plot, the sequential fragmentation proceeding through the AB^{2+} intermediate can be clearly identified as a uniform angular distribution in the angle $\theta_{AB,C}$. This process is then repeated for different intermediate fragments (e.g. BC^{2+} or AC^{2+}) to identify events corresponding to sequential breakup with those intermediates.

Figure 4.10 shows the results of the native frames analysis for the case of the $C_2H_4^+ + {}^{81}Br^+ + {}^{81}Br^+$ fragmentation channel in EDB. All 3-body fragmentation events in the $C_2H_4^+ + {}^{81}Br^+ + {}^{81}Br^+$ breakup channel are plotted as a function of KER_{AB} and $\theta_{AB,C}$ where AB^{2+} and C^+ are the ions formed in the first step of sequential fragmentation. Figure 4.10(a) shows the plot for the intermediate $AB = (C_2H_4{}^{81}Br)^{2+}$ and $C = {}^{81}Br^+$. The uniform distribution in angle $\theta_{AB,C}$ can be clearly seen (highlighted by the white arrow), which corresponds to the sequential events with the intermediate $(C_2H_4{}^{81}Br)^{2+}$. Other features in this plot correspond to concerted breakup and sequential breakup via different intermediates. Figure 4.10(b) shows the same data plotted for the intermediate $AB = ({}^{81}Br{}^{81}Br)^{2+}$ and C

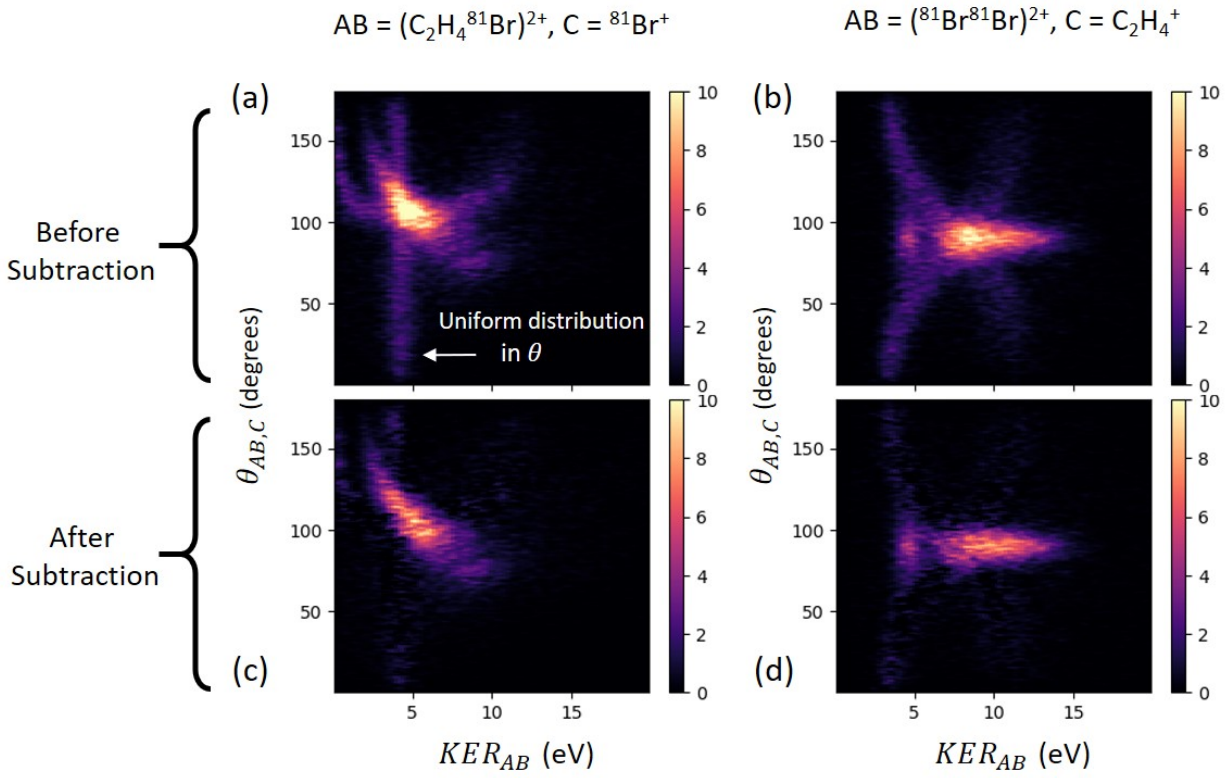

Figure 4.10: *Total events in the 3-body coincidence channel, $C_2H_4^+ + {}^{81}Br^+ + {}^{81}Br^+$, plotted as a function of KER_{AB} and $\theta_{AB,C}$ for two different choices of AB: (a) AB = $(C_2H_4{}^{81}Br)^{2+}$, C = $^{81}Br^+$, (b) AB = $(^{81}Br^{81}Br)^{2+}$, C $C_2H_4^+$ (Adapted from [144]).*

$= C_2H_4^+$. One can easily conclude given the geometry of the molecule that the intermediate chosen in this case is very unlikely to be the intermediate in a sequential breakup since the two bromine atoms are not directly bonded to each other. As expected, the plot does not show a uniform distribution over all angles, indicating no contribution from sequential fragmentation with a $(^{81}Br^{81}Br)^{2+}$ intermediate. Nevertheless, Fig. 4.10(b) is useful for separating the contributions from anti and gauche concerted breakup events, which can be seen as two clearly separate spots in this representation and each of which can thus be easily selected using a rectangular region-of-interest (ROI) (discussed in section 4.4).

To subtract the sequential breakup events in order to retrieve the concerted breakup yield for anti and gauche conformers, the native frames method exploits the uniform distribution

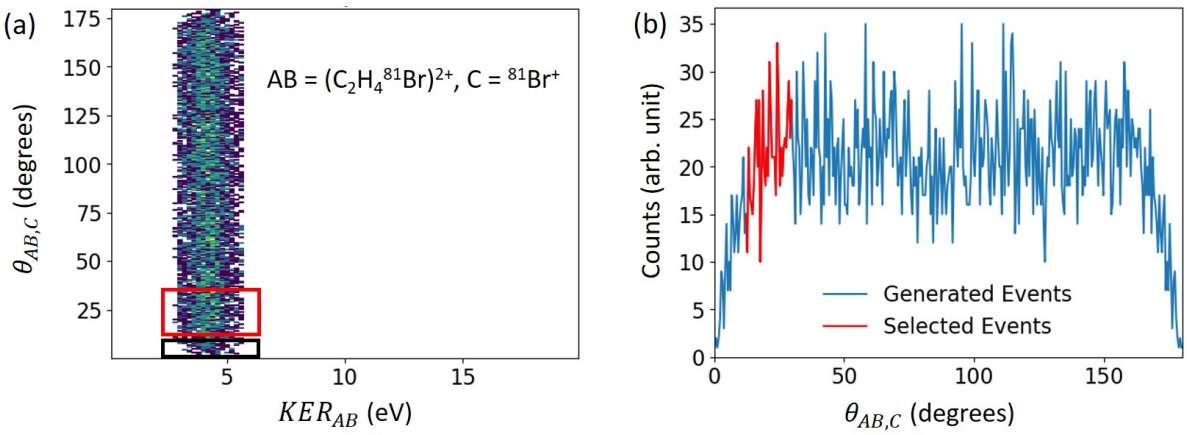

Figure 4.11: *Generated uniformly distributed sequential events (a) KER_{AB} vs $\theta_{AB,C}$ plot showing the uniformly distributed sequential events and the region of interest (ROI) used for generating the events (red for reconstructing equivalent events and black for reconstructing dips), (b) Projection of generated events onto theta.*

of events over $\theta_{AB,C}$ in the KER_{AB} vs $\theta_{AB,C}$ plot. We choose only that part of the data in Fig. 4.10(a) where the events from the sequential breakup are clearly separated from the other contributions (in this case, we chose the range of $\theta_{AB,C}$ = [10,30]). Additional events for the remaining $\theta_{AB,C}$ range are then generated by duplicating the data from the chosen range and randomly assigning a value for $\theta_{AB,C}$ to each event. We thus generate a uniform distribution of events in $\theta_{AB,C}$ while preserving the statistical fluctuations in the data. This is shown in Fig. 4.11(a) and (b). The red box shown in panel (a) corresponds to the events chosen for generating the uniform distribution, while the black box represents the "dip" which is replicated for angles close to 180 degrees [143]. Panel (b) shows the projection onto angle $\theta_{AB,C}$. The generated data is then subtracted from the distribution of events in Fig. 4.10(a) in order to separate out the distribution of concerted events in the region where they strongly overlap with sequential events. Figures 4.10(c) and (d) show the resulting plots after subtracting the sequential breakup events from panels 4.10(a) and (b). Some of the weak structures which appear after subtraction are due to the "leftover" sequential events which are not statistically significant, which is verified by integrating the

yield around the weaker structures.

The concerted breakup distributions can also be plotted as Newton plots to verify the procedure. Figure 4.12(a) shows all events in the $C_2H_4^+ + {}^{81}Br^+ + {}^{81}Br^+$ breakup channel. Figure 4.12(b)and (c) show the resulting Newton plots containing only the sequential events (generated using the native frames method) with $^{81}Br^+$ emitted in the first step and the $(C_2H_4{}^{81}Br)^{2+}$ intermediate breaking up as a second step. As discussed in section 4.4, the semi-circular ring in Fig. 4.12(b) is a signature of the intermediate fragment $(C_2H_4{}^{81}Br)^{2+}$ rotating with respect to the $^{81}Br^+$ fragment (represented by the black arrow), which is emitted in the first step of the sequential breakup. The difference between Fig. 4.12(b) and (c) is that the former is plotted using those $^{81}Br^+$ as reference ions that are emitted in the first step of the sequential breakup (as identified by the native frames method), while the latter is plotted with those $^{81}Br^+$ as a reference that are emitted in second step of sequential breakup. Figure 4.12(d) shows only the "concerted" events, after subtracting the "sequential" events generated using the native frames method.

Another representation which is often used to identify sequential and concerted fragmentation pathways, and also highlights the energy sharing between the fragments, is the Dalitz plot [140, 143, 145]. These representation are also often used in the interpretation of molecular geometries prior to dissociation. For the coincidence channel, $C_2H_4^+ + {}^{81}Br^+ + {}^{81}Br^+$, the Dalitz plot shown in Fig. 4.13 is generated by plotting the fraction of energy carried by the $C_2H_4^+$ ion along the y-axis and the difference in the fraction of energy between the two $^{81}Br^+$ ions along the x-axis. Figure 4.13(a) shows all events in the coincidence channel. The symbols $\epsilon 1$, $\epsilon 2$ and $\epsilon 3$ in x and y axis labels represents kinetic energy of $C_2H_4^+$, $^{81}Br^+$ and $^{81}Br^+$ divided by the total kinetic energy release. Figures 4.13(b) and (c) show the sequential breakup events with the intermediate $(C_2H_4{}^{81}Br)^{2+}$ (separated by using Native frames method). This unique signature with a linear distribution is a key feature of sequential fragmentation observed in previous experiments [145–148]. Figure 4.13(d) shows "only concerted events" obtained by subtracting panel (b) and (c) from panel (a). It can

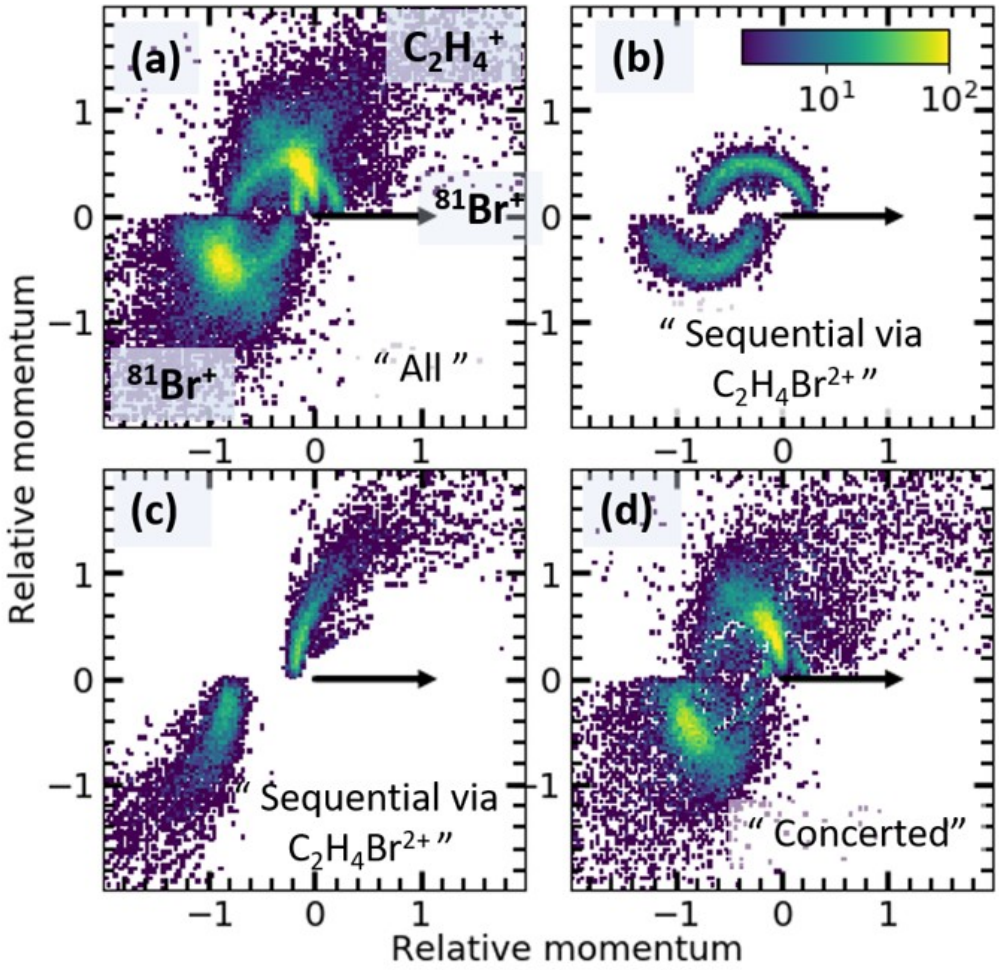

Figure 4.12: *Newton plots showing the normalized relative momenta of each fragment in the 3-body coincidence channel $C_2H_4^+ + {}^{81}Br^+ + {}^{81}Br^+$, with one of the $^{81}Br^+$ fragments chosen as the reference ion plotted along the X axis, the $C_2H_4^+$ fragment in the upper half of the plot, and the other $^{81}Br^+$ fragment in the lower half. (a) All events, (b) Sequential breakup channel with $(C_2H_4{}^{81}Br)^{2+}$ as an intermediate. The events are generated via the native frames method (see text). (c) Sequential breakup channel with $(C_2H_4{}^{81}Br)^{2+}$ as an intermediate, plotted for the incorrect breakup sequence. (d) Concerted breakup channel, obtained by subtracting the events in panel (b) and (c) from all events.*

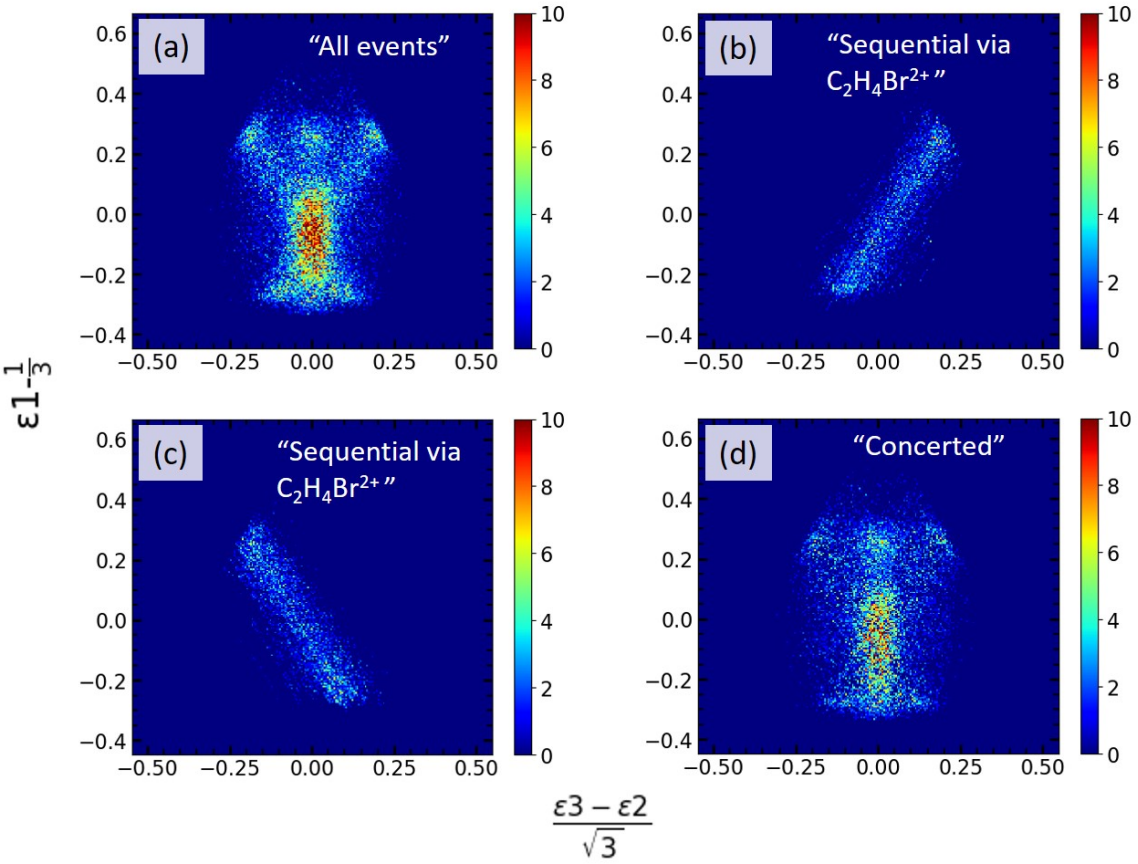

Figure 4.13: *Dalitz plot for the events in coincidence channel, $C_2H_4^+ + {}^{81}Br^+ + {}^{81}Br^+$. The x-axis shows the difference in the fraction of energy between the two $^{81}Br^+$ ions and y-axis shows the fraction of energy carried by the $C_2H_4^+$. (a) All events (b),(c) sequential breakup events with the intermediate $(C_2H_4{}^{81}Br)^{2+}$ (d) Concerted events.*

be seen that the distribution is centered around zero on the x axis as both the $^{81}Br^+$ ions are emitted with similar energies.

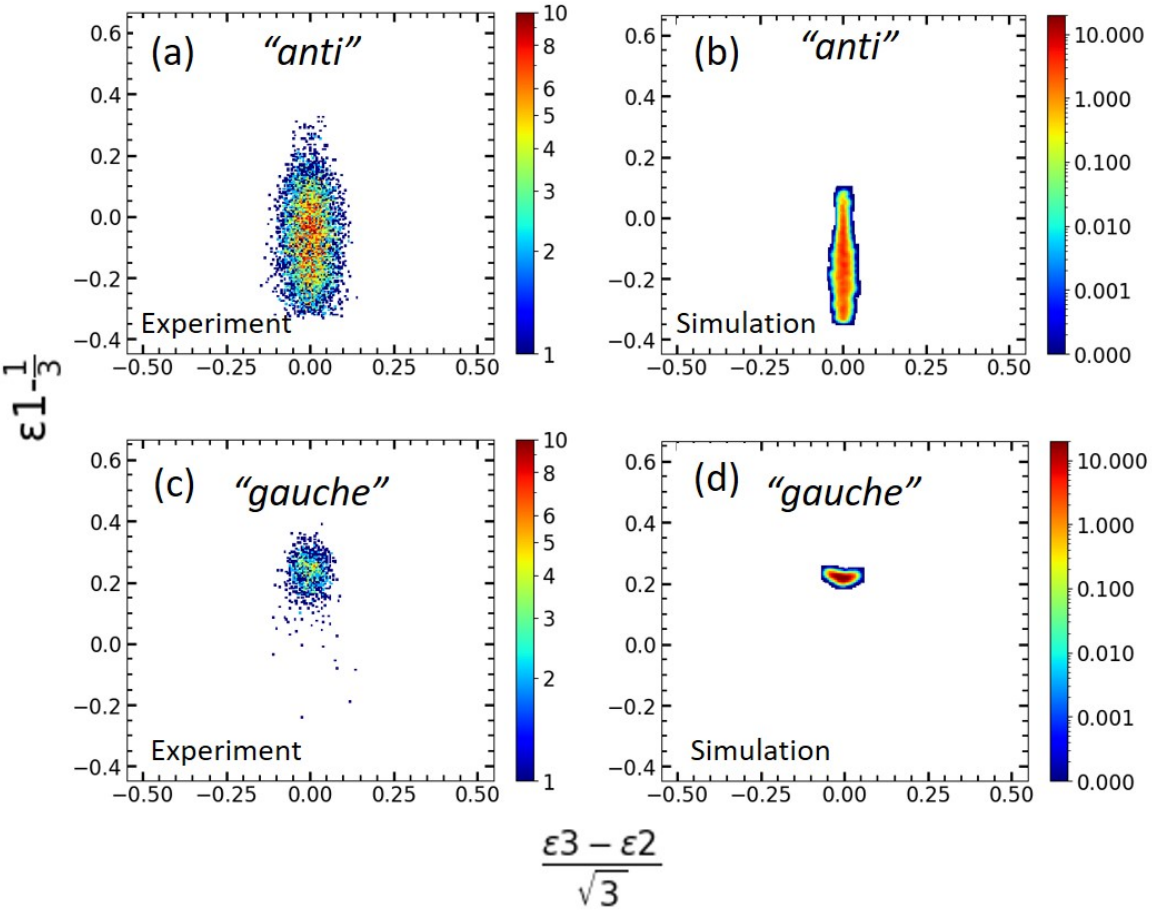

Figure 4.14: *Dalitz plots for the concerted events in coincidence channel* $C_2H_4^+ + {}^{81}Br^+ + {}^{81}Br^+$. *The x axis shows the difference in the fraction of energy between the two* ${}^{81}Br^+$ *ions and the y axis shows the fraction of energy carried by the* $C_2H_4^+$. *(a) Anti conformer, (b) Coulomb simulation results for the 1000 near-equilibrium geometries of anti conformer, (c) Gauche conformer, (d) Coulomb simulation results for the 1000 near-equilibrium geometries of gauche conformer.*

4.6 Exploring differences in experimental signatures for *gauche* and *anti* conformers

In section 4.4, the methodology chosen to disentangle contributions from *gauche* and *anti* conformers, and the differences in the features in Newton plots and kinetic energies of

fragments for *gauche* and *anti* conformers was discussed. In this section, we will discuss how fragmentation of *gauche* and *anti* conformers of EDB can lead to different features in Dalitz plots, Br-Br angular distributions, and energy sharing between the Br fragments. After retrieving concerted breakup events by subtracting sequential breakup events, the contribution from *gauche* and *anti* conformers is found by selecting those events from the KER_{AB} vs $\theta_{AB,C}$ plot, with intermediate AB = $(^{81}Br^{81}Br)^{2+}$ (see section 4.4). Figure 4.14 (a) and (c) show these events plotted in Dalitz plots for *anti* and *gauche* conformers, respectively. It can be seen that the mean value of the y coordinate is higher for *gauche* conformers than for *anti* conformers. Since the y coordinate in our notation of Dalitz plots represents the fraction of kinetic energy acquired by $C_2H_4^+$, it is expected to be higher for the *gauche* conformer based on geometry. In other words, $C_2H_4^+$ acquires higher momentum from a *gauche* conformer than from an *anti* conformer when the molecular ion fragments.

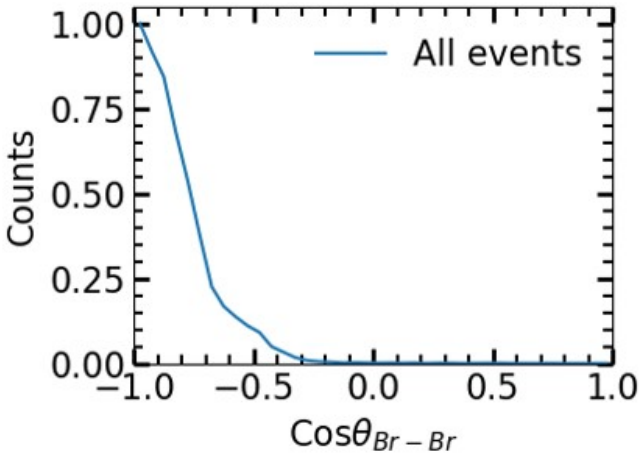

Figure 4.15: *Angle between two $^{81}Br^+$ ions for all events in coincidence channel, $C_2H_4^+$ + $^{81}Br^+$ + $^{81}Br^+$.*

To verify the experimental results simple coulomb simulations were performed for 1000 near-equilibrium geometries for both *gauche* and *anti* conformers. The equations of motion were solved for the free motion of 3 point charges starting at the equilibrium positions of the ionic fragments in the parent molecule. The details related to the simulations are summarized in appendix A. Figure 4.14 (b) and (b) show the simulation results for *anti* and

gauche conformers, respectively. The results match very well with the experimental results. The broad distribution in experimental data is attributed to lower momentum resolution and background due to false coincidence events.

In some of the previous works [126, 129], the method adopted to distinguish between different isomers was to identify the signatures in the angle between different ionic fragments. However, if the yield of one of the two isomers is very small then it may be difficult to distinguish them. In such cases, the current method could be more suitable to differentiate these isomers. Figure 4.15 shows the angle between two $^{81}Br^+$ ions for all events in coincidence channel, $C_2H_4^+ + {}^{81}Br^+ + {}^{81}Br^+$. It can be seen that most of the events show back-to-back emission of the two $^{81}Br^+$ ions, which corresponds to *anti* conformer.

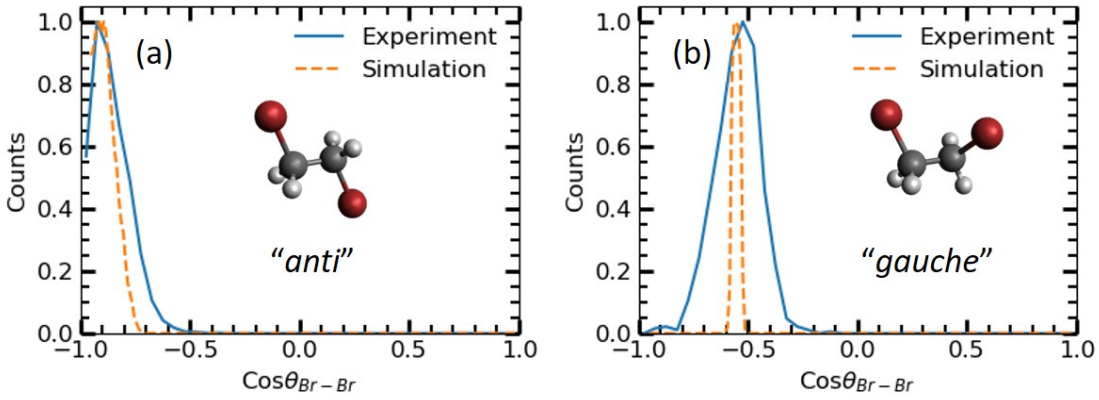

Figure 4.16: *Experimental and simulated cosine of angle between two $^{81}Br^+$ ions for concerted breakup events in coincidence channel $C_2H_4^+ + {}^{81}Br^+ + {}^{81}Br^+$. (a) anti conformer, (b) gauche conformer.*

Figure 4.16 shows the experimental and simulated cosine of angle between two $^{81}Br^+$ ions for *concerted* breakup events for *gauche* and *anti* conformers. The experimental and simulated results agree well, except for a very narrow distribution in the simulated results for the *gauche* conformers. This could be due to the model not being able to capture dominant vibrational modes of the molecule (see appendix A).

Another useful method for visualizing possible breakup pathways is the energy sharing

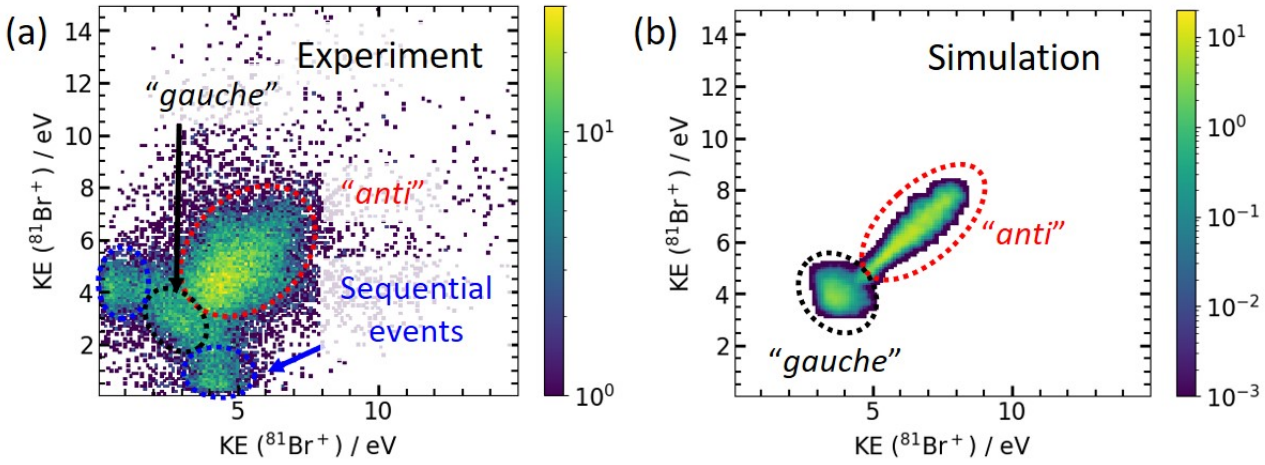

Figure 4.17: *Experimental and simulated energy sharing plot for the two $^{81}Br^+$ ions showing different features corresponding to gauche and anti conformers from concerted breakup. Also shown in the experimental plot (on left) the contribution from sequential breakup events.*

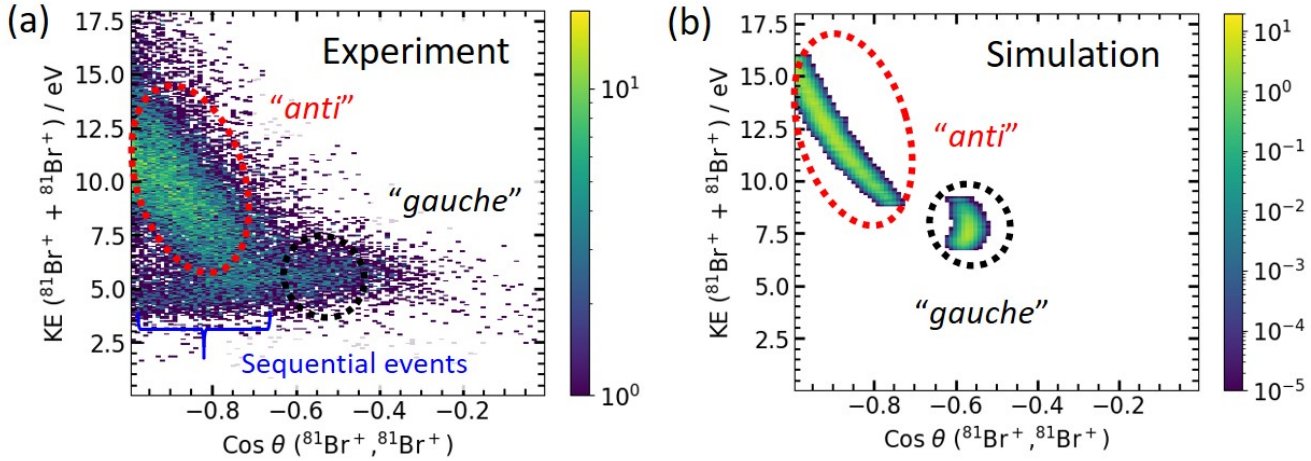

Figure 4.18: *Experimental and simulated plot for the two $^{81}Br^+$ ions showing the two-dimensional histogram of sum of kinetic energies of the $^{81}Br^+$ ions and the cosine of angle between them.*

plot for the two $^{81}Br^{+}$ ions. This is shown in Figure 4.17. The experimental plot shown on the left is labeled with the breakup events corresponding to *gauche* and *anti* conformers. It can be seen that for the *anti* conformer both the $^{81}Br^{+}$ ions are ejected with higher energies than for the *gauche* conformer. The simulated results agree well but cannot fully capture the spread in the distribution.

Figure 4.18 shows the two-dimensional histogram of the sum of kinetic energies of the $^{81}Br^{+}$ ions and the cosine of the angle between them. This type of representation is also often useful in separating different geometries. The simulation results shown in right panel agree well with the experimental data considering that the simulations are performed on the ground state geometries and that the dicationic and tricationic geometries are not considered.

The several different plots shown in this section also highlights the strength of the coincidence momentum imaging method, where contributions from different molecular species or processes can be distinguished in one of the several representations.

4.7 Summary and outlook

In this chapter, we discussed the results of coincidence ion momentum imaging experiments for distinguishing conformational isomers. Specifically, we were able to distinguish and quantify the yield of two conformational isomers of 1,2-dibromoethane, namely *gauche* and *anti*. These conformational isomers only slightly differ in the geometry (by a rotation around a single bond) and co-exist in a fixed ratio at a fixed temperature. With this technique, it is also possible to measure the small change in ratio of these isomers with temperature.

To obtain the insights about the geometry prior to fragmentation, the concerted breakup events were disentangled from sequential breakup events using the native frames method. The relative yield of events from the two conformers determines the relative concentration of the *gauche* and *anti* conformers. In addition, the ratio of *gauche* and *anti* conformers was

measured for different sample temperatures. The expected change in ratio was confirmed by the experimental results. Several visualization techniques such as Newton plots, Dalitz plots and energy sharing plots were also discussed, as these representations can be useful to distinguish different fragmentation channels and pathways depending upon the molecular geometry and breakup pattern.

Future experiments such as time-resolved experiments may benefit from the ability of coincidence momentum imaging to track these subtle molecular changes for certain molecules. For time-resolved experiments, the probe pulse can be from a synchrotron, a free-electron laser, a high-harmonic source or a femtosecond NIR laser. The ratio of sequential fragmentation to concerted fragmentation may increase with the time it takes to charge-up the molecules to highly charged states. Hence, high-photon energy, high photon flux and shorter temporal duration may be good probe parameters for a coincidence ion momentum imaging experiment for gaining information related to geometry. Time-resolved experiments are planned in future on 1,2-dibromoethane and other systems to study the time scales of interconversion between these conformers.

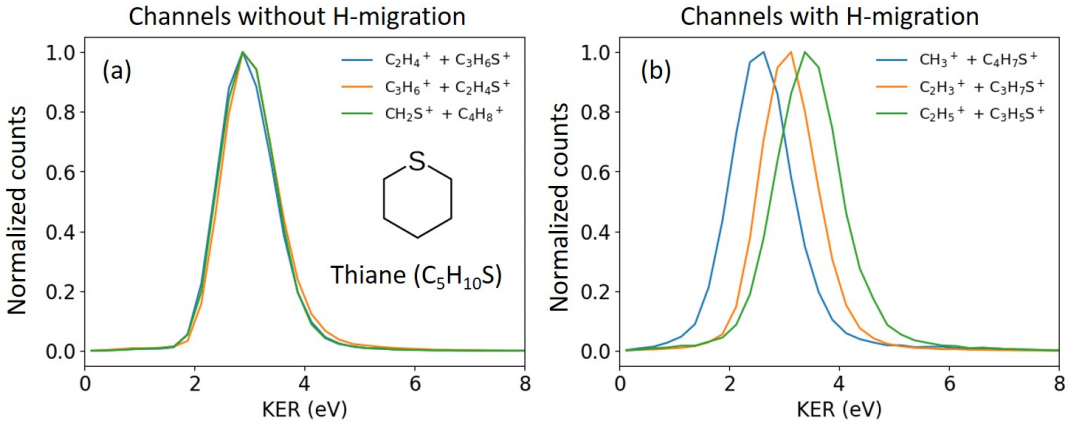

Figure 4.19: *Kinetic energy release (KER) for different two-body fragmentation channels post photoionization of Thiane at 220 eV (a) Channels without hydrogen migration, (b) Channels with hydrogen migration.*

Coincidence momentum imaging is also used to obtain insights about another simple

isomerism called hydrogen migration, where hydrogen moves from one site to another within the molecule. Multiple photofragmentation studies have shown [113, 149–151] that studying different coincidence channel yield and kinetic energy release (KER) gives detailed insights related to hydrogen migration in simple molecules. One such study is to understand the hydrogen migration in the ring molecule thiane ($C_5H_{10}S$) after photoionization by 220 eV photons. It is observed that the hydrogen migrated 2-body fragmentation channels (for example, $CH_3^+ + C_4H_7S^+$) always have higher yield than non-hydrogen-migrated channels ($CH_2^+ + C_4H_8S^+$). Figure 4.19 shows the KER for different two-body fragmentation channels post photoionization of Thiane at 220 eV. It can be seen that the hydrogen migrated channels have different KER spectra while all the non-hydrogen-migrated channels show very similar KER spectra. Detailed analysis related to these features are planned in future, which might reveal the pathways for the hydrogen migration.

With the everyday advancements in temporal and energy resolution of various light sources, there are tremendous opportunities to explore structural dynamics using coincidence momentum imaging. In addition to the great opportunities there are several challenges as well, such as differentiating the molecular structures when no concerted breakup occurs or extracting signatures of molecules from a pool of similar looking photoproducts. Further research in this direction would shed light on the possible ways to overcome these issues.

Chapter 5

Understanding molecular fragmentation and ionization using photoelectron-photoion coincidences

In addition to ions, electrons also possess a wealth of information regarding nuclear dynamics in atoms and molecules. In this chapter, the photoelectron-photoion coincidence (PEPICO) technique is used for studying reaction dynamics and dissociation pathways. Experimental results on thiophenone and furan are discussed, which are obtained by incorporating the PEPICO technique using a synchrotron and a lab-based XUV source.

5.1 Background and motivation

The excitation of the core electrons by x-ray radiation can be site-specific [152–154], meaning that specific atomic species or elements at different molecular sites can be photoionized. Chapter 4 (section 4.2) discusses the site-specific ionization from Br(3d) in the 1,2-dibromoethane molecule. Site-specific studies in molecules are often benefited by the coincident detection of the ionized photoelectrons, Auger electrons, and subsequent ionic frag-

ments that can help infer the dissociation pathways and internal energy of ionic fragments. Figure 5.1 shows the schematic of the relationship between electron kinetic energy and ion internal energy. After the absorption of a photon with energy (hν) higher than the ionization energy (IE) of the molecule, the ion internal energy can be written as E_{int} = hν - IE - E_e + $E_{thermal}$, where E_e is the electron energy and $E_{thermal}$ is the thermal energy of a neutral molecule.

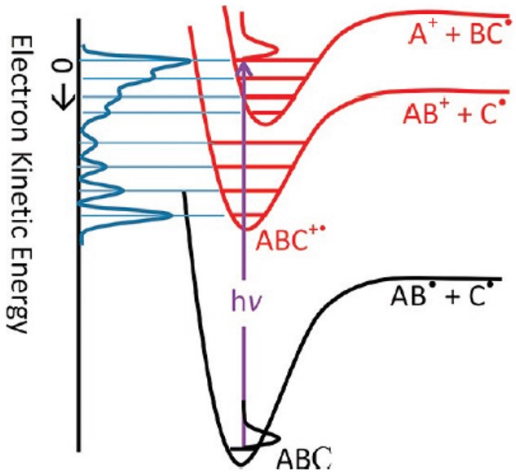

Figure 5.1: *Schematic showing the relationship between electron kinetic energy and ion internal energy (Adapted from [155]).*

Recently, ion-electron coincidence measurements have been used to correlate Auger final states with the fragmentation and isomerization channels. One such example is the study by Bolognesi *et al.* [156], where it is shown that in the 2Br-pyrimidine molecule, preferential production of specific ionic fragments is possible. The probability of formation is dependent on the population of singly-charged valence or inner-valence electronic states. Another study from Kukk *et al.* [157] studied internal energy dependence in x-ray induced fragmentation of thiophene using PEPICO. This study also shows that the probabilities of several dissociating channels are extremely sensitive to the internal energy of the molecule after photoabsorption at 191 eV. Moreover, combining experimental data with theoretical simulations (the self-consistent-charge density-functional tight-binding (SCC-DFTB) method [157]), the

branching ratios of ring-opening isomerization, hydrogen migration, and ring-fragmentation channels are determined. Based on these and other related studies [158–160], the PEPICO technique may also be used to study structural dynamics in complex molecules.

Apart from inner-shell ionization, a few other PEPICO studies [161–163] are also performed using soft x-ray/XUV radiation, probing inner-valence electrons. In particular, Lafosse *et al.* [161] have determined velocity correlations in dissociative photoionization of NO molecules. This study's electron and ion kinetic energy correlations reveal three dissociation limits or reaction paths and their branching ratios.

The studies mentioned above show that the PEPICO method could be useful for gaining information related to reaction pathways in both XUV and x-ray photoionization regimes. Both the ALS-DVMI (see section 2.3.2) and KAMP apparatuses (see section 2.3.1) are capable of measuring ions and electrons in coincidence. In the next two sections, results are shown from the experiments performed using the PEPICO technique combined with the ALS-DVMI and KAMP apparatuses.

5.2 PEPICO study of thiophenone after photoionization at 23 eV

The motivation of this experiment was to disentangle different fragmentation pathways, using PEPICO, after valence/inner-valence ionization of 2(5H)-thiophenone (C_4H_4OS). The experiment was performed at beamline 10.0.1.3 of the Advanced Light Source (ALS) synchrotron situated in the Lawrence Berkeley National Laboratory during the standard ALS multi-bunch top-off mode of operation. The PEPICO experiments were performed using a double-sided VMI setup (ALS-DVMI, see section 2.3.2). The details of the experimental setup and light source are described in detail in chapter 2. Thiophenone (purity ~98%) was commercially purchased from Sigma Aldrich. Thiophenone is a colorless (with a yellow tint) liquid at room temperature and has a very low vapor pressure (<1 Torr at 25 °C).

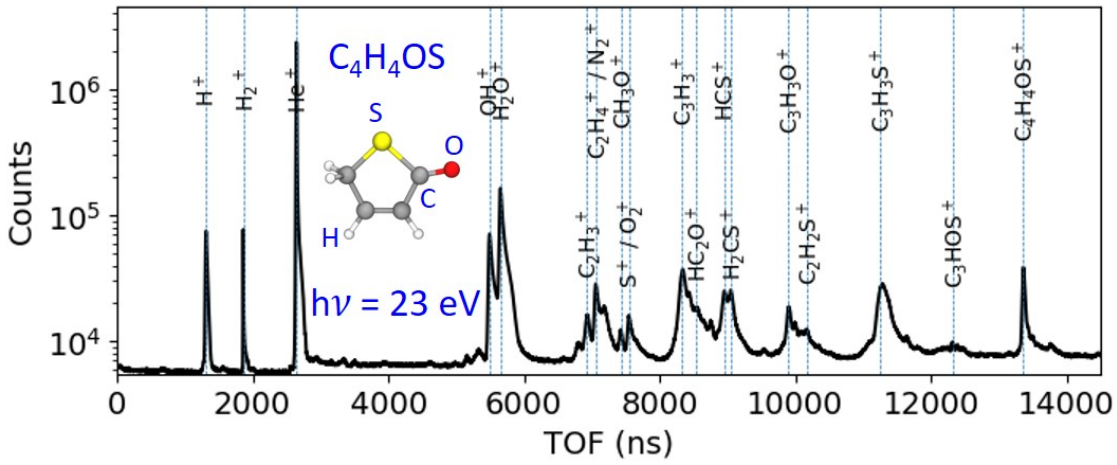

Figure 5.2: *Time-of-flight (TOF) spectrum of thiophenone photoionized at 23 eV and recorded using ALS-DVMI. The equilibrium geometry of thiophenone is also shown.*

It was loaded into a bubbler (∼10-15 ml), degassed using several freeze-pump-thaw cycles, and inserted into the experimental chamber, which is under ultra-high vacuum, using a supersonic expansion through a nozzle 30 μm in diameter. Due to the low vapor pressure of thiophenone, it isn't easy to achieve the required target density in the interaction region for recording data with a good signal-to-noise ratio. To overcome this, helium was used as a carrier gas. Also, the sample delivery system was heated with a positive temperature gradient from the bubbler to the nozzle in order to avoid any sample condensation. The nozzle was kept at a temperature of 105 °C, and the bubbler was at 50 °C. The sample delivery system was allowed to reach equilibrium temperature before recording data. The molecular beam is skimmed using a 500 μm (diameter) skimmer before reaching the interaction region inside the ALS-DVMI spectrometer.

Thiophenone molecules were ionized using a single XUV photon of 23 eV energy. This was chosen to suppress the ionization signal from helium, which has an ionization energy of 24.6 eV. Figure 5.2 shows the time-of-flight (TOF) spectrum for thiophenone ionized by the 23 eV photon beam. The ionization from helium can be seen in the TOF spectrum. One possible explanation could be that the photon energy of 23 eV is at the lower end

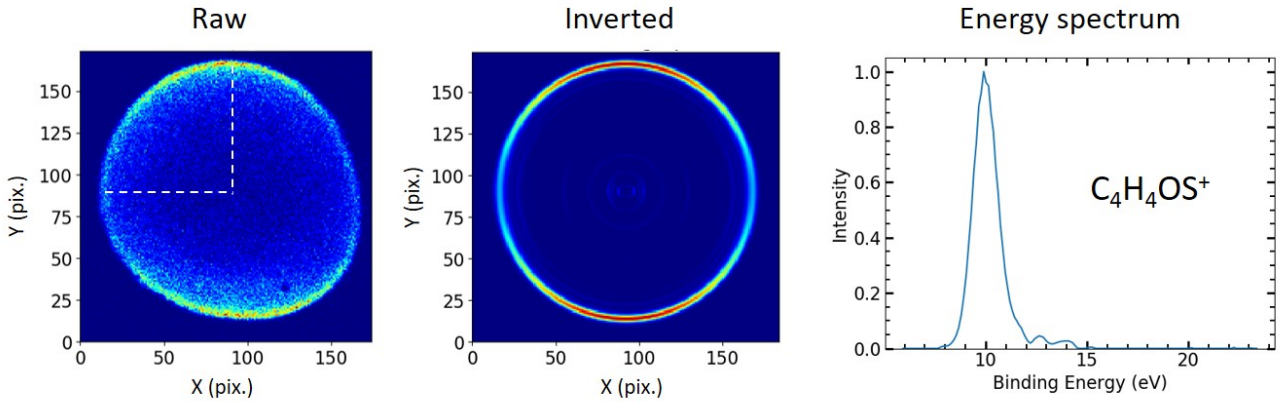

Figure 5.3: *Photoelectron position (raw and inverted) and energy spectrum of singly-charged thiophenone molecule ($C_4H_4OS^+$) after ionization with 23 eV photon energy. The quadrant selected to replicate and circularize the raw image (see text) is shown in white dashed lines.*

of the photon energy range available at beamline 10.0.1.3 [18]. This beamline has a large contribution of second- and third-order photon energies besides the fundamental. These high-energy photons can ionize helium atoms.

For this experiment, double ionization of thiophenone was not observed. This was also confirmed by plotting the photoion-photoion coincidence (PIPICO) map, where no coincidences are observed. The TOF spectrum also does not show a peak corresponding to doubly-ionized thiophenone. Although the double ionization energy is not known for thiophenone, some studies on thiophene and related ring-molecules [164, 165] have measured the double ionization energy to be above $\sim$ 25 eV. The double ionization energy of thiophenone is assumed to be greater than 25 eV since it has a slightly higher single ionization energy ($\sim$ 9.6 eV) than thiophene ($\sim$ 8.8 eV). In the absence of double ionization of thiophenone, each ionization event produces only one charged fragment. Hence, the ionic fragment peaks in the TOF spectrum can be selected to extract information about the electron energies for that dissociation channel. In addition to ion TOF, the ion positions are also gated to reduce the background in the photoelectron position spectrum.

Figure 5.3 shows the photoelectrons recorded in coincidence with singly-charged thio-

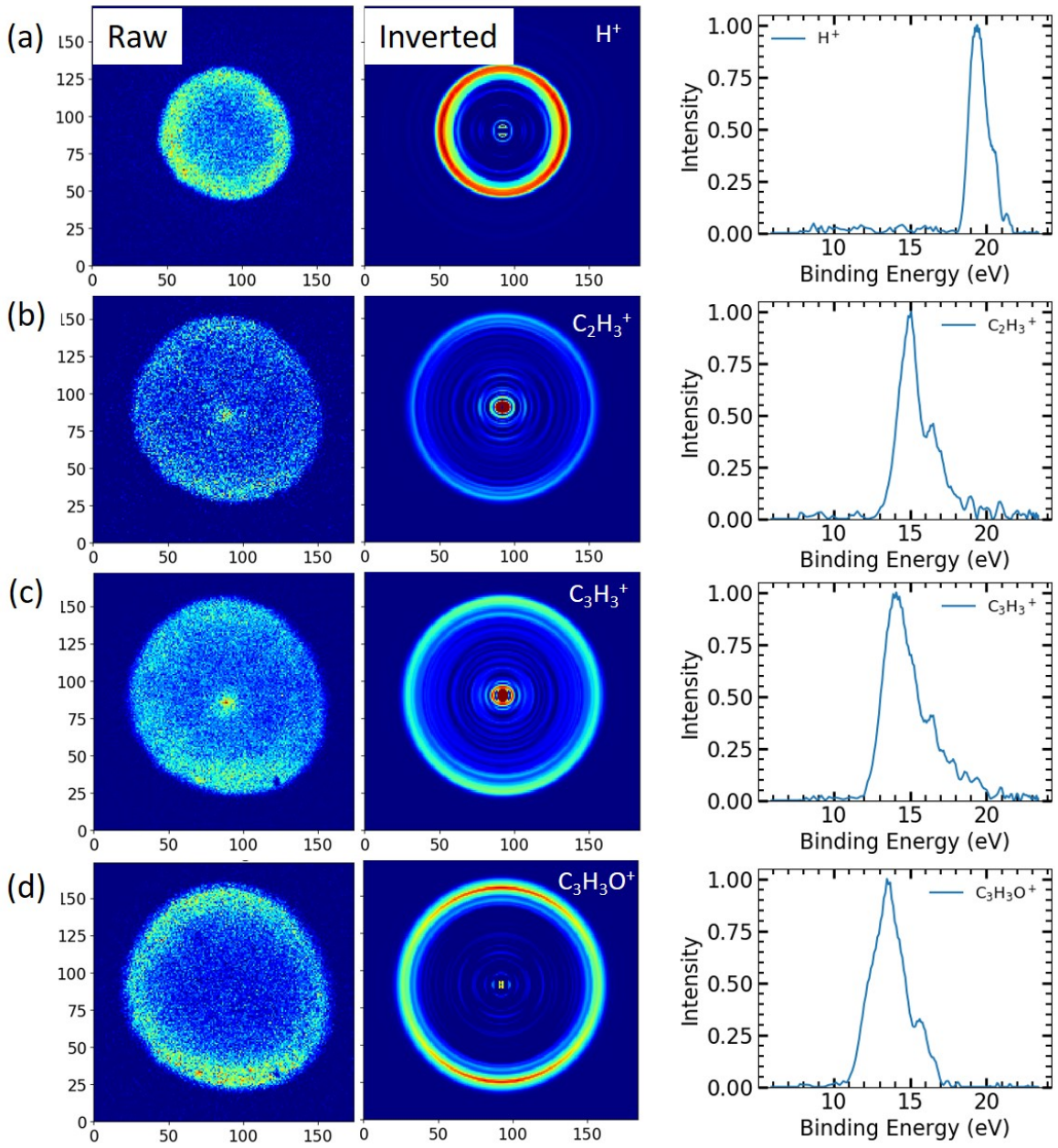

Figure 5.4: *Photoelectron position (raw and inverted) and energy spectrum obtained by gating on different ionic fragments of thiophenone after ionization at 23 eV (a) H^+, (b) $C_2H_3^+$, (c) $C_3H_3^+$, (d) $C_3H_3O^+$.*

phenone molecules ($C_4H_4OS^+$). The photoelectron position spectrum recorded during the experiment (raw position spectrum) shows some distortion due to the imperfect alignment of the spectrometer w.r.t. the detector and/or the stray magnetic field leaking into the spectrometer. To get rid of this distortion, a circularization algorithm [166, 167] can be used on the raw photoelectron position spectrum. Another method, which exploits the cylindrical symmetry of the VMI detection, selects half or a quarter of the position image and replicates it to complete the full image. Once the raw image is circularized, it can be used to generate an Abel-inverted position image by using the inverse Abel transform (see section 2.3.5). The inverted images shown in this section are generated by selecting a quadrant (second quadrant) of the raw image and replicating it to obtain a complete image. After this, a circularization algorithm is used to correct any remaining distortions, thereby generating a circular image, which is then used to generate an Abel-inverted position image by using a pBasex algorithm. The quadrant selected for replicating is marked in the raw image shown in Fig. 5.3. This figure also shows the binding energy spectrum of photoelectrons detected in coincidence with $C_4H_4OS^+$. The binding energy is calculated by subtracting the photoelectron energy (obtained from inverted photoelectron position image) from the photon energy (23 eV).

The photoelectron position image and the binding energy spectrum can be plotted for all the major fragments observed in the TOF spectrum. This is shown in Fig. 5.4 and 5.5. It can be seen that the distribution of binding energy for the fragments ranges from 10 eV to 20 eV. The general trend observed from experimental data shows that the photoelectrons have higher kinetic energy (lower binding energy) for the heavier ionic fragments, although the broad distribution in photoelectron energies can be seen for most of the ionic fragments (or dissociation channels). In principle, based on binding energies, it is possible to assign a dissociation pathway precisely to the location (orbital) of the removal of an electron. For example, one can assign a dissociation channel to the removal of an electron from n_S, n_O or π_{CC} molecular orbitals, which correspond to a lone pair of sulfur, lone pair of oxygen, and

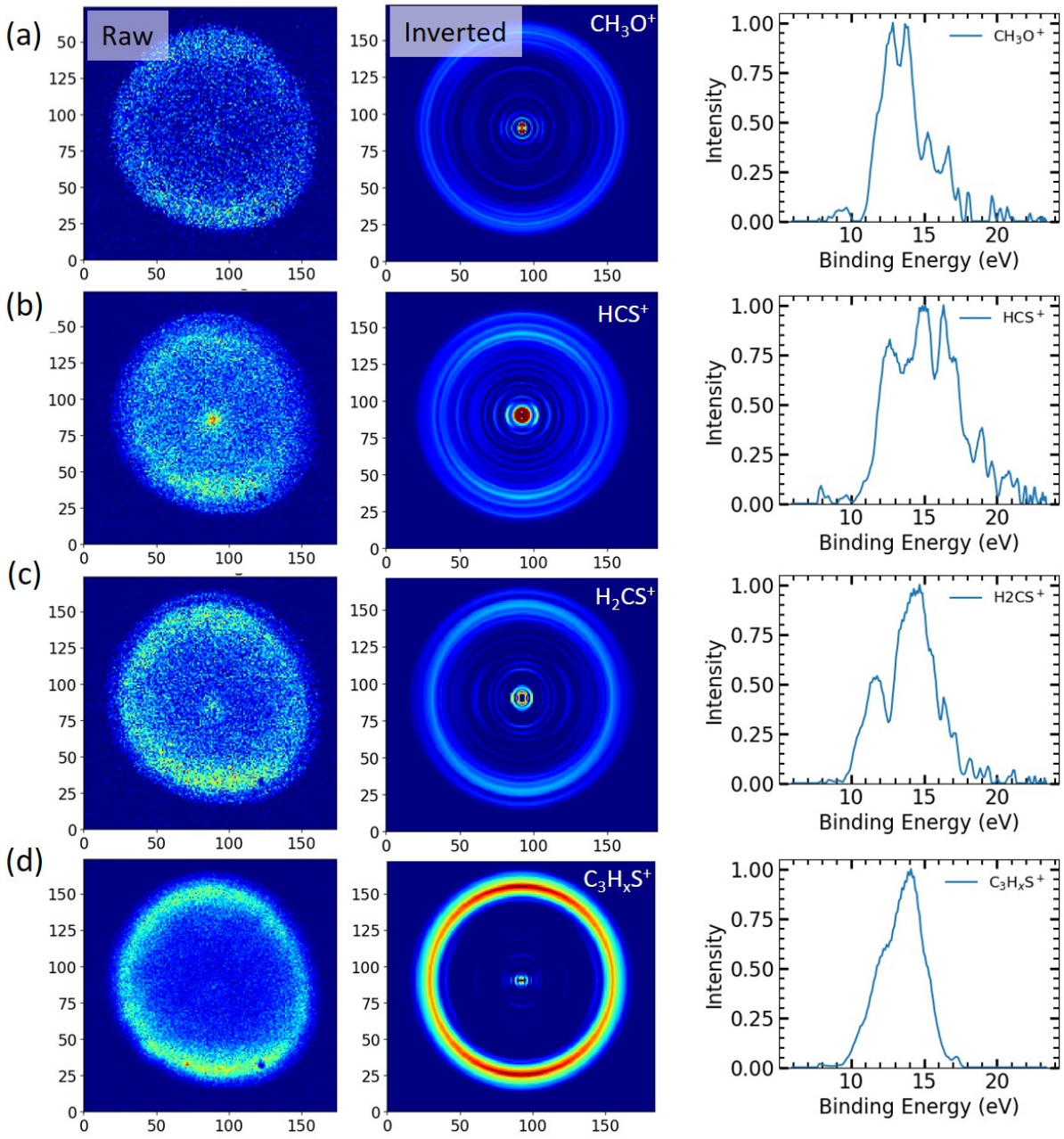

Figure 5.5: *Photoelectron position (raw and inverted) and energy spectrum obtained by gating on different ionic fragments of thiophenone after ionization at 23 eV (a) CH_3O^+, (b) HCS^+, (c) H_2CS^+, (d) $C_3H_xS^+$ (x=3,4).*

Channel	Mass (a.u.)	Normalized yield	Asymmetry parameter (β)
$C_4H_4OS^+$	100	0.93	0.9
$C_3H_4S^+$	72	0.60	0.47
$C_3H_3S^+$	71	0.81	0.32
$C_3H_4O^+$	56	0.36	0.47
$C_3H_3O^+$	55	0.49	0.32
H_2CS^+	46	0.62	0.03
HCS^+	45	0.63	0.42
$C_3H_3^+$	39	1	0.12
CH_3O^+	31	0.23	0.08
$C_2H_3^+$	27	0.35	0.08

Table 5.1: *Normalized yield (w.r.t $C_3H_3^+$) and photoelectron asymmetry parameter (for dominant signal) for major ionic channels after photoionization of thiophenone at 23 eV.*

π orbital of a C-C bond. In reality, however, it can often be difficult to do this as different excited cationic states are usually coupled. The wavepacket, after excitation into one of the cationic states, can often cross over to another state.

Nevertheless, the channel-resolved electron data can help us in getting some valuable insights. For the case of thiophenone, the binding energy distributions (Fig. 5.4 and 5.5) are widely distributed for most of the channels. Apart from binding energies, asymmetry parameter (β) can also be extracted from the inverted photoelectron images shown in Fig. 5.4 and 5.5. A brief description of the asymmetry parameter is given below.

The photoelectron angular distribution resulting from photoionization of state $|i\rangle$ by linearly polarized photons leaving the ion in the state $|j\rangle$ is given by [168]-

$$\frac{d\sigma_{ij}}{d\Omega} = \frac{\sigma_{ij}}{4\pi}[1 + \beta_{ij}P_2(cos\theta)] \tag{5.1}$$

where σ_{ij} is the total photoionization cross-section for $|j\rangle$, β_{ij} is the asymmetry parameter, and θ is the angle between the polarization and photoelectron momentum vector. The parameter β can be negative, positive, or zero. Positive values represent asymmetry along the light polarization direction, while negative values represent asymmetry perpendicular

to the polarization direction, and a value of zero represents isotropic distribution (i.e., no asymmetry). The asymmetry parameter (for the dominant signal) is calculated for the photoelectron spectra shown in Fig. 5.4 and 5.5 and the results are summarized in table 5.1. From table 5.1, it can be seen that the channels leading to the formation of heavier ionic fragments have higher anisotropy (larger asymmetry parameter). The photoelectrons detected in coincidence with the parent thiophenone ion ($C_4H_4OS^+$) have the highest anisotropy in the light polarization direction and have an asymmetry parameter of $\beta = 0.9$.

To compare different dissociation channels, Fig. 5.6 shows the photoelectron energy distributions (converted to binding energy) for major ionic fragments, normalized with the relative yield of each channel. Also, shown in the dashed black line is the binding energy spectrum for thiophenone measured by Chin *et al.* [68] using a helium discharge lamp (He I, 25 meV spectral resolution). From the channel-resolved photoelectron energy spectrum (Fig. 5.6(a)), we observe that - (i) the parent thiophenone ion ($C_4H_4OS^+$) is formed by the removal of an electron mainly from the n_S or n_O orbital (orbital assignments are taken from [68]), (ii) $C_3H_3^+$, which is one of the dominant ionic fragments (see Fig. 5.2), is formed via removal of an electron either from σ_{CC}, π_{CO} or π_{CH_2} orbitals (iii) $C_2H_3^+$, which has lower photoelectron energy (higher binding energy) in comparison to $C_3H_3^+$, is formed via removal of an electron mainly from a π_{CO} or π_{CH_2} orbital.

Figure 5.6(b) shows the sum of all channel-resolved electron spectra shown in Fig. 5.6(a). Also, the spectra from Chin *et al.* [68] and the orbital assignment are plotted for comparison. Since the measurement from Chin *et al.* [68] used a He I lamp with a resolution of 25 meV, the peaks shown in the black dashed curve are well resolved as compared to the blue curve, where the resolution was $\Delta E/E = 0.1$. This resolution was obtained by fitting photoelectrons detected in coincidence with the parent thiophenone ion ($C_4H_4OS^+$). A detailed analysis on the resolution of valence photoelectrons for ALS-DVMI is discussed in the study by Ablikim *et al.* [29]. The peak positions corresponding to the removal of electrons from different orbitals match well between the two experiments. The relative intensities for higher binding

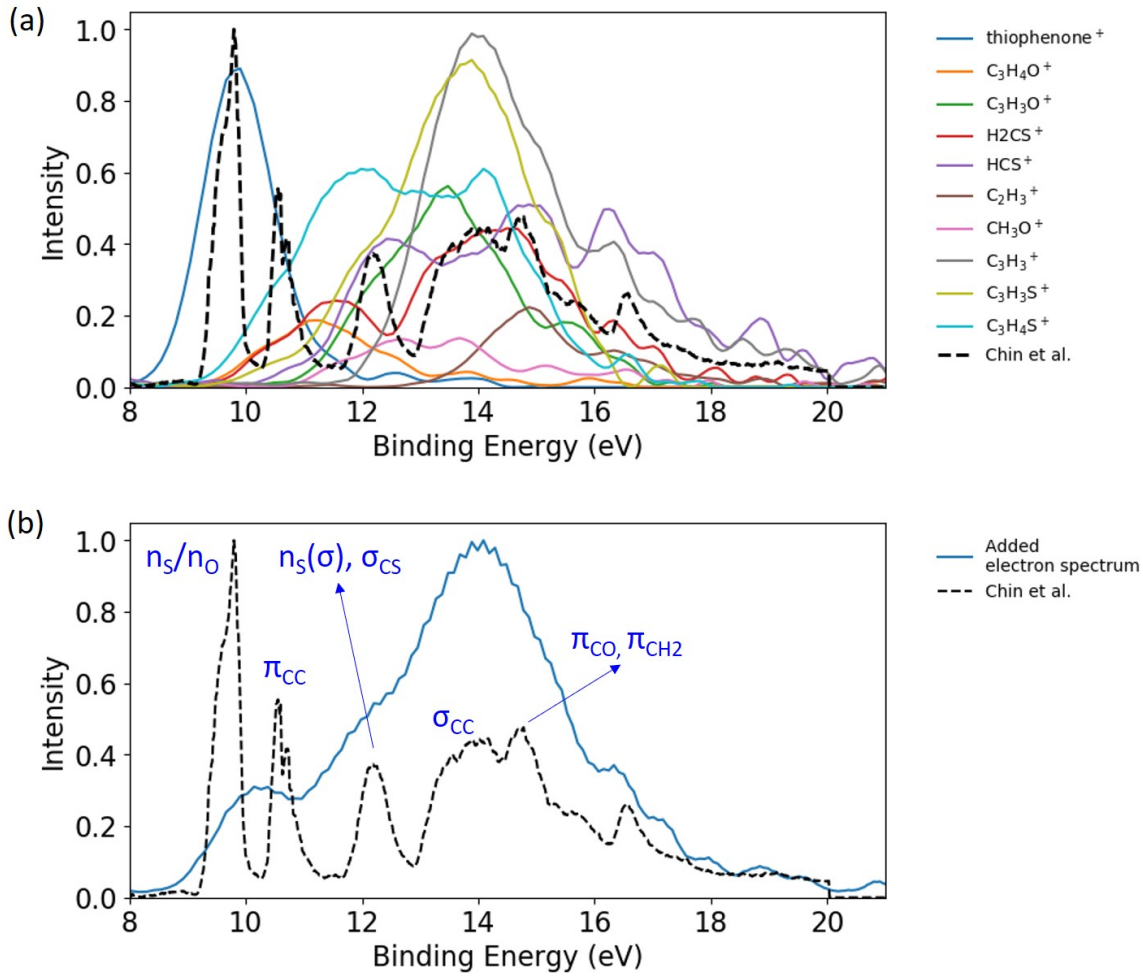

Figure 5.6: *Channel-resolved photoelectron energy spectrum (converted to binding energy) of thiophenone post ionization at 23 eV. The black dashed line is the photoelectron spectrum measure by Chin et al. [68] (a) Photoelectron energy spectra for all major ionic channels normalized w.r.t. relative yields, (b) All major channels from (a) summed together.*

energies for the measurement from Chin *et al.* are likely suppressed due to the transmission of the hemispherical analyzer, which is not the case for VMI photoelectron detection. For ALS-DVMI, we expect the parent thiophenone ions to have a lower detection efficiency as they hit the center of the MCP detector (due to the damage at the center of the ion MCP detector). This could possibly explain the lower intensity of the photoelectron peak at low binding energy in the sum electron spectrum.

5.3 High-harmonic source coupled with KAMP apparatus for PEPICO study of furan

In this section, the extreme ultraviolet (XUV) source combined with a double-sided VMI (KAMP, discussed in section 2.3.1) and some of the preliminary results from the study involving photoionization of a heterocyclic ring molecule (furan, C_4H_4O) is discussed. The commissioning of the KAMP apparatus and combining it with the XUV source was a part of this dissertation and the dissertation by Seyyed Javad Robatjazi [14], Kansas State University. In this section, some of the salient features and capabilities of this setup and the photoionization results from furan are described. Some of the first experiments using this setup to study atoms and small molecules (such as Xe, CO_2, methanol, and ethanol) using the PEPICO technique are described in this dissertation [14].

5.3.1 High-harmonic generation and the semi-classical three-step model

High-harmonic generation (HHG) is the process used for generating sub-femtosecond and highly coherent (both spatial and temporal) light ranging from XUV to x-ray wavelengths [169–173]. XUV and x-ray photon wavelengths are achieved by converting the central wavelength of the laser beam (λ) into its higher harmonics (λ/n, n = odd number) [174]. It is possible to generate high harmonics using gaseous, solid, and liquid samples. HHG sources are also compact and tabletop sources. This is of significant advantage compared to many other XUV and x-ray sources such as synchrotrons and free-electron lasers (FEL). HHG sources are capable of producing attosecond pulses [169], which is extremely useful in studying electron dynamics in molecules (see chapter 1). Such capability was demonstrated for a FEL recently [175, 176] and is available at very few FEL facilities around the world. While HHG sources offer some advantages over synchrotrons and FELs, they have lower photon flux (due to low conversion efficiency) and lack energy tunability, both of which can be achieved

at synchrotrons and FELs relatively easily.

The harmonic spectrum generated using HHG is characterized by a plateau and a sharp cut-off [177, 178]. The cut-off energy for high-harmonics generated from a gas target of ionization energy, I_p, is given by-

$$E_{max} = I_p + 3.17U_p \tag{5.2}$$

where $U_p = I/4\omega^2$ is the ponderomotive energy, I is the input laser intensity, and ω is the frequency.

The three-step model (TSM) provides an intuitive as well as quantitative explanation for the HHG process [177–179]. The first step in this model is ionization. In this step, in the presence of an intense laser field, the electron tunnels through the potential barrier created by the laser electric field. In this model, the ionization is approximated by tunneling, which determines the ionization probability. In the second step, the liberated electron gains kinetic energy (∼50-1000 eV) [169] in the presence of the laser's field. As the field flips its sign, the electron is accelerated back toward the ion. If the electron recombines with the ion, it emits a high-energy photon due to the additional energy acquired by the electron in the acceleration process. With a certain probability, the electron can also re-scatter from the parent ion. The recombination process makes the third step of the TSM.

5.3.2 XUV generation using extreme ultraviolet ultrafast source

The XUV source used in this dissertation, e**X**treme **U**ltraviolet **U**ltrafast **S**ource (XUUS), is a commercial XUV source, designed by KM labs [180]. It is a fiber-based XUV source where an intense laser beam focuses on a hollow-core fiber, filled with a noble gas such as argon or neon. The gas pressure inside the fiber can be precisely controlled using a flow control unit and is usually set between 20-80 Torr. XUV photons with energies ranging from 20 eV to 100 eV can be generated. However, higher photon energies are very sensitive to the

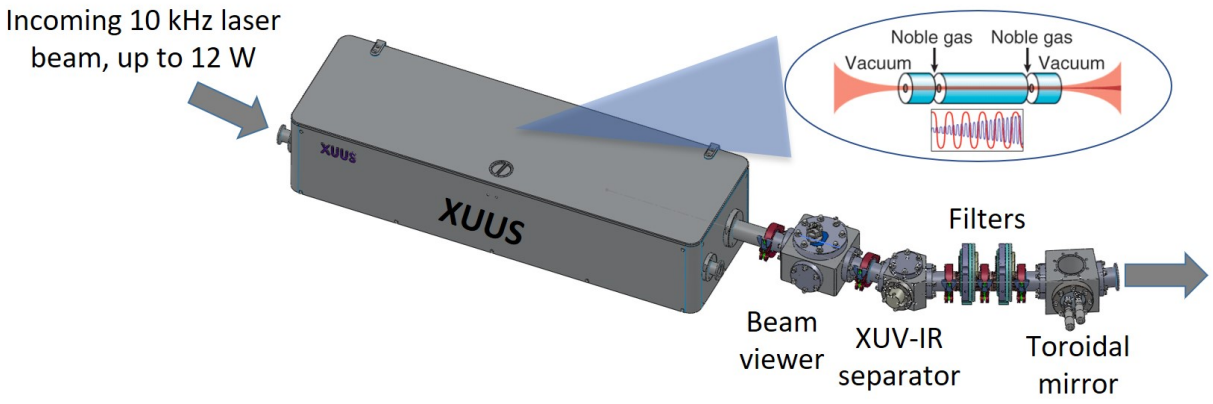

Figure 5.7: *Schematic of a fiber-based XUV source, XUUS. Also shown is the XUV-IR separator module, filters for selecting XUV photon energies and a toroidal mirror for focusing the XUV beam.*

in-coupling laser beam parameters. Small (a few percent) changes in the intensity and the divergence of the laser beam could significantly deteriorate the yield of high-energy photons ($>$ ∼50 eV). Moreover, a large spatial drift can also damage the fiber. To compensate for the spatial drift of the coupling laser beam, a beam stabilization unit (Aligna/Beamlock 4D from TEM Messtechnik) was installed consisting of position-sensitive diodes and actuating mirrors, which compensate for the spatial drift.

Figure 5.7 shows the schematic of the XUUS setup and the hollow-core fiber which sits inside the XUUS box. The hollow-core fiber has an inner diameter of 150 μm. The coupling laser beam is focused inside a hollow-core fiber, which is filled with a noble gas. As the intense laser beam interacts with the gas atoms, XUV radiation is generated. These high-energy XUV photons can be easily absorbed by most of the gases present in the atmosphere. Hence, for the propagation of the XUV beam, the XUV beamline is kept under vacuum (∼10^{-7} Torr). After the XUV is generated, it is separated from the NIR beam using an XUV-IR separator. The XUV-IR separator is coated with a ZrO_2 coating and is placed at 12.5 degrees w.r.t. the incident beam. It reflects the XUV beam and transmits most

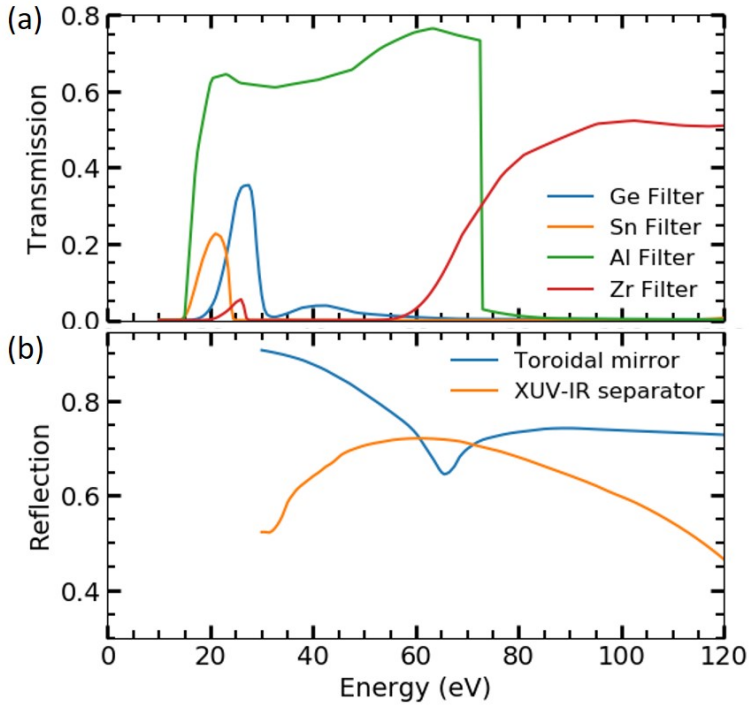

Figure 5.8: *Filter transmission and mirror reflection curves for XUV (a) Filter transmission curves for germanium (Ge), tin (Sn), aluminium (Al), and zirconium (Zr) filters. The thickness of each fiter is 200 nm. (b) XUV reflection for toroidal mirror (Ni, 4 degree incidence) and XUV-IR separator (ZrO_2, 12.5 degree incidence) (values taken from [181, 182]).*

(∼99%) of the NIR beam. Once the XUV beam is reflected, the photon energies can be selected by using aluminum, zirconium, tin, germanium, or any combination of these filters. The thickness of these filters is 200 nm. Figure 5.8(a) shows the transmission of the XUV beam from these filters as a function of photon energy. Figure 5.8(b) shows the reflection of the XUV beam from the XUV-IR separator and the toroidal mirror. The toroidal mirror is coated with a nickel coating and is placed at 4 degrees grazing angle w.r.t. incident beam. It is used to focus the XUV beam.

5.3.3 Photoionization of furan using XUV

In this section, the results from the photoionization of gas-phase furan molecules are discussed. The experiments were performed using a double-sided VMI, KAMP (see section 2.3.1), coupled with an XUV source, XUUS. The laser system used for generating high-harmonics has specifications of 2 mJ energy per pulse, 25 fs temporal width, and 10 kHz repetition rate (see PULSAR in section 2.2.3). Furan (purity >99%) was commercially purchased from Sigma Aldrich. Furan is a colorless liquid at room temperature and has a very high vapor pressure (∼493 Torr at 20 °C). It was loaded into a bubbler (∼10-15 ml), degassed using several freeze-pump-thaw cycles, and inserted into the experimental chamber (KAMP), which was under high vacuum ($\sim 10^{-9}$), using a capillary with 200 μm diameter. Since furan has a high vapor pressure, carrier gas was not required to assist with the sample delivery. The flow of furan was controlled by using a needle valve. The electrons and ions were detected in coincidence using the KAMP apparatus after photoionization with XUV.

Figure 5.9 shows the harmonic spectrum recorded during the experiment. Germanium (Ge) and tin (Sn) filters were used to select the range of harmonics for the photoionization of furan. With the Sn filter, mainly the 13^{th} harmonic (20.4 eV) and very little 15^{th} harmonic (23.5 eV) can be selected (see figure 5.8 and 5.9), while with the Ge filter, the 17^{th} and 19^{th} harmonics (26.7 eV and 29.8 eV) and a small contribution from the 13^{th} and 15^{th} harmonics (20.4 eV and 23.5 eV) can be selected.

Figure 5.10 shows the ion TOF spectra of furan obtained after photoionization with XUV using Ge and Sn filters. The peaks marked with '#' are mainly from the secondary electrons created by ion impact on the mesh that terminates the drift tube and is mounted 5 mm in front of the detector. These electrons are accelerated toward the MCP, where they are detected at slightly shorter flight times than the corresponding ions. However, some of these peaks (at early TOF) could be from the stray electrons. The peaks from the background gases are labeled in red. A cartoon representation of the equilibrium structure of furan is also shown. Both TOF traces (for Ge and Sn) shown in Fig. 5.10 are normalized

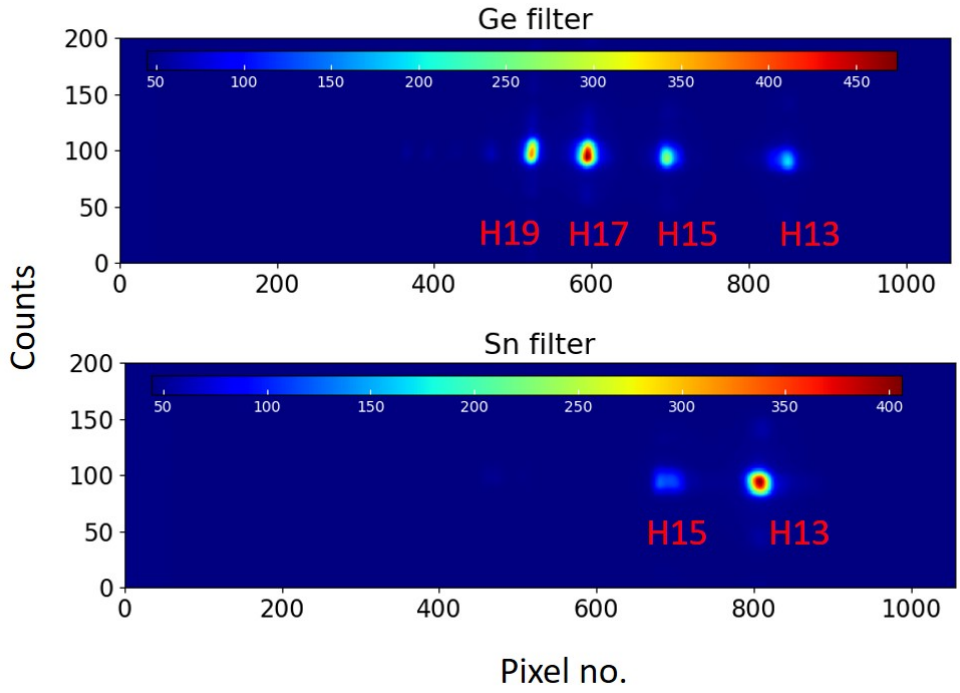

Figure 5.9: *The high-harmonic spectrum obtained from the XUV source, XUUS, after filtering the harmonics using Sn and Ge filters.*

w.r.t. to total ion yield. It can be seen that some of the fragments, such as C^+ and CH^+, only appear for the Ge filter, while H^+, H_2^+, $C_2H_2^+$, $C_4H_2^+$ have a higher yield for the Ge filter in comparison to the Sn filter.

Figure 5.11 shows the photoelectron position and energy spectrum obtained for the electrons detected in coincidence with singly-charged furan molecules ($C_4H_4O^+$). Figure 5.11(a),(b) show photoionization by a range of harmonics selected by a Sn filter (mainly, H13 or 20.4 eV, see Fig. 5.9). Similarly, Fig. 5.11(c),(d) shows the photoionization by a range of harmonics selected by a Ge filter (H13, H15, H17 and H19 or 20.4 eV, 23.5 eV, 26.7 eV and 29.8 eV, see Fig. 5.9). For the Ge filter, the identical peak structures separated by the energy gap of $\sim$ 3.1 eV are due to four harmonics which are selected and shown in Fig. 5.9. The intensity difference for different photon energies (different harmonics) is likely due to the combination of photoabsorption cross-section and beamline transmission (see Fig. 5.8).

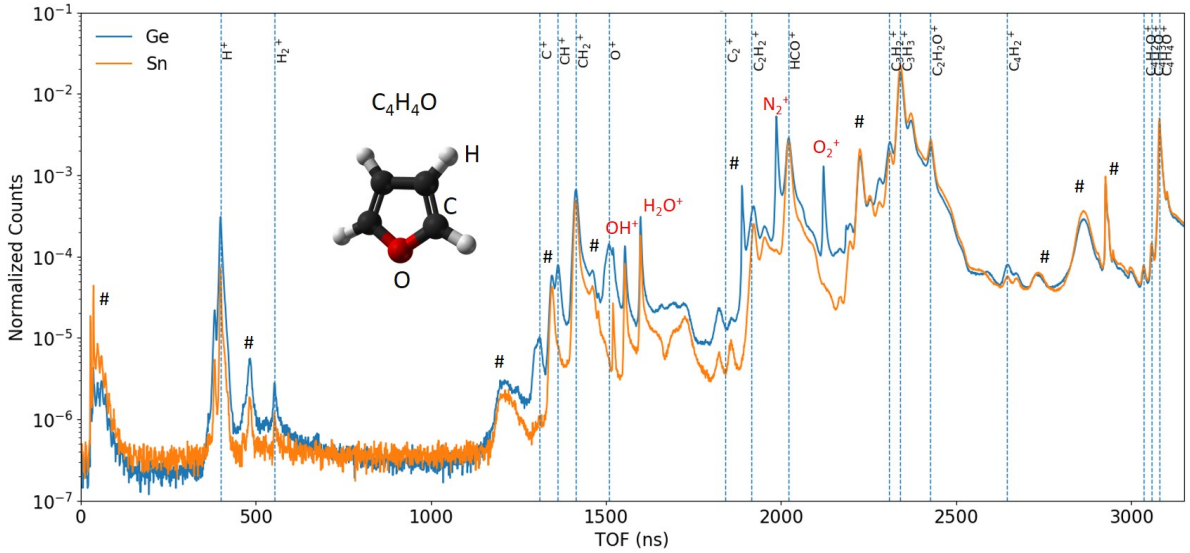

Figure 5.10: *Time-of-flight spectrum of furan ionized after photoionization with high harmonics generated by an XUV source, XUUS, and selected using Sn and Ge filters. The peaks marked with '#' are mainly from the secondary electrons created by ion impact on the mesh (see text). Also shown is the cartoon representation of the furan molecule.*

A split in the photoelectron energy can be seen for the Sn filter, where the photon energy is dominated by a single harmonic (H13, 20.4 eV). The difference in peak energies is $\sim$ 1.3 eV and the peak positions are $\sim$ 10.3 eV and $\sim$ 11.6 eV. The photoelectron energy can be converted to binding energy by subtracting the photoelectron energy from the photon energy of H13 (20.4 eV). Hence, for the two peaks, the binding energies are 8.8 eV and 10.1 eV. These two photoelectron peaks likely come from the photoionization of furan from different molecular orbitals.

Some of the earlier studies have recorded a high-resolution photoelectron spectrum of furan after valence ionization [183, 184]. Figure 5.12 shows the photoelectron spectrum recorded by Holland *et al.* [183] for furan. From these measurements, the binding energy ranges (including vibrational progressions) for the two states $\tilde{X}^2A_2$ and $\tilde{A}^2B_1$ are (8.00-9.65) eV and (9.65-11.45) eV respectively. Holland *et al.* also validated their experimental observations using the ADC(3) many-body Green's function method (Fig. 5.12). The pho-

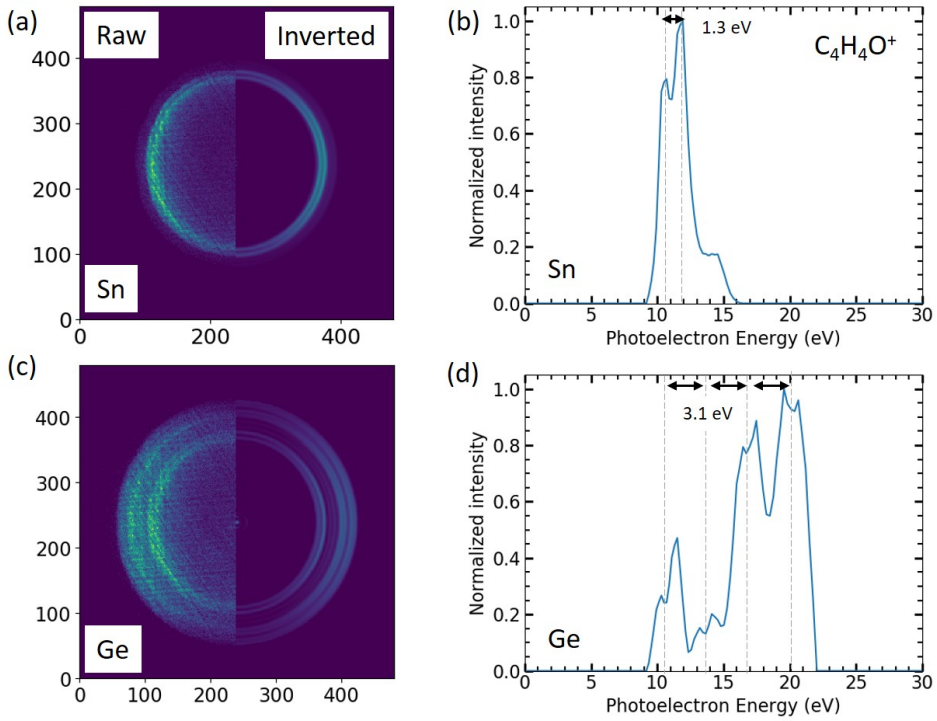

Figure 5.11: *Photoelectron position and energy spectrum of the singly-charged furan molecule ($C_4H_4O^+$) (a) Sn filter, raw and inverted photoelectron position spectrum, (b) Sn filter, photoelectron energy spectrum, (c) Ge filter, raw and inverted photoelectron position spectrum, (d) Ge filter, photoelectron energy spectrum.*

toelectrons detected in coincidence with the singly-charged furan molecule ($C_4H_4O^+$) at binding energies 8.8 eV and 10.1 eV are consistent with the values reported by Holland *et al.* for the states $\tilde{X}^2A_2$ and $\tilde{A}^2B_1$. Hence, the peaks observed in our experiment at 8.8 eV and 10.1 eV can be assigned to the electrons removed from $\tilde{X}^2A_2$ and $\tilde{A}^2B_1$, respectively.

Figure 5.13 shows the position and energy spectrum for photoelectrons detected in coincidence with different ionic fragments. For the energy spectrum shown for different fragments, a small contribution at high photoelectron energies likely originates from H15. Some experimental observations include a clear difference in the photoelectron energies, which are a few eV lower than the photoelectrons detected in coincidence with singly-charged furan molecule ($C_4H_4O^+$). Also, in Fig. 5.13 (b) and (c), the contribution of electrons removed from inner orbitals (lower photoelectron energy) can be seen clearly for the photoelectrons from $C_3H_3^+$,

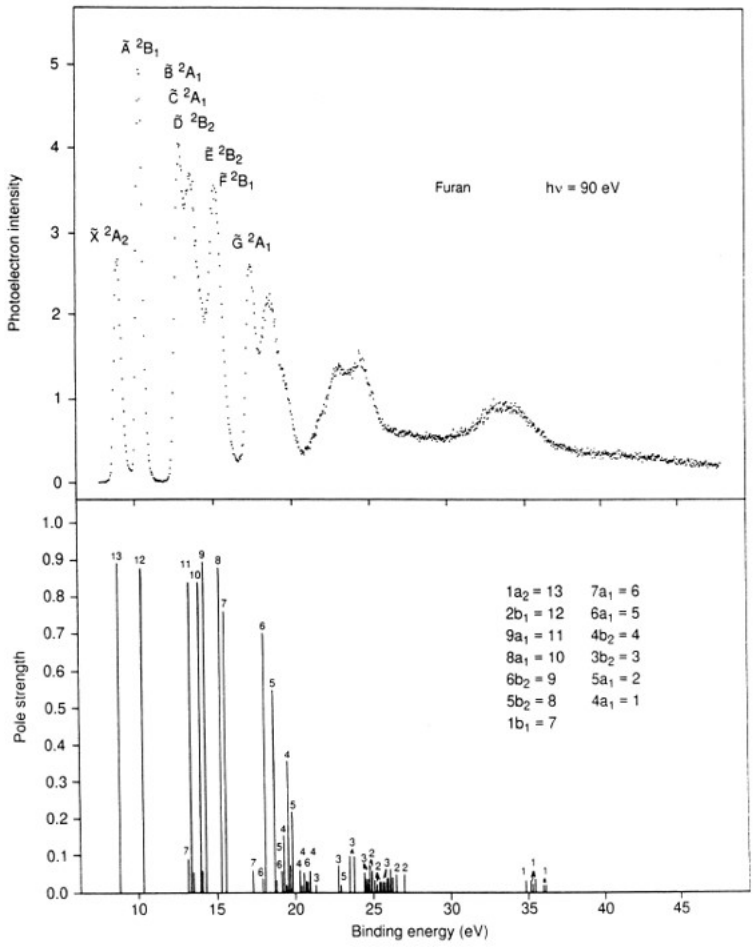

Figure 5.12: *High-resolution valence shell photoelectron spectrum of furan recorded at a photon energy of 90 eV (top). A theoretical spectrum of furan obtained using the ADC(3) many-body Green's function method (bottom) (Adapted from [183]).*

in contrast to $C_3H_4^+$. The photoelectrons detected in coincidence with $C_3H_4^+$ have an energy of 7.7 eV, which is about 3.9 eV lower than the photoelectrons detected in coincidence with the singly-charged furan molecule ($C_4H_4O^+$). $C_3H_4^+$ is formed when a neutral CO is eliminated, which can be a common fragmentation pathway in C and O containing heterocyclic molecules. A theoretical study performed recently [185] gave more insights regarding CO elimination and other isomerization pathways in furan after ionization with XUV. In this study, several methods were combined, including molecular dynamics simulations, and it was found that between 17 eV and 23 eV, the dominant pathway is skeleton fragmentation,

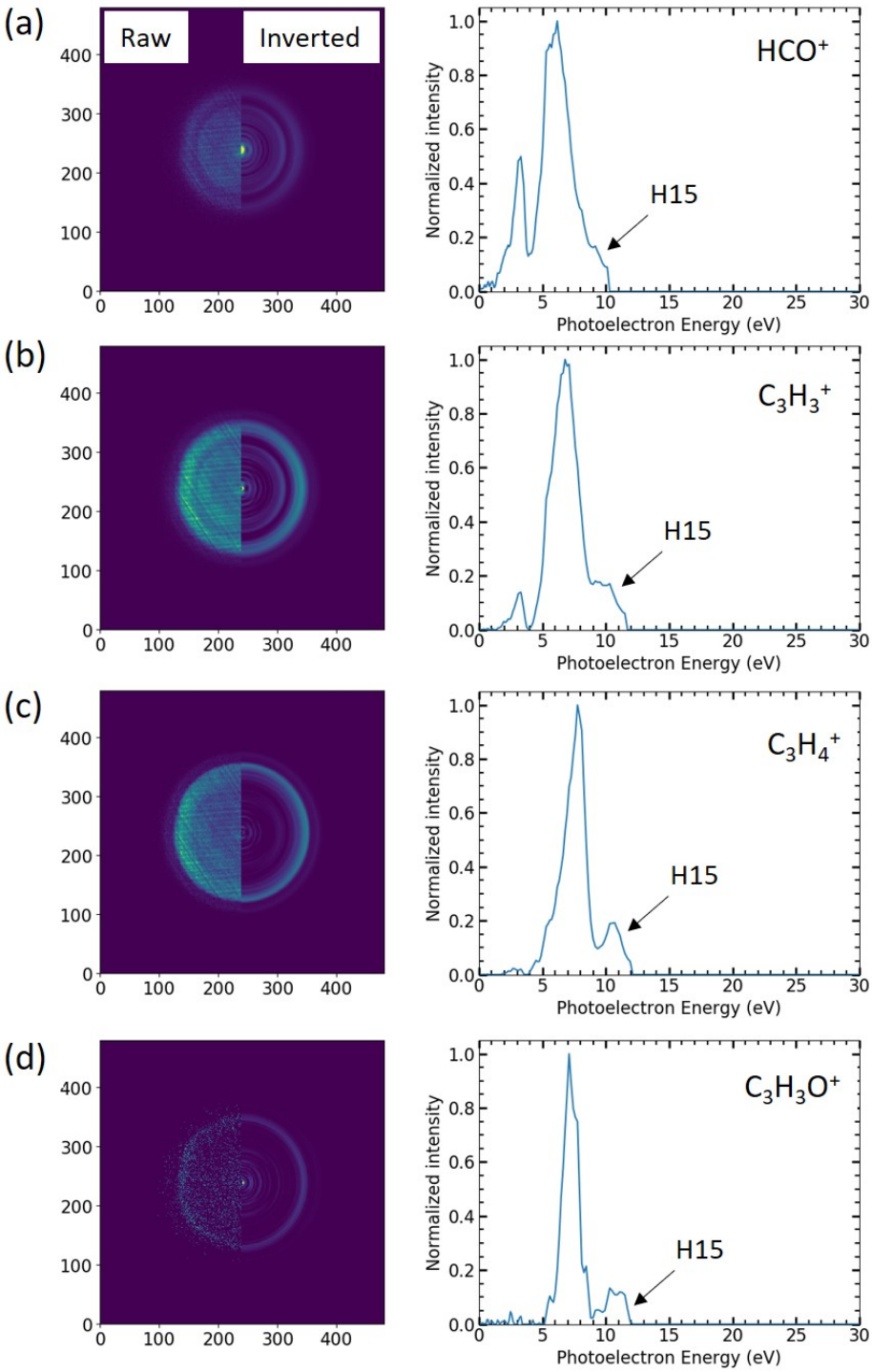

Figure 5.13: *Photoelectron position (raw and inverted) and energy spectrum obtained by gating on different ionic fragments of furan after ionization by the 13th harmonic (20.4 eV), with a small contribution from the 15th harmonic (23.5 eV), (a) HCO^+, (b) $C_3H_3^+$, (c) $C_3H_4^+$, (d) $C_3H_3O^+$.*

i.e., breaking of a CC bond, after CO breaking/isomerization (see Fig. 5.14(a)). This leads to the formation of $C_3H_3^+$ or $C_3H_4^+$ ionic fragments post CO elimination. This agrees well with the experimental results, where a dominant contribution from $C_3H_3^+$ and $C_3H_4^+$ ionic fragments can be seen (see Fig. 5.10).

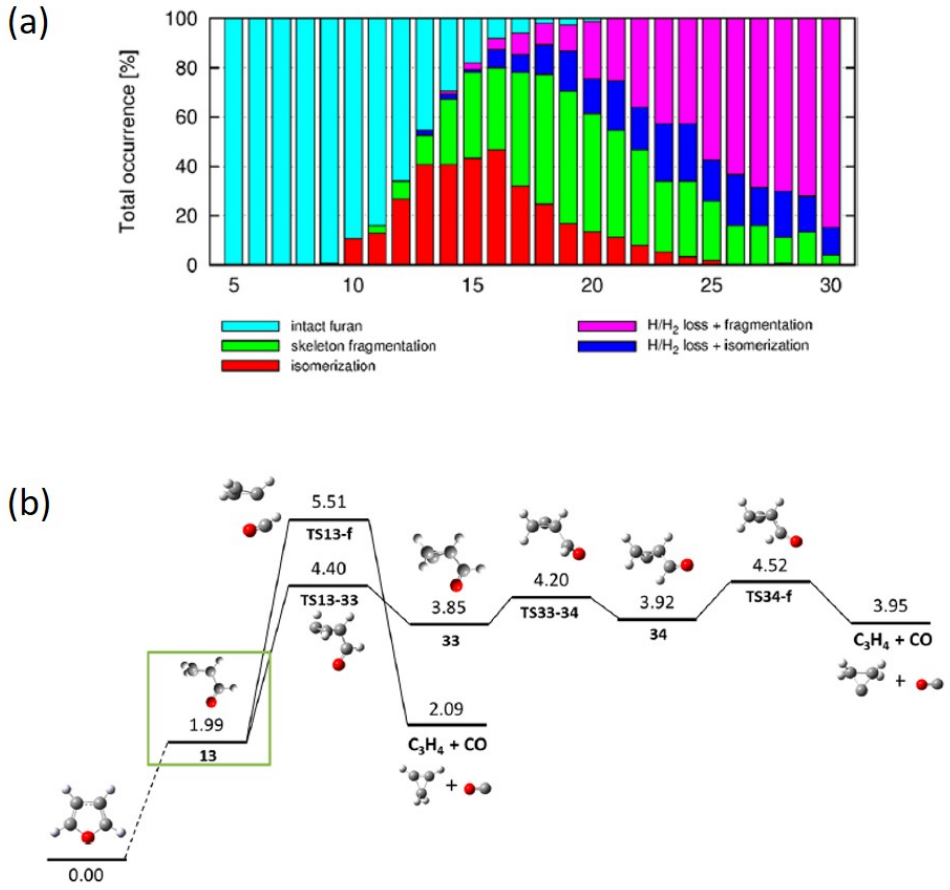

Figure 5.14: *Results from theoretical modeling of furan fragmentation using statistical and molecular dynamics calculations by Erdmann et al. [185] (a) Processes at different photon energies, (b) One of the pathways showing skeleton fragmentation.*

Figure 5.14(a) shows the results from Erdmann *et al.* [185], where skeleton fragmentation can be seen as a major process happening at 20 eV. Figure 5.14(b) also shows two of the skeleton fragmentation pathways where CO elimination occurs. The energy difference calculated by Erdmann *et al.* [185] between furan and C_3H_4 formed after CO elimination

matches well with the photoelectron energy difference between photoelectrons from the singly-charged furan molecule ($C_4H_4O^+$) and $C_3H_4^+$ (3.9 eV). Although other CO elimination pathways were the dominant pathways, as found by Erdmann *et al.*, a thorough understanding of channel resolved electron spectra would reveal further insights about the involvement of deeper molecular orbitals and isomerization pathways.

Further experiments are planned in this direction to continue this work. The experiments were temporarily stopped as the XUV source, XUUS, had to be coupled to a new laser system, FLAME (see chapter 6), to achieve optimum performance. Time-resolved experiments on furan coupled with PEPICO measurement may reveal the timescale of CO elimination and isomerization.

Chapter 6

Summary and outlook

With the rapid advancements in light sources and experimental techniques, it is now possible to observe the evolution of gas-phase molecular structures with (sub)-angstrom spatial resolution and femtosecond temporal resolution. Even with the advancement in experimental techniques, each experimental technique has certain limitations, which limit what we can learn about the photochemistry of a certain photoinduced isomerization reaction. However, combining results from several techniques often leads to a deeper understanding that truly advances the field. In this dissertation, we have worked toward developing our understanding of the photoinduced structural dynamics in polyatomic molecules by using several experimental techniques. We have developed tools and techniques which could be helpful for future studies of different photoinduced reactions. The key results obtained during this dissertation and their scientific significance are summarized below.

A significant portion of this dissertation explores the photoinduced (ring-opening) isomerization process in a prototypical heterocyclic ring molecule, thiophenone. The ultraviolet (UV) induced photoisomerization of thiophenone was studied with state-sensitive (or rather: "energy-sensitive") time-resolved photoelectron spectroscopy (TRPES) as well as "structure-sensitive" mega-electronvolt ultrafast electron diffraction (MeV UED). These experimental techniques are combined with theoretical calculations such as trajectory surface

hopping (TSH) for gaining insights about the excited-state dynamics and ab-initio molecular dynamics (AIMD) for distinguishing the ground-state photoproduct geometries (discussed in chapter 3). In the TRPES experiment, thiophenone molecules were excited with a UV pulse and later ionized by an XUV pulse from the FERMI free-electron laser (FEL). This study shows the ultrafast de-excitation of the excited-state molecules and an increase in photoelectron intensity attributed to the formation of ring-opened photoproducts based on theoretical calculations. The theoretical work predicts the formation of three ring-opened photoproducts and the formation of "vibrationally-hot" ground state thiophenone molecules, which is consistent with the experimental observations. The formation of these photoproducts is driven by a ballistic ring opening that is completed within ∼350 fs. These timescales match closely with the experimentally observed increase in photoelectron intensities. Although the TRPES study coupled with theoretical calculations reveals crucial insights related to the excited-state dynamics and photochemistry, it cannot distinguish the photoproduct geometries. To obtain insights about the photoproduct geometries experimentally, we performed the MeV UED experiment. This study was performed toward the end of my dissertation work, and the preliminary results from these experiments confirm the formation of three main photoproducts, which were predicted by the theoretical calculations. The combined study using TRPES, MeV UED, and theoretical calculations has shown that it is possible to advance our understanding towards other ring-opening reactions that are considered as candidates for designing ultrafast molecular switches. We believe our work also takes us a step closer to creating the "molecular movie", revealing detailed insights about both excited-state and ground-state dynamics.

In the next part of this dissertation, the coincident ion momentum imaging technique is used to demonstrate its capability of distinguishing subtle molecular structural changes. The conformational isomers of dibromoethane that only differ by a rotation around a single bond were distinguished using this method. The *concerted* and *sequential* breakup pathways were disentangled using the new Native Frames method developed by our colleagues at

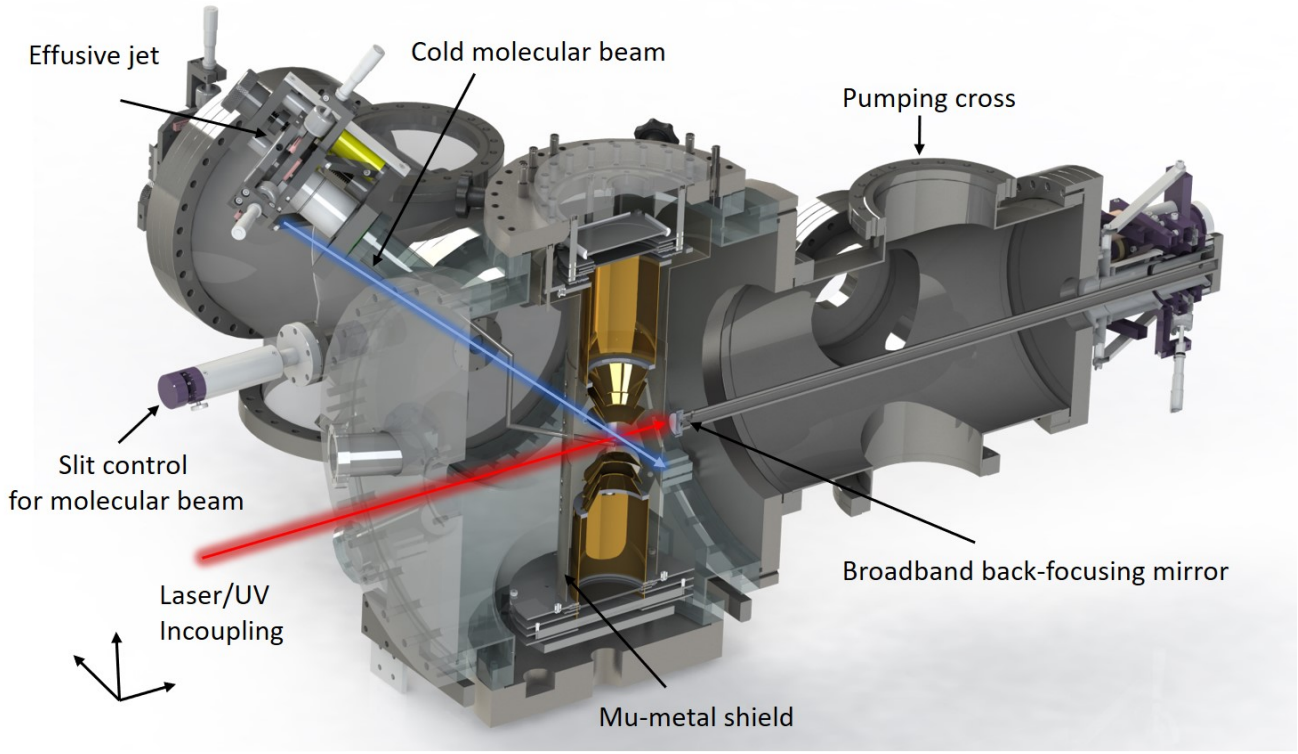

Figure 6.1: *KAMP setup (see section 2.3.1) with a modified design including a back-focusing mirror for coincidence experiments*

the James R. Macdonald Laboratory. After disentangling the sequential breakup events, the concerted breakup events were used to determine the yield of the *gauche* and *anti* conformations of dibromoethane. These yields were also measured for different sample temperatures, and the small changes in yield that were detected by the experiment match well with the theoretical estimates. Based on our results and results from other studies, we conclude that coincident ion momentum imaging has enormous potential to identify interconverting molecular structures. These geometries can be identified for particular cases, and their evolution can then be studied using time-resolved studies.

Apart from the coincident ion imaging technique, the photoelectron-photoion coincidence (PEPICO) technique is also used in this dissertation to study dissociation dynamics post absorption of an XUV photon. These experiments were performed on thiophenone and

furan. The experimental results revealed that the channel-resolved photoelectron spectrum reveals insights into dissociation pathways, such as CO elimination. These experiments can be combined with time-resolved measurements and are planned for future studies. To achieve this, we have modified the design of the KAMP instrument (see section 2.3.1). The new design is equipped with a back-focusing mirror that allows us to perform multi-ion coincidence and PEPICO measurements. The setup is coupled with a new laser system, FLAME (see section 2.2.3). In the future, we plan to couple the XUUS XUV source (see section 5.3.2) with KAMP, which will allow us to perform TRPES experiments with better time resolution using a lab-based setup instead of using free-electron lasers and synchrotrons.

Collectively, the work presented in this dissertation uses a variety of experimental techniques to provide a general understanding of light-induced isomerization and fragmentation by investigating simple molecules and moderately complex systems. In addition, our work provides insights into the prototypical light-induced reactions, which has opened doors for future investigations.

Bibliography

[1] J. P. Marangos. The measurement of ultrafast electronic and structural dynamics with x-rays. *Philosophical Transactions of the Royal Society A: Mathematical, Physical and Engineering Sciences*, 377(2145):20170481, 2019. doi: 10.1098/rsta.2017.0481. URL https://royalsocietypublishing.org/doi/abs/10.1098/rsta.2017.0481.

[2] Ahmed H. Zewail. Femtochemistry. past, present, and future. *Pure and Applied Chemistry*, 72(12):2219–2231, 2000. doi: doi:10.1351/pac200072122219. URL https://doi.org/10.1351/pac200072122219.

[3] Ahmed H. Zewail. Laser femtochemistry. *Science*, 242(4886):1645–1653, 1988. ISSN 0036-8075. doi: 10.1126/science.242.4886.1645. URL https://science.sciencemag.org/content/242/4886/1645.

[4] Ahmed H. Zewail. Femtochemistry: Atomic-scale dynamics of the chemical bond using ultrafast lasers (Nobel Lecture). *Angewandte Chemie International Edition*, 39 (15):2586–2631, 2000. doi: https://doi.org/10.1002/1521-3773(20000804)39:15⟨2586::AID-ANIE2586⟩3.0.CO;2-O. URL https://onlinelibrary.wiley.com/doi/abs/10.1002/1521-3773%2820000804%2939%3A15%3C2586%3A%3AAID-ANIE2586%3E3.0.CO%3B2-O.

[5] Benjamin W. Toulson, Mario Borgwardt, Han Wang, Florian Lackner, Adam S. Chatterley, C. D. Pemmaraju, Daniel M. Neumark, Stephen R. Leone, David Prendergast, and Oliver Gessner. Probing ultrafast C–Br bond fission in the UV photochemistry of bromoform with core-to-valence transient absorption spectroscopy.

Structural Dynamics, 6(5):054304, 2019. doi: 10.1063/1.5113798. URL https://doi.org/10.1063/1.5113798.

[6] Romain Geneaux, Hugo J. B. Marroux, Alexander Guggenmos, Daniel M. Neumark, and Stephen R. Leone. Transient absorption spectroscopy using high harmonic generation: a review of ultrafast x-ray dynamics in molecules and solids. *Philosophical Transactions of the Royal Society A: Mathematical, Physical and Engineering Sciences*, 377(2145):20170463, 2019. doi: 10.1098/rsta.2017.0463. URL https://royalsocietypublishing.org/doi/abs/10.1098/rsta.2017.0463.

[7] M. P. Minitti, J. M. Budarz, A. Kirrander, J. S. Robinson, D. Ratner, T. J. Lane, D. Zhu, J. M. Glownia, M. Kozina, H. T. Lemke, M. Sikorski, Y. Feng, S. Nelson, K. Saita, B. Stankus, T. Northey, J. B. Hastings, and P. M. Weber. Imaging molecular motion: Femtosecond x-ray scattering of an electrocyclic chemical reaction. *Phys. Rev. Lett.*, 114:255501, Jun 2015. doi: 10.1103/PhysRevLett.114.255501. URL https://link.aps.org/doi/10.1103/PhysRevLett.114.255501.

[8] Albert Stolow, Arthur E. Bragg, and Daniel M. Neumark. Femtosecond time-resolved photoelectron spectroscopy. *Chemical Reviews*, 104(4):1719–1758, 2004. doi: 10.1021/cr020683w. URL https://doi.org/10.1021/cr020683w.

[9] Daniel M. Neumark. Transition state spectroscopy. *Science*, 272(5267):1446–1447, 1996. ISSN 0036-8075. doi: 10.1126/science.272.5267.1446. URL https://science.sciencemag.org/content/272/5267/1446.

[10] Ahmed H. Zewail. Femtochemistry: recent progress in studies of dynamics and control of reactions and their transition states. *The Journal of Physical Chemistry*, 100 (31):12701–12724, 1996. doi: 10.1021/jp960658s. URL https://doi.org/10.1021/jp960658s.

[11] Daniel M Neumark. Time-resolved photoelectron spectroscopy of molecules and clusters. *Annual Review of Physical Chemistry*, 52(1):255–277, 2001. doi: 10.1146/annurev.physchem.52.1.255. URL https://doi.org/10.1146/annurev.physchem.52.1.255.

[12] Z. VAGER, R. NAAMAN, and E. P. KANTER. Coulomb explosion imaging of small molecules. *Science*, 244(4903):426–431, 1989. ISSN 0036-8075. doi: 10.1126/science.244.4903.426. URL https://science.sciencemag.org/content/244/4903/426.

[13] Chelsea E. Liekhus-Schmaltz, Ian Tenney, Timur Osipov, Alvaro Sanchez-Gonzalez, Nora Berrah, Rebecca Boll, Cedric Bomme, Christoph Bostedt, John D. Bozek, Sebastian Carron, Ryan Coffee, Julien Devin, Benjamin Erk, Ken R. Ferguson, Robert W. Field, Lutz Foucar, Leszek J. Frasinski, James M. Glownia, Markus GÃ¼hr, Andrei Kamalov, Jacek Krzywinski, Heng Li, Jonathan P. Marangos, Todd J. Martinez, Brian K. McFarland, Shungo Miyabe, Brendan Murphy, Adi Natan, Daniel Rolles, Artem Rudenko, Marco Siano, Emma R. Simpson, Limor Spector, Michele Swiggers, Daniel Walke, Song Wang, Thorsten Weber, Philip H. Bucksbaum, and Vladimir S. Petrovic. Ultrafast isomerization initiated by x-ray core ionization. *Nature Communications*, 6(1):8199, Sep 2015. ISSN 2041-1723. doi: 10.1038/ncomms9199. URL https://doi.org/10.1038/ncomms9199.

[14] Dissertation - "Ion-electron coincidence studies of femtosecond dynamics triggered by extreme ultraviolet photoionization of atoms and molecules" by Javad Robatjazi, https://krex.k-state.edu/dspace/handle/2097/41460.

[15] Nenad Ban, Poul Nissen, Jeffrey Hansen, Peter B. Moore, and Thomas A. Steitz. The complete atomic structure of the large ribosomal subunit at 2.4 å resolution. *Science*, 289(5481):905–920, 2000. ISSN 0036-8075. doi: 10.1126/science.289.5481.905. URL https://science.sciencemag.org/content/289/5481/905.

[16] The Nobel Prize in Chemistry (2009) https://www.nobelprize.org/prizes/chemistry/2009/summary/.

[17] Beamlines at Advanced light source https://als.lbl.gov/beamlines/.

[18] Zulfiqar Ali, Yi-De Chuang, David Kilcoyne, Alejandro Aguilar, Sung-Kwan Mo, and Zahid Hussain. Upgrade of the beamline 10.0.1 at the advanced light source. In Shunji Goto, Christian Morawe, and Ali M. Khounsary, editors, *Advances in X-Ray/EUV Optics and Components VII*, volume 8502, pages 189 – 198. International Society for Optics and Photonics, SPIE, 2012. doi: 10.1117/12.930328. URL https://doi.org/10.1117/12.930328.

[19] John Bozek, Art Robinson, and Scot Kellar. New als beamline for high-resolution electron spectroscopy below 340 ev. *Synchrotron Radiation News*, 12(5):37–39, 1999. doi: 10.1080/08940889908261036. URL https://doi.org/10.1080/08940889908261036.

[20] E. Allaria, R. Appio, L. Badano, W. A. Barletta, S. Bassanese, S. G. Biedron, A. Borga, E. Busetto, D. Castronovo, P. Cinquegrana, S. Cleva, D. Cocco, M. Cornacchia, P. Craievich, I. Cudin, G. D'Auria, M. Dal Forno, M. B. Danailov, R. De Monte, G. De Ninno, P. Delgiusto, A. Demidovich, S. Di Mitri, B. Diviacco, A. Fabris, R. Fabris, W. Fawley, M. Ferianis, E. Ferrari, S. Ferry, L. Froehlich, P. Furlan, G. Gaio, F. Gelmetti, L. Giannessi, M. Giannini, R. Gobessi, R. Ivanov, E. Karantzoulis, M. Lonza, A. Lutman, B. Mahieu, M. Milloch, S. V. Milton, M. Musardo, I. Nikolov, S. Noe, F. Parmigiani, G. Penco, M. Petronio, L. Pivetta, M. Predonzani, F. Rossi, L. Rumiz, A. Salom, C. Scafuri, C. Serpico, P. Sigalotti, S. Spampinati, C. Spezzani, M. Svandrlik, C. Svetina, S. Tazzari, M. Trovo, R. Umer, A. Vascotto, M. Veronese, R. Visintini, M. Zaccaria, D. Zangrando, and M. Zangrando. Highly coherent and stable pulses from the fermi seeded free-electron laser in the extreme ultraviolet. *Nature Photonics*, 6(10):699–704, Oct 2012. doi: 10.1038/nphoton.2012.233. URL https://doi.org/10.1038/nphoton.2012.233.

[21] C. Pellegrini, A. Marinelli, and S. Reiche. The physics of x-ray free-electron lasers. *Rev. Mod. Phys.*, 88:015006, Mar 2016. doi: 10.1103/RevModPhys.88.015006. URL https://link.aps.org/doi/10.1103/RevModPhys.88.015006.

[22] D. Ratner, R. Abela, J. Amann, C. Behrens, D. Bohler, G. Bouchard, C. Bostedt, M. Boyes, K. Chow, D. Cocco, F. J. Decker, Y. Ding, C. Eckman, P. Emma, D. Fairley, Y. Feng, C. Field, U. Flechsig, G. Gassner, J. Hastings, P. Heimann, Z. Huang, N. Kelez, J. Krzywinski, H. Loos, A. Lutman, A. Marinelli, G. Marcus, T. Maxwell, P. Montanez, S. Moeller, D. Morton, H. D. Nuhn, N. Rodes, W. Schlotter, S. Serkez, T. Stevens, J. Turner, D. Walz, J. Welch, and J. Wu. Experimental demonstration of a soft x-ray self-seeded free-electron laser. *Phys. Rev. Lett.*, 114:054801, Feb 2015. doi: 10.1103/PhysRevLett.114.054801. URL https://link.aps.org/doi/10.1103/PhysRevLett.114.054801.

[23] M. Zangrando, A. Abrami, D. Bacescu, I. Cudin, C. Fava, F. Frassetto, A. Galimberti, R. Godnig, D. Giuressi, L. Poletto, L. Rumiz, R. Sergo, C. Svetina, and D. Cocco. The photon analysis, delivery, and reduction system at the FERMI@Elettra free electron laser user facility. *Review of Scientific Instruments*, 80(11):113110, 2009. doi: 10.1063/1.3262502. URL https://doi.org/10.1063/1.3262502.

[24] Xiaoming Ren, A M Summers, Kanaka Raju P, Aram Vajdi, Varun Makhija, C W Fehrenbach, Nora G Kling, K J Betsch, Z Wang, M F Kling, K D Carnes, I Ben-Itzhak, Carlos Trallero-Herrero, and Vinod Kumarappan. Single-shot carrier-envelope-phase tagging using an f–2f interferometer and a phase meter: a comparison. *Journal of Optics*, 19(12):124017, nov 2017. doi: 10.1088/2040-8986/aa9865. URL https://doi.org/10.1088/2040-8986/aa9865.

[25] André T. J. B. Eppink and David H. Parker. Velocity map imaging of ions and electrons using electrostatic lenses: Application in photoelectron and photofragment

ion imaging of molecular oxygen. *Review of Scientific Instruments*, 68(9):3477–3484, 1997. doi: 10.1063/1.1148310. URL https://doi.org/10.1063/1.1148310.

[26] Lothar Strueder, Sascha Epp, Daniel Rolles, Robert Hartmann, Peter Holl, Gerhard Lutz, Heike Soltau, Rouven Eckart, Christian Reich, Klaus Heinzinger, Christian Thamm, Artem Rudenko, Faton Krasniqi, Kai-Uwe Kuehnel, Christian Bauer, Claus-Dieter Schroeter, Robert Moshammer, Simone Techert, Danilo Miessner, and Matteo Porro. Large-format, high-speed, x-ray pnCCDs combined with electron and ion imaging spectrometers in a multipurpose chamber for experiments at 4th generation light sources. *Nuclear Instruments and Methods in Physics Research Section A, Accelerators, Spectrometers, Detectors and Associated Equipment*, 614(3):483–496, Mar 2010. ISSN 0168-9002. URL http://inis.iaea.org/search/search.aspx?orig_q=RN:41074908. INSTRUMENTATION RELATED TO NUCLEAR SCIENCE AND TECHNOLOGY.

[27] Benjamin Erk, Jan P. Müller, Cédric Bomme, Rebecca Boll, Günter Brenner, Henry N. Chapman, Jonathan Correa, Stefan Düsterer, Siarhei Dziarzhytski, Stefan Eisebitt, Heinz Graafsma, Sören Grunewald, Lars Gumprecht, Robert Hartmann, Günter Hauser, Barbara Keitel, Clemens von Korff Schmising, Marion Kuhlmann, Bastian Manschwetus, Laurent Mercadier, Erland Müller, Christopher Passow, Elke Plönjes, Daniel Ramm, Dimitrios Rompotis, Artem Rudenko, Daniela Rupp, Mario Sauppe, Frank Siewert, Dieter Schlosser, Lothar Strüder, Angad Swiderski, Simone Techert, Kai Tiedtke, Thomas Tilp, Rolf Treusch, Ilme Schlichting, Joachim Ullrich, Robert Moshammer, Thomas Möller, and Daniel Rolles. CAMP@FLASH: an end-station for imaging, electron- and ion-spectroscopy, and pump–probe experiments at the FLASH free-electron laser. *Journal of Synchrotron Radiation*, 25(5):1529–1540, Sep 2018. doi: 10.1107/S1600577518008585. URL https://doi.org/10.1107/S1600577518008585.

[28] Timur Osipov, Christoph Bostedt, J.-C. Castagna, Ken R. Ferguson, Maximilian

Bucher, Sebastian C. Montero, Michele L. Swiggers, Razib Obaid, Daniel Rolles, Artem Rudenko, John D. Bozek, and Nora Berrah. The lamp instrument at the linac coherent light source free-electron laser. *Review of Scientific Instruments*, 89(3): 035112, 2018. doi: 10.1063/1.5017727. URL https://doi.org/10.1063/1.5017727.

[29] Utuq Ablikim, Cédric Bomme, Timur Osipov, Hui Xiong, Razib Obaid, René C. Bilodeau, Nora G. Kling, Ileana Dumitriu, Sven Augustin, Shashank Pathak, Kirsten Schnorr, David Kilcoyne, Nora Berrah, and Daniel Rolles. A coincidence velocity map imaging spectrometer for ions and high-energy electrons to study inner-shell photoionization of gas-phase molecules. *Review of Scientific Instruments*, 90(5):055103, 2019. doi: 10.1063/1.5093420. URL https://doi.org/10.1063/1.5093420.

[30] D. Rolles, Z.D. Pešić, M. Perri, R.C. Bilodeau, G.D. Ackerman, B.S. Rude, A.L.D. Kilcoyne, J.D. Bozek, and N. Berrah. A velocity map imaging spectrometer for electron–ion and ion–ion coincidence experiments with synchrotron radiation. *Nuclear Instruments and Methods in Physics Research Section B: Beam Interactions with Materials and Atoms*, 261(1):170–174, 2007. ISSN 0168-583X. doi: https://doi.org/10.1016/j.nimb.2007.04.186. URL https://www.sciencedirect.com/science/article/pii/S0168583X07009949.

[31] Arno Vredenborg, Wim G. Roeterdink, and Maurice H. M. Janssen. A photoelectron-photoion coincidence imaging apparatus for femtosecond time-resolved molecular dynamics with electron time-of-flight resolution of =18ps and energy resolution ee=3.5%. *Review of Scientific Instruments*, 79(6):063108, 2008. doi: 10.1063/1.2949142. URL https://doi.org/10.1063/1.2949142.

[32] SIMION. version 8.1, The field and particle trajectory simulator, Scientific Instrument Services, Inc (2013). https://simion.com/.

[33] . Hamamatsu MCP documentation. https://www.hamamatsu.com/resources/pdf/etd/MCP_assembly_TMCP0003E.pdf .

[34] . RoentDek detector manual (MCP Detector with Delay-Line Anode) https://www.roentdek.com/manuals/MCP%20Delay%20Line%20manual.pdf .

[35] RoentDek TDC8HP system manual https://www.roentdek.com/manuals/TDC8HP%20Manual.pdf .

[36] C. Bordas, F. Paulig, H. Helm, and D. L. Huestis. Photoelectron imaging spectrometry: Principle and inversion method. *Review of Scientific Instruments*, 67(6):2257–2268, 1996. doi: 10.1063/1.1147044. URL https://doi.org/10.1063/1.1147044.

[37] Gustavo A. Garcia, Laurent Nahon, and Ivan Powis. Two-dimensional charged particle image inversion using a polar basis function expansion. *Review of Scientific Instruments*, 75(11):4989–4996, 2004. doi: 10.1063/1.1807578. URL https://doi.org/10.1063/1.1807578.

[38] Vladimir Dribinski, Alexei Ossadtchi, Vladimir A. Mandelshtam, and Hanna Reisler. Reconstruction of Abel-transformable images: The gaussian basis-set expansion Abel transform method. *Review of Scientific Instruments*, 73(7):2634–2642, 2002. doi: 10.1063/1.1482156. URL https://doi.org/10.1063/1.1482156.

[39] L. Montgomery Smith, Dennis R. Keefer, and S.I. Sudharsanan. Abel inversion using transform techniques. *Journal of Quantitative Spectroscopy and Radiative Transfer*, 39 (5):367–373, 1988. doi: https://doi.org/10.1016/0022-4073(88)90101-X. URL https://www.sciencedirect.com/science/article/pii/002240738890101X.

[40] Viktor Lyamayev et al. A modular end-station for atomic, molecular, and cluster science at the low density matter beamline of FERMI@Elettra. *J. Phys. B: At. Mol. Opt. Phys.*, 46:164007, 2013. URL https://iopscience.iop.org/article/10.1088/0953-4075/46/16/164007.

[41] Cristian Svetina, Cesare Grazioli, Nicola Mahne, Lorenzo Raimondi, Claudio Fava, Marco Zangrando, Simone Gerusina, Michele Alagia, Lorenzo Avaldi, Giuseppe

Cautero, Monica de Simone, Michele Devetta, Michele Di Fraia, Marcel Drabbels, Vitaliy Feyer, Paola Finetti, Raphael Katzy, Antti Kivimäki, Viktor Lyamayev, Tommaso Mazza, Angelica Moise, Thomas Möller, Patrick O'Keeffe, Yevheniy Ovcharenko, Paolo Piseri, Oksana Plekan, Kevin C. Prince, Rudi Sergo, Frank Stienkemeier, Stefano Stranges, Marcello Coreno, and Carlo Callegari. The Low Density Matter (LDM) beamline at FERMI: optical layout and first commissioning. *Journal of synchrotron radiation*, 22(3):538–543, May 2015. doi: 10.1107/S1600577515005743. URL https://pubmed.ncbi.nlm.nih.gov/25931066.

[42] J. H. D. Eland, O. Vieuxmaire, T. Kinugawa, P. Lablanquie, R. I. Hall, and F. Penent. Complete two-electron spectra in double photoionization: The rare gases ar, kr, and xe. *Phys. Rev. Lett.*, 90:053003, Feb 2003. doi: 10.1103/PhysRevLett.90.053003. URL https://link.aps.org/doi/10.1103/PhysRevLett.90.053003.

[43] John H. D. Eland, P. Linusson, Melanie Mucke, and Raimund Feifel. Homonuclear site-specific photochemistry by an ion-electron multi-coincidence spectroscopy technique. *Chemical Physics Letters*, 548:90–94, 2012. doi: 10.1016/j.cplett.2012.08.018.

[44] Akitaka Matsuda, Mizuho Fushitani, Chien-Ming Tseng, Yasumasa Hikosaka, John H. D. Eland, and Akiyoshi Hishikawa. A magnetic-bottle multi-electron-ion coincidence spectrometer. *Review of Scientific Instruments*, 82(10):103105, 2011. doi: 10.1063/1.3648133. URL https://doi.org/10.1063/1.3648133.

[45] Devens Gust, Thomas A. Moore, and Ana L. Moore. Molecular switches controlled by light. *Chem. Commun.*, pages 1169–1178, 2006. doi: 10.1039/B514736K. URL http://dx.doi.org/10.1039/B514736K.

[46] Masahiro Irie, Seiya Kobatake, and Masashi Horichi. Reversible surface morphology changes of a photochromic diarylethene single crystal by photoirradiation. *Science*, 291 (5509):1769–1772, 2001. ISSN 0036-8075. doi: 10.1126/science.291.5509.1769. URL https://science.sciencemag.org/content/291/5509/1769.

[47] D. Geppert, L. Seyfarth, and R. de Vivie-Riedle. Laser control schemes for molecular switches. *Applied Physics B*, 79(8):987–992, Dec 2004. ISSN 1432-0649. doi: 10.1007/s00340-004-1636-x. URL https://doi.org/10.1007/s00340-004-1636-x.

[48] Rienk Eelkema, Michael M. Pollard, Javier Vicario, Nathalie Katsonis, Blanca Serrano Ramon, Cees W. M. Bastiaansen, Dirk J. Broer, and Ben L. Feringa. Nanomotor rotates microscale objects. *Nature*, 440(7081):163–163, Mar 2006. ISSN 1476-4687. doi: 10.1038/440163a. URL https://doi.org/10.1038/440163a.

[49] Wesley R. Browne and Ben L. Feringa. Making molecular machines work. *Nature Nanotechnology*, 1(1):25–35, Oct 2006. ISSN 1748-3395. doi: 10.1038/nnano.2006.45. URL https://doi.org/10.1038/nnano.2006.45.

[50] K. L. Kompa and R. D. Levine. A molecular logic gate. *Proceedings of the National Academy of Sciences*, 98(2):410–414, 2001. ISSN 0027-8424. doi: 10.1073/pnas.98.2.410. URL https://www.pnas.org/content/98/2/410.

[51] Hector F. Deluca. History of the discovery of vitamin d and its active metabolites. *BoneKEy reports*, 3:479–479, Jan 2014. ISSN 2047-6396. doi: 10.1038/bonekey.2013.213. URL https://pubmed.ncbi.nlm.nih.gov/24466410. 24466410[pmid].

[52] Chong-Yu Ruan, Vladimir A. Lobastov, Ramesh Srinivasan, Boyd M. Goodson, Hyotcherl Ihee, and Ahmed H. Zewail. Ultrafast diffraction and structural dynamics: The nature of complex molecules far from equilibrium. *Proceedings of the National Academy of Sciences*, 98(13):7117–7122, 2001. ISSN 0027-8424. doi: 10.1073/pnas.131192898. URL https://www.pnas.org/content/98/13/7117.

[53] Hyotcherl Ihee, Vladimir A. Lobastov, Udo M. Gomez, Boyd M. Goodson, Ramesh Srinivasan, Chong-Yu Ruan, and Ahmed H. Zewail. Direct imaging of transient molecular structures with ultrafast diffraction. *Science*, 291(5503):458–462, 2001. ISSN

0036-8075. doi: 10.1126/science.291.5503.458. URL https://science.sciencemag.org/content/291/5503/458.

[54] Ray C. Dudek and Peter M. Weber. Ultrafast diffraction imaging of the electrocyclic ring-opening reaction of 1,3-cyclohexadiene. *The Journal of Physical Chemistry A*, 105(17):4167–4171, 2001. doi: 10.1021/jp010122t. URL https://doi.org/10.1021/jp010122t.

[55] T. J. A. Wolf, D. M. Sanchez, J. Yang, R. M. Parrish, J. P. F. Nunes, M. Centurion, R. Coffee, J. P. Cryan, M. GÃ¼hr, K. Hegazy, A. Kirrander, R. K. Li, J. Ruddock, X. Shen, T. Vecchione, S. P. Weathersby, P. M. Weber, K. Wilkin, H. Yong, Q. Zheng, X. J. Wang, M. P. Minitti, and T. J. MartÃnez. The photochemical ring-opening of 1,3-cyclohexadiene imaged by ultrafast electron diffraction. *Nature Chemistry*, 11(6): 504–509, Jun 2019. ISSN 1755-4349. doi: 10.1038/s41557-019-0252-7. URL https://doi.org/10.1038/s41557-019-0252-7.

[56] Jennifer M. Ruddock, Haiwang Yong, Brian Stankus, Wenpeng Du, Nathan Goff, Yu Chang, Asami Odate, Andrés Moreno Carrascosa, Darren Bellshaw, Nikola Zotev, Mengning Liang, Sergio Carbajo, Jason Koglin, Joseph S. Robinson, Sébastien Boutet, Adam Kirrander, Michael P. Minitti, and Peter M. Weber. A deep uv trigger for ground-state ring-opening dynamics of 1,3-cyclohexadiene. *Science Advances*, 5 (9), 2019. doi: 10.1126/sciadv.aax6625. URL https://advances.sciencemag.org/content/5/9/eaax6625.

[57] Narayanan Kuthirummal, Fedor M. Rudakov, Conor L. Evans, and Peter M. Weber. Spectroscopy and femtosecond dynamics of the ring opening reaction of 1,3-cyclohexadiene. *The Journal of Chemical Physics*, 125(13):133307, 2006. doi: 10.1063/1.2345203. URL https://doi.org/10.1063/1.2345203.

[58] W. Fuß, W. E. Schmid, and S. A. Trushin. Time-resolved dissociative intense-laser field ionization for probing dynamics: Femtosecond photochemical ring opening of

1,3-cyclohexadiene. *The Journal of Chemical Physics*, 112(19):8347–8362, 2000. doi: 10.1063/1.481478. URL https://doi.org/10.1063/1.481478.

[59] M. Garavelli, C. S. Page, P. Celani, M. Olivucci, W. E. Schmid, S. A. Trushin, and W. Fuss. Reaction path of a sub-200 fs photochemical electrocyclic reaction. *The Journal of Physical Chemistry A*, 105(18):4458–4469, 2001. doi: 10.1021/jp010359p. URL https://doi.org/10.1021/jp010359p.

[60] K. Kosma, S. A. Trushin, W. Fuß, and W. E. Schmid. Cyclohexadiene ring opening observed with 13 fs resolution: coherent oscillations confirm the reaction path. *Phys. Chem. Chem. Phys.*, 11:172–181, 2009. doi: 10.1039/B814201G. URL http://dx.doi.org/10.1039/B814201G.

[61] R. B. Woodward and Roald Hoffmann. The conservation of orbital symmetry. *Angewandte Chemie International Edition in English*, 8(11):781–853, 1969. doi: https://doi.org/10.1002/anie.196907811. URL https://onlinelibrary.wiley.com/doi/abs/10.1002/anie.196907811.

[62] B Hudson and B Kohler. Linear polyene electronic structure and spectroscopy. *Annual Review of Physical Chemistry*, 25(1):437–460, 1974. doi: 10.1146/annurev.pc.25.100174.002253. URL https://doi.org/10.1146/annurev.pc.25.100174.002253.

[63] BRUCE S. HUDSON, BRYAN E. KOHLER, and KLAUS SCHULTEN. Linear polyene electronic structure and potential surfaces. volume 6 of *Excited States*, pages 1–95. Elsevier, 1982. doi: https://doi.org/10.1016/B978-0-12-227206-6.50006-5. URL https://www.sciencedirect.com/science/article/pii/B9780122272066500065.

[64] Daniel Murdock, Stephanie J. Harris, Joel Luke, Michael P. Grubb, Andrew J. Orr-Ewing, and Michael N. R. Ashfold. Transient uv pump–ir probe investigation of heterocyclic ring-opening dynamics in the solution phase: the role played by n* states in the photoinduced reactions of thiophenone and furanone. *Phys. Chem. Chem.*

Phys., 16:21271–21279, 2014. doi: 10.1039/C4CP03653K. URL http://dx.doi.org/10.1039/C4CP03653K.

[65] Sanghamitra Deb and Peter M. Weber. The ultrafast pathway of photon-induced electrocyclic ring-opening reactions: The case of 1,3-cyclohexadiene. *Annual Review of Physical Chemistry*, 62(1):19–39, 2011. doi: 10.1146/annurev.physchem.012809.103350. URL https://doi.org/10.1146/annurev.physchem.012809.103350. PMID: 21054174.

[66] Bin-Bin Xie and Wei-Hai Fang. Combined quantum trajectory mean-field and molecular mechanical (qtmf/mm) nonadiabatic dynamics simulations on the photoinduced ring-opening reaction of 2(5h)-thiophenone. *ChemPhotoChem*, 3(9):897–906, 2019. doi: https://doi.org/10.1002/cptc.201900076. URL https://chemistry-europe.onlinelibrary.wiley.com/doi/abs/10.1002/cptc.201900076.

[67] Thomas Wolf, Private communication, November 2020.

[68] Wee Shong Chin, Zhi Ping Xu, Chup Yew Mok, Hsing Hua Huang, Hideki Mutoh, and Shigeru Masuda. He i and he ii photoelectron spectra of thiophenones. *Journal of Electron Spectroscopy and Related Phenomena*, 88-91:97–101, 1998. ISSN 0368-2048. doi: https://doi.org/10.1016/S0368-2048(97)00253-3. URL https://www.sciencedirect.com/science/article/pii/S0368204897002533. Proceedings of the Seventh International Conference on Electron Spectroscopy.

[69] Supplementary Information - "Tracking the ultraviolet-induced photochemistry of thiophenone during and after ultrafast ring opening". https://static-content.springer.com/esm/art%3A10.1038%2Fs41557-020-0507-3/MediaObjects/41557_2020_507_MOESM1_ESM.pdf .

[70] Masafumi Jinno, Iwao Watanabe, Yu Yokoyama, and Shigero Ikeda. He i photoelectron spectra of ethylene carbonate and related compounds. *Bulletin of the Chemical Society*

of Japan, 50(3):597–603, 1977. doi: 10.1246/bcsj.50.597. URL https://doi.org/10.1246/bcsj.50.597.

[71] Shashank Pathak, Lea M. Ibele, Rebecca Boll, Carlo Callegari, Alexander Demidovich, Benjamin Erk, Raimund Feifel, Ruaridh Forbes, Michele Di Fraia, Luca Giannessi, Christopher S. Hansen, David M. P. Holland, Rebecca A. Ingle, Robert Mason, Oksana Plekan, Kevin C. Prince, Arnaud Rouzée, Richard J. Squibb, Jan Tross, Michael N. R. Ashfold, Basile F. E. Curchod, and Daniel Rolles. Tracking the ultraviolet-induced photochemistry of thiophenone during and after ultrafast ring opening. *Nature Chemistry*, 12(9):795–800, Sep 2020. ISSN 1755-4349. doi: 10.1038/s41557-020-0507-3. URL https://doi.org/10.1038/s41557-020-0507-3.

[72] Francesca Calegari, Andrea Trabattoni, Alicia Palacios, David Ayuso, Mattea C Castrovilli, Jason B Greenwood, Piero Decleva, Fernando Martín, and Mauro Nisoli. Charge migration induced by attosecond pulses in bio-relevant molecules. *Journal of Physics B: Atomic, Molecular and Optical Physics*, 49(14):142001, jun 2016. doi: 10.1088/0953-4075/49/14/142001. URL https://doi.org/10.1088/0953-4075/49/14/142001.

[73] G. te Velde, F. M. Bickelhaupt, E. J. Baerends, C. Fonseca Guerra, S. J. A. van Gisbergen, J. G. Snijders, and T. Ziegler. Chemistry with adf. *Journal of Computational Chemistry*, 22(9):931–967, 2001. doi: https://doi.org/10.1002/jcc.1056. URL https://onlinelibrary.wiley.com/doi/abs/10.1002/jcc.1056.

[74] D Toffoli, M Stener, G Fronzoni, and P Decleva. Convergence of the multicenter b-spline dft approach for the continuum. *Chemical Physics*, 276(1):25–43, 2002. ISSN 0301-0104. doi: https://doi.org/10.1016/S0301-0104(01)00549-3. URL https://www.sciencedirect.com/science/article/pii/S0301010401005493.

[75] Ramesh Srinivasan, VladimirA. Lobastov, Chong-Yu Ruan, and AhmedH. Zewail. Ultrafast electron diffraction (ued). *Helvetica Chimica Acta*, 86(6):1761–1799, 2003.

doi: https://doi.org/10.1002/hlca.200390147. URL https://onlinelibrary.wiley.com/doi/abs/10.1002/hlca.200390147.

[76] Istvan Hargittai and Magdolna Hargittai. Stereochemical applications of gas-phase electron diffraction, part a. 1988. URL https://www.wiley.com/en-us/Stereochemical+Applications+of+Gas+Phase+Electron+Diffraction%2C+Part+A-p-9780471186892.

[77] Richard Henderson. The potential and limitations of neutrons, electrons and x-rays for atomic resolution microscopy of unstained biological molecules. *Quarterly Reviews of Biophysics*, 28(2):171–193, 1995. doi: 10.1017/S003358350000305X.

[78] Aaron Klug – Facts. NobelPrize.org. Nobel Media AB 2021. Sat. 5 Jun 2021. https://www.nobelprize.org/prizes/chemistry/1982/klug/facts/.

[79] H. Mark and R. Wierl. Über Elektronenbeugung am einzelnen Molekül. *Naturwissenschaften*, 18(9):205–205, February 1930. doi: 10.1007/BF01494849.

[80] H. Mark and R. Wierl. Die ermittlung von molekülstrukturen durch beugung von elektronen an einem dampfstrahl. *Zeitschrift für Elektrochemie und angewandte physikalische Chemie*, 36(9):675–676, 1930. doi: https://doi.org/10.1002/bbpc.19300360921. URL https://onlinelibrary.wiley.com/doi/abs/10.1002/bbpc.19300360921.

[81] L. O. Brockway. Electron diffraction by gas molecules. *Rev. Mod. Phys.*, 8:231–266, Jul 1936. doi: 10.1103/RevModPhys.8.231. URL https://link.aps.org/doi/10.1103/RevModPhys.8.231.

[82] Linus Pauling and L. O. Brockway. The radial distribution method of interpretation of electron diffraction photographs of gas molecules. *Journal of the American Chemical Society*, 57(12):2684–2692, 1935. doi: 10.1021/ja01315a103. URL https://doi.org/10.1021/ja01315a103.

[83] Ahmed H. Zewail. Femtochemistry: atomic-scale dynamics of the chemical bond. *The Journal of Physical Chemistry A*, 104(24):5660–5694, 2000. doi: 10.1021/jp001460h. URL https://doi.org/10.1021/jp001460h.

[84] Dmitry Shorokhov, Sang Tae Park, and Ahmed H. Zewail. Ultrafast electron diffraction: Dynamical structures on complex energy landscapes. *ChemPhysChem*, 6(11):2228–2250, 2005. doi: https://doi.org/10.1002/cphc.200500330. URL https://chemistry-europe.onlinelibrary.wiley.com/doi/abs/10.1002/cphc.200500330.

[85] J. Spencer Baskin and Ahmed H. Zewail. Ultrafast electron diffraction: Oriented molecular structures in space and time. *ChemPhysChem*, 6(11):2261–2276, 2005. doi: https://doi.org/10.1002/cphc.200500331. URL https://chemistry-europe.onlinelibrary.wiley.com/doi/abs/10.1002/cphc.200500331.

[86] J. Charles Williamson and Ahmed H. Zewail. Ultrafast electron diffraction. 4. molecular structures and coherent dynamics. *The Journal of Physical Chemistry*, 98 (11):2766–2781, 1994. doi: 10.1021/j100062a010. URL https://doi.org/10.1021/j100062a010.

[87] A. M. Michalik, E. Ya. Sherman, and J. E. Sipe. Theory of ultrafast electron diffraction: The role of the electron bunch properties. *Journal of Applied Physics*, 104(5): 054905, 2008. doi: 10.1063/1.2973157. URL https://doi.org/10.1063/1.2973157.

[88] K. Hedberg. *Electron diffraction in gases* by M. I. Davis. *Acta Crystallographica Section A*, 28(5):475, Sep 1972. doi: 10.1107/S0567739472001305. URL https://doi.org/10.1107/S0567739472001305.

[89] E. Arnold, Andre Authier, G.Bricogne, Philip Coppens, J.M. Cowley, R. Diamond, D.L. Dorset, F. Frey, C. Giacovazzo, J.K. Gjonnes, P. Goodman, R.W. Grosse-Kunstleve, Jean-Pierre Guigay, T. Haibach, S.R. Hall, H. Jagodzinski, R.E. Marsh,

R.P. Millane, and B.B. Zvyagin. *International Tables for Crystallography, Volume B: Reciprocal Space*. 01 2001. ISBN 0-7923–6592-5.

[90] MeV-UED Schematics https://lcls.slac.stanford.edu/instruments/mev-ued/schematics.

[91] S. P. Weathersby, G. Brown, M. Centurion, T. F. Chase, R. Coffee, J. Corbett, J. P. Eichner, J. C. Frisch, A. R. Fry, M. Gühr, N. Hartmann, C. Hast, R. Hettel, R. K. Jobe, E. N. Jongewaard, J. R. Lewandowski, R. K. Li, A. M. Lindenberg, I. Makasyuk, J. E. May, D. McCormick, M. N. Nguyen, A. H. Reid, X. Shen, K. Sokolowski-Tinten, T. Vecchione, S. L. Vetter, J. Wu, J. Yang, H. A. Dürr, and X. J. Wang. Mega-electron-volt ultrafast electron diffraction at slac national accelerator laboratory. *Review of Scientific Instruments*, 86(7):073702, 2015. doi: 10.1063/1.4926994. URL https://doi.org/10.1063/1.4926994.

[92] Jie Yang, Markus Guehr, Theodore Vecchione, Matthew S. Robinson, Renkai Li, Nick Hartmann, Xiaozhe Shen, Ryan Coffee, Jeff Corbett, Alan Fry, Kelly Gaffney, Tais Gorkhover, Carsten Hast, Keith Jobe, Igor Makasyuk, Alexander Reid, Joseph Robinson, Sharon Vetter, Fenglin Wang, Stephen Weathersby, Charles Yoneda, Martin Centurion, and Xijie Wang. Diffractive imaging of a rotational wavepacket in nitrogen molecules with femtosecond megaelectronvolt electron pulses. *Nature Communications*, 7(1):11232, Apr 2016. ISSN 2041-1723. doi: 10.1038/ncomms11232. URL https://doi.org/10.1038/ncomms11232.

[93] H Ihee, J Cao, and A.H Zewail. Ultrafast electron diffraction: structures in dissociation dynamics of fe(co)5. *Chemical Physics Letters*, 281(1):10–19, 1997. ISSN 0009-2614. doi: https://doi.org/10.1016/S0009-2614(97)01167-6. URL https://www.sciencedirect.com/science/article/pii/S0009261497011676.

[94] Chaehyuk Ko, Benjamin Levine, A. Toniolo, Leslie Manohar, Seth Olsen, Hans-Joachim Werner, and Todd J. Martínez. Ab initio excited-state dynamics of the

photoactive yellow protein chromophore. *Journal of the American Chemical Society*, 125(42):12710–12711, 2003. doi: 10.1021/ja0365025. URL https://doi.org/10.1021/ja0365025. PMID: 14558810.

[95] Ulrich K. Genick, S. Michael Soltis, Peter Kuhn, Ilona L. Canestrelli, and Elizabeth D. Getzoff. Structure at 0.85â€ã... resolution of an early protein photocycle intermediate. *Nature*, 392(6672):206–209, Mar 1998. ISSN 1476-4687. doi: 10.1038/32462. URL https://doi.org/10.1038/32462.

[96] Silke Allmann and Ian T. Baldwin. Insects betray themselves in nature to predators by rapid isomerization of green leaf volatiles. *Science*, 329(5995):1075–1078, 2010. ISSN 0036-8075. doi: 10.1126/science.1191634. URL https://science.sciencemag.org/content/329/5995/1075.

[97] Feng Gai, K. C. Hasson, J. Cooper McDonald, and Philip A. Anfinrud. Chemical dynamics in proteins: The photoisomerization of retinal in bacteriorhodopsin. *Science*, 279(5358):1886–1891, 1998. ISSN 0036-8075. doi: 10.1126/science.279.5358.1886. URL https://science.sciencemag.org/content/279/5358/1886.

[98] GEORGE WALD. The molecular basis of visual excitation. *Nature*, 219(5156):800–807, Aug 1968. ISSN 1476-4687. doi: 10.1038/219800a0. URL https://doi.org/10.1038/219800a0.

[99] G Hayward, W Carlsen, A Siegman, and L Stryer. Retinal chromophore of rhodopsin photoisomerizes within picoseconds. *Science*, 211(4485):942–944, 1981. ISSN 0036-8075. doi: 10.1126/science.7466366. URL https://science.sciencemag.org/content/211/4485/942.

[100] 1942 Nelson, David L. (David Lee). *Lehninger principles of biochemistry*. Fourth edition. New York : W.H. Freeman, 2005., 2005. URL https://search.library.wisc.edu/catalog/999964334502121. Includes bibliographical references and index.

[101] RW Schoenlein, LA Peteanu, RA Mathies, and CV Shank. The first step in vision: femtosecond isomerization of rhodopsin. *Science*, 254(5030):412–415, 1991. ISSN 0036-8075. doi: 10.1126/science.1925597. URL https://science.sciencemag.org/content/254/5030/412.

[102] Henry F. Schaefer. The 1,2 hydrogen shift: a common vehicle for the disappearance of evanescent molecular species. *Accounts of Chemical Research*, 12(8):288–296, 1979. doi: 10.1021/ar50140a004. URL https://doi.org/10.1021/ar50140a004.

[103] R. Thissen, J. Delwiche, J. M. Robbe, D. Duflot, J. P. Flament, and J. H. D. Eland. Dissociations of the ethyne dication c2h2+2. *The Journal of Chemical Physics*, 99(9): 6590–6599, 1993. doi: 10.1063/1.465851. URL https://doi.org/10.1063/1.465851.

[104] Glyn Cooper, Toshio Ibuki, Yoshihiro Iida, and C.E. Brion. Absolute dipole oscillator strengths for photoabsorption and the molecular and dissociative photoionization of acetylene. *Chemical Physics*, 125(2):307–320, 1988. ISSN 0301-0104. doi: https://doi.org/10.1016/0301-0104(88)87085-X. URL https://www.sciencedirect.com/science/article/pii/030101048887085X.

[105] T. Osipov, C. L. Cocke, M. H. Prior, A. Landers, Th. Weber, O. Jagutzki, L. Schmidt, H. Schmidt-Böcking, and R. Dörner. Photoelectron-photoion momentum spectroscopy as a clock for chemical rearrangements: Isomerization of the di-cation of acetylene to the vinylidene configuration. *Phys. Rev. Lett.*, 90:233002, Jun 2003. doi: 10.1103/PhysRevLett.90.233002. URL https://link.aps.org/doi/10.1103/PhysRevLett.90.233002.

[106] Y. H. Jiang, A. Rudenko, O. Herrwerth, L. Foucar, M. Kurka, K. U. Kühnel, M. Lezius, M. F. Kling, J. van Tilborg, A. Belkacem, K. Ueda, S. Düsterer, R. Treusch, C. D. Schröter, R. Moshammer, and J. Ullrich. Ultrafast extreme ultraviolet induced isomerization of acetylene cations. *Phys. Rev. Lett.*, 105:263002, Dec 2010.

doi: 10.1103/PhysRevLett.105.263002. URL https://link.aps.org/doi/10.1103/PhysRevLett.105.263002.

[107] Zheng Li, Ludger Inhester, Chelsea Liekhus-Schmaltz, Basile F. E. Curchod, James W. Snyder, Nikita Medvedev, James Cryan, Timur Osipov, Stefan Pabst, Oriol Vendrell, Phil Bucksbaum, and Todd J. Martinez. Ultrafast isomerization in acetylene dication after carbon k-shell ionization. *Nature Communications*, 8(1):453, Sep 2017. ISSN 2041-1723. doi: 10.1038/s41467-017-00426-6. URL https://doi.org/10.1038/s41467-017-00426-6.

[108] Akiyoshi Hishikawa, Akitaka Matsuda, Mizuho Fushitani, and Eiji J. Takahashi. Visualizing recurrently migrating hydrogen in acetylene dication by intense ultrashort laser pulses. *Phys. Rev. Lett.*, 99:258302, Dec 2007. doi: 10.1103/PhysRevLett.99.258302. URL https://link.aps.org/doi/10.1103/PhysRevLett.99.258302.

[109] E. Wells, C. E. Rallis, M. Zohrabi, R. Siemering, Bethany Jochim, P. R. Andrews, U. Ablikim, B. Gaire, S. De, K. D. Carnes, B. Bergues, R. de Vivie-Riedle, M. F. Kling, and I. Ben-Itzhak. Adaptive strong-field control of chemical dynamics guided by three-dimensional momentum imaging. *Nature Communications*, 4(1):2895, Dec 2013. ISSN 2041-1723. doi: 10.1038/ncomms3895. URL https://doi.org/10.1038/ncomms3895.

[110] Xinhua Xie, Katharina Doblhoff-Dier, Huailiang Xu, Stefan Roither, Markus S. Schöffler, Daniil Kartashov, Sonia Erattupuzha, Tim Rathje, Gerhard G. Paulus, Kaoru Yamanouchi, Andrius Baltuška, Stefanie Gräfe, and Markus Kitzler. Selective control over fragmentation reactions in polyatomic molecules using impulsive laser alignment. *Phys. Rev. Lett.*, 112:163003, Apr 2014. doi: 10.1103/PhysRevLett.112.163003. URL https://link.aps.org/doi/10.1103/PhysRevLett.112.163003.

[111] M. Kübel, R. Siemering, C. Burger, Nora G. Kling, H. Li, A. S. Alnaser, B. Bergues, S. Zherebtsov, A. M. Azzeer, I. Ben-Itzhak, R. Moshammer, R. de Vivie-Riedle, and

M. F. Kling. Steering proton migration in hydrocarbons using intense few-cycle laser fields. *Phys. Rev. Lett.*, 116:193001, May 2016. doi: 10.1103/PhysRevLett.116.193001. URL https://link.aps.org/doi/10.1103/PhysRevLett.116.193001.

[112] C. Burger, A. Atia-Tul-Noor, T. Schnappinger, H. Xu, P. Rosenberger, N. Haram, S. Beaulieu, F. Légaré, A. S. Alnaser, R. Moshammer, R. T. Sang, B. Bergues, M. S. Schuurman, R. de Vivie-Riedle, I. V. Litvinyuk, and M. F. Kling. Time-resolved nuclear dynamics in bound and dissociating acetylene. *Structural Dynamics*, 5(4): 044302, 2018. doi: 10.1063/1.5037686. URL https://doi.org/10.1063/1.5037686.

[113] Nagitha Ekanayake, Muath Nairat, Balram Kaderiya, Peyman Feizollah, Bethany Jochim, Travis Severt, Ben Berry, Kanaka Raju Pandiri, Kevin D. Carnes, Shashank Pathak, Daniel Rolles, Artem Rudenko, Itzik Ben-Itzhak, Christopher A. Mancuso, B. Scott Fales, James E. Jackson, Benjamin G. Levine, and Marcos Dantus. Mechanisms and time-resolved dynamics for trihydrogen cation (h3+) formation from organic molecules in strong laser fields. *Scientific Reports*, 7(1):4703, Jul 2017. ISSN 2045-2322. doi: 10.1038/s41598-017-04666-w. URL https://doi.org/10.1038/s41598-017-04666-w.

[114] Enliang Wang, Xueguang Ren, and Alexander Dorn. Role of the environment in quenching the production of h_3^+ from dicationic clusters of methanol. *Phys. Rev. Lett.*, 126:103402, Mar 2021. doi: 10.1103/PhysRevLett.126.103402. URL https://link.aps.org/doi/10.1103/PhysRevLett.126.103402.

[115] Tomoyuki Endo, Simon P. Neville, Vincent Wanie, Samuel Beaulieu, Chen Qu, Jude Deschamps, Philippe Lassonde, Bruno E. Schmidt, Hikaru Fujise, Mizuho Fushitani, Akiyoshi Hishikawa, Paul L. Houston, Joel M. Bowman, Michael S. Schuurman, François Légaré, and Heide Ibrahim. Capturing roaming molecular fragments in real time. *Science*, 370(6520):1072–1077, 2020. ISSN 0036-8075. doi: 10.1126/science.abc2960. URL https://science.sciencemag.org/content/370/6520/1072.

[116] Ester Livshits, Itamar Luzon, Krishnendu Gope, Roi Baer, and Daniel Strasser. Time-resolving the ultrafast h2 roaming chemistry and h3+ formation using extreme-ultraviolet pulses. *Communications Chemistry*, 3(1):49, Apr 2020. ISSN 2399-3669. doi: 10.1038/s42004-020-0294-1. URL https://doi.org/10.1038/s42004-020-0294-1.

[117] David D. Boehr, Ruth Nussinov, and Peter E. Wright. The role of dynamic conformational ensembles in biomolecular recognition. *Nature Chemical Biology*, 5(11): 789–796, Nov 2009. ISSN 1552-4469. doi: 10.1038/nchembio.232. URL https://doi.org/10.1038/nchembio.232.

[118] Patrick Sweeney, Hyunsun Park, Marc Baumann, John Dunlop, Judith Frydman, Ron Kopito, Alexander McCampbell, Gabrielle Leblanc, Anjli Venkateswaran, Antti Nurmi, and Robert Hodgson. Protein misfolding in neurodegenerative diseases: implications and strategies. *Translational Neurodegeneration*, 6(1):6, Mar 2017. ISSN 2047-9158. doi: 10.1186/s40035-017-0077-5. URL https://doi.org/10.1186/s40035-017-0077-5.

[119] Myung Hwa Kim, Lei Shen, Hongli Tao, Todd J. Martinez, and Arthur G. Suits. Conformationally controlled chemistry: Excited-state dynamics dictate ground-state reaction. *Science*, 315(5818):1561–1565, 2007. ISSN 0036-8075. doi: 10.1126/science.1136453. URL https://science.sciencemag.org/content/315/5818/1561.

[120] Sang Tae Park, Sang Kyu Kim, and Myung Soo Kim. Observation of conformation-specific pathways in the photodissociation of 1-iodopropane ions. *Nature*, 415(6869): 306–308, Jan 2002. ISSN 1476-4687. doi: 10.1038/415306a. URL https://doi.org/10.1038/415306a.

[121] Brian C. Dian, Jasper R. Clarkson, and Timothy S. Zwier. Direct measurement of energy thresholds to conformational isomerization in tryptamine. *Science*, 303

(5661):1169–1173, 2004. ISSN 0036-8075. doi: 10.1126/science.1093731. URL https://science.sciencemag.org/content/303/5661/1169.

[122] Brian C. Dian, Gordon G. Brown, Kevin O. Douglass, and Brooks H. Pate. Measuring picosecond isomerization kinetics via broadband microwave spectroscopy. *Science*, 320 (5878):924–928, 2008. ISSN 0036-8075. doi: 10.1126/science.1155736. URL https://science.sciencemag.org/content/320/5878/924.

[123] Yuan-Pin Chang, Karol Długołecki, Jochen Küpper, Daniel Rösch, Dieter Wild, and Stefan Willitsch. Specific chemical reactivities of spatially separated 3-aminophenol conformers with cold ca+ ions. *Science*, 342(6154):98–101, 2013. ISSN 0036-8075. doi: 10.1126/science.1242271. URL https://science.sciencemag.org/content/342/6154/98.

[124] Martin Pitzer, Maksim Kunitski, Allan S. Johnson, Till Jahnke, Hendrik Sann, Felix Sturm, Lothar Ph. H. Schmidt, Horst Schmidt-Böcking, Reinhard Dörner, Jürgen Stohner, Julia Kiedrowski, Michael Reggelin, Sebastian Marquardt, Alexander Schießer, Robert Berger, and Markus S. Schöffler. Direct determination of absolute molecular stereochemistry in gas phase by coulomb explosion imaging. *Science*, 341(6150):1096–1100, 2013. ISSN 0036-8075. doi: 10.1126/science.1240362. URL https://science.sciencemag.org/content/341/6150/1096.

[125] Martin Pitzer, Gregor Kastirke, Maksim Kunitski, Till Jahnke, Tobias Bauer, Christoph Goihl, Florian Trinter, Carl Schober, Kevin Henrichs, Jasper Becht, Stefan Zeller, Helena Gassert, Markus Waitz, Andreas Kuhlins, Hendrik Sann, Felix Sturm, Florian Wiegandt, Robert Wallauer, Lothar Ph. H. Schmidt, Allan S. Johnson, Manuel Mazenauer, Benjamin Spenger, Sabrina Marquardt, Sebastian Marquardt, Horst Schmidt-Böcking, Jürgen Stohner, Reinhard Dörner, Markus Schöffler, and Robert Berger. Absolute configuration from different multifragmentation pathways in light-induced coulomb explosion imaging. *ChemPhysChem*, 17(16):2465–2472, 2016.

doi: https://doi.org/10.1002/cphc.201501118. URL https://chemistry-europe.onlinelibrary.wiley.com/doi/abs/10.1002/cphc.201501118.

[126] Utuq Ablikim, CÃ©dric Bomme, Hui Xiong, Evgeny Savelyev, Razib Obaid, Balram Kaderiya, Sven Augustin, Kirsten Schnorr, Ileana Dumitriu, Timur Osipov, RenÃ© Bilodeau, David Kilcoyne, Vinod Kumarappan, Artem Rudenko, Nora Berrah, and Daniel Rolles. Identification of absolute geometries of cis and trans molecular isomers by coulomb explosion imaging. *Scientific Reports*, 6(1):38202, Dec 2016. ISSN 2045-2322. doi: 10.1038/srep38202. URL https://doi.org/10.1038/srep38202.

[127] Michael Burt, Kasra Amini, Jason W. L. Lee, Lars Christiansen, Rasmus R. Johansen, Yuki Kobayashi, James D. Pickering, Claire Vallance, Mark Brouard, and Henrik Stapelfeldt. Communication: Gas-phase structural isomer identification by coulomb explosion of aligned molecules. *The Journal of Chemical Physics*, 148(9):091102, 2018. doi: 10.1063/1.5023441. URL https://doi.org/10.1063/1.5023441.

[128] Heide Ibrahim, Benji Wales, Samuel Beaulieu, Bruno E. Schmidt, Nicolas Thiré, Emmanuel P. Fowe, Éric Bisson, Christoph T. Hebeisen, Vincent Wanie, Mathieu Giguére, Jean-Claude Kieffer, Michael Spanner, André D. Bandrauk, Joseph Sanderson, Michael S. Schuurman, and Francois Légaré. Tabletop imaging of structural evolutions in chemical reactions demonstrated for the acetylene cation. *Nature Communications*, 5(1):4422, Jul 2014. ISSN 2041-1723. doi: 10.1038/ncomms5422. URL https://doi.org/10.1038/ncomms5422.

[129] Utuq Ablikim, Cédric Bomme, Evgeny Savelyev, Hui Xiong, Rajesh Kushawaha, Rebecca Boll, Kasra Amini, Timur Osipov, David Kilcoyne, Artem Rudenko, Nora Berrah, and Daniel Rolles. Isomer-dependent fragmentation dynamics of inner-shell photoionized difluoroiodobenzene. *Phys. Chem. Chem. Phys.*, 19:13419–13431, 2017. doi: 10.1039/C7CP01379E. URL http://dx.doi.org/10.1039/C7CP01379E.

[130] Carrie J. Christiansen and Joseph S. Francisco. Atmospheric oxidation mechanism of 1,2-dibromoethane. *The Journal of Physical Chemistry A*, 113(26):7189–7204, 2009. doi: 10.1021/jp807966p. URL https://doi.org/10.1021/jp807966p. PMID: 19117383.

[131] Conformations of 1,2-dibromoethane http://butane.chem.uiuc.edu/jsmoore/chem232/notes_current/Conformation/NOTES-Anti_and_Gauche_Conformational_States.pdf.

[132] Atomic Calculation of Photoionization Cross-Sections and Asymmetry Parameters. The data are taken from: J.J. Yeh, Atomic Calculation of Photoionization Cross-Sections and Asymmetry Parameters, Gordon and Breach Science Publishers, Langhorne, PE (USA), 1993 and from J.J. Yeh and I.Lindau, Atomic Data and Nuclear Data Tables, 32, 1-155 (1985). https://vuo.elettra.eu/services/elements/mnu_elem.cgi?ACTION=SHOWGRAPH&ELEMENT=br&C0=3d&C3=4p&C4=4s.

[133] X-RAY DATA BOOKLET, Center for X-ray Optics and Advanced Light Source, Lawrence Berkeley National Laboratory https://xdb.lbl.gov/xdb-new.pdf.

[134] Jens Viefhaus, Markus Braune, Sanja Korica, Axel Reinköster, Daniel Rolles, and Uwe Becker. Auger cascades versus direct double auger: relaxation processes following photoionization of the kr 3d and xe 4d, 3d inner shells. *Journal of Physics B: Atomic, Molecular and Optical Physics*, 38(21):3885–3903, oct 2005. doi: 10.1088/0953-4075/38/21/011. URL https://doi.org/10.1088/0953-4075/38/21/011.

[135] J. Viefhaus, A.N. Grum-Grzhimailo, N.M. Kabachnik, and U. Becker. Electron–electron coincidence study of double auger processes in atoms. *Journal of Electron Spectroscopy and Related Phenomena*, 141(2):121–126, 2004. ISSN 0368-2048. doi: https://doi.org/10.1016/j.elspec.2004.06.013. URL https://www.sciencedirect.com/science/article/pii/S0368204804003305. Frontiers of Coincidence Experiments.

[136] Thomas A. Carlson and Manfred O. Krause. Experimental evidence for double electron emission in an auger process. *Phys. Rev. Lett.*, 14:390–392, Mar 1965. doi: 10.1103/PhysRevLett.14.390. URL https://link.aps.org/doi/10.1103/PhysRevLett.14.390.

[137] Thomas A. Carlson and Manfred O. Krause. Measurement of the electron energy spectrum resulting from a double auger process in argon. *Phys. Rev. Lett.*, 17:1079–1083, Nov 1966. doi: 10.1103/PhysRevLett.17.1079. URL https://link.aps.org/doi/10.1103/PhysRevLett.17.1079.

[138] Dissertation - Scattering and Coherence Phenomena in the Photoionization of Small Molecules by Daniel Rolles https://depositonce.tu-berlin.de/bitstream/11303/1382/1/Dokument_42.pdf.

[139] Shizuka Hsieh and John H D Eland. Reaction dynamics of three-body dissociations in triatomic molecules from single-photon double ionization studied by a time- and position-sensitive coincidence method. *Journal of Physics B: Atomic, Molecular and Optical Physics*, 30(20):4515–4534, oct 1997. doi: 10.1088/0953-4075/30/20/015. URL https://doi.org/10.1088/0953-4075/30/20/015.

[140] R.H. Dalitz. Cxii. on the analysis of -meson data and the nature of the -meson. *The London, Edinburgh, and Dublin Philosophical Magazine and Journal of Science*, 44 (357):1068–1080, 1953. doi: 10.1080/14786441008520365. URL https://doi.org/10.1080/14786441008520365.

[141] Shashank Pathak, Razib Obaid, Surjendu Bhattacharyya, Johannes Bürger, Xiang Li, Jan Tross, Travis Severt, Brandin Davis, René C. Bilodeau, Carlos A. Trallero-Herrero, Artem Rudenko, Nora Berrah, and Daniel Rolles. Differentiating and quantifying gas-phase conformational isomers using coulomb explosion imaging. *The Journal of Physical Chemistry Letters*, 11(23):10205–10211, 2020. doi: 10.1021/acs.jpclett.0c02959. URL https://doi.org/10.1021/acs.jpclett.0c02959. PMID: 33206545.

[142] Jyoti Rajput, T. Severt, Ben Berry, Bethany Jochim, Peyman Feizollah, Balram Kaderiya, M. Zohrabi, U. Ablikim, Farzaneh Ziaee, Kanaka Raju P., D. Rolles, A. Rudenko, K. D. Carnes, B. D. Esry, and I. Ben-Itzhak. Native frames: Disentangling sequential from concerted three-body fragmentation. *Phys. Rev. Lett.*, 120: 103001, Mar 2018. doi: 10.1103/PhysRevLett.120.103001. URL https://link.aps.org/doi/10.1103/PhysRevLett.120.103001.

[143] Dissertation - Imaging light-induced molecular fragmentation dynamics by Travis Severt, Kansas State University, 2021.

[144] Supplementary Information - Differentiating and Quantifying Gas-Phase Conformational Isomers Using Coulomb Explosion Imaging https://pubs.acs.org/doi/suppl/10.1021/acs.jpclett.0c02959/suppl_file/jz0c02959_si_001.pdf.

[145] Benji Wales, Éric Bisson, Reza Karimi, Samuel Beaulieu, Ali Ramadhan, Mathieu Giguère, ZiJian Long, Wing-Ki Liu, Jean-Claude Kieffer, François Légaré, and Joseph Sanderson. Coulomb imaging of the concerted and stepwise break up processes of ocs ions in intense femtosecond laser radiation. *Journal of Electron Spectroscopy and Related Phenomena*, 195:332–336, 2014. ISSN 0368-2048. doi: https://doi.org/10.1016/j.elspec.2014.05.003. URL https://www.sciencedirect.com/science/article/pii/S0368204814001121.

[146] Zhenjie Shen, Enliang Wang, Maomao Gong, Xu Shan, and Xiangjun Chen. Fragmentation dynamics of carbonyl sulfide in collision with 500 ev electron. *The Journal of Chemical Physics*, 145(23):234303, 2016. doi: 10.1063/1.4972064. URL https://doi.org/10.1063/1.4972064.

[147] Chengyin Wu, Cong Wu, Yameng Fan, Xiguo Xie, Peng Wang, Yongkai Deng, Yunquan Liu, and Qihuang Gong. Three-body fragmentation of CO_2 driven by intense laser pulses. *The Journal of Chemical Physics*, 142(12):124303, 2015. doi: 10.1063/1.4916045. URL https://doi.org/10.1063/1.4916045.

[148] N. Neumann, D. Hant, L. Ph. H. Schmidt, J. Titze, T. Jahnke, A. Czasch, M. S. Schöffler, K. Kreidi, O. Jagutzki, H. Schmidt-Böcking, and R. Dörner. Fragmentation dynamics of CO_2^{3+} investigated by multiple electron capture in collisions with slow highly charged ions. *Phys. Rev. Lett.*, 104:103201.

[149] Akiyoshi Hishikawa, Akitaka Matsuda, Mizuho Fushitani, and Eiji J. Takahashi. Visualizing recurrently migrating hydrogen in acetylene dication by intense ultrashort laser pulses. *Phys. Rev. Lett.*, 99:258302, Dec 2007. doi: 10.1103/PhysRevLett.99.258302. URL https://link.aps.org/doi/10.1103/PhysRevLett.99.258302.

[150] Akitaka Matsuda, Mizuho Fushitani, Eiji J. Takahashi, and Akiyoshi Hishikawa. Visualizing hydrogen atoms migrating in acetylene dication by time-resolved three-body and four-body coulomb explosion imaging. *Phys. Chem. Chem. Phys.*, 13:8697–8704, 2011. doi: 10.1039/C0CP02333G. URL http://dx.doi.org/10.1039/C0CP02333G.

[151] Akiyoshi Hishikawa, Akitaka Matsuda, Eiji J. Takahashi, and Mizuho Fushitani. Acetylene-vinylidene isomerization in ultrashort intense laser fields studied by triple ion-coincidence momentum imaging. *The Journal of Chemical Physics*, 128(8):084302, 2008. doi: 10.1063/1.2828557. URL https://doi.org/10.1063/1.2828557.

[152] Shin-ichi Nagaoka, Hironobu Fukuzawa, Georg Prümper, Mai Takemoto, Osamu Takahashi, Katsuhiro Yamaguchi, Takuhiro Kakiuchi, Kiyohiko Tabayashi, Isao H. Suzuki, James R. Harries, Yusuke Tamenori, and Kiyoshi Ueda. A study to control chemical reactions using si:2p core ionization: Site-specific fragmentation. *The Journal of Physical Chemistry A*, 115(32):8822–8831, 2011. doi: 10.1021/jp203664r. URL https://doi.org/10.1021/jp203664r.

[153] J.H.D. Eland, P. Linusson, M. Mucke, and R. Feifel. Homonuclear site-specific photochemistry by an ion–electron multi-coincidence spectroscopy technique. *Chemical Physics Letters*, 548:90–94, 2012. ISSN 0009-2614. doi: https://doi.org/10.1016/j.

cplett.2012.08.018. URL https://www.sciencedirect.com/science/article/pii/S0009261412009347.

[154] H. Iwayama, N. Sisourat, P. Lablanquie, F. Penent, J. Palaudoux, L. Andric, J. H. D. Eland, K. Bučar, M. Žitnik, Y. Velkov, Y. Hikosaka, M. Nakano, and E. Shigemasa. A local chemical environment effect in site-specific auger spectra of ethyl trifluoroacetate. *The Journal of Chemical Physics*, 138(2):024306, 2013. doi: 10.1063/1.4773294. URL https://doi.org/10.1063/1.4773294.

[155] T. Baer, A. Bodi, and B. Sztáray. Photoelectron–photoion coincidence methods in mass spectrometry, (pepico). In John C. Lindon, George E. Tranter, and David W. Koppenaal, editors, *Encyclopedia of Spectroscopy and Spectrometry (Third Edition)*, pages 635–649. Academic Press, Oxford, third edition edition, 2017. ISBN 978-0-12-803224-4. doi: https://doi.org/10.1016/B978-0-12-409547-2.11311-3. URL https://www.sciencedirect.com/science/article/pii/B9780124095472113113.

[156] P. Bolognesi, J. A. Kettunen, A. Cartoni, R. Richter, S. Tosic, S. Maclot, P. Rousseau, R. Delaunay, and L. Avaldi. Site- and state-selected photofragmentation of 2br-pyrimidine. *Phys. Chem. Chem. Phys.*, 17:24063–24069, 2015. doi: 10.1039/C5CP02601F. URL http://dx.doi.org/10.1039/C5CP02601F.

[157] E. Kukk, D. T. Ha, Y. Wang, D. G. Piekarski, S. Diaz-Tendero, K. Kooser, E. Itälä, H. Levola, M. Alcamí, E. Rachlew, and F. Martín. Internal energy dependence in x-ray-induced molecular fragmentation: An experimental and theoretical study of thiophene. *Phys. Rev. A*, 91:043417, Apr 2015. doi: 10.1103/PhysRevA.91.043417. URL https://link.aps.org/doi/10.1103/PhysRevA.91.043417.

[158] Peter Salén, Luca Schio, Robert Richter, Michele Alagia, Stefano Stranges, and Vitali Zhaunerchyk. Resonant auger electron-ion-coincidence spectroscopy of *n*-methyltrifluoroacetamide: Site-specific fragmentation studies. *Phys. Rev. A*, 102:

032817, Sep 2020. doi: 10.1103/PhysRevA.102.032817. URL https://link.aps.org/doi/10.1103/PhysRevA.102.032817.

[159] D. T. Ha, M. A. Huels, M. Huttula, S. Urpelainen, and E. kukk. Experimental and ab initio study of the photofragmentation of dna and rna sugars. *Phys. Rev. A*, 84: 033419, Sep 2011. doi: 10.1103/PhysRevA.84.033419. URL https://link.aps.org/doi/10.1103/PhysRevA.84.033419.

[160] Marius Gerlach, Felipe Fantuzzi, Lilith Wohlfart, Karina Kopp, Bernd Engels, John Bozek, Christophe Nicolas, Dennis Mayer, Markus Gühr, Fabian Holzmeier, and Ingo Fischer. Fragmentation of isocyanic acid, hnco, following core excitation and ionization. *The Journal of Chemical Physics*, 154(11):114302, 2021. doi: 10.1063/5.0044506. URL https://doi.org/10.1063/5.0044506.

[161] A. Lafosse, M. Lebech, J. C. Brenot, P. M. Guyon, O. Jagutzki, L. Spielberger, M. Vervloet, J. C. Houver, and D. Dowek. Vector correlations in dissociative photoionization of diatomic molecules in the vuv range: Strong anisotropies in electron emission from spatially oriented no molecules. *Phys. Rev. Lett.*, 84:5987–5990, Jun 2000. doi: 10.1103/PhysRevLett.84.5987. URL https://link.aps.org/doi/10.1103/PhysRevLett.84.5987.

[162] Etienne Gagnon, Predrag Ranitovic, Xiao-Min Tong, C. L. Cocke, Margaret M. Murnane, Henry C. Kapteyn, and Arvinder S. Sandhu. Soft x-ray-driven femtosecond molecular dynamics. *Science*, 317(5843):1374–1378, 2007. ISSN 0036-8075. doi: 10.1126/science.1144920. URL https://science.sciencemag.org/content/317/5843/1374.

[163] Arvinder S. Sandhu, Etienne Gagnon, Robin Santra, Vandana Sharma, Wen Li, Phay Ho, Predrag Ranitovic, C. Lewis Cocke, Margaret M. Murnane, and Henry C. Kapteyn. Observing the creation of electronic feshbach resonances in soft x-ray–induced o2 dissociation. *Science*, 322(5904):1081–1085, 2008. ISSN 0036-8075.

doi: 10.1126/science.1164498. URL https://science.sciencemag.org/content/322/5904/1081.

[164] R Wehlitz and T Hartman. Double photoionization of thiophene. *Journal of Physics: Conference Series*, 493:012002, mar 2014. doi: 10.1088/1742-6596/493/1/012002. URL https://doi.org/10.1088/1742-6596/493/1/012002.

[165] P. Linusson, L. Storchi, F. Heijkenskjöld, E. Andersson, M. Elshakre, B. Pfeifer, M. Colombet, J. H. D. Eland, L. Karlsson, J.-E. Rubensson, F. Tarantelli, and R. Feifel. Double photoionization of thiophene and bromine-substituted thiophenes. *The Journal of Chemical Physics*, 129(23):234303, 2008. doi: 10.1063/1.3039082. URL https://doi.org/10.1063/1.3039082.

[166] Jason R. Gascooke, Stephen T. Gibson, and Warren D. Lawrance. A "circularisation" method to repair deformations and determine the centre of velocity map images. *The Journal of Chemical Physics*, 147(1):013924, 2017. doi: 10.1063/1.4981024. URL https://doi.org/10.1063/1.4981024.

[167] PyAbel - Circularization of images https://pyabel.readthedocs.io/en/latest/circularize_image.html.

[168] David A. Shirley Uwe Becker. *VUV and Soft X-Ray Photoionization*. Springer, Boston, MA, 1996.

[169] P. B. Corkum and Ferenc Krausz. Attosecond science. *Nature Physics*, 3(6):381–387, Jun 2007. ISSN 1745-2481. doi: 10.1038/nphys620. URL https://doi.org/10.1038/nphys620.

[170] D. G. Lee, J. J. Park, J. H. Sung, and C. H. Nam. Wave-front phase measurements of high-order harmonic beams by use of point-diffraction interferometry. *Opt. Lett.*, 28(6):480–482, Mar 2003. doi: 10.1364/OL.28.000480. URL http://ol.osa.org/abstract.cfm?URI=ol-28-6-480.

[171] T. Ditmire, E. T. Gumbrell, R. A. Smith, J. W. G. Tisch, D. D. Meyerhofer, and M. H. R. Hutchinson. Spatial coherence measurement of soft x-ray radiation produced by high order harmonic generation. *Phys. Rev. Lett.*, 77:4756–4759, Dec 1996. doi: 10.1103/PhysRevLett.77.4756. URL https://link.aps.org/doi/10.1103/PhysRevLett.77.4756.

[172] Randy A. Bartels, Ariel Paul, Hans Green, Henry C. Kapteyn, Margaret M. Murnane, Sterling Backus, Ivan P. Christov, Yanwei Liu, David Attwood, and Chris Jacobsen. Generation of spatially coherent light at extreme ultraviolet wavelengths. *Science*, 297 (5580):376–378, 2002. ISSN 0036-8075. doi: 10.1126/science.1071718. URL https://science.sciencemag.org/content/297/5580/376.

[173] Craig Benko, Thomas K. Allison, Arman CingÃ¶z, Linqiang Hua, FranÃ§ois Labaye, Dylan C. Yost, and Jun Ye. Extreme ultraviolet radiation with coherence time greater than 1â s. *Nature Photonics*, 8(7):530–536, Jul 2014. ISSN 1749-4893. doi: 10.1038/nphoton.2014.132. URL https://doi.org/10.1038/nphoton.2014.132.

[174] Chii-Dong Lin Anh-Thu Le Cheng Jin, Hui Wei. Attosecond and strong-field physics. *Cambridge University Press*, 2018.

[175] Praveen Kumar Maroju, Cesare Grazioli, Michele Di Fraia, Matteo Moioli, Dominik Ertel, Hamed Ahmadi, Oksana Plekan, Paola Finetti, Enrico Allaria, Luca Giannessi, Giovanni De Ninno, Carlo Spezzani, Giuseppe Penco, Simone Spampinati, Alexander Demidovich, Miltcho B. Danailov, Roberto Borghes, George Kourousias, Carlos Eduardo Sanches Dos Reis, Fulvio Billé, Alberto A. Lutman, Richard J. Squibb, Raimund Feifel, Paolo Carpeggiani, Maurizio Reduzzi, Tommaso Mazza, Michael Meyer, Samuel Bengtsson, Neven Ibrakovic, Emma Rose Simpson, Johan Mauritsson, Tamás Csizmadia, Mathieu Dumergue, Sergei Kühn, Harshitha Nandiga Gopalakrishna, Daehyun You, Kiyoshi Ueda, Marie Labeye, Jens Egebjerg Bkhøj, Kenneth J. Schafer, Elena V. Gryzlova, Alexei N. Grum-Grzhimailo, Kevin C. Prince, Carlo Callegari, and Giuseppe

Sansone. Attosecond pulse shaping using a seeded free-electron laser. *Nature*, 578 (7795):386–391, Feb 2020. ISSN 1476-4687. doi: 10.1038/s41586-020-2005-6. URL https://doi.org/10.1038/s41586-020-2005-6.

[176] Joseph Duris, Siqi Li, Taran Driver, Elio G. Champenois, James P. MacArthur, Alberto A. Lutman, Zhen Zhang, Philipp Rosenberger, Jeff W. Aldrich, Ryan Coffee, Giacomo Coslovich, Franz-Josef Decker, James M. Glownia, Gregor Hartmann, Wolfram Helml, Andrei Kamalov, Jonas Knurr, Jacek Krzywinski, Ming-Fu Lin, Jon P. Marangos, Megan Nantel, Adi Natan, Jordan T. Oâ€™Neal, Niranjan Shivaram, Peter Walter, Anna Li Wang, James J. Welch, Thomas J. A. Wolf, Joseph Z. Xu, Matthias F. Kling, Philip H. Bucksbaum, Alexander Zholents, Zhirong Huang, James P. Cryan, and Agostino Marinelli. Tunable isolated attosecond x-ray pulses with gigawatt peak power from a free-electron laser. *Nature Photonics*, 14(1):30–36, Jan 2020. ISSN 1749-4893. doi: 10.1038/s41566-019-0549-5. URL https://doi.org/10.1038/s41566-019-0549-5.

[177] Jeffrey L. Krause, Kenneth J. Schafer, and Kenneth C. Kulander. High-order harmonic generation from atoms and ions in the high intensity regime. *Phys. Rev. Lett.*, 68:3535–3538, Jun 1992. doi: 10.1103/PhysRevLett.68.3535. URL https://link.aps.org/doi/10.1103/PhysRevLett.68.3535.

[178] P. B. Corkum. Plasma perspective on strong field multiphoton ionization. *Phys. Rev. Lett.*, 71:1994–1997, Sep 1993. doi: 10.1103/PhysRevLett.71.1994. URL https://link.aps.org/doi/10.1103/PhysRevLett.71.1994.

[179] K. J. Schafer, Baorui Yang, L. F. DiMauro, and K. C. Kulander. Above threshold ionization beyond the high harmonic cutoff. *Phys. Rev. Lett.*, 70:1599–1602, Mar 1993. doi: 10.1103/PhysRevLett.70.1599. URL https://link.aps.org/doi/10.1103/PhysRevLett.70.1599.

[180] XUUS – high harmonic generation source for EUV and soft X-ray, https://www.kmlabs.com/product/xuus/.

[181] B.L. Henke, E.M. Gullikson, and J.C. Davis. X-ray interactions: Photoabsorption, scattering, transmission, and reflection at E = 50-30,000 eV, Z = 1-92. *Atomic Data and Nuclear Data Tables*, 54(2):181–342, 1993. ISSN 0092-640X. doi: https://doi.org/10.1006/adnd.1993.1013. URL https://www.sciencedirect.com/science/article/pii/S0092640X83710132.

[182] X-Ray Interactions With Matter https://henke.lbl.gov/optical_constants/.

[183] D.M.P. Holland, L. Karlsson, and W. von Niessen. The identification of the outer valence shell -photoelectron bands in furan, pyrrole and thiophene. *Journal of Electron Spectroscopy and Related Phenomena*, 113(2):221–239, 2001. ISSN 0368-2048. doi: https://doi.org/10.1016/S0368-2048(00)00427-8. URL https://www.sciencedirect.com/science/article/pii/S0368204800004278.

[184] E.E. Rennie, L. Cooper, C.A.F. Johnson, J.E. Parker, R.A. Mackie, L.G. Shpinkova, D.M.P. Holland, D.A. Shaw, and M.A. Hayes. A study of the unimolecular decomposition of internal-energy-selected furan molecular ions by threshold-photoelectron–photoion coincidence spectroscopy. *Chemical Physics*, 263(1):149–165, 2001. ISSN 0301-0104. doi: https://doi.org/10.1016/S0301-0104(00)00346-3. URL https://www.sciencedirect.com/science/article/pii/S0301010400003463.

[185] Ewa Erdmann, Marta Łabuda, Néstor F. Aguirre, Sergio Díaz-Tendero, and Manuel Alcamí. Furan fragmentation in the gas phase: New insights from statistical and molecular dynamics calculations. *The Journal of Physical Chemistry A*, 122(16):4153–4166, 2018. doi: 10.1021/acs.jpca.8b00881. URL https://doi.org/10.1021/acs.jpca.8b00881.

[186] Avogadro: an open-source molecular builder and visualization tool. Version 1.2.0 https://avogadro.cc/.

[187] Marcus D. Hanwell, Donald E. Curtis, David C. Lonie, Tim Vandermeersch, Eva Zurek, and Geoffrey R. Hutchison. Avogadro: an advanced semantic chemical editor, visualization, and analysis platform. *Journal of Cheminformatics*, 4(1):17, Aug 2012. ISSN 1758-2946. doi: 10.1186/1758-2946-4-17. URL https://doi.org/10.1186/1758-2946-4-17.

Appendix A

Coulomb simulations for near-equlibrium geometries of *gauche* and *anti* conformations of 1,2-dibromoethane

This section discusses the coulomb simulations (CES) for the concerted breakup of 1,2-dibromoethane ($C_2H_4Br_2$, EDB) into the coincidence channel $C_2H_4^+ + {}^{81}Br^+ + {}^{81}Br^+$. The equilibrium geometries of *gauche* and *anti* conformations are first computed using the open-source package Avogadro [186, 187]. Classical CES are performed considering three point charges – one at the position of each of the two bromine atoms and the third charge at the center-of-mass (c.o.m.) of $C_2H_4^+$. In order to account for small geometry changes of the molecule, e.g., because of vibrations in the neutral or ionic states, either due to the initial temperature of the sample or due to vibrational excitation during the ionization process, we randomly vary the position of both bromine atoms within a sphere around their equilibrium position.

For the simulations shown in Chapter 4, the radius of this sphere is chosen to be 5% of

the C-Br bond distance. We generate 1000 randomly sampled pairs of bromine coordinates and determine the coordinate of a third point charge (at the c.o.m. of the $C_2H_4^+$ moiety) such that the c.o.m. of the distorted molecule remains the same as in the equilibrium geometry, since the c.o.m. of the molecule does not move during vibrations along the normal modes of the molecule. For each geometry, we consider the molecule to be at rest and neglect the velocity that an atom might possess due to vibrational motion. For each distribution of three point charges, the classical equations of motions under the influence of Coulomb repulsion are then solved using a standard ordinary differential equation solver to determine the trajectories and the asymptotic velocity/momentum of each charged fragment.

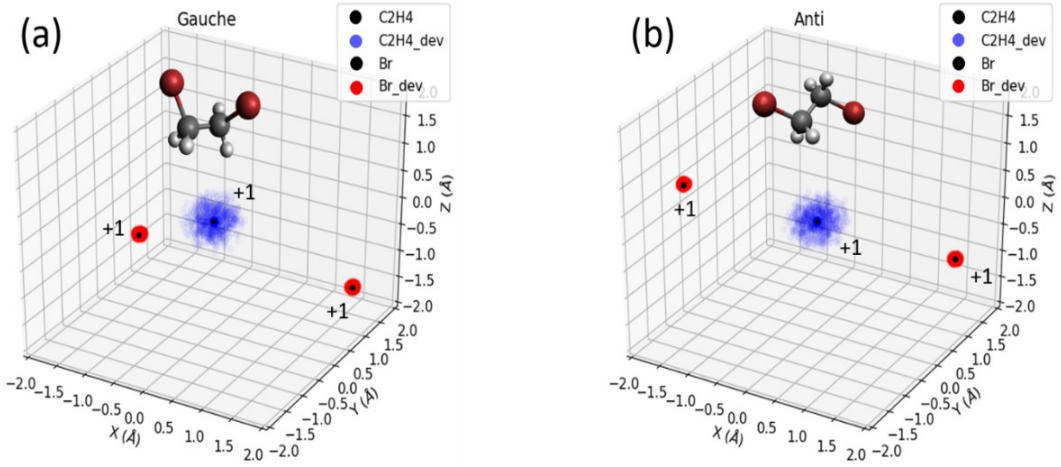

Figure A.1: *Distribution of point charges for 1000 randomly generated near-equilibrium geometries of (a) gauche and (b) anti conformations for which the Coulomb explosion simulations were performed (see text). The solid black dots show the equilibrium positions for the two bromine atoms and the c.o.m. of the C_2H_4. The red and blue dots show the deviation (from the equilibrium position) of bromine atoms and c.o.m. of C_2H_4 respectively, as chosen for the simulation (Adapted from [144]).*

The main goal behind choosing a uniform distribution of charge around the equilibrium positions of the two Br^+ atoms is to make a simple model to calculate the fragment kinetic energies that incorporate small geometry variations in the anti and gauche conformations without further knowledge of possible excitation mechanisms and modes. The radius of the uniform spherical distribution is simply chosen as X% of the C-Br bond length (X=5, as

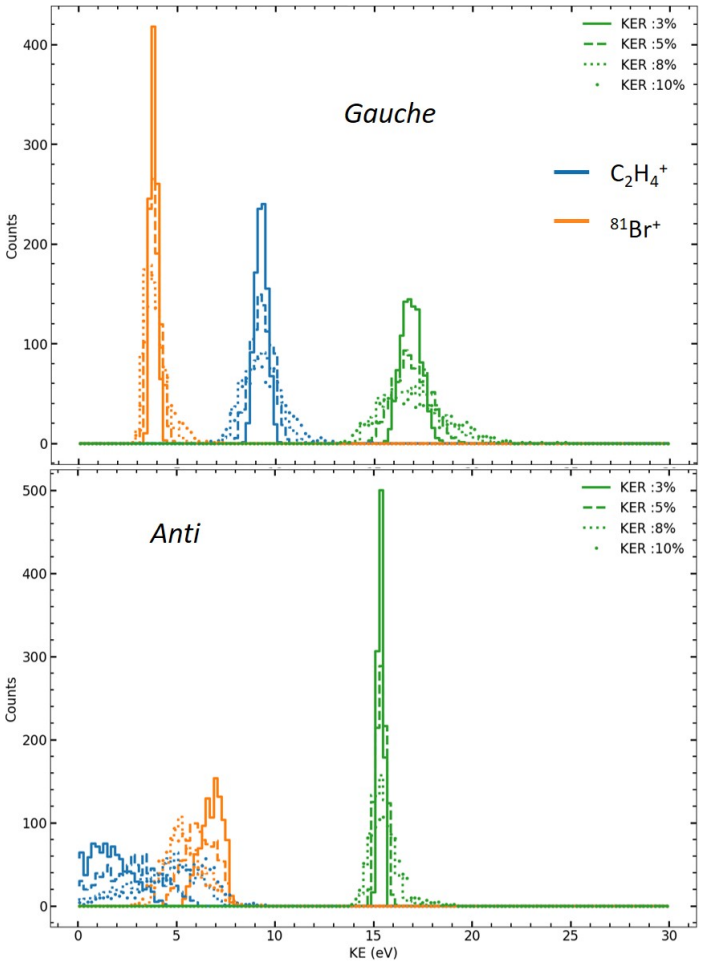

Figure A.2: *Simulations of kinetic energies for gauche and anti conformations assuming different radii of the distributions (see text).*

shown above). Despite its simplicity, the assumption of a spherical distribution produces an overall very reasonable agreement with the experimental data (see section 4.4 and 4.6). However, the simulation starts to deviate if we choose a significantly larger radius of the spherical distribution. To expand on this further, Fig. A.2 shows plots with the simulations for *gauche* and *anti* conformations assuming different radii of the distributions (X=3,5,8,10). A 5% change gives good agreement for the widths of the distributions for the gauche conformation while still reproducing the right energies and reasonable widths for the fragment distributions for the anti conformation. However, the simulated width of the KER distribution for the 'anti' conformation is indeed too narrow. For larger radii, the KER distribution

becomes wider, but the agreement for the fragments gets significantly worse. This suggests that the geometry variations cannot be approximated well by our simple model assuming uniform distributions and that detailed modeling incorporating specific vibrational modes might be required, which is beyond the scope of this work.

Appendix B

Ultrafast electron diffraction - extracting the static diffraction signal

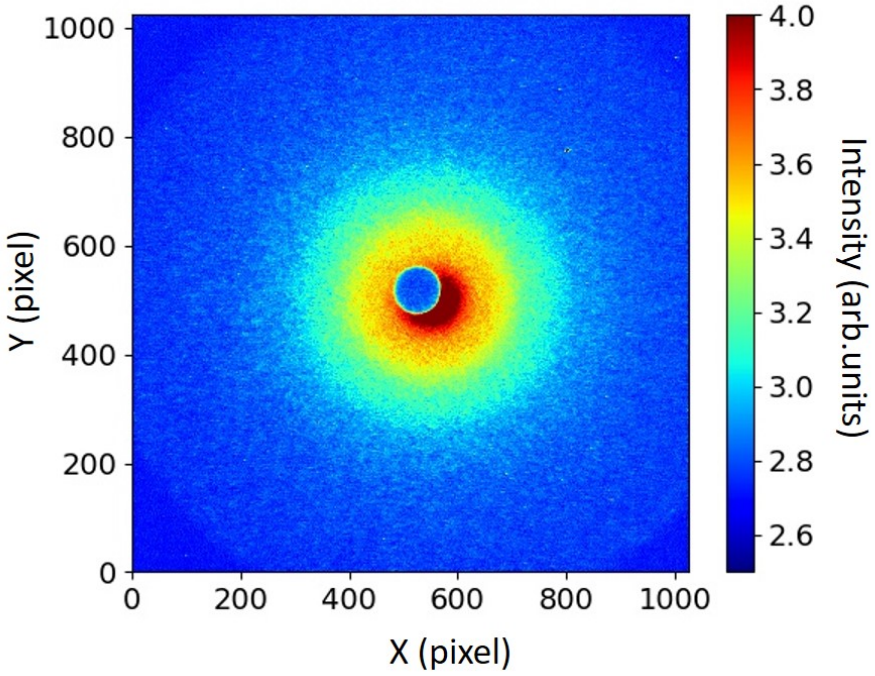

Figure B.1: *Electron diffraction image of thiophenone.*

To determine the static diffraction signal from the molecules, the diffraction images first need to be processed and cleaned. A diffraction image for the thiophenone molecules recorded at the MeV UED facility at SLAC national laboratory is shown in Fig. B.1. The first step in cleaning the diffraction images involves subtracting the baseline of the camera signal. This is done by subtracting the average counts in the four corners of the image shown in Fig. B.1.

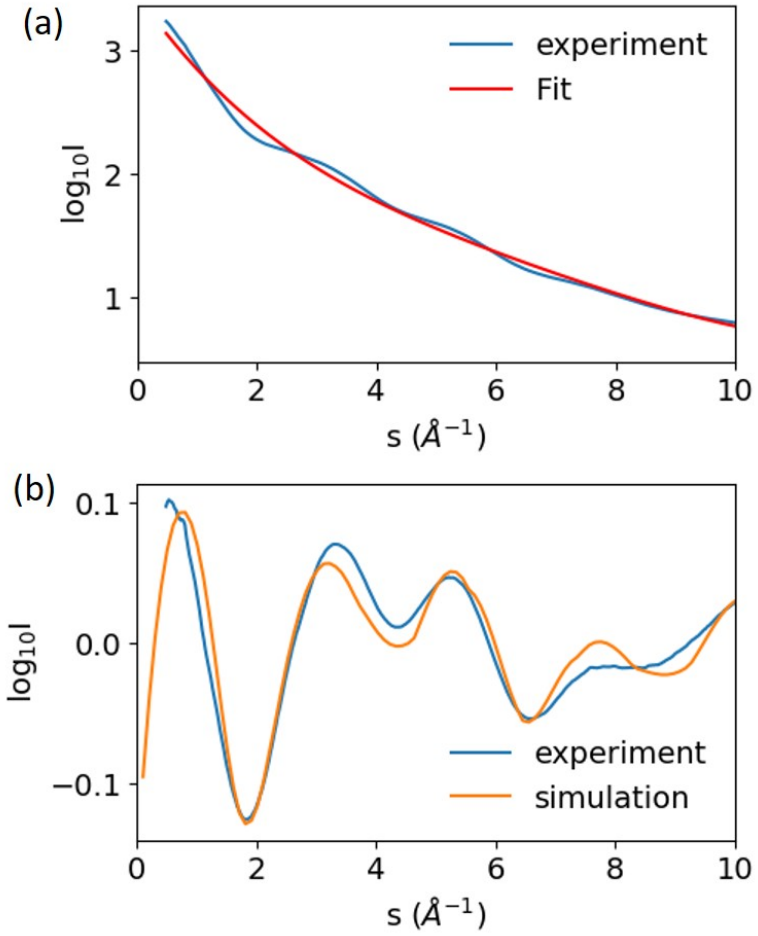

Figure B.2: *Comparing the static diffraction signal with a simulation. (a) The logarithm of total scattering intensity fitted with a fourth-order polynomial. (b) The fitting curve in (a) was subtracted from the logarithm of total scattering intensity for experiment and simulation.*

The next step is to remove the x-ray hits, which are often seen as long stripes in the image. To remove these hits, each diffraction image for the same temporal delay (between

UV and electron beam) is compared pixel-by-pixel. The pixels having counts more than four standard deviations over the mean of identical pixels are removed. This procedure is repeated for all time delays. After this, any remaining artifacts in the detector image are carefully removed. Once all the steps above are performed, the center of the image is determined.

After carefully determining the center of the diffraction images, the intensities can be azimuthally summed for negative delays (electron beam preceding UV) to determine the static diffraction signal. To determine the molecular scattering intensity (I_M), the atomic intensities must be subtracted from the total scattering intensity. Figure B.2(a) shows the logarithm of total scattering intensity observed in the experiment fitted with a fourth-order polynomial. Figure B.2(b) shows the difference between the experiment and fit shown in Fig. B.2(a) plotted for both experiment and simulation. A good agreement in peak positions between the experiment and simulation in Fig. B.2(b) confirms the pixel calibration value.

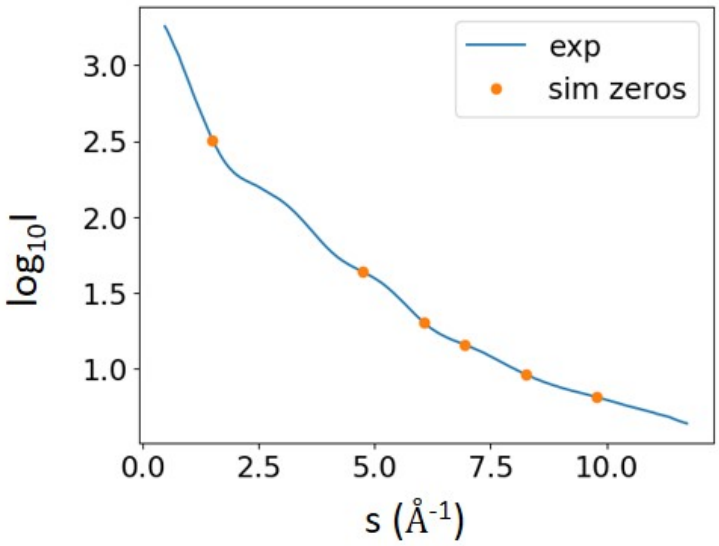

Figure B.3: *Determining experimental sM(s) using zero crossings from simulation. The orange points correspond to the s values for which the simulated sM(s) is zero.*

For determining modified molecular scattering intensity (sM), the zero-crossings from

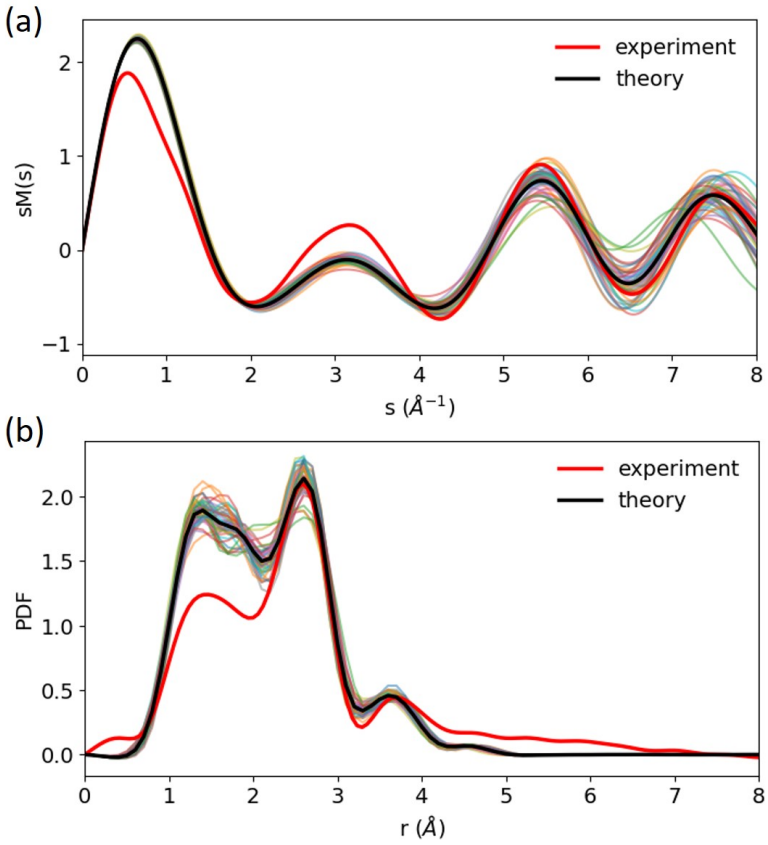

Figure B.4: *Static diffraction signal for thiophenone. (a) sM(s). (b) PDF(r).*

the simulations are used in order to fit the background precisely [75]. Figure B.3 shows the logarithm of total scattering intensity with the zero-crossing points marked in orange. Figure B.4 shows the sM(s) and PDF(r) after using the simulated zero-crossing points for the subtraction of background. The black curve in Figure B.4 from theory is the mean of simulations for different geometries sampled from the Wigner distribution of ground state thiophenone molecules (see section 3.5.1). The simulations from the individual geometries can be seen in the light color distribution around the mean. The experiment and theory show a slight disagreement which can be due to improper subtraction of background or the presence of other geometries.